frontiers | Research Topics

Genetic engineering, pretreatment, thermochemical, and biochemconversion for lignocellulose valorization

Edited by
Xiaojun Shen, Chen Huang, Chaofeng Zhang, Arthur Jonas Ragauskas and Jia-Long Wen

Published in
Frontiers in Bioengineering and Biotechnology

ISSN 1664-8714
ISBN 978-2-8325-3406-9
DOI 10.3389/978-2-8325-3406-9

About Frontiers

Frontiers is more than just an open access publisher of scholarly articles: it is a pioneering approach to the world of academia, radically improving the way scholarly research is managed. The grand vision of Frontiers is a world where all people have an equal opportunity to seek, share and generate knowledge. Frontiers provides immediate and permanent online open access to all its publications, but this alone is not enough to realize our grand goals.

Frontiers journal series

The Frontiers journal series is a multi-tier and interdisciplinary set of open-access, online journals, promising a paradigm shift from the current review, selection and dissemination processes in academic publishing. All Frontiers journals are driven by researchers for researchers; therefore, they constitute a service to the scholarly community. At the same time, the *Frontiers journal series* operates on a revolutionary invention, the tiered publishing system, initially addressing specific communities of scholars, and gradually climbing up to broader public understanding, thus serving the interests of the lay society, too.

Dedication to quality

Each Frontiers article is a landmark of the highest quality, thanks to genuinely collaborative interactions between authors and review editors, who include some of the world's best academicians. Research must be certified by peers before entering a stream of knowledge that may eventually reach the public - and shape society; therefore, Frontiers only applies the most rigorous and unbiased reviews. Frontiers revolutionizes research publishing by freely delivering the most outstanding research, evaluated with no bias from both the academic and social point of view. By applying the most advanced information technologies, Frontiers is catapulting scholarly publishing into a new generation.

What are Frontiers Research Topics?

Frontiers Research Topics are very popular trademarks of the *Frontiers journals series*: they are collections of at least ten articles, all centered on a particular subject. With their unique mix of varied contributions from Original Research to Review Articles, Frontiers Research Topics unify the most influential researchers, the latest key findings and historical advances in a hot research area.

Find out more on how to host your own Frontiers Research Topic or contribute to one as an author by contacting the Frontiers editorial office: frontiersin.org/about/contact

Genetic engineering, pretreatment, thermochemical, and biochemconversion for lignocellulose valorization

Topic editors

Xiaojun Shen — Beijing Forestry University, China

Chen Huang — Institute of Chemical Industry of Forest Products, Chinese Academy of Forestry, China

Chaofeng Zhang — Nanjing Forestry University, China

Arthur Jonas Ragauskas — The University of Tennessee, Knoxville, United States

Jia-Long Wen — Beijing Forestry University, China

Citation

Shen, X., Huang, C., Zhang, C., Ragauskas, A. J., Wen, J.-L., eds. (2023). *Genetic engineering, pretreatment, thermochemical, and biochemconversion for lignocellulose valorization*. Lausanne: Frontiers Media SA.

doi: 10.3389/978-2-8325-3406-9

Table of contents

frontiers | Frontiers in Bioengineering and Biotechnology

TYPE Editorial
PUBLISHED 21 August 2023
DOI 10.3389/fbioe.2023.1265271

OPEN ACCESS

EDITED AND REVIEWED BY
Alirio Rodrigues,
University of Porto, Portugal

*CORRESPONDENCE
Xiaojun Shen,
shenxiaojun@bjfu.edu.cn
Chen Huang,
huangchen3127@njfu.edu.cn

RECEIVED 22 July 2023
ACCEPTED 31 July 2023
PUBLISHED 21 August 2023

CITATION
Shen X, Wen J-L, Huang C, Ragauskas AJ and Zhang C (2023), Editorial: Genetic engineering, pretreatment, thermochemical, and biochemconversion for lignocellulose valorization.
Front. Bioeng. Biotechnol. 11:1265271.
doi: 10.3389/fbioe.2023.1265271

Editorial: Genetic engineering, pretreatment, thermochemical, and biochemconversion for lignocellulose valorization

Xiaojun Shen[1]*, Jia-Long Wen[1], Chen Huang[2]*, Arthur J. Ragauskas[3,4,5] and Chaofeng Zhang[6]

[1]Beijing Key Laboratory of Lignocellulosic Chemistry, Beijing Forestry University, Beijing, China, [2]Jiangsu Province Key Laboratory of Biomass Energy and Materials, Institute of Chemical Industry of Forest Products, Chinese Academy of Forestry, Nanjing, China, [3]Department of Chemical and Biomolecular Engineering, University of Tennessee Knoxville, Knoxville, TN, United States, [4]Department of Forestry Wildlife and Fisheries, Center for Renewable Carbon, The University of Tennessee Institute of Agriculture, Knoxville, TN, United States, [5]Joint Institute for Biological Science, Biosciences Division, Oak Ridge National Laboratory, Oak Ridge, TN, United States, [6]Jiangsu Co-Innovation Center of Efficient Processing and Utilization of Forest Resources, College of Light Industry and Food Engineering, Nanjing Forestry University, Nanjing, China

KEYWORDS

lignocellulose, fractionation, structural characterization, genetic engineering, enzymatic hydrolysis, thermconversion, bioconversion

Editorial on the Research Topic
Genetic engineering, pretreatment, thermochemical, and biochemconversion for lignocellulose valorization

Introduction

Lignocellulosic biomass, comprising cellulose, hemicelluloses, and lignin, is a remarkable renewable resource with the potential to replace fossil feedstocks and drive a sustainable bioeconomy (Queneau and Han, 2022; Shen et al., 2022). However, the complex structure of lignocellulose presents challenges in effectively converting it into high-value products (Huang et al., 2022; Cai et al., 2023). The need to unlock its full potential has led to the development of biorefineries, aiming to fractionate lignocellulose and convert it into bioenergy, biomaterials, and biochemicals. Since the complex compositional structure of lignocellulosic biomass and biomass recalcitrance severely inhibited their effective conversion and selective production of high-value products. To overcome this disadvantage, using genetic and chemical approaches can modify cell wall composition and change interactions between the major cell wall polymers-cellulose, hemicelluloses and lignin, which would reduce the biomass recalcitrance and facilitate the subsequent fractionation and conversion of the feedstocks (Huang et al., 2022). Despite its vast potential, only a small fraction of lignocellulose is currently valorized, with the majority being wasted or burned. To address this issue, advanced technologies, including genetic, biotechnological, and chemical approaches, are required to fractionate and convert lignocellulose into valuable products efficiently.

The Research Topic "*Genetic engineering, pretreatment, thermochemical, and biochemconversion for lignocellulose valorization*" covers the new biotechnological approaches for value-added utilization of biomass, new biomass fractionation techniques for improving lignin and cellulose quality, new catalytic biomass valorization strategies, and applications of lignocellulosic materials and derivatives in related fields. Here, we sincerely appreciate the 61 authors for their excellent work on this Research Topic. Following are the highlights drawn from their contributions to this Research Topic.

New biotechnological approaches for value-added utilization of biomass

In the enzymatic hydrolysis process of cellulose, the presence of lignin leads to non-specific adsorption of cellulose hydrolyzing enzymes, resulting in low cellulose conversion rates. Additionally, water-soluble lignin in the liquid phase also acts as an inhibitor of enzymatic hydrolysis. Therefore, the existence of lignin has long been a hindrance to the conversion of carbohydrate biomass. Tang et al. addressed this issue by subjecting pretreated residues to enzymatic hydrolysis for glucose production, during which lytic polysaccharide monooxygenase (LPMO) was introduced. Despite the presence of lignin, the cellulose enzymatic hydrolysis conversion rate was increased by 25%, surpassing the enhancement achieved with microcrystalline cellulose by 14%. This significant improvement is mainly attributed to lignin and its derivatives serving as electron donors, facilitating LPMO in catalyzing the oxidative cleavage of glycosidic bonds in cellulose, thus generating more targets for hydrolysis. This study offers a novel approach to overcoming the challenges posed by lignin during carbohydrate enzymatic conversion processes and provides new insights into the utilization of lignin in such contexts. Besides, Reger et al. developed a novel hybrid process strategy that tackles the key challenges of current biomanufacturing of either low productivity or high media consumption, representing a new and innovative approach for future process intensification efforts. In addition, most enzymes used for carbohydrate hydrolysis are mesophilic enzymes, limiting their industrial applications. Zhang et al. utilized thermophilic filamentous fungi to produce xylanase and obtained a heat-tolerant mutant M 2103, through atmospheric and room temperature plasma (ARTP) mutagenesis. The M 2103 mutant exhibited stable enzymatic activity for xylanase within a temperature range of 70°C–85°C, with an optimum temperature of 75°C, surpassing the wild-type strain by 15°C. The xylanase activity of the mutant increased by 21.71% compared to the original strain. This provides an alternative biocatalyst for producing xylo-oligosaccharides and holds promising potential in the mutagenesis of thermostable mutants. In addition to agricultural and forestry waste, cigar filler leaves, when subjected to fermentation using nine different aroma-producing yeasts, were found to possess distinct profiles that can enhance the quality of cigar filler leaves Yao et al.

New biomass fractionation techniques for improving lignin and cellulose quality

In plant cell walls, hemicellulose and lignin are linked by covalent and hydrogen bonds to form a heterogeneous structure, which wraps around cellulose, creating a robust "natural recalcitrance barrier." This barrier significantly limits the efficiency of biomass refinement. Pretreatment is essential to overcome biomass recalcitrance and achieve efficient fractionation of biomass components. Cui et al. employed a synthesized deep eutectic solvent of choline chloride/lactic acid combined with ethanol for the pretreatment of Broussonetia papyrifera, which efficiently separated cellulose and lignin. When the deep eutectic solvent and ethanol were mixed at a ratio of 1:1, and the pretreatment conditions were set at 160°C for 1 h, the majority of hemicellulose and lignin in the residue was removed, resulting in the highest cellulose enzymatic hydrolysis efficiency of up to 46.25%. Furthermore, the study revealed that with an increase in pretreatment temperature, the content of phenolic hydroxyl groups in the separated lignin also increased, enhancing the antioxidant capacity of lignin.

New catalytic biomass valorization strategies

The depolymerization of lignin to produce fuels and chemicals is crucial for converting lignocellulosic biomass into second-generation biofuels, promoting value-added utilization of lignin. Shao et al. employed formic acid as an *in-situ* hydrogen donor, and synergistically catalyzed the depolymerization of lignin using a noble metal catalyst Ru/C in combination with Lewis acid zinc chloride. Under the optimal process conditions, the bio-oil yield reached 91.1 wt%, with monomer yield accounting for 13.4 wt%. The presence of Lewis acid promoted the formation of monomeric guaiacyl compounds and 2,3-dihydrobenzofurans during the reaction.

Compared to lignin, carbohydrates have a simpler structure and can be industrially prepared as chemicals, especially hemicellulose. Currently, cellulose and hemicellulose can be efficiently and selectively converted to produce a range of platform chemicals, which can increase the profitability of biomass refining. Hemicellulose-derived furfural is a sustainable alternative to petrochemical intermediates in bulk chemical and fuel production. However, existing methods for converting xylose or hemicellulose in single/dual-phase systems involve non-selective sugar separation or lignin condensation, limiting the value-added utilization of lignocellulosic biomass. Previously, Huang et al. achieved efficient biomass separation using an aldehyde protection system, obtaining diformylxylose. This aldehyde-protected xylose derivative can efficiently produce furfural in a dual-phase system. In a water-methyl isobutyl ketone biphase system, diformylxylose can be converted to more than 76 mol% furfural at higher temperatures and shorter reaction times, which is more than twice the conversion efficiency of free xylose without aldehyde protection. Moreover, due to the advantages of separating highly active lignin using the formaldehyde-stabilized fractionation method, this combined approach not only improves the conversion

efficiency from hemicellulose to furfural but also promotes the comprehensive utilization of the three main biopolymers in lignocellulose.

He et al. developed an efficient cascade reaction combining chemical catalysis and enzymatic biocatalysis to convert hemicellulose in lignocellulose to furfurylamine. Firstly, solid acid catalysis was used in a deep eutectic solvent composed of ethylenediamine hydrochloride and glycerol to convert hemicellulose to furfural efficiently. Subsequently, in the presence of NH_4Cl (as the amine donor), *Escherichia coli* CCZU-XLS160 cells effectively aminated the formed furfural to furfurylamine with a yield exceeding 99%.

Applications of lignocellulosic materials and derivatives in related fields

Currently, efficient separation of cellulose, hemicellulose, and lignin from lignocellulosic biomass can be achieved through specific isolation methods, promoting high-value utilization of individual components. Food safety is of paramount importance, making the production of food-safe detection materials from biobased materials highly attractive. Qin et al. successfully prepared starch films with pH-responsive and sensitive current responses by introducing innovative fractionation techniques, advanced characterization methods, and metabolic engineering strategies for carboxymethyl cellulose into starch. These films hold potential applications in rapid and real-time detection of liquid safety. Additionally, Xiang et al. utilized natural macromolecule xylan as a reducing and stabilizing agent to successfully synthesize stable bimetallic gold-silver nanoparticles, which were immobilized on paper surfaces to create paper-based surface-enhanced Raman scattering materials. This material effectively detected trace amounts of pesticides, showcasing the significant potential for rapid food safety monitoring.

Conclusion

This Research Topic represents a significant advancement in lignocellulosic biomass valorization. The articles collectively emphasize the need to exploit genetic, biotechnological, and chemical approaches to fully understand the heterogeneous structure of lignocellulose. Researchers can efficiently convert lignocellulose into high-value chemical products and functional materials through thermochemical and biochemical conversion by employing innovative fractionation techniques, advanced characterization methods, and metabolic engineering strategies. The successful implementation of these approaches holds great promise for achieving large-scale, cost-effective production of biofuels and biomaterials, contributing to a more sustainable and renewable future.

Author contributions

XS: Supervision, Writing–original draft, Writing–review and editing. J-LW: Writing–review and editing. CH: Writing–original draft, Writing–review and editing. AR: Writing–review and editing. CZ: Writing–review and editing.

Conflict of interest

The authors declare that the research was conducted in the absence of any commercial or financial relationships that could be construed as a potential conflict of interest.

The author(s) declared that they were an editorial board member of Frontiers, at the time of submission. This had no impact on the peer review process and the final decision.

Publisher's note

References

Cai, C., Zhang, C., Li, N., Liu, H., Xie, J., Lou, H., et al. (2023). Changing the role of lignin in enzymatic hydrolysis for a sustainable and efficient sugar platform. *Renew. Sustain. Energy Rev.* 183, 113445. doi:10.1016/j.rser.2023.113445

Huang, C., Jiang, X., Shen, X., Hu, J., Tang, W., Wu, X., et al. (2022). Lignin-enzyme interaction: A roadblock for efficient enzymatic hydrolysis of lignocellulosics. *Renew. Sustain. Energy Rev.* 154, 111822. doi:10.1016/j.rser.2021.111822

Queneau, Y., and Han, B. (2022). Biomass: Renewable carbon resource for chemical and energy industry. *innovation* 3, 100184. doi:10.1016/j.xinn.2021.100184

Shen, X., Zhang, C., Han, B., and Wang, F. (2022). Catalytic self-transfer hydrogenolysis of lignin with endogenous hydrogen: Road to the carbon-neutral future. *Chem. Soc. Rev.* 51, 1608–1628. doi:10.1039/d1cs00908g

frontiers | Frontiers in Bioengineering and Biotechnology

TYPE Original Research
PUBLISHED 30 September 2022
DOI 10.3389/fbioe.2022.1031152

OPEN ACCESS

EDITED BY
Chen Huang,
Chinese Academy of Forestry, China

REVIEWED BY
Qianqian Wang,
Jiangsu University, China
Zhe Ling,
Nanjing Forestry University, China

*CORRESPONDENCE
Zhouyang Xiang,
fezyxiang@scut.edu.cn
Xingxiang Ji,
xxjt78@163.com

SPECIALTY SECTION
This article was submitted to Bioprocess Engineering,
a section of the journal
Frontiers in Bioengineering and Biotechnology

RECEIVED 29 August 2022
ACCEPTED 12 September 2022
PUBLISHED 30 September 2022

CITATION
Xiang Z, He M, Li L, Bobokalonov J, Dzhonmurodov A and Ji X (2022), A xylan assisted surface-enhanced Raman scattering substrate for rapid food safety detection.
Front. Bioeng. Biotechnol. 10:1031152.
doi: 10.3389/fbioe.2022.1031152

A xylan assisted surface-enhanced Raman scattering substrate for rapid food safety detection

Zhouyang Xiang[1,2]*, Mengyun He[2], Li Li[2], Jamshed Bobokalonov[3], Abduvali Dzhonmurodov[3] and Xingxiang Ji[1]*

[1]State Key Laboratory of Biobased Material and Green Papermaking, Qilu University of Technology, Shandong Academy of Sciences, Jinan, China, [2]State Key Laboratory of Pulp and Paper Engineering, South China University of Technology, Guangzhou, China, [3]V.I. Nikitin Institute of Chemistry, National Academy of Sciences of Tajikistan, Dushanbe, Tajikistan

Cellulose fiber/paper-based surface-enhanced Raman scattering (SERS) is considered as a promising food safety detection technology due to its non-toxicity, low cost, flexibility, and hygroscopicity for possible rapid on-site agricultural product contaminant detection. However, it faces the problems of poor noble metal adhesion and toxic noble metal reducing agent. In this study, a natural macromolecule—xylan was used as both a reducing agent and a stabilizing agent to prepare stable Au-Ag bimetal nanoparticles, which were anchored on the paper surface by xylans in order to fabricate a paper-based Au-Ag bimetallic SERS substrate. The results show that the SERS substrate has a high Raman enhancement performance and reproductively. The substrate can effectively detect trace pesticide, i.e., thiram, and the limit of detection is as low as 1×10^{-6} mol/L (0.24 ppm). In addition, the paper-based SERS substrate can be used for direct detection of pesticide residues on the surface of fruit. The paper-based SERS substrate developed in this study has great potential in applications for rapid food safety detection.

KEYWORDS

xylan, bimetal nanoparticle, paper base, surface-enhanced Raman scattering, food safety detection

1 Introduction

Since food safety has become a worldwide issue, in the process of food production, processing, preservation, packaging, transportation and consumption, monitoring contaminants such as pesticides, antibiotics, illegal additives, bacteria, pathogens and heavy metals in food is of great significance (Hu et al., 2021a). Currently, the commonly used detection methods include Enzyme Linked Immunosorbent Assay (ELISA), High Performance Liquid Chromatography (HPLC), Gas Chromatography-Mass Chromatography (GC-MS), High Performance Thin-layer Chromatography, Supercritical Fluid Extraction, etc. (Guo et al., 2021). These methods are labor-

intense, time-consuming and require expensive instruments and skilled workers, which are difficult to meet the requirements of rapid on-site detection and screening a large batch of samples. Therefore, it is urgent to develop sensitive, efficient and convenient food detection technology.

Surface-enhanced Raman scattering (SERS) is considered as a promising food safety detection technology due to its nondestructive, fingerprint and high sensitivity. In recent years, with the development of nanotechnology, researchers have established a series of rapid monitoring methods for common food contaminants (mycotoxins, drug residues, pesticides and illegal additives, etc.) based on SERS technology. Generally, traditional SERS active substrates are generally composed of noble metals (such as Au, Ag, Pt, etc.) in the form of nanoparticle aggregation or array (Hu et al., 2021a). Localized surface plasmon resonance (LSPR) excited on the surface of metal nanoparticles (NPs) generates a strong electromagnetic field to achieve the enhancement of Raman signals. The dominant enhancement often observed is the electromagnetic enhancement of targeted molecules adsorbed on the metal surface, with the enhancement factors ranging from 10^4 to 10^{12} (Zong et al., 2018). Non-metallic materials such as semiconductor, graphene quantum dots and photonic crystal fiber have also been used to prepare SERS substrate due to their high chemical stability, good biocompatibility and high carrier mobility (Yang et al., 2019; Beffara et al., 2020). However, rigid solid SERS substrates such as metals, silicon wafer, glass or graphite are expensive and not suitable for direct *in-situ* detection of irregular-shaped agricultural products, which hinders the practical application of SERS technology. In recent years, due to their weak SERS response, low background signal and interference signal during detection, cellulose fibers or paper bases are used as the supports for noble metals to prepare flexible SERS substrates, which are considered to be one of the most promising materials for preparing test paper for *in-situ* food detection.

Recent developments of using various forms of cellulose, such as cellulose fiber, cellulose membrane, paper base, cellulose nano-fiber (CNF), cellulose nano-crystal (CNC), bacterial cellulose, and various cellulose derivatives in fabricating functional materials have been extensively studied (Ling et al., 2022a; Ling et al., 2022b). The applications of different forms of cellulose in SERS substrate for food safety detection have been explored. Vávrová et al. (Vávrová et al., 2022) successfully prepared Au NPs using dicarboxylic cellulose (DCC) and hyaluronate (DCH) as reducing agent and end-capping reagent, and applied the Au NPs to detect the Raman signal of N-acetylcysteine (NAC). The enhanced effect was subjected to further improvement, which may be due to the presence of DCC and DCH hinder the contact of NAC with Au NPs. Marques et al. (2008) used sodium citrate as a reducing agent to prepare Ag NPs/BC composite by *in-situ* reduction, and used it as a surface-enhanced Raman scattering (SERS) substrate to detect thiosalicylic acid and 2,2-dithio-bipyridine. The detection limit was about 10^{-4} mol/L, but there is room for improvement in sensitivity. Barbosa et al. (2021) prepared a novel SERS substrate by coating a layer of Ag NPs on the β-D-glucan film by laser ablation method. The SERS activity was evaluated by using crystal violet as probe molecules. The results showed that the enhanced effect reached 10^6, which means that this substrate had stronger SERS effect than silver colloid. Hu et al. (2021b) successfully prepared a 3D cellulose nanocomposite doped with Au NPs by one-pot method, and the Raman signal of R6G can be collected on its surface at a concentration of 1×10^{-9} mol/L, which indicates that the sensitivity of this SERS substrate is greatly improved. In addition, due to the porous structure of the SERS substrate, melamine in milk could be directly detected with a detection limit of 2.5 mg/kg. Significantly, a good SERS base should ensure homogeneity stability and repeatability in trace detection. Therefore, it is necessary to utilize chemical reducing agents and stabilizers to control the size and shape of metal nanoparticles during the preparation of SERS substrates. Due to the weak reducing ability of cellulose, compounds such as $NaBH_4$, hydroxylamine, CTAB, and PVP were often added as reducing agents or stabilizers. On the one hand, such compounds are toxic and unfriendly to the environment; on the other hand, the reducing agents and stabilizers doped in the substrate may interfere with the SERS signal.

Polysaccharides are the most abundant natural polymers and widely found in animals, plants and microorganisms. Common polysaccharides include hemicelluloses, pectin, starch, chitosan, etc. The differences in sugar compositions and molecular chain structures endow polysaccharides with unique physicochemical properties. In recent years, the use of polysaccharides and their derivatives as reducing agents or stabilizers to prepare metal nanoparticle for SERS substrate materials has aroused the interests of researchers (Zhao et al., 2015; Puente et al., 2021). Xylan is a type of hemicelluloses, widely present in various lignocellulosic biomass. Due to the containing of abundant reducing functional groups, e.g. hydroxyls and aldehydes, and its unique rheological properties, it can be used as a green reducing agent and stabilizer for the preparation of metal nanoparticles (Zong et al., 2018). Compared with other reducing agents, such as $NaBH_4$ and hydrazine hydrate, xylan is more environmentally friendly and does not require additional stabilizers. Using xylan as the reducing agent and stabilizer, Cai et al. (Cai et al., 2019) prepared two kinds of nanoparticles, Au@Ag and Au-Ag, with different shell thicknesses by microwave heating-assisted reduction and applied them to fabricate SERS substrate; SERS substrate with embedded xylan wrapped Au@Ag particles had an excellent enhancement effect on Raman signal of 4-mercaptobenzoic acid and a detection limit as low as 1 nmol/L. Bi-metal core-shell structure is more advantageous than single metal SERS substrate materials (Guo et al., 2019). Firstly, the surface plasmon resonance effect could be regulated by adjusting

core-shell composition ratio. Secondly, the protective effect of the shell can improve the stability of the materials. Although core-shell structure has an excellent SERS effect, its application process involves multiple steps, i.e. mixing the analyte with the core-shell particles before detection, which could cause agglomeration.

Aiming at the above problems, an environmental friendly and flexible SERS substrate was designed. Xylans were used as a green reducing agent and stabilizer, while chloroauric acid was used as Au precursor to prepare Au NPs, which were immobilized on paper base by coating. Tollens reagent was then used as the Ag precursor and microwave-assisted reduction was used to prepare SERS substrates loaded with Au-Ag bimetallic NPs. The SERS activity and signal uniformity of the substrate were evaluated by using thiram as the probe molecule. Finally, the *in-situ* detection of pesticide residues on real fruit surfaces using this paper-based SERS substrate was conducted.

2 Experimental

2.1 Material

Sodium chlorite, gold (III) chloride trihydrate, ammonium hydroxide solution, tetramethylthiuram disulfide (thiram) were purchased from Shanghai Macklin Biochemical Co., LTD. (Shanghai, China). Silver nitrate was obtained from Shanghai Fine Chemical Materials Research Institute (Shanghai, China). Sugarcane bagasse used in the experiment was supplied by Xinping Nan'en Sugar and Paper Manufacturing Co., Ltd. (Yunnan, China). The filter paper was purchased from General Electric Biotechnology Co., Ltd. (Hangzhou, China).

2.2 Extraction of xylan

The oven dried bagasse raw materials was first dewaxed in a Soxhlet apparatus with 95% ethanol for 6 h. After dewaxing, bagasse was successively bleached with 4 wt% $NaClO_2$ solution and 2 wt% $NaClO_2$ solution (w/w) at 75°C and pH 3.9–4.0 for 1 h. The solid-liquid ratio was 1:12 (w/v). The obtained solid residue, i.e., holocellulose, was washed three times with deionized (DI) water and one time with anhydrous ethanol. The holocellulose was extracted with 2 wt % NaOH at 90°C for 3 h under stirring with a solid/liquid ratio of 1:20 (w/v, g/mL). After the filtrate was neutralized to pH 5.5 with acetic acid, the filtrate was concentrated to 1/3 of its original volume by rotary evaporation and then was precipitated in 95% ethanol of the volumes of three times of the concentrated filtrate. Finally, the xylan was separated by centrifugation, washed with 75% ethanol and freeze-dried for further use. The compositional analysis of xylan followed the methods described by Jin (Jin et al., 2019).

2.3 Preparation of the paper-based Au-Ag bimetallic SERS substrate

The extracted xylan was used as reducing agent and stabilizer to prepare gold nanoparticles (Au NPs) according to the method reported by Luo (Luo et al., 2015). In detail, 0.12 g of xylan was dispersed in 3 ml DI water, and $HAuCl_4$ $3H_2O$ of different mass (5–40 mg) was dissolved in 12 ml DI water. The two were mixed. The reaction temperature and time varied between 60–100°C and 10–80 min, respectively. The sample was properly diluted and the characteristic adsorption peak of Au NPs were detected by UV spectrophotometer with a scanning range of 300–800 nm.

The xylan/gold nanoparticle dispersion prepared by the reaction of 0.12 g xylan and 5–40 mg $HAuCl_4$ $3H_2O$ at 80°C for 20 min was coated on the surface of the paper base by a hand-coating machine. Filter paper sheets were cut into 3 cm × 3 cm specimens. Each specimen was coated both sides and each side was coated 10 times to control the amount of Au NPs. In each time of coating, 0.15 mL of the xylan/gold nanoparticle dispersion was used. After each time of coating, the paper base was placed in an oven at 60°C to dry for 15 min, and then the second coating was performed. The gold nanoparticles-filter paper (Au-FP) was finally obtained.

According to the method of Luo (Luo et al., 2015), Au-Ag bimetallic nanoparticles were prepared. In detail, the Au-FP was placed in a three-port round-bottom flask with xylans and Tollens reagent added and the mixture was subjected to 30-min microwave reaction at 800 W and 65°C. Tollens reagents were prepared by 0.1 mol/L $AgNO_3$ solution, 2 wt% NaOH solution and 2 wt% ammonium hydroxide; the amount of 0.1 mol/L $AgNO_3$ used was varied to give different Ag/Au mole ratio ranging from 0.5 to 10 (the mole of Au was calculated based on the amount of xylan/gold nanoparticle dispersion used for coating). They were then dried in a vacuum oven for 24 h to obtain different Au-Ag-FP. Different Au-Ag bimetallic nanoparticles are denoted as Au-Ag_m-n, where m represents Ag/Au mole ratio (m varied from 0.5 to 10), n represents different amounts of xylan added when preparing Ag (n = 0, 1, 2, 3, 4, 5, and 6 correspond to 0, 5.71×10^{-8}, 5.71×10^{-7}, 5.71×10^{-6}, 5.71×10^{-5} and 5.71×10^{-4} mol of anhydrous xylose units). The surface morphology and elements distribution were characterized by FESEM (LEO1530VP, Carl Zeiss, Germany). The electron valence states and chemical properties of Au and Ag were determined by X-ray photoelectron spectroscopy (XPS) (K-Alpha, Thermo Fisher, United States). Au-Ag bimetallic nanoparticles embedded on the paper surface were separated by ultrasound and centrifugation. The nanoparticles were then

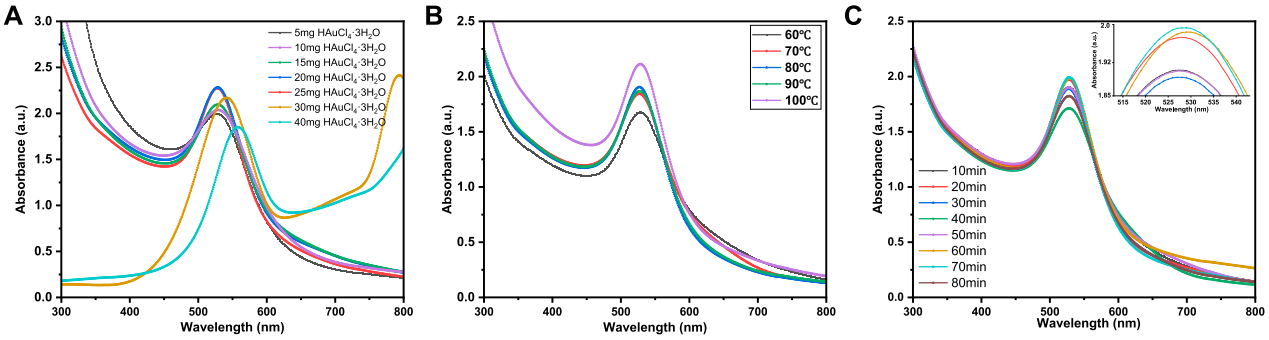

FIGURE 1
UV-vis spectra of xylan/Au NPs dispersions at **(A)** different reactant ratios (0.12 g Xylan: 5–40 mg $HAuCl_4{\cdot}3H_2O$), **(B)** different reaction temperature and **(C)** different reaction time.

evaluated by a UV spectrophotometry with a scanning range of 300–800 nm and a transmission electron microscopy (Talos F200s, Thermo Scientific, United States).

2.4 Analysis of the SERS performance of substrates

To evaluate the Raman enhancement performance of different Au-Ag-FP, 10 μL thiram (concentration between 1×10^{-3}–10^{-6} mol/L) solution was dropped onto the substrate and placed in a 50°C oven for 5 min. After ethanol volatilization, a Micro-Raman Spectroscopy System (LabRAM Aramis, Horiba Jobin Yvon, France) with excitation wavelength of 633 nm was used to collect the spectra of the substrate. In addition, on the same Au-Ag_8-3-FP substrate, after dropping thiram solution, 20 points were randomly selected for SERS detection.

In order to test the feasibility of *in-situ* extraction and detection of pesticide residues on fruit surface with the substrate, slightly wetted Au-Ag_8-3-FP substrate was used to wipe the surface of apple containing thiram, and then the Micro-Raman Spectroscopy System was used to irradiated the substrate to collect SERS spectra.

3 Results and discussion

3.1 Characterization of Au nanoparticles

The extracted sugarcane bagasse xylan had a sugar composition of 58.6% xylose, 17.2% glucose, 9.1% arabinose, 2.1% galactose, 1.2% mannose and 5.3% uronic acid. Previous studies have found that the presence of side-chain groups plays an important role in preventing the crystallization/aggregation of xylan molecules, and the low-branching xylan extracted from bagasse is easy to crystallize and cannot form water casting film (Xiang et al., 2020). Based on previous studies, the branching degree of xylan used in this study (arabinoglycan + uronic acid/xylan) was deliberately controlled at about 0.24, thus providing good film formation and suitable for coating applications in this paper.

Au NPs prepared by xylan as reducing agent were characterized by UV-vis spectroscopy. In Figure 1, a strong adsorption peak can be observed at 524 nm, which is the characteristic surface plasmon resonance peak (SPR) of Au NPs, indicating the formation of Au NPs (Chen et al., 2012). In Figure 1A, when 5 mg $HAuCl_4{\cdot}3H_2O$ was used as gold source, the adsorption peak was weak, indicating that very few Au NPs were formed under this condition. With the increase of Au^{3+} concentration, a strong and narrow peak appeared in the UV spectra, indicating that the amount of Au NPs increased. When the amount of $HAuCl_4{\cdot}3H_2O$ increased to 25 mg, the adsorption peak was the largest among different amounts of $HAuCl_4{\cdot}3H_2O$ addition. As the amount of $HAuCl_4{\cdot}3H_2O$ further increased, the adsorption peak became weaker and wider with red shift. This is due to Au NPs aggregation, resulting in the weak adsorption strength of Au NPs at 524 nm. Furthermore, the larger size of Au NPs may lead to longitudinal plasma resonance due to plasma coupling between particles (Sun et al., 2004). The absorbance of Au NPs coupled plasma in close contact leads to red shift in UV-vis spectra, and SPR broadening indicates that the surface ligand provides a new relaxation channel for plasma excitation (Itoh et al., 2004). All these phenomena indicate that excessive $HAuCl_4{\cdot}3H_2O$ lead to aggregation of Au NPs. Therefore, the suitable mass ratio is 0.12 g xylan: 25 mg $HAuCl_4{\cdot}3H_2O$, which was selected in subsequent experiments.

Figure 1B shows the UV-vis spectra of Au NPs prepared at different reaction temperatures. At 60°C, the absorption peak intensity was low because the reaction was incomplete due to the low temperature, and fewer Au NPs were generated. When the

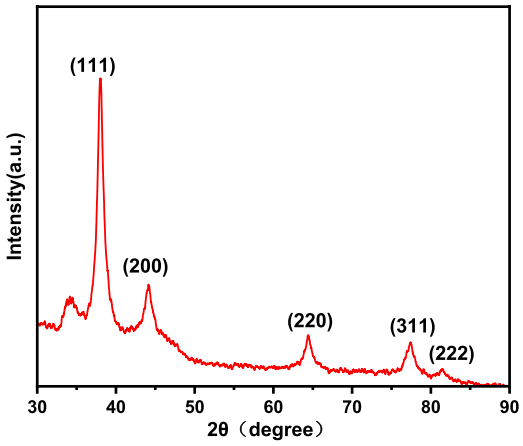

FIGURE 2
X-ray diffraction patterns of Au-FP.

reaction temperature was raised to 80°C, the absorbance value of UV-vis spectra reached the maximum, but when the reaction temperature was raised further, the absorption peak widened. This may be due to the relatively high temperature that the generation of a large amount of Au NPs may lead to the agglomeration phenomenon of AuNPs, thus widening the SPR absorption peak and redshifting the absorption peak. Therefore, 80 °C was chosen as the optimum reaction temperature for subsequent experiments.

In Figure 1C, the influence of reaction time on Au NPs formation was discussed. With the increase of reaction time from 10 min to 20 min, the intensity of SPR peak increases significantly, confirming the formation of Au NPs. It should be noted that at 20 min, the SPR absorption peak intensity of xylan/Au NPs composite already shows a relatively high value. Further increase of heating time, the SPR absorption peak intensity does not vary significantly. At 80 min, the peak intensity even decreases significantly, indicating that long reaction time leads to Au NPs aggregation and unstable xylan/Au NPs composite. Therefore, the optimal reaction time is determined to be 20 min.

The XRD spectrum of Au-FP is shown in Figure 2. The diffraction peaks of Au NPs are at 2θ = 38.02°, 44.11°, 64.45°, 77.42°, 81.49° correspond to the (111), (200), (220), (311), and (222) planes of Au, respectively. These peaks match well with the diffraction peaks of standard Au NPs (JCPDS No. 04–0784) and is consistent with previous literatures (Luo et al., 2015).

3.2 Characterization of the paper-based Au-Ag bimetallic SERS substrate

In order to determine the chemical valence state of Au and Ag, Au-Ag-FP was characterized by XPS, and the results were calibrated with C1s = 284.8eV binding energy standard, as shown in Figure 3. In Figure 3A, Au and Ag are found on the surface of Au-Ag-FP in addition to C and O. The C and O may be derived from xylan or cellulose on the surface of paper base, while the peaks at Au 4f and Ag 3 days are derived from Au-Ag bimetal nanoparticles on the paper base.

In the XPS narrow spectrum scanning of Au 4f (Figure 3B), the peaks with binding energies of 87.66 eV (4f5/2) and 83.96 eV (4f7/2) correspond to Au (0). In the XPS narrow spectrum scanning of Ag 3 days (Figure 3C), the peaks of 374.16 eV (3d3/2) and 368.16 eV (3d5/2) are the characteristic peaks of Ag (0). It shows that xylan has good reducibility so that Au^{3+} and Ag^{+} are successfully reduced to Au and Ag.

In order to further understand the dispersion of Au-Ag on the paper surface, the surface morphology and surface element

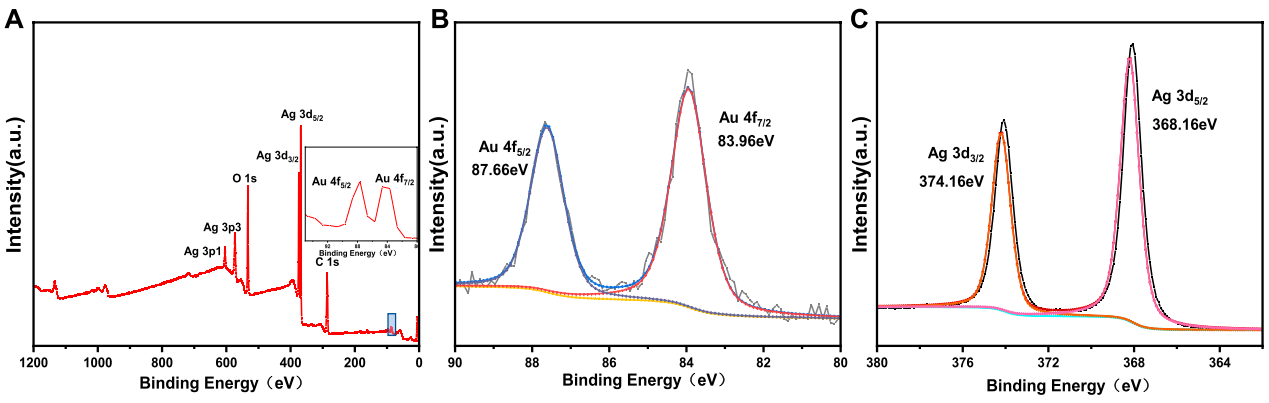

FIGURE 3
XPS spectra of Au-Ag_8-3-FP: **(A)** wide scan spectra, **(B)** high-resolution XPS sprectra of Au 4f, **(C)** high-resolution XPS sprectra of Ag 3 d

10.3389/fbioe.2022.1031152

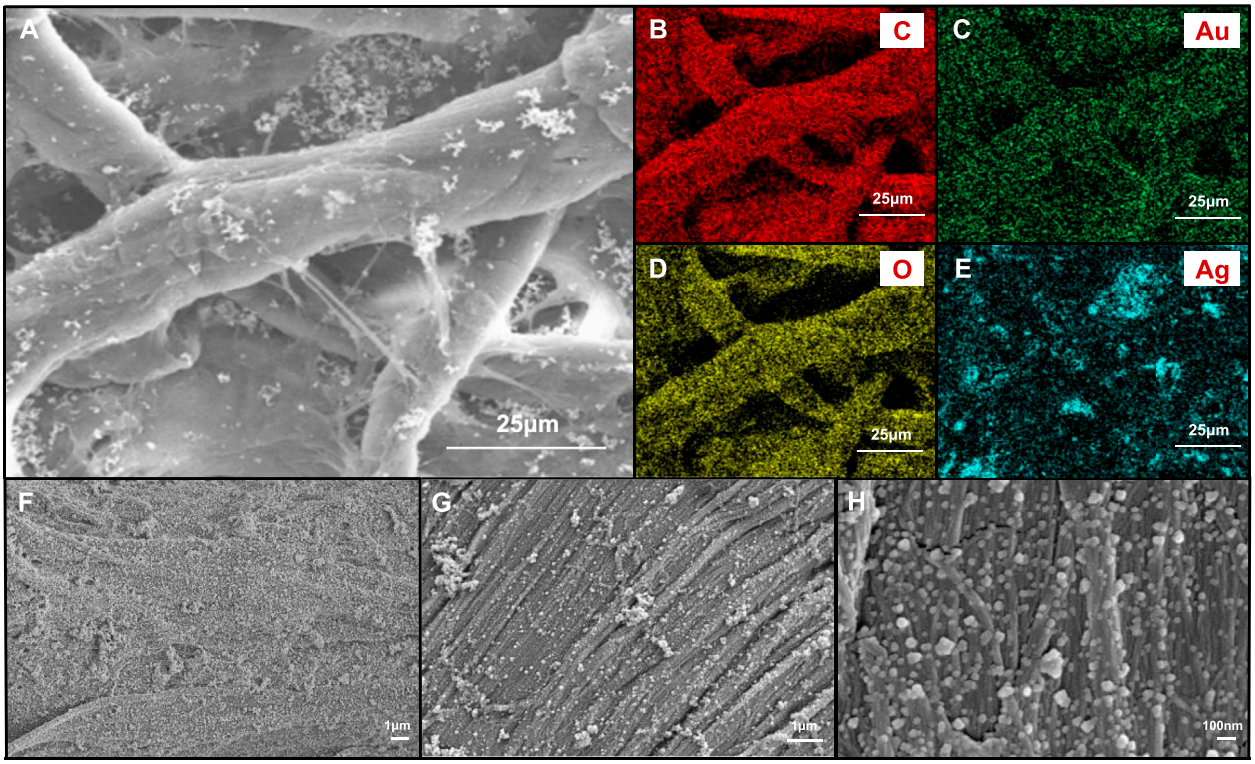

FIGURE 4
(A) FESEM images of Au-Ag_8-3-FP surface and images with elemental mapping of **(B)** C, **(C)** Au, **(D)** O, **(E)** Ag, respectively. FESEM images of Au-Ag_8-3-FP surface with **(F)** 5 k magnification, **(G)** 10 k magnification and **(H)** 50 k magnification.

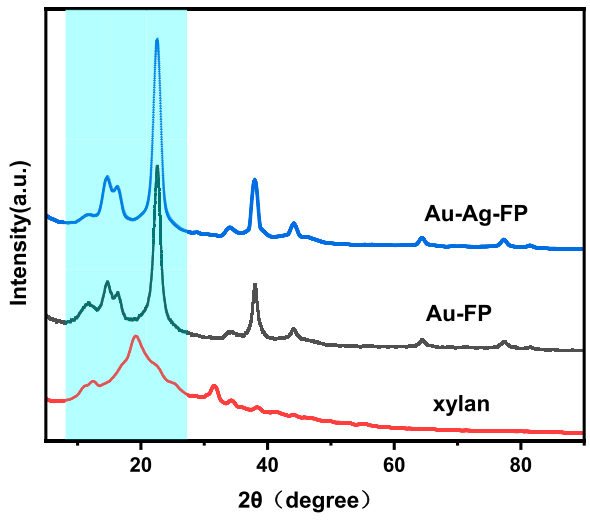

FIGURE 5
X-ray diffraction patterns of Au-Ag-FP, Au-FP and xylan.

distribution of Au-Ag_8-3-FP surface were characterized by FESEM (Figure 4). From Figure 4H, it can be observed that a large number of metal nanoparticles are attached to the surface of the paper base, and the distribution is relatively uniform, with only a slight aggregation phenomenon. However, when the magnification is reduced to 10 k and 5 k, some agglomeration occurs. Through the element distribution map, it can also be found that some aggregations of Ag NPs can be observed. It indicates that although the hydroxyl groups on xylan can coordinate and interact with metal nanoparticles, the ability to stabilize metal nanoparticles is not ideal; when the concentration of metal nanoparticles is high, aggregation is easy to occur. In Figure 5, it can be observed that there are some obvious XRD diffraction peaks between 10–35°. These diffraction peaks belong to the xylan hydrate crystals. Since alkali extraction cleaves the acetyls on xylan, xylans with low degree of branching may crystalize with water forming xylan hydrate crystals (Xiang et al., 2020). The xylan extracted from sugarcane has a high degree of branching, and its XRD pattern shows a mostly amorphous structure. However, the crystallinity of the xylan after

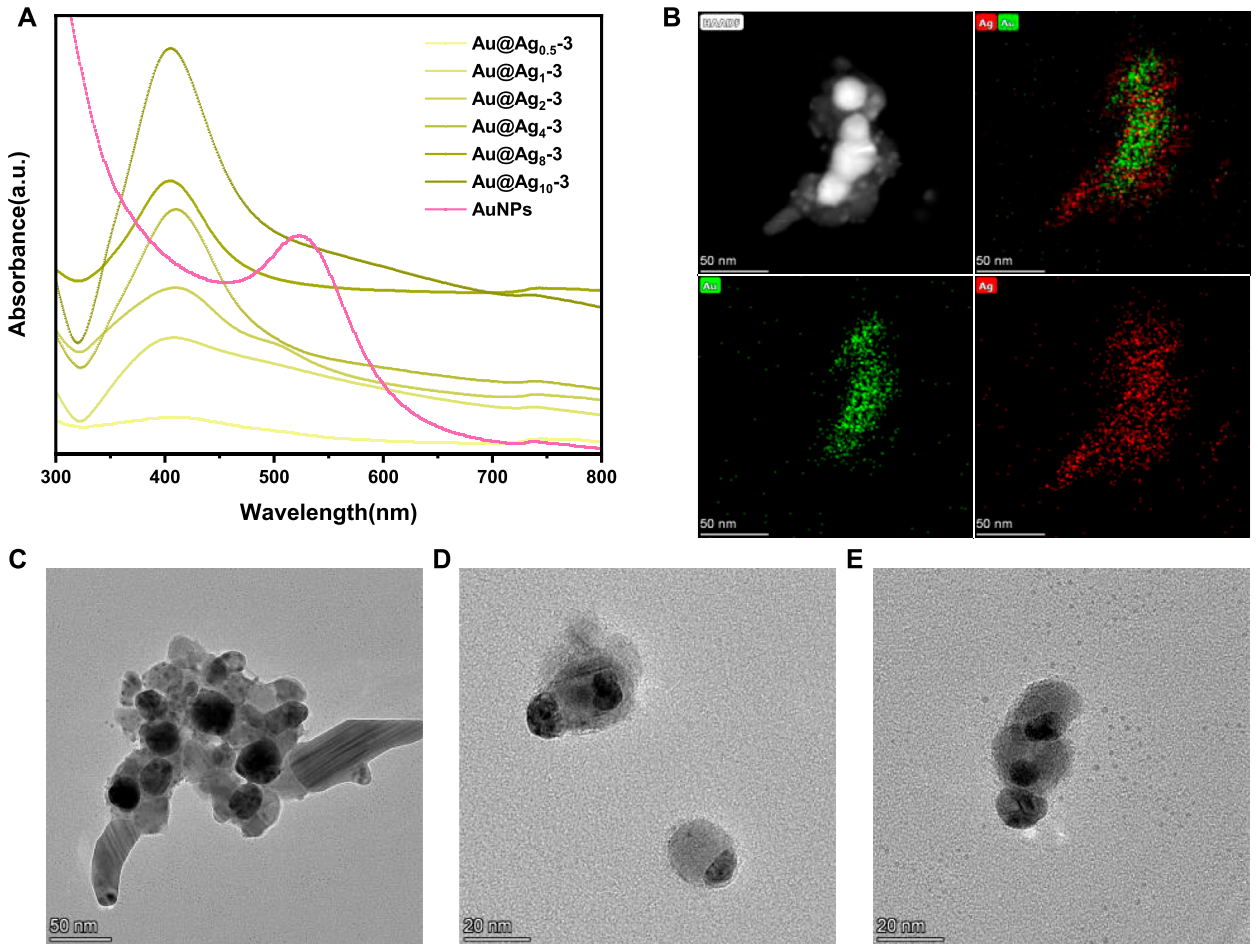

FIGURE 6
(A) UV-vis spectra of the nanoparticles on Au-Ag_m-3-FP, **(B)** STEM dark-field picture and EDS mapping pictures of nanoparticles on Au-Ag_8-3-FP, **(C)**, **(D)**, **(E)** TEM images of nanoparticles on Au-Ag_8-3-FP.

the reaction increases significantly with the appearance of evident characteristic XRD peaks of xylan hydrate crystals (Li and Xiang, 2022). The forming of xylan hydrate crystals may be due to the destruction of xylan branches during the reaction with Tollens reagent at high pH (Xiang et al., 2020).

As mentioned above, Au NPs exhibit a strong surface plasmon resonance peak at 524 nm. According to previous studies, the adsorption peak of silver nanoparticles is generally at around 410 nm, and red shift or blue shift would occur with the change of particle size (Zhang et al., 2007). In Figure 6A, it can be found that with the increase of silver content, the resonance of silver gradually dominates and the adsorption peak gradually blue shifts. In order to further explore the structure of nanoparticles, STEM dark-field images and EDS elemental mapping tests were carried out. As can be seen from Figure 6B, multiple nanoparticles with a bright inner core and a dark outer shell aggregate together, with gold element in the inner core and silver element in the outer shell, suggesting the successful formation of bimetallic core–shell nanoparticles (Cai et al., 2019). Figures 6D,E shows that some Ag NPs do not completely wrap the Au NPs, which may be due to that, after the Au NPs are coated on the paper-based surface, only the exposed surface can be in contact with the Ag NPs. Figures 6C–E show that some Au-Ag nanoparticles have slight agglomerations, which may be caused by the ultrasonic and centrifugal operation when Au-Ag bimetal nanoparticles are separated from the paper-based surface.

3.3 The SERS performance of the paper-based Au-Ag bimetallic SERS substrate

The Raman enhancement performance of Au-Ag-FP substrates prepared with different Au/Ag molar ratios was evaluated, and the results were shown in Figure 7A. After thiram was dropped on the surface of Au-Ag_m-3-FP, the strongest Raman spectrum peak of 10^{-3} mol/L thiram was located at 1377 cm^{-1}, corresponding to the

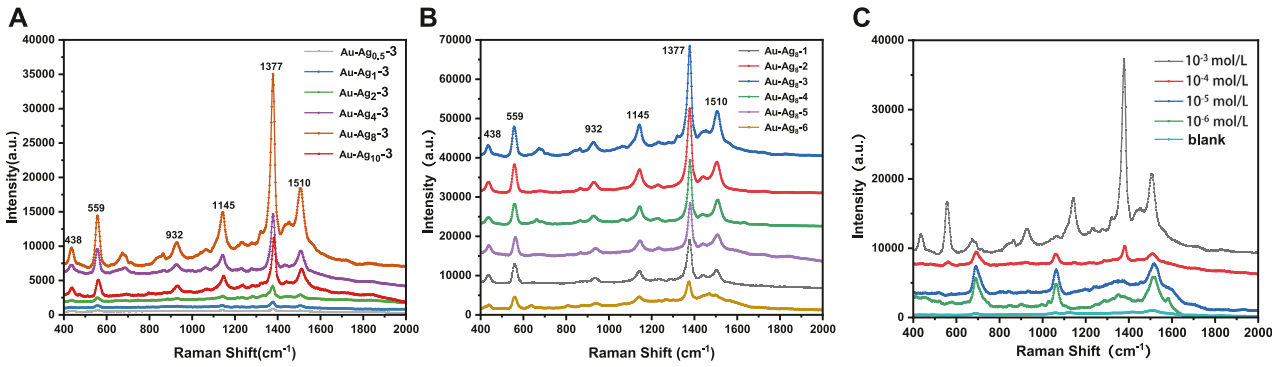

FIGURE 7
(A) The Raman spectra of thiram at 10^{-3} mol/L on the surface of Au-Ag_m-3-FP, **(B)** the Raman spectra of thiram at 10^{-3} mol/L on the surface of Au-Ag_8-n-FP, **(C)** the Raman spectra of different concentrations (10^{-3}–10^{-6} mol/L) of thiram on the surface of Au-Ag_8-3-FP.

stretching vibration of C-N bonds and the symmetric stretching vibration of CH_3. The peak at 1145 cm^{-1} is attributed to the antisymmetric vibration of CH_3, the peak at 1510 cm^{-1} and 1145 cm^{-1} corresponds to the stretching vibration of C-N and the in-plane bending vibration of CH_3, the stretching vibration peak of C=S and CH_3N corresponds to the peak at 932 cm^{-1}, and the vibration peak of S-S is at 559 cm^{-1}. The peak at 444 cm^{-1} corresponds to the bending vibration of CH_3NC and the stretching vibration of C=S (Kang et al., 2002). With the increase of Ag dosage, the Raman enhancement effect of the substrate is obviously enhanced. When the mole quantity of Ag is 8 times of Au (Au-Ag_8-3-FP), the Raman intensity is the highest, which is about 80 times of Au-$Ag_{0.5}$-3-FP. However, with further increase of Ag dosage, the enhancement performance of the substrate decreases, which may be due to the stabilizing effect of xylan on nanoparticles is not strong enough, leading to agglomeration phenomenon (Figure 4H) and uneven size and shape of Au-Ag particles.

Raman enhancement performance of Au-Ag_8-n-FP prepared with different amounts of xylan is shown in Figure 7B. With the increase of xylan addition during Ag NP preparation, the Raman spectra of 10^{-3} mol/L thrima dropped on Au-Ag8-n-FP have increased intensities for peaks at 559, 932, 1145, 1377 and 1510 cm^{-1}. Au-Ag_8-2-FP and Au-Ag_8-3-FP have the largest intensity, which indicates that they have a strong Raman enhancement. However, with further increase of the xylan addition during Ag NP preparation, the peak intensities of the substrates (Au-Ag_8-4-FP, Au-Ag_8-5-FP and Au-Ag_8-6-FP) decreases. This phenomenon indicates that the addition of xylan is beneficial to reducing the aggregation of nanoparticles, leading to a strong Raman enhancement effect. However, it can also be postulated that with further increase of the xylan dosage, excessive xylans may cover or bury the Ag NPs leading to a weakened Raman enhancement effect.

In order to explore the practical application performance of the SERS substrates, the Raman enhancement performance of Au-Ag_8-3-FP on common pesticide pollutant thiram was evaluated. As can be seen from Figure 7C, the higher the thiram concentration, the stronger the SERS signal peak is. In the SERS spectrum for 10^{-3} mol/L thiram, very strong signal peaks are observed at 1377 cm^{-1}, 1510 cm^{-1}, 1145 cm^{-1} and 559 cm^{-1}. With the decrease of thiram concentration, the signal peak intensity at 1377 cm^{-1} weakens significantly, but the signal peak at 1510 cm^{-1} increases. This may be due to that at a low concentration, the thiram adsorbed on the Au-Ag may not completely cover the metal surface. The charges transferred from thiram molecule to metal redistribute the electron density of thiram and enhance the intensity of Raman peaks (Dao et al., 2021).

Practical application of SERS substrate not only requires high sensitivity, but also requires good reproducibility. The reproducibility of Au-Ag_8-3-FP substrate was studied by using thiram as the probe molecule. Approximately 15 μL 200 ppm thiram ethanol solution was dropped on the substrate, and then 20 points were randomly selected to collect the SERS spectrum of thiram. The SERS spectra of different points (Figure 8A) show high similarity in quantity, location and intensity of characteristic peaks. Figure 8B plots the intensity of Raman characteristic peak at 1377 cm^{-1} from the 20 points, which is used to demonstrate the reproducibility of SERS base. According to the standard formula of relative intensity deviation of SERS spectrum (Luo et al., 2015), RSD was calculated to be 10.43%, showing good reproducibility. The paper-based SERS has good flexibility, which enables the substrate to make good contact with the surface of the object to be measured. The three-dimensional porous structure of filter paper acts as a capillary, giving it good water adsorption performance. Based on the above characteristics, the use of Au-Ag_8-3-FP substrate should be able to achieve effective extraction and rapid detection of complex sample surface. The Au-Ag_8-3-FP substrate was slightly wetted with 15 μL ethanol solution, and

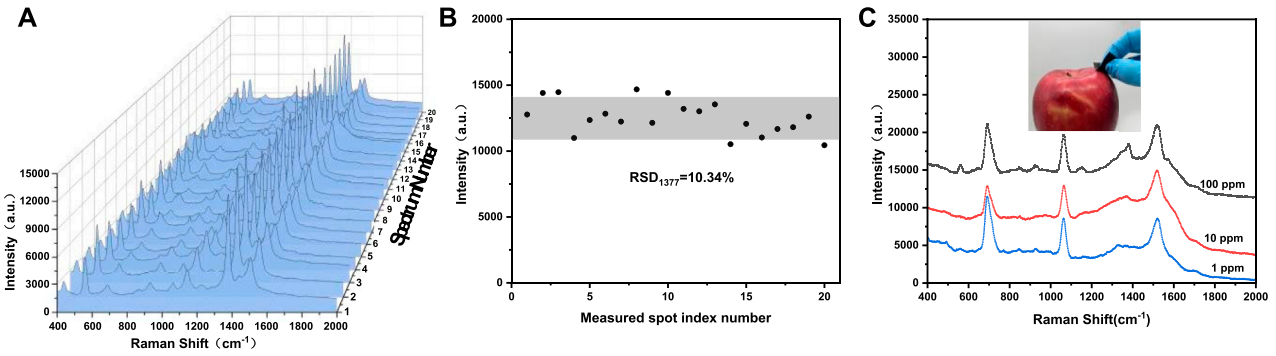

FIGURE 8
(A) Raman spectra of 200 ppm thiram collected from 20 randomly selected spots from the same Au-Ag_8-3-FP substrate, **(B)** the scatter diagram of intensity distribution of the 1377 cm^{-1} peak of thiram corresponding to spectra in **(A)**, **(C)** Raman spectra of thiram with different concentration swabbed from the apple surface.

TABLE 1 Cellulose-based SERS material for food safety detection.

Cellulose form	Substrate	Analyte	Method	LOD[a]	References
filter paper	Au-Ag/filter paper	thiram	*in-situ* reduction	0.24 ppm	This paper
	Ag@SiO_2/filter paper		Droping	1 nmol/L	Sun et al. (2019)
	AgNPs/AKD/filter paper		Droping	0.46 nmol/L	Lee et al. (2018)
	AgNPs/filter paper		Droping	1 ppm	Zhang et al. (2019)
	Au@Ag cellulose membrane/filter paper		transfer	0.24 ppm	Lin et al. (2019)
cellulose	Ag coated cellulose		magnetron sputtering	0.20 ppm	Gao et al. (2020)

[a]LOD, limit of detection.

then the apple surface was dried after dropping with 15 μL thiram ethanol solution. The SERS spectrum of the substrate collected with thiram was shown in Figure 8C. The characteristic peak of thiram could still be observed when the solution concentration is as low as 1 ppm. The results show that SERS substrate could be used for rapid extraction and detection of pesticide residues on real vegetable and fruit surface.

In recent years, it has been reported that various metal nanoparticles supported by cellulose as the substrate were used for food safety SERS detection (Table 1). The SERS substrate developed in this study has better or comparable performance in detection limits compared to some recent studies (Table 1). In addition, the detection limit of Au-$Ag_{8\text{-}3}$-FP in this study is 1×10^{-6} mol/L (i.e. 0.24 ppm), which is lower than the maximum thiram residue level of 7 ppm regulated by US Environmental Protection Agency (Sun et al., 2017) and 5 ppm required by the National Food Safety Standard of China (Zhang et al., 2019) indicating that the substrate developed in this study can potentially be used in food safety detection.

4 Conclusion

Using natural macromolecule xylan as a reducing agent, a stabilizing agent and an anchoring agent, Au-Ag bimetal nanoparticles were successfully prepared and steadily anchored on the paper base to fabricate a paper-based Au-Ag bimetallic SERS substrate. Different SERS substrates were prepared by adjusting the amounts of xylan, $HAuCl_4{\cdot}3H_2O$ and Tollens reagent. The results show that these SERS substrates have high Raman enhancement performance and reproductively. The substrate fabricated through Ag/Au mole ratio of 8 and xylan addition during Ag preparation of 5.71×10^{-6} mol has the highest Raman intensity. The substrate can effectively detect trace pesticide, i.e., thiram, and the limit of detection is as low as 1×10^{-6} mol/L (0.24 ppm). In addition, the good water adsorption performance of the paper-based SERS substrate makes it possible for direct detection of pesticide residues on the surface of fruit. The paper-based Au-Ag bimetallic SERS substrate developed in this study has better or comparable performance in detection limits compared to some recent studies in cellulose-based SERS substrates, showing a great potential in applications for rapid food safety detection.

Data availability statement

The original contributions presented in the study are included in the article/supplementary material, further inquiries can be directed to the corresponding authors.

Author contributions

ZX: Original idea, writing original manuscript, editing manuscript and providing funding; MH: Methodology, conducting experiment and writing original manuscript; LL: Conducting experiment; JB and AD: Methodology and editing manuscript; XJ: Providing funding and project supervision.

Funding

This work was supported by the Foundation (No. GZKF202002) of State Key Laboratory of Biobased Material and Green Papermaking, Qilu University of Technology, Shandong Academy of Sciences, the Natural Science Foundation of Guangdong Province (No. 2020A1515011021), Jinan Innovation Team (No. 2021GXRC023) and Taishan Scholars Program.

Conflict of interest

The authors declare that the research was conducted in the absence of any commercial or financial relationships that could be construed as a potential conflict of interest.

Publisher's note

All claims expressed in this article are solely those of the authors and do not necessarily represent those of their affiliated organizations, or those of the publisher, the editors and the reviewers. Any product that may be evaluated in this article, or claim that may be made by its manufacturer, is not guaranteed or endorsed by the publisher.

References

Barbosa, I. B., Barbosa-Dekker, A. M., Dekker, R. F. H., Bezerra, A. G., De Santana, H., and Orsato, A. (2021). Polysaccharide-based substrate for surface-enhanced Raman spectroscopy. *Spectrochimica Acta Part A Mol. Biomol. Spectrosc.* 249, 119255. doi:10.1016/j.saa.2020.119255

Beffara, F., Humbert, G., Auguste, J. L., Perumal, J., Dinish, U. S., and Olivo, M. (2020). Optimization and performance analysis of SERS-active suspended core photonic crystal fibers. *Opt. Express* 28, 23609–23619. doi:10.1364/oe.393251

Cai, J. H., Li, Y. C., Liu, C. F., and Wang, X. Y. (2019). Green and controllable synthesis of Au-Ag bimetal nanoparticles by xylan for surface-enhanced Raman scattering. *ACS Sustain. Chem. Eng.* 7, 15154–15162. doi:10.1021/acssuschemeng.9b00260

Chen, R., Chen, Q., Huo, D., Ding, Y., Hu, Y., and Jiang, X. Q. (2012). *In situ* formation of chitosan-gold hybrid hydrogel and its application for drug delivery. *Colloids Surfaces B Biointerfaces* 97, 132–137. doi:10.1016/j.colsurfb.2012.03.027

Dao, D. Q., Truong, D. H., Nguyen, T. L. A., Ngo, T. C., An, N. T. T., and Huy, B. T. (2021). Insight into SERS chemical enhancement mechanism of fungicide thiram adsorbed on silver nanoparticles. *J. Clust. Sci.* doi:10.1007/s10876-021-02197-z

Gao, W., Xu, J. T., Cheng, C., Qiu, S., and Jiang, S. X. (2020). Rapid and highly sensitive SERS detection of fungicide based on flexible "wash free" metallic textile. *Appl. Surf. Sci.* 512, 144693. doi:10.1016/j.apsusc.2019.144693

Guo, H., Zhao, A., He, Q., Chen, P., Wei, Y., Chen, X., et al. (2019). Multifunctional Fe_3O_4@mTiO_2@noble metal composite NPs as ultrasensitive SERS substrates for trace detection. *Arabian J. Chem.* 12, 2017–2027. doi:10.1016/j.arabjc.2019.01.007

Guo, Z. M., Chen, P., Yosri, N., Chen, Q. S., Elseedi, H. R., Zou, X. B., et al. (2021). Detection of heavy metals in food and agricultural products by surface-enhanced Raman spectroscopy. *Food Rev. Int.*, 1–22. doi:10.1080/87559129.2021.1934005

Hu, B. X., Pu, H. B., and Sun, D. W. (2021a). Multifunctional cellulose based substrates for SERS smart sensing: Principles, applications and emerging trends for food safety detection. *Trends Food Sci. Technol.* 110, 304–320. doi:10.1016/j.tifs.2021.02.005

Hu, X. M., Yang, B. B., Wen, X. D., Su, J. N., Jia, B. Q., Fu, F. Y., et al. (2021b). One-pot synthesis of a three-dimensional Au-decorated cellulose nanocomposite as a surface-enhanced Raman scattering sensor for selective detection and *in situ* monitoring. *ACS Sustain. Chem. Eng.* 9, 3324–3336. doi:10.1021/acssuschemeng.0c09296

Itoh, H., Naka, K., and Chujo, Y. (2004). Synthesis of gold nanoparticles modified with ionic liquid based on the imidazolium cation. *J. Am. Chem. Soc.* 126, 3026–3027. doi:10.1021/ja039895g

Jin, X. C., Hu, Z. H., Wu, S. F., Song, T., Yue, F. X., and Xiang, Z. Y. (2019). Promoting the material properties of xylan-type hemicelluloses from the extraction step. *Carbohydr. Polym.* 215, 235–245. doi:10.1016/j.carbpol.2019.03.092

Lee, M., Oh, K., Choi, H. K., Lee, S. G., Youn, H. J., Lee, H. L., et al. (2018). Subnanomolar sensitivity of filter paper-based SERS sensor for pesticide detection by hydrophobicity change of paper surface. *ACS Sens.* 3, 151–159. doi:10.1021/acssensors.7b00782

Kang, J. S., Hwang, S. Y., Lee, C. J., and Lee, M. S. (2002). SERS of dithiocarbamate pesticides adsorbed on silver surface; Thiram. *Bull. Korean Chem. Soc.* 23, 1604–1610. doi:10.5012/bkcs.2002.23.11.1604

Li, L., and Xiang, Z. Y. (2022). Crystallization properties of acetylated beta-(1-4)-d-xylan. *Cellulose* 29, 107–115. doi:10.1007/s10570-021-04277-9

Lin, X., Lin, S., Liu, Y. L., Zhao, H. Y., Liu, B. K., and Wang, L. (2019). Lab-on-paper surface-enhanced Raman spectroscopy platform based on self-assembled Au@Ag nanocube monolayer for on-site detection of thiram in soil. *J. Raman Spectrosc.* 50, jrs.5595–925. doi:10.1002/jrs.5595

Ling, Z., Chen, J., Wang, X. Y., Shao, L. P., Wang, C., Chen, S., et al. (2022a). Nature-inspired construction of iridescent CNC/Nano-lignin films for UV resistance and ultra-fast humidity response. *Carbohydr. Polym.* 296, 119920. doi:10.1016/j.carbpol.2022.119920

Ling, Z., Zhao, J., Xie, Y., Dai, L., Feng, L., Ma, J., et al. (2022b). Facile nanofibrillation of strong bamboo holocellulose via mild acid-assisted DES treatment. *Industrial Crops Prod.* 187, 115485. doi:10.1016/j.indcrop.2022.115485

Luo, Y. Q., Shen, S. Q., Luo, J. W., Wang, X. Y., and Sun, R. C. (2015). Green synthesis of silver nanoparticles in xylan solution via Tollens reaction and their detection for Hg^{2+}. *Nanoscale* 7, 690–700. doi:10.1039/c4nr05999a

Marques, P. A. A. P., Nogueira, H. I. S., Pinto, R. J. B., Neto, C. P., and Trindade, T. (2008). Silver-bacterial cellulosic sponges as active SERS substrates. *J. Raman Spectrosc* 39, 439–443. doi:10.1002/jrs.1853

Puente, C., Sanchez-Dominguez, M., Brosseau, C. L., and Lopez, I. (2021). Silver-chitosan and gold-chitosan substrates for surface-enhanced Raman spectroscopy (SERS): Effect of nanoparticle morphology on SERS performance. *Mater. Chem. Phys.* 260, 124107. doi:10.1016/j.matchemphys.2020.124107

Sun, H. B., Liu, H., and Wu, Y. Y. (2017). A green, reusable SERS film with high sensitivity for *in-situ* detection of thiram in apple juice. *Appl. Surf. Sci.* 416, 704–709. doi:10.1016/j.apsusc.2017.04.159

Sun, M. Z., Li, B. H., Liu, X. J., Chen, J. Y., Mu, T. T., Zhu, L. Q., et al. (2019). Performance enhancement of paper-based SERS chips by shell-isolated nanoparticle-enhanced Raman spectroscopy. *J. Mater. Sci. Technol.* 35, 2207–2212. doi:10.1016/j.jmst.2019.05.055

Sun, X. P., Dong, S. J., and Wang, E. K. (2004). One-step synthesis and characterization of polyelectrolyte-protected gold nanoparticles through a thermal process. *Polymer* 45, 2181–2184. doi:10.1016/j.polymer.2004.01.010

Vávrová, A., Capkova, T., Kuritka, I., Vicha, J., and Munster, L. (2022). One-step synthesis of gold nanoparticles for catalysis and SERS applications using selectively dicarboxylated cellulose and hyaluronate. *Int. J. Biol. Macromol.* 206, 927–938. doi:10.1016/j.ijbiomac.2022.03.043

Xiang, Z. Y., Jin, X. C., Huang, C. X., Li, L., Wu, W. H., Qi, H. S., et al. (2020). Water cast film formability of sugarcane bagasse xylans favored by side groups. *Cellulose* 27, 7307–7320. doi:10.1007/s10570-020-03291-7

Yang, L. L., Peng, Y. S., Yang, Y., Liu, J. J., Huang, H. L., Yu, B. H., et al. (2019). A novel ultra-sensitive semiconductor SERS substrate boosted by the coupled resonance effect. *Adv. Sci. (Weinh).* 6, 1900310. doi:10.1002/advs.201900310

Zhang, C. M., You, T. T., Yang, N., Gao, Y. K., Jiang, L., and Yin, P. G. (2019). Hydrophobic paper-based SERS platform for direct-droplet quantitative determination of melamine. *Food Chem.* 287, 363–368. doi:10.1016/j.foodchem.2019.02.094

Zhang, W., Qiao, X., and Chen, J. (2007). Synthesis of silver nanoparticles - effects of concerned parameters in water/oil microemulsion. *Mater. Sci. Eng. B* 142, 1–15. doi:10.1016/j.mseb.2007.06.014

Zhao, Y., Tian, Y., Ma, P. Y., Yu, A. M., Zhang, H. Q., and Chen, Y. H. (2015). Determination of melamine and malachite green by surface-enhanced Raman scattering spectroscopy using starch-coated silver nanoparticles as substrates. *Anal. Methods* 7, 8116–8122. doi:10.1039/c5ay01540e

Zong, C., Xu, M. X., Xu, L. J., Wei, T., Ma, X., Zheng, X. S., et al. (2018). Surface-enhanced Raman spectroscopy for bioanalysis: Reliability and challenges. *Chem. Rev.* 118, 4946–4980. doi:10.1021/acs.chemrev.7b00668

frontiers | Frontiers in Bioengineering and Biotechnology

TYPE Original Research
PUBLISHED 13 December 2022
DOI 10.3389/fbioe.2022.1071159

OPEN ACCESS

EDITED BY
Jia-Long Wen,
Beijing Forestry University, China

REVIEWED BY
Ling-Ping Xiao,
Dalian Polytechnic University, China
Hua-Min Liu,
Henan University of Technology, China

*CORRESPONDENCE
Leif J. Jönsson,
leif.jonsson@umu.se

SPECIALTY SECTION
This article was submitted to Bioprocess Engineering, a section of the journal Frontiers in Bioengineering and Biotechnology

RECEIVED 15 October 2022
ACCEPTED 01 December 2022
PUBLISHED 13 December 2022

CITATION
Tang C, Gandla ML and Jönsson LJ (2022), Comparison of solid and liquid fractions of pretreated Norway spruce as reductants in LPMO-supported saccharification of cellulose. *Front. Bioeng. Biotechnol.* 10:1071159. doi: 10.3389/fbioe.2022.1071159

Comparison of solid and liquid fractions of pretreated Norway spruce as reductants in LPMO-supported saccharification of cellulose

Chaojun Tang, Madhavi Latha Gandla and Leif J. Jönsson*

Department of Chemistry, Umeå University, Umeå, Sweden

The role of lignin in enzymatic saccharification of cellulose involving lytic polysaccharide monooxygenase (LPMO) was investigated in experiments with the solid and liquid fractions of pretreated Norway spruce from a biorefinery demonstration plant using hydrothermal pretreatment and impregnation with sulfur dioxide. Pretreated biomass before and after enzymatic saccharification was characterized using HPAEC, HPLC, *Py*-GC/MS, 2D-HSQC NMR, FTIR, and SEM. Chemical characterization indicated that relatively harsh pretreatment conditions resulted in that the solid phase contained no or very little hemicellulose but considerable amounts of pseudo-lignin, and that the liquid phase contained a relatively high concentration (~5 g/L) of lignin-derived phenolics. As judged from reactions continuously supplied with either air or nitrogen gas, lignin and lignin fragments from both the solid and the liquid phases efficiently served as reductants in LPMO-supported saccharification. When air was used to promote LPMO activity, the enzymatic conversion of cellulose after 72 h was 25% higher in reactions with pretreated solids and buffer, and 14% higher in reactions with pretreatment liquid and microcrystalline cellulose. Research in this area is useful for designing efficient saccharification steps in biochemical conversion of lignocellulosic biomass.

KEYWORDS

lignocellulose bioconversion, Norway spruce, enzymatic saccharification, lytic polysaccharide monooxygenase, cellulose, reductant, lignin, pretreatment liquid

1 Introduction

Lignocellulose is an abundant bioresource that has gained wide attention in the production of bio-based commodities (Zhang, 2008). Enzymatic deconstruction of cellulose and hemicelluloses in lignocellulosic biomass to sugars offers a renewable alternative to the refining of fossil resources, which are associated with environmental problems and problems concerning energy security (Kaparaju et al., 2009). Biochemical conversion typically includes hydrothermal pretreatment, enzymatic saccharification of

cellulose, microbial fermentation of sugars, and valorization of the lignin-rich solid residue, often referred to as hydrolysis lignin (Martín et al., 2022). The challenges of biochemical conversion are highly dependent on achieving high sugar yields from cellulose at low cost, thus making it more competitive (Østby et al., 2020).

Enzymatic saccharification of cellulose has typically been achieved using hydrolytic enzymes, such as cellobiohydrolase, endoglucanase, and β-glucosidase (Van Dyk and Pletschke, 2012). More recently, an oxidoreductase called LPMO (lytic polysaccharide monooxygenase) has emerged as a new tool in the deconstruction of recalcitrant lignocellulose, contributing to higher sugar yields (Horn et al., 2012). LPMO is a typical component of currently available commercial enzyme cocktails due to its ability to boost the action of enzymes involved in saccharification of cellulose. It serves as a complement to hydrolytic enzymes due to its ability to catalyze oxidative cleavage of glycosidic bonds of cellulose to create more targets for hydrolysis, which is achieved in the presence of molecular oxygen as co-substrate and an electron donor (Hemsworth et al., 2015).

LPMO-catalyzed reactions can involve different types of electron donors, both small and large molecules. Small organic molecules that serve as electron donors include ascorbic acid (Vaaje-Kolstad et al., 2010) and gallic acid (Quinlan et al., 2011). Larger molecules, such as fungal CDH (cellobiose dehydrogenase) (Phillips et al., 2011), polyphenol oxidase (Frommhagen et al., 2017), and glucose-methanol-choline (GMC) oxidoreductase, have also been proposed to serve as electron donors (Kracher et al., 2016).

Lignin, one of the main components of lignocellulosic biomass, may also increase the activity of GH61 enzymes (later renamed as auxiliary activity family AA9, LPMO) (Dimarogona et al., 2012). Lignin has been proposed to be an electron donor since LPMO has been found to have the ability to oxidize lignocellulosic substrates without addition of an external electron donor, such as ascorbic acid (Cannella et al., 2012; Westereng et al., 2015). This is industrially important, because if lignin or lignin derivatives are sufficient to sustain LPMO-supported saccharification, addition of costly external reaction chemicals, such as ascorbic acid, can be minimized. However, relatively few studies have so far focused on reactions with real industrial lignocellulosic substrates, commercial cellulase cocktails under industrially relevant conditions, and with a controlled supply of gas in the reaction mixtures.

Other reasons for studying lignin and lignin derivatives as electron donors for LPMO include that the lignin content and type of lignin of lignocellulosic biomass differ depending on the biological origin, and that the structure and the fraction of lignin in the raw material are affected in different ways by different types of pretreatments and pretreatment conditions (Martín et al., 2022). The lignin content (DW, dry-weight) in biomass differs from below 20% in grasses and many agricultural residues (Ralph et al., 2004) to around 30% in softwood (Sjöström, 1993). Furthermore, the phenylpropane units in softwood lignin are predominantly G (guaiacyl) units, whereas the lignin of many agricultural residues consists of considerable proportions of G, S (syringyl), and H (*p*-hydroxyphenyl) units (Ralph et al., 2004). The fractions of different interunit linkages also vary in different forms of biomass, although the β-O-4-aryl ether linkage is the most common (Ralph et al., 2004). Although it is hemicellulose rather than lignin that is the target of hydrothermal pretreatment under acidic conditions (Galbe and Wallberg, 2019; Martín et al., 2022), the lignin is also affected. A minor fraction of the lignin is degraded and ends up as phenylic substances (i.e., phenolic and non-phenolic aromatic substances) in the liquid phase after the pretreatment (Ko et al., 2015; Jönsson and Martín, 2016). So far, the role of lignin-derived phenolics as inhibitors has received considerable attention (Jönsson and Martín, 2016), whereas their potential positive role as electron donors for LPMO is not well understood. Due to the large differences between different lignins, more studies on the action of LPMO are needed, especially with lignins and lignin derivatives from industrially important feedstocks and pretreatment processes.

Depending on the industrial process scenario, the liquid phase of pretreated biomass (i.e., the pretreatment liquid or the hemicellulosic hydrolysate) could either be included or excluded during enzymatic saccharification. A common approach is to use a slurry (i.e., a mixture of the solid and the liquid phases obtained after pretreatment) as a substrate for enzymatic saccharification. In that case, both the lignin in the solid phase and water-soluble lignin degradation products in the liquid phase would be present during enzymatic saccharification, and both could potentially serve as reductants in LPMO-catalyzed reactions. However, an alternative approach is to separate the solid and the liquid phases after pretreatment, and in that case only the solid phase would be present during enzymatic saccharification. Then, only the lignin in the solid phase would serve as reductant in LPMO-catalyzed reactions. The question then arises how the electron donor capacity of the pretreated biomass is divided between the solid and the liquid phases.

In this investigation we address the question about how the electron donor capacity is divided between the phases using pretreated biomass from a demonstration plant operated by a commercial company and a novel experimental set-up allowing controlled gas addition to six parallel reaction mixtures. Thereby, better control of the redox environment was achieved, and statistical analysis of results from parallel reaction mixtures was made possible. Even if LPMO is present in modern enzyme preparations, it is not always clear that its capacity is fully exploited due to insufficient supply of reductant and/or molecular oxygen. This makes an experimental set-up with gas addition advantageous, permitting controlled addition of oxygen. Research in this area provides more knowledge about LPMO-catalyzed

reactions and guidance on how to best perform enzymatic saccharification in industrially relevant settings.

2 Materials and methods

2.1 Raw material and pretreatment

Chipped unbarked Norway spruce (*Picea abies*) was pretreated in the Biorefinery Demonstration Plant (BDP) (Örnsköldsvik, Sweden) by SEKAB E-Technology AB. The wood chips were impregnated with sulfur dioxide (approx. 2% based on the dry weight of the biomass), and subsequent pretreatment was performed using continuous steam explosion at 205°C for approx. 10 min. The pH of the generated slurry was approx. 1.8, and the dry-matter content was around 30%.

Prior to enzymatic saccharification experiments, the pH of the slurry was adjusted to 5.2 using a 10 M aqueous solution of sodium hydroxide, and the total solid (TS) content was adjusted to 12.5% (w/w) by dilution with ultra-pure water. The solid and liquid phases of the slurry were separated by centrifugation (Avanti J-26 XP, Beckman Coulter, United States). The solid phase was extensively washed with ultra-pure water until glucose was no longer detectable in the filtrate through analysis with a glucometer (Accu-Chek Aviva, Roche Diagnostics GmBH). The solids were then air-dried before further use. The dry-matter content of the washed and dried solids was 96.6% according to measurements using an HG63 moisture analyzer (Mettler-Toledo, Greifensee, Switzerland). Particles remaining in the liquid phase after centrifugation were removed by passing it through Nalgene™ Rapid-Flow™ sterile filters (0.2 µm, PES, Thermo Fisher Scientific, Waltham, MA, United States). The pretreated solids (PS) and the pretreatment liquid (PL) were then used in enzymatic saccharification experiments.

2.2 Enzymatic saccharification

Two series of enzymatic saccharification experiments were performed. One consisted of pretreatment liquid (PL) with microcrystalline cellulose (Avicel® PH-101 obtained from Sigma-Aldrich, St. Louis, MO, United States) and the other consisted of pretreated solids (PS) with 20 mM sodium acetate buffer, pH 5.2. Reaction mixtures consisted of 8.75 g (dry-weight) solids (PS or Avicel, used as substrate in the enzymatic reaction), 61.25 g liquid phase (buffer or PL), 540 µL Cellic® CTec3 (Novozymes A/S, Bagsvaerd, Denmark) (1.13 g/mL), and 88 µL antifoaming agent (Tween-80). A separate experiment was performed to assure that inclusion of antifoaming agent did not affect the enzymatic reaction (data not shown).

Enzymatic saccharification experiments were carried out using 125 mL gas wash bottles (Quickfit® Drechsel bottle, Sigma-Aldrich). Aerobic and anaerobic conditions were achieved by continuous supply of air or N_2 to the gas wash bottles through Polyamide 12 tubing (outer diameter 6 mm). The set-up could accommodate up to six gas wash bottles in parallel in each experiment, allowing for two sets of triplicates (one set with air and one set with N_2) and subsequent statistical analysis of the results. For each gas supply, a gas distributor divided the gas into three strands, and each gas strand was connected with a flow meter (Porter F65, Parker, United States). The purity of the N_2 was 99.996%. The gas flow was kept at one vvm (based on flow rate and reaction mixture volume). The gas wash bottles were positioned on a multipoint stirrer (Cimarec from Thermo Scientific) immersed in a water bath to allow for temperature control. The bottles were equipped with magnetic stirrer bars (cylindrical 40 × 8 mm), and the stirring speed was 215 rpm. Incubation was performed at 45°C for 72 h, and samples (0.5 mL each) were withdrawn after 24 h, 48 h, and 72 h by using an automatic pipette. Zero samples (0 h) were collected after adding enzyme. Reactions were conducted in triplicates, and the monosaccharides produced in the reactions were analyzed using HPAEC (Section 2.3.1).

After enzymatic saccharification experiments, the mixtures were centrifuged to separate the solid and the liquid phases. Solid phases were washed with abundant ultra-pure water until no glucose was detectable in the filtrate. Washed solids were air-dried until the dry-matter content was over 90%, and they were then sieved using sieve shakers (Retsch AS 200) with an aperture size of 100 µm to homogenize the solid fraction. Liquid phases were stored at 4°C until further analysis.

2.3 Analysis of liquid phase

2.3.1 Analysis of monosaccharides and glucan conversion

Analysis of monosaccharides was performed using high-performance anion-exchange chromatography (HPAEC) with pulsed amperometric detection (PAD). The separation system consisted of an ICS-5000 system equipped with an electrochemical detector, a CarboPac PA1 (4 mm × 250 mm) separation column, and a CarboPac PA1 (4 mm × 50 mm) guard column (all from Dionex, Sunnyvale, CA, United States). The temperature of the column oven was kept at 30°C and all samples were diluted with ultra-pure water and filtered through 0.20 µm nylon membrane filters (Merck Millipore Ltd., Cork, Ireland). Samples were eluted for 25 min with ultra-pure water at a flow rate of 1 mL/min. The column was regenerated by washing for 11 min with a mixture containing 60% of an aqueous solution of 300 mM sodium hydroxide and 40% of an aqueous solution consisting of a mixture of 200 mM sodium hydroxide and 170 mM sodium acetate, followed by 3 min equilibration with ultra-pure water. External calibration standards of monosaccharide mixtures in the range of 0.5 mg/L–30 mg/L

were prepared, and each sample was analyzed in triplicate. Data analysis was performed using the Chromeleon 7.1 software (Dionex).

The conversion of cellulose to glucose (glucan conversion) in the enzymatic hydrolysis was calculated by the ratio of glucose produced during enzymatic hydrolysis in relation to the glucan in the substrate using Eq. 1 (Lu et al., 2012)

$$\text{Glucan conversion } (\%) = \frac{\text{produced glucose concentration} \times \text{M} \times 0.9}{\text{glucan content} \times \text{m}} \times 100 \quad (1)$$

In Eq. 1, the "produced glucose concentration" refers to the glucose concentration determined using HPAEC in (g/L) with potential glucose in the reaction mixture prior to the enzymatic reaction deducted. "M" refers to the total mass (in g) of the enzymatic reaction mixture (solid and liquid) in the beginning of the reaction, and "m" refers to the mass (in g) of total solids. The glucan content of PS was calculated on basis of compositional analysis (Section 2.4.1) and the glucan content of the model substrate Avicel PH-101 was assumed to be 97.6% on basis of literature data (Yu et al., 2012).

2.3.2 Analysis of total phenolics

Folin - Ciocalteu's reagent (Singleton et al., 1999) was used for determination of total phenolics in the PL. Vanillin was used as the calibration standard. The color generated after 40 min incubation at room temperature was measured as the absorbance at 760 nm using a BioTek Epoch Microplate Spectrophotometer (Agilent, Santa Clara, CA, United States). Reactions were performed in triplicates.

2.3.3 Analysis of total carboxylic acid content

The total carboxylic acid content (TCAC) was determined as previously described (Wang et al., 2018a). Briefly, titration using an aqueous sodium hydroxide solution (200 mM) was performed in the range from pH 2.8 to pH 7.0.

2.3.4 Analysis of total aromatic content

Total aromatic content (TAC) covers both aromatics (phenolic and non-phenolic aromatics) and heteroaromatics, such as 5-hydroxymethylfurfural (HMF) and furfural (Wang et al., 2018a). TAC was measured as absorbance units at 280 nm (AU_{280}) using a UV 1800 spectrophotometer (Shimadzu, Kyoto, Japan) with a dilution factor of 1,000.

2.3.5 Analysis of furan aldehydes

Quantitation of HMF and furfural was performed using a Thermo Scientific UltiMate 3,000 HPLC system (Dionex Softron GmbH, Germany) equipped with a detector. The eluents were ultra-pure water with 0.1% (v/v) formic acid (Eluent A) and acetonitrile with 0.1% (v/v) formic acid (Eluent B). The flow rate was 0.5 mL/min. Chromatographic separation was conducted on a Zorbax RRHT SB-C18 column (3.0 mm × 50 mm, 1.8 µm particle size) with 3% of eluent B for 3 min. This was followed by a 4 min cleaning step with 20% of eluent B, and finally the column was equilibrated for 4 min with 3% of eluent B. The absorption at 282 nm was recorded, and the temperature of the column oven was 40°C. An external calibration curve covering the interval 5 µM–250 µM and the Chromeleon 7.1 software were used for quantitation.

2.3.6 Analysis of LPMO oxidation products

Tentative C1 and C4 oxidation products from LPMO-catalyzed reactions were analyzed using the ICS-5000 system and pulsed amperometric detection. Separation was performed on a CarboPac PA1 column for 20 min with a flow rate of 1 mL/min. Gradient elution was carried out for 1.5 min using an aqueous solution of 0.3 M sodium hydroxide, followed by elution for 15.5 min with an aqueous solution consisting of a mixture of 0.3 M sodium hydroxide and 0.5 M sodium acetate. Finally, an aqueous solution of 0.3 M sodium hydroxide was added for 3 min to condition the column before the next sample injection.

2.4 Analysis of pretreated solids

2.4.1 Two-step treatment with sulfuric acid

The contents of carbohydrates and lignin (Klason lignin and acid-soluble lignin) of the solid were determined using the TSSA method. The analysis was performed according to the NREL/TP-510–42618 protocol (Sluiter et al., 2012), with some modifications. Monosaccharides were analyzed by using HPAEC instead of HPLC. Prior to monosaccharides analysis, samples were diluted with ultra-pure water and filtered through 0.20 µm nylon membranes (Section 2.3.1). Acid-insoluble lignin (Klason lignin) was determined gravimetrically by using glass crucibles with integral glass sintered discs (Pyrex 2, porosity 10 µm–16 µm). Acid-soluble lignin (ASL) was determined spectrophotometrically at λ 240 nm (UV-1800 spectrometer, Shimadzu, Kyoto, Japan). All analyses were performed in triplicates.

2.4.2 Pyrolysis-gas chromatography/mass spectrometry

Py-GC/MS was used to determine the lignin-carbohydrate fraction of pretreated solids. The analysis was performed at the Biopolymer Analytical Platform (BAP) of the KBC Chemical-Biological Center (Umeå, Sweden). The instrument consisted of an oven pyrolyzer equipped with an autosampler (PY-2020iD and AS-1020E, Frontier Labs, Koriyama, Japan) connected to a GC/MS system (Agilent 7890A/5975C). The method has been described in detail by Gerber et al. (2016).

2.4.3 Phenolic content of solids

The determination of the phenolic groups content of pretreated solids was performed by MoRe Research AB (Örnsköldsvik, Sweden) using a method based on the study by Lai et al. (Lai et al., 1990). The relative standard error was estimated to 10%.

2.4.4 Fourier transform infrared spectroscopy

FTIR analysis was conducted at the Vibrational Spectroscopy Core Facility (ViSp) of the KBC Chemical-Biological Center. The samples were prepared using potassium bromide (Spectrograde KBr, Fisher Scientific, Waltham, MA, United States). The spectra were obtained on a Bruker IFS 66v/S FTIR spectrometer, equipped with a standard deuterated triglycine sulfate detector and fitted with a diffuse reflectance accessory (Bruker Corporation, Billerica, MA, United States). Spectra between 800 and 1800 cm^{-1} were recorded using 256 scans and 4 cm^{-1} resolution.

2.4.5 2D-HSQC NMR

A portion (25 mg) of each sample was transferred to a 5 mm NMR-tube to which 600 µL DMSO-d6 was added. Samples were analyzed using 2D ^{1}H-^{13}C Heteronuclear Single Quantum Coherence (HSQC) NMR with a Bruker 600 MHz Avance III HD spectrometer equipped with a BBO cryoprobe and using the pulse program hsqcetgpsisp 2.2. For each of the 256 t1-increments, 32 scans were recorded with an inter-scan delay of 1.5 s, resulting in an experimental time of approximately 3 h and 50 min. Experiments were performed at 298 K. Alcohol-insoluble residue (AIR) of wood of Norway spruce was dissolved in DMSO-d6 and used as non-pretreated reference. Spectra were processed using Topspin 3.6 (Bruker Biospin, Germany) with Gaussian window function in F2 and a 90-degree shifted squared sine-bell window function in F1.

2.4.6 Scanning electron microscopy

After washing with water and drying (Section 2.1), dried PS were dispersed onto carbon conductive tape mounted on an aluminum specimen stub and coated with 10 nm platinum using a carbon-sputter coater (Quorum Q150T-ES). The morphology of the PS samples was analyzed by field-emission scanning electron microscopy (FESEM, Carl Zeiss Merlin GmbH) using an in-lens secondary electron detector at a voltage of 3 kV and a probe current of 30 pA. The SEM analysis was conducted at the Umeå Core Facility Electron Microscopy (UCEM) of the KBC Chemical-Biological Center.

3 Results and discussion

3.1 Analysis of pretreated biomass

The liquid and solid fractions of pretreated softwood from the demonstration plant were analyzed to get an overview of lignin-related material and carbohydrates in the fractions. According to compositional analysis using TSSA (Table 1), the pretreated solids contained (DW) 44.5% glucan and 51.6% total lignin (Klason lignin and ASL). No other carbohydrates than glucan were detected. This indicates that the pretreatment conditions had been very harsh, as all hemicellulosic carbohydrates had been removed and as the lignin content was higher than the glucan content. From the beginning, it is the other way around, as untreated spruce wood contains 27.4% lignin and 41.7% cellulose (Sjöström, 1993). The aim with the pretreatment is to achieve an almost quantitative removal of hemicelluloses, without degrading cellulose, which is left for enzymatic saccharification. The fact that the total lignin content was higher than the glucan content indicates partial degradation of cellulose, formation of pseudo-lignin from hemicelluloses, or occurrence of both these events. Pseudo-lignin is a Klason-lignin-positive aromatic substance formed from carbohydrates during thermal treatment under harsh conditions (Shinde et al., 2018; Martín et al., 2022; Yao et al., 2022).

Analysis using *Py*-GC/MS (Table 1) suggested that the pretreated material predominantly (~70%) consisted of carbohydrates and that around a quarter of the content was lignin. As expected for softwood (Ralph et al., 2004) such as spruce, the lignin predominantly consisted of G units (Table 1). With respect to the determined fractions, the discrepancy compared to the results from the TSSA analysis can be explained by pseudo-lignin being characterized as carbohydrates in the *Py*-GC/MS analysis, which has been observed previously (Wang et al., 2018a). Thus, compositional analysis using TSSA and *Py*-GC/MS indicated that the hemicelluloses had been quantitatively removed or degraded and that the pretreated material predominantly consisted of three substances: glucan, lignin, and pseudo-lignin.

The pretreated solids were analyzed further using HSQC NMR (Figure 1). Pretreated solids exhibited relatively poor solubility in DMSO compared to non-pretreated Norway spruce wood, and the signals were weaker. The pretreatment affected the aromatic region of the lignin, as indicated by the lower intensity of G2 and G6 after pretreatment. Signals from common interunit lignin linkages, such as β-O-4 and phenylcoumaran, were weak in the pretreated material (Figure 1). These changes are in agreement with previous studies of lignin after pretreatment under acidic conditions (Yao et al., 2022). An attempt to solubilize more of the pretreated material using a mixture of DMSO-d6 and pyridine-d5 (Kim and Ralph, 2010) to obtain stronger signals was unsuccessful.

SEM was used to further investigate the structure of the solid fractions. Micrographs of PS showed nano-sized particles or droplets on fibrillar surfaces (Figure 2A). There are previous reports on droplets on biomass surfaces caused by relocalization of lignin (Selig et al., 2007; Donohoe et al., 2008) and by pseudo-lignin formation

TABLE 1 Analysis of the solid phase of pretreated Norway spruce.

Analysis and constituent		PS[g]	PS-Air[g]	PS-N_2[g]
TSSA[a]	Glucan	44.5 (1.6)	28.8 (1.2)	37.5 (1.0)
	Xylan	ND	ND	ND
	Mannan	ND	ND	ND
	Arabinan	ND	ND	ND
	Galactan	ND	ND	ND
	Klason lignin	44.8 (0.7)	56.2 (2.7)	47.9 (1.4)
	ASL[f]	6.8 (0.1)	6.3 (0.2)	5.8 (0.1)
	Ash	≤ 0.3	≤ 0.3	≤ 0.3
Py-GC/MS[b]	Carbohydrates	67.4 (1.0)	58.6 (1.0)	63.7 (1.1)
	G	21.3 (0.6)	28.7 (0.7)	24.7 (0.6)
	H	2.5 (0.1)	3.3 (0.1)	2.9 (0.1)
	Total lignin	24.2 (0.6)	32.6 (0.8)	28.0 (0.7)
	Carb./lignin	2.8 (0.1)	1.8 (0.1)	2.3 (0.1)
Phenolic hydroxyl groups[c]	mmol/kg DS[d]	760	1,030	970
	mmol/kg total lignin[e]	1,460	1,650	1810

[a]Two-step treatment with sulfuric acid. Values given in percent dry weight with standard deviations in parentheses.
[b]Values given in percent of peak area, according to method described by Gerber et al. (2016).
G, guaiacyl; H, *p*-hydroxyphenyl. Standard deviations in parentheses.
[c]Method described by Lai et al. (1990), with relative standard error estimated to 10%.
[d]Values given in mmol/kg dry solids.
[e]Mmol/kg total lignin (compositional analysis).
[f]ASL: acid-soluble lignin.
[g]PS, pretreated solids; PS-Air, solid fraction after 72 h enzymatic saccharification with air; PS-N_2, solid fraction after 72 h enzymatic saccharification with N_2.

(Sannigrahi et al., 2011) during pretreatment under acidic conditions. Such droplets could vary significantly in size, such as from 5 nm up to 10 μm (Donohoe et al., 2008) or 0.3 μm–8.0 μm (Sannigrahi et al., 2011). It is a possibility that harsh, acidic pretreatment conditions contributed to the formation of these structures (Figure 2A). After enzymatic saccharification with air, the surfaces appeared somewhat smoother (Figure 2B). This was less pronounced in reactions with N_2 (Figure 2C), where the enzymatic saccharification had reached less far.

As expected considering the relatively high content of galactoglucomannan in spruce wood (Sjöström, 1993), mannose was the predominant hemicellulosic monosaccharide in the PL (Table 2). The total concentration of hemicellulosic sugars (mannose, xylose, galactose, and arabinose) (Table 2) was 36 g/L, and the concentration of glucose was around 31 g/L (Table 3). Even if it is not intentional to degrade cellulose in the pretreatment, the glucose could come either from hemicelluloses or from partial degradation of cellulose.

The concentrations of substances in the pretreatment liquid (Tables 2, 3) can be compared to those found in a series of pretreatment liquids from Norway spruce pretreated with sulfur dioxide under low, medium, and high severity (Wang et al., 2018a; Martín et al., 2018). The TCAC content was just below 200 mM (Table 2), which is very high for a TS content of 12.5% considering that it was 203 mM after the most severe treatment when the TS was 25% (Wang et al., 2018a). The content of total phenolics was around 5 g/L, which again is very high compared to 1.6 g/L after the most severe treatment in a previous study of material with TS ~30% (Martín et al., 2018). The combined concentration of furfural and HMF was around 59 mM (Table 2). Considering the TS, 12.5%, that is higher than the highest combined value for furfural and HMF reported by Martín et al. (2018), which was 87 mM at a TS of around 30%. The TAC value (1.2 with 1,000 × dilution) was also relatively high compared to previous studies, as Wang et al. (2018a) reported values from 0.59 up to 2.74 with TS 25% and 500 × dilution. That is consistent with the high values for total phenolics and furan aldehydes, as TAC covers both of these groups of substances.

The results of the analysis of the liquid phase are consistent with the results of the analysis of the solid phase, as both data sets point to very harsh pretreatment and, consequently, high contents of Klason lignin and phenolics. The content of lignin

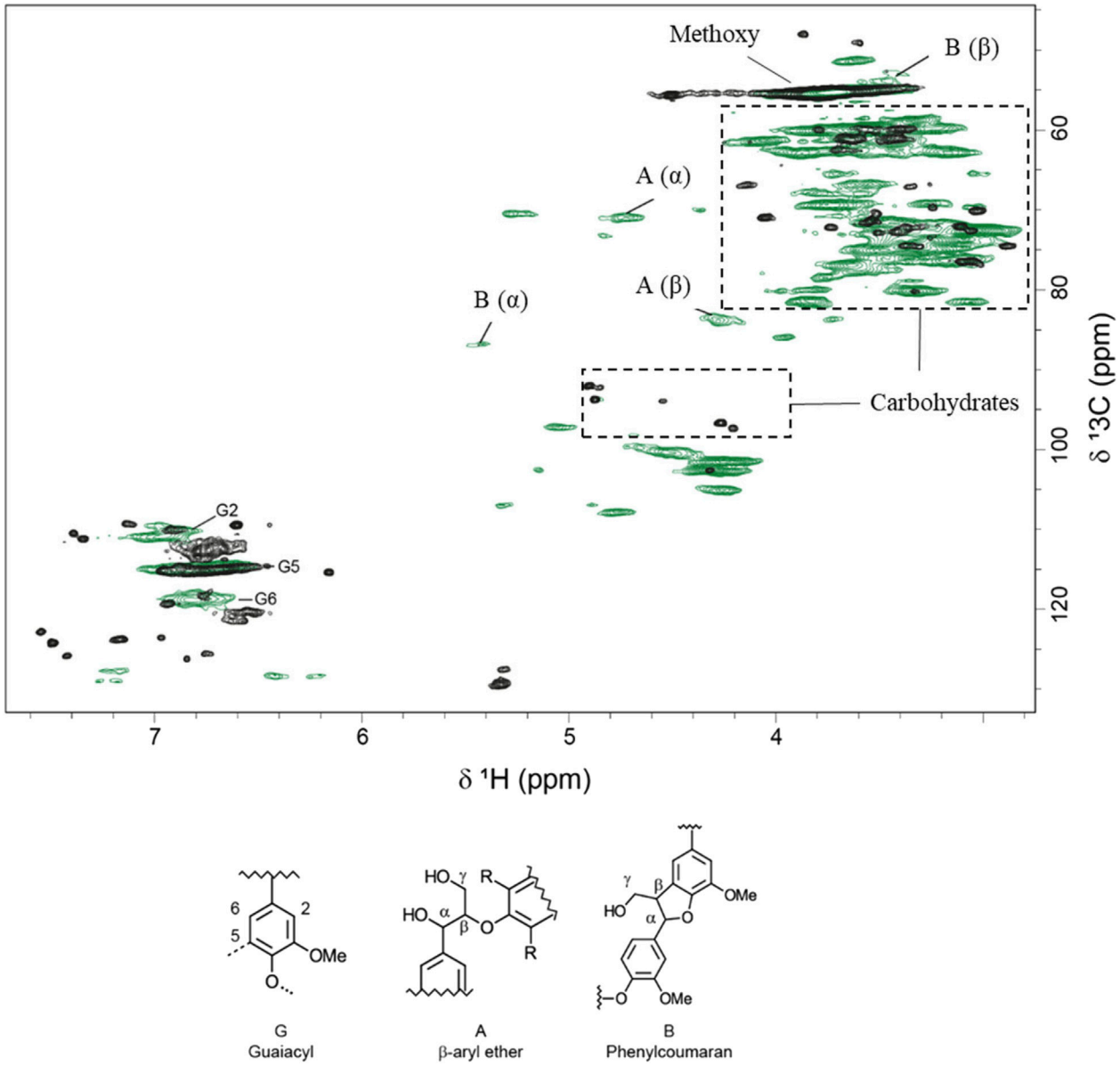

FIGURE 1
Overlay of two-dimensional $^{1}H-^{13}C$ HSQC NMR spectra of alcohol-insoluble residue from Norway spruce (in green) and pretreated solids (in black).

in the solid phase and the content of phenolics in the liquid phase would be relevant, as it may affect the ability of these fractions to serve as reductants in reactions with LPMO. In addition to that, substances in the PL might inhibit cellulolytic enzymes. Such substances include both sugars (causing feedback inhibition of cellulases) and aromatics, such as phenolics (Zhai et al., 2016; Martín et al., 2022).

The total monosaccharide concentration (~67 g/L) of the PL used in this work was similar to the total monosaccharide concentrations (64 g/L–77 g/L) of the PLs studied by Wang et al. (2018a). As all PLs studied by Wang et al. (2018a) had total monosaccharide concentrations that were inhibitory to the cellulolytic enzyme preparations, it is safe to assume that the PL used in this work also caused sugar inhibition. All PLs studied by Wang et al. (2018a) were also clearly inhibitory to cellulolytic enzyme preparations with respect to other substances than monosaccharides, such as phenolics, despite that the concentrations of phenolics in the PLs [0.7 g/L–1.6 g/L according to data from Martín et al. (2018)] were much lower than in the PL used in this work (~5 g/L). It is therefore likely that

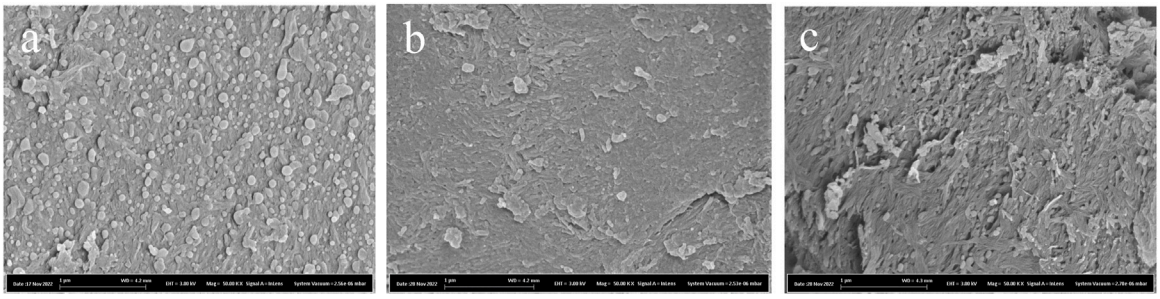

FIGURE 2
SEM micrographs of washed pretreated solids prior to enzymatic saccharification reactions **(A)**, and after 72 h of enzymatic saccharification in reactions supplemented with **(B)** air and **(C)** N_2. The scale bar length is 1 μm.

TABLE 2 Analysis of pH-adjusted pretreatment liquid and the liquid phases after 72 h saccharification.[a]

Property/substance	PL	PL-air	PL-N_2
pH	5.1	4.6	5.0
TCAC (mM)[b]	192 (5)	261 (2)	244 (8)
Total phenolics (g/L)[c]	5.1 (0.3)	5.6 (0.2)	5.9 (0.6)
HMF (mM)	26.6 (0.2)	31.1 (0.3)	29.8 (2.1)
Furfural (mM)	32.2 (0.2)	0.5 (0.1)	0.6 (0.1)
TAC[d]	1.2 (0.1)	0.8 (0.1)	0.8 (0.1)
Mannose (g/L)[e]	20.0 (0.7)	25.0 (0.7)	26.8 (1.4)
Xylose (g/L)[e]	10.2 (0.4)	14.2 (0.3)	14.8 (0.7)
Galactose (g/L)[e]	3.9 (0.2)	5.0 (0.2)	5.3 (0.3)
Arabinose (g/L)[e]	2.3 (0.1)	2.7 (0.1)	2.9 (0.2)

[a]Standard deviations are shown in parentheses.
[b]Total Carboxylic Acid Content determined using titration with a solution of sodium hydroxide.
[c]Concentration of total phenolics using the Folin-Ciocalteu assay with vanillin as the standard.
[d]Total Aromatic Content indicated as absorbance units at 280 nm (AU_{280}) with a dilution factor of 1,000.
[e]Concentration of hemicellulosic monosaccharides. Values from PL, are zero samples while values from PL-Air and PL-N_2, are from 72 h of saccharification.

TABLE 3 Sugar yields from reaction mixtures with pretreated solids or pretreatment liquid.[a,b]

Reaction Mixture		Glucose concentration (g/L)[c]				Glucan conversion (% w/w) after 72 h[d]	Increase in glucan conversion in aerated reaction after 72 h (%)
		0 h	24 h	48 h	72 h		
PS with buffer	Air	3.0 (0.4)	27.7 (2.6)***	38.2 (4.9)*	56.3 (5.2)***	85.9 (8.1)***	25
	N_2	2.8 (0.4)	23.7 (2.1)	33.5 (3.5)	45.3 (4.1)	68.6 (6.3)	
Avicel with PL	Air	31.3 (1.2)	63.9 (1.1) ***	77.9 (2.5)***	85.7 (2.6)***	40.1 (1.5)***	14
	N_2	30.6 (1.2)	52.4 (1.4)	65.8 (2.6)	78.4 (3.8)	35.2 (3.2)	

[a]Enzymatic saccharification of pretreated solids (PS) in 20 mM sodium acetate buffer (pH 5.2) and of Avicel PH-101, in pretreatment liquid (PL).
[b]Standard deviations in parentheses. Asterisks indicate significant differences (Student *t*-test) between aerobic and corresponding anaerobic conditions: ***$p \leq 0.01$; ** $0.01 < p \leq 0.05$; * $0.05 < p \leq 0.1$.
[c]Glucose concentrations (g/L) analyzed using HPAEC.
[d]Glucan conversion (% w/w) was calculated according to Eq. 1, with a glucan content of 44.5% in PS, and 97.6% in Avicel PH-101.

the PL used in this work also contained inhibitory concentrations of phenolics.

3.2 Sugar yields in enzymatic saccharification experiments

The enzymatic saccharification reactions contained the same amount of solids (8.75 g Avicel or PS), but different glucan content. Whereas Avicel consists almost exclusively of glucan (in the form of microcrystalline cellulose), the PS had a glucan content of 44.5%, and therefore the reaction mixtures with PS contained 3.89 g glucan rather than 8.75. Reactions with PS also contained lignin and pseudo-lignin, which have a negative effect on saccharification (Shinde et al., 2018; Martín et al., 2022; Yao et al., 2022). Avicel would therefore be a much better substrate than PS, but the reactions with Avicel also contained PL and therefore also sugars and phenolics that inhibit enzymatic saccharification. For these reasons, it was not self-evident which set of reactions that would result in the highest enzymatic saccharification yields.

Data on glucose concentrations and glucan conversion are shown in Table 3. As expected (Arantes and Saddler, 2011), the glucose concentrations increased rapidly in the beginning and leveled off at the end. The glucose concentrations (in g/L) generated between the zero sample and 72 h were: PS/air, 53.3; PS/N_2 42.5; Avicel/air, 54.4; Avicel/N_2, 47.8. Thus, reactions with air always resulted in more glucose than the corresponding reactions with N_2 (25% more for PS and 14% more for Avicel). This can be attributed to the catalytic action of LPMO, and it was apparent both with PS and PL without any addition of external reductant. Although the glucose yields of enzymatic saccharification were rather similar for reactions with air (53 g/L–54 g/L) and for reactions with N_2 (42 g/L–48 g/L), the glucan conversion was higher for reactions with PS (68.6%–85.9%) than for reactions with Avicel (35.2%–40.1%). This phenomenon can be attributed to the presence of enzyme inhibitors in PL having a negative effect on the reactions with Avicel, and perhaps also to the enzyme:glucan ratio being more than twice as high in experiments with PS as in experiments with Avicel.

This work differs from previous studies of LPMO-catalyzed reactions with pretreated biomass in several different ways; as it (i) covers the separated solid and liquid phases from the pretreated biomass, (ii) involves controlled continuous gas addition using air or N_2, (iii) is based on hydrothermal pretreatment of spruce wood with sulfur dioxide in a demonstration plant, (iv) involves no redox-active chemicals except oxygen in air in additions after pretreatment, and (v) involves detailed characterization of the liquid and solid phases, for instance with respect to the occurrence of pseudo-lignin. In a series of experiments with steam-pretreated lodgepole pine with different lignin content, Hu et al. (2014) found that addition of an external reducing agent (gallate) had a positive effect on the LPMO reaction only with a completely delignified substrate, but not when the lignin content was 12% or higher. Rodríguez-Zúñiga et al. (2015) investigated washed pretreated solids from sugarcane bagasse, wheat straw, and corn stover. The gas phase was not controlled, but determination of gluconic acid, an oxidation product from the LPMO reaction, suggested that substrates with low (9.6% or less) Klason lignin content were associated with no or very small LPMO activity. Müller et al. (2015) showed improved saccharification of pretreated birch wood in flasks containing air in the headspace compared to reactions in flasks in which the headspace was flushed with N_2 and in which cysteine was added to the reaction mixtures to remove residual oxygen. Chylenski et al. (2017) investigated saccharification of sulfite-pulped softwood, and therefore their biomass contained much less lignin (4%–9% acid-insoluble lignin) than that used by Müller et al. (2015) or that used in the present study. As a result, improved saccharification with air in the headspace was observed only when an electron donor, such as ascorbic acid or lignosulfonates, was added to the reaction mixtures (Chylenski et al., 2017). These results agree with our findings, as the lignin content of the solid phase used in our experiments was clearly higher than the lignin contents of substrates for which no or very little LPMO activity has been detected without addition of an external reductant.

3.3 Analysis of liquid phase after enzymatic saccharification

The liquid phases at the end of the reactions with Avicel (PL-Air and PL-N_2) were analyzed with regard to other substances than glucose (Table 2; Figure 3). Smaller increases (0.4 g/L–6.8 g/L) in the concentrations of sugars other than glucose (Table 2) can be attributed to enzymatic saccharification of oligosaccharides and disaccharides, and also to concentration of reaction mixtures at the end of the experiments due to evaporation caused by gas flow.

The pH decreased somewhat in PL-Air, and the TCAC value was higher than for PL-N_2. It is a possibility that oxidation products from LPMO-catalyzed reactions contribute to the high acid content in PL-Air. This is supported by data in Figure 3, which shows analysis of tentative C1 and C4 oxidation products. As judged from the elution time, the tentative C1 product [RT (retention time) 8.83] would correspond to gluconic acid (RT 8.84 for gluconic acid reference), and, at the end of the reaction (48 h), the peak area was much larger for reactions with air than for reactions with N_2 (Figure 3C). The area of an unidentified peak at RT 13.4 increased for reactions with air, which was not observed for reactions with N_2 (Figure 3B). This could tentatively reflect formation of a C4 oxidation product.

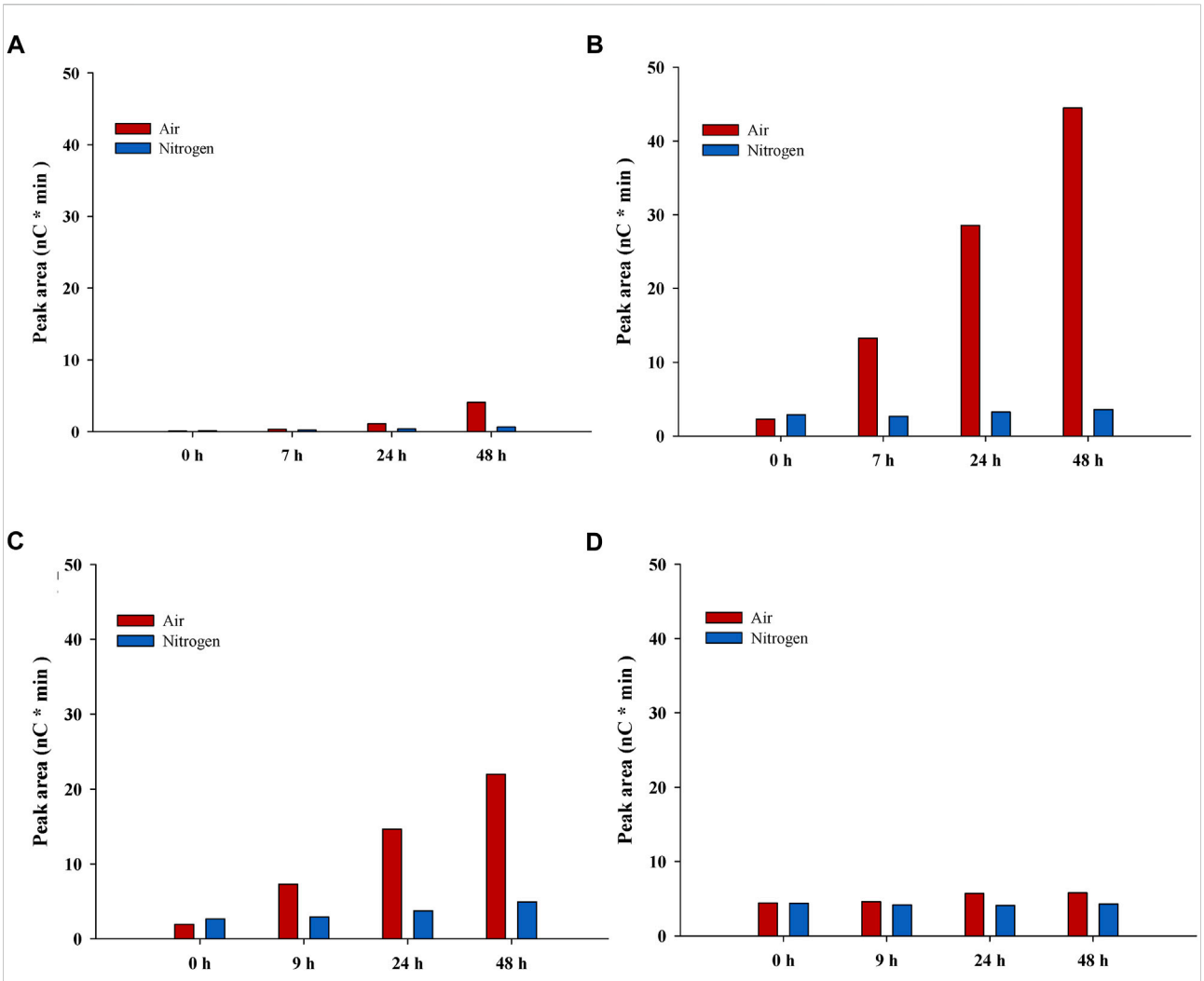

FIGURE 3
Estimation of oxidation products from LPMO-catalyzed reactions. The figure shows data for peaks with oxidation products from reactions with pretreated solids in buffer **(A)** and **(B)** and with Avicel in pretreatment liquid **(C)** and **(D)**. Left-hand panels **(A)** and **(C)** show the tentative C1 product, while right-hand panels **(B)** and **(D)** show the tentative C4 product. Red bars, reactions with air; blue bars, reactions with N_2.

Minor concentrations of the tentative C1 and C4 products were present also in reaction mixtures with N_2, but that could be due to that those reactions were not completely devoid of molecular oxygen or other oxidants. Also, N_2 contains molecular oxygen as contaminant, so small amounts of molecular oxygen would be added throughout the experiment even in reactions with N_2.

LPMO-catalyzed cleavage of cellulose leads to oxidation of carbons in the β-1,4-glycosidic bonds, i.e., oxidation of C1 or C4. Using Cellic CTec2, Cannella et al. (2012) studied C1 oxidation products, such as gluconic acid and cellobionic acid, in reactions with pretreated wheat straw. Müller et al. (2015) quantified C4-oxidized cellobiose in reaction mixtures with pretreated birch wood and Cellic CTec2.

With regard to aromatic and heteroaromatic substances, the concentrations of total phenolics and HMF did not change very much throughout the experiment (Table 2). The concentration of furfural decreased from 32 mM in PL to around 1 mM in PL-Air and PL-N_2. This is because furfural is much more volatile than HMF and the gas flow will remove it, as has also been observed in previous studies (Larsson et al., 1999). The TAC value decreased somewhat in both PL-Air and PL-N_2, which can be attributed to the removal of furfural, as both aromatics and heteroaromatics contribute to TAC. The total phenolic content was somewhat higher after the reactions than in the original PL (Table 2). One reason for this could be contribution to total phenolics by the enzyme preparation, which was not yet added to the PL when samples for analysis of total phenolics were withdrawn.

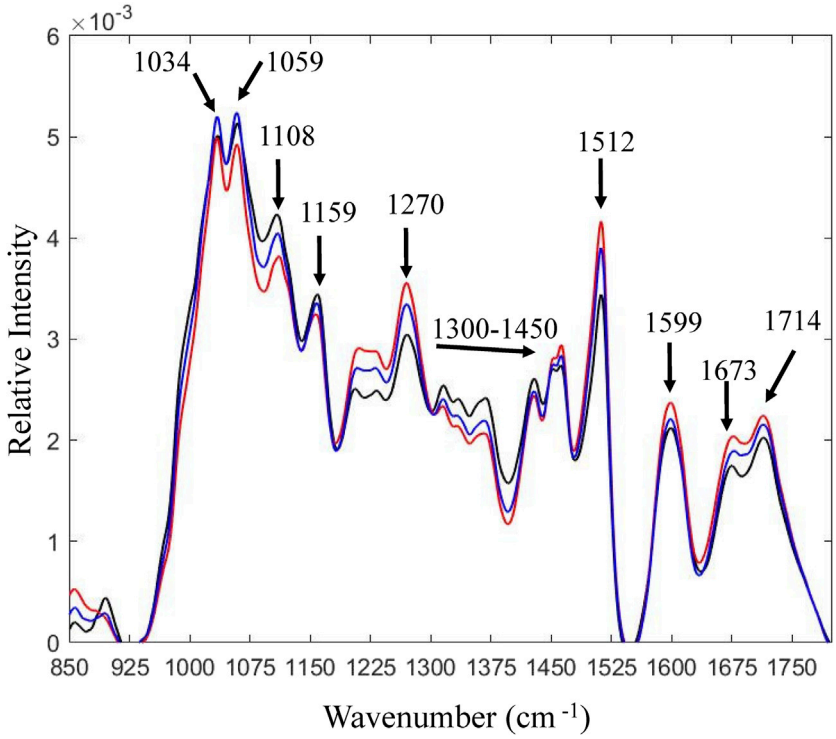

FIGURE 4
FTIR analysis of pretreated solids and solid fractions after 72 h of enzymatic saccharification. Black line, pretreated solids; blue line, reaction with N_2; red line, reaction with air. Observed differences reflect relative compositional changes [total area normalization was performed on the spectra using MATLAB software developed by ViSp (Vibrational Spectroscopy Core Facility)].

3.4 Analysis of solid phase after enzymatic saccharification

As expected on basis of the saccharification data in Table 3, the glucan (TSSA) and carbohydrate (Py-GC/MS) contents of PS-Air and PS-N_2 decreased compared to that of PS, while Klason lignin (TSSA) and total lignin (Py-GC/MS) increased (Table 1). The changes compared to PS were consistently larger for PS-Air than for PS-N_2. This can also be seen as shifts in the carbohydrate:lignin ratio according to the Py-GC/MS analysis (Table 1).

Spruce lignin contains around 20.5 phenolic hydroxyl groups per 100 C9 (phenylpropane) units (Adler, 1977). The content of phenolic hydroxyl groups on dry solids increased in PS-Air and PS-N_2 compared to PS (Table 1). This is expected, as the enzymatic saccharification of cellulose increases the fraction of lignin. When calculated as phenolic hydroxyl groups on total lignin (Klason lignin and ASL), the values for PS-Air and PS-N_2 were still slightly higher than for PS.

Solid residues from PS-Air and PS-N_2 reactions were analyzed using HSQC-NMR and FTIR. As for PS (Figure 1), the solubility was rather poor and the signals were relatively weak. Using FTIR, the solid fraction after enzymatic saccharification was compared to PS (Figure 4). Lower wavenumber regions, such as 1,030 cm^{-1}–1,060 cm^{-1} and 1,108 cm^{-1} (ring vibrations) were assigned to polysaccharides (Labbé et al., 2005; Fackler et al., 2010; Durmaz et al., 2016). Lower band intensities for the reaction with air are consistent with more efficient enzymatic saccharification. This is also supported by differences observed for the bands at ~ 1,150 cm^{-1} (Labbé et al., 2005) and 1,158 cm^{-1} (Pandey and Nagveni, 2007), which are associated with C-O-C asymmetric vibrations. Bands from 1,300 cm^{-1} to 1,450 cm^{-1} were assigned to C-H vibrations attributed to cellulose (Labbé et al., 2005). Lignin exhibits characteristic bands at 1,510 cm^{-1} and 1,600 cm^{-1}. These bands are assigned to aromatic carbon-carbon double bonds (Sarkanen and Ludwig, 1971) and the band at 1,510 cm^{-1} is especially assigned for G units of lignin (Faix, 1991). In addition, an increase at 1,595 cm^{-1} is associated with aromatic skeletal vibrations (Faix, 1991; Faix and Böttcher, 1992) and indicates formation of pseudo-lignin (Wang et al., 2018b). According to previous studies (Faix, 1991; Pandey, 1999; Pandey and Nagveni, 2007), the band at 1,268 cm^{-1} is attributed to guaiacyl rings and carbonyl stretching in lignin. The band at 1,714 cm^{-1} is related to C = O stretching in unconjugated ketones, associated with pseudo-lignin (Sannigrahi et al., 2011), whereas the band at 1,672 cm^{-1} has been assigned to conjugated carbonyl groups (Gillgren et al., 2017).

4 Conclusion

The benefits of exploiting the LPMO present in a commercial enzyme mixture was investigated in experiments with softwood pretreated using continuous steam explosion with sulfur dioxide as catalyst. Harsh pretreatment conditions created a solid phase consisting mainly of Klason lignin and cellulose, with pseudo-lignin but without detectable amounts of hemicelluloses, and a liquid phase with high contents of lignin-derived phenols. Experiments with reaction mixtures that were continuously supplied with air or N_2 indicate that both insoluble lignin in the solid phase and water-soluble lignin fragments in the liquid phase efficiently served as reductants in LPMO-supported saccharification of cellulose. Although relatively high concentrations of pretreatment by-products in the liquid phase had a suppressing effect on the saccharification reactions due to inhibition of cellulolytic enzymes, they also had a positive effect in the presence of air by supporting the LPMO reaction. Further research is needed to elucidate more details regarding the effects of water-soluble lignin fragments and potential effects of pseudo-lignin on LPMO-supported saccharification of cellulose.

Data availability statement

The original contributions presented in the study are included in the article/Supplementary Material, further inquiries can be directed to the corresponding author.

Author contributions

Experiments and draft of the manuscript, CT; writing-review and editing, MG and LJ; supervision, MG and LJ; funding acquisition LJ. All authors read and approved the manuscript.

Funding

This work was supported by funding from the Swedish Energy Agency (P47516-1) and Bio4Energy (www.bio4energy.se).

Acknowledgments

We are grateful to Sekab-E Technology AB (Örnsköldsvik, Sweden) for providing pretreated material from the Biorefinery Demo Plant. We are also grateful for the services offered by the analytical facilities of the KBC Chemical-Biological Center (Umeå, Sweden): Junko Takahashi-Schmidt at the Biopolymer Analytical Platform for Py-GC/MS analysis, Mattias Hedenström at the NMR Core Facility, András Gorzsás at the Vibrational Spectroscopy Core Facility for FTIR analysis and Lee Cheng Choo at Umeå Centre for Electron Microscopy (UCEM) and National Microscopy Infrastructure (NMI).

Conflict of interest

The authors declare that the research was conducted in the absence of any commercial or financial relationships that could be construed as a potential conflict of interest.

Publisher's note

References

Adler, E. (1977). Lignin chemistry - past, present and future. *Wood Sci. Technol.* 11, 169–218. doi:10.1007/bf00365615

Arantes, V., and Saddler, J. N. (2011). Cellulose accessibility limits the effectiveness of minimum cellulase loading on the efficient hydrolysis of pretreated lignocellulosic substrates. *Biotechnol. Biofuels* 4, 3–17. doi:10.1186/1754-6834-4-3

Cannella, D., Hsieh, C. W., Felby, C., and Jørgensen, H. (2012). Production and effect of aldonic acids during enzymatic hydrolysis of lignocellulose at high dry matter content. *Biotechnol. Biofuels* 5, 26. doi:10.1186/1754-6834-5-26

Chylenski, P., Petrović, D. M., Müller, G., Dahlström, M., Bengtsson, O., Lersch, M., et al. (2017). Enzymatic degradation of sulfite-pulped softwoods and the role of LPMOs. *Biotechnol. Biofuels* 10, 177. doi:10.1186/s13068-017-0862-5

Dimarogona, M., Topakas, E., Olsson, L., and Christakopoulos, P. (2012). Lignin boosts the cellulase performance of a GH-61 enzyme from *Sporotrichum thermophile*. *Bioresour. Technol.* 110, 480–487. doi:10.1016/j.biortech.2012.01.116

Donohoe, B. S., Decker, S. R., Tucker, M. P., Himmel, M. E., and Vinzant, T. B. (2008). Visualizing lignin coalescence and migration through maize cell walls following thermochemical pretreatment. *Biotechnol. Bioeng.* 101, 913–925. doi:10.1002/bit.21959

Durmaz, S., Özgenc, Ö., Boyaci, I. H., Yıldız, Ü. C., and Erişir, E. (2016). Examination of the chemical changes in spruce wood degraded by brown-rot fungi using FT-IR and FT-Raman spectroscopy. *Vib. Spectrosc.* 85, 202–207. doi:10.1016/j.vibspec.2016.04.020

Fackler, K., Stevanic, J. S., Ters, T., Hinterstoisser, B., Schwanninger, M., and Salmén, L. (2010). Localisation and characterisation of incipient brown-rot decay within spruce wood cell walls using FT-IR imaging microscopy. *Enzyme Microb. Technol.* 47, 257–267. doi:10.1016/j.enzmictec.2010.07.009

Faix, O., and Böttcher, J. H. (1992). The influence of particle size and concentration in transmission and diffuse reflectance spectroscopy of wood. *Holz Roh. Werkst.* 50, 221–226. doi:10.1007/bf02650312

Faix, O. (1991). Classification of lignins from different botanical origins by FT-IR spectroscopy. *Holzforschung* 45, 21–28. doi:10.1515/hfsg.1991.45.s1.21

Frommhagen, M., Mutte, S. K., Westphal, A. H., Koetsier, M. J., Hinz, S. W. A., Visser, J., et al. (2017). Boosting LPMO-driven lignocellulose degradation by polyphenol oxidase-activated lignin building blocks. *Biotechnol. Biofuels* 10, 121. doi:10.1186/s13068-017-0810-4

Galbe, M., and Wallberg, O. (2019). Pretreatment for biorefineries: A review of common methods for efficient utilisation of lignocellulosic materials. *Biotechnol. Biofuels* 12, 294. doi:10.1186/s13068-019-1634-1

Gerber, L., Öhman, D., Kumar, M., Ranocha, P., Goffner, D., and Sundberg, B. (2016). High-throughput microanalysis of large lignocellulosic sample sets by pyrolysis-gas chromatography/mass spectrometry. *Physiol. Plant.* 156, 127–138. doi:10.1111/ppl.12397

Gillgren, T., Hedenström, M., and Jönsson, L. J. (2017). Comparison of laccase-catalyzed cross-linking of organosolv lignin and lignosulfonates. *Int. J. Biol. Macromol.* 105, 438–446. doi:10.1016/j.ijbiomac.2017.07.061

Hemsworth, G. R., Johnston, E. M., Davies, G. J., and Walton, P. H. (2015). Lytic polysaccharide monooxygenases in biomass conversion. *Trends Biotechnol.* 33, 747–761. doi:10.1016/j.tibtech.2015.09.006

Horn, S. J., Vaaje-Kolstad, G., Westereng, B., and Eijsink, V. G. H. (2012). Novel enzymes for the degradation of cellulose. *Biotechnol. Biofuels* 5, 45. doi:10.1186/1754-6834-5-45

Hu, J. G., Arantes, V., Pribowo, A., Gourlay, K., and Saddler, J. N. (2014). Substrate factors that influence the synergistic interaction of AA9 and cellulases during the enzymatic hydrolysis of biomass. *Energy Environ. Sci.* 7, 2308–2315. doi:10.1039/c4ee00891j

Jönsson, L. J., and Martín, C. (2016). Pretreatment of lignocellulose: Formation of inhibitory by-products and strategies for minimizing their effects. *Bioresour. Technol.* 199, 103–112. doi:10.1016/j.biortech.2015.10.009

Kaparaju, P., Serrano, M., Thomsen, A. B., Kongjan, P., and Angelidaki, I. (2009). Bioethanol, biohydrogen and biogas production from wheat straw in A biorefinery concept. *Bioresour. Technol.* 100, 2562–2568. doi:10.1016/j.biortech.2008.11.011

Kim, H., and Ralph, J. (2010). Solution-state 2D NMR of ball-milled plant cell wall gels in DMSO-d6/pyridine-d5. *Org. Biomol. Chem.* 8, 576–591. doi:10.1039/b916070a

Ko, J. K., Um, Y., Park, Y. C., Seo, J. H., and Kim, K. H. (2015). Compounds inhibiting the bioconversion of hydrothermally pretreated lignocellulose. *Appl. Microbiol. Biotechnol.* 99, 4201–4212. doi:10.1007/s00253-015-6595-0

Kracher, D., Scheiblbrandner, S., Felice, A. K., Breslmayr, E., Preims, M., Ludwicka, K., et al. (2016). Extracellular electron transfer systems fuel cellulose oxidative degradation. *Science* 352, 1098–1101. doi:10.1126/science.aaf3165

Labbé, N., Rials, T. G., Kelley, S. S., Cheng, Z. M., Kim, J. Y., and Li, Y. (2005). FT-IR imaging and pyrolysis-molecular beam mass spectrometry: New tools to investigate wood tissues. *Wood Sci. Technol.* 39, 61–76. doi:10.1007/s00226-004-0274-0

Lai, Y. Z., Guo, X. P., and Situ, W. (1990). Estimation of phenolic hydroxyl-groups in wood by a periodate-oxidation method. *J. Wood Chem. Technol.* 10, 365–377. doi:10.1080/02773819008050245

Larsson, S., Reimann, A., Nilvebrant, N. O., and Jönsson, L. J. (1999). Comparison of different methods for the detoxification of lignocellulose hydrolyzates of spruce. *Appl. Biochem. Biotechnol.* 77, 91–104. doi:10.1385/Abab:77:1-3:91

Lu, J., Li, X. Z., Zhao, J., and Qu, Y. B. (2012). Enzymatic saccharification and ethanol fermentation of reed pretreated with liquid hot water. *J. Biomed. Biotechnol.* 2012, 1–9. doi:10.1155/2012/276278

Martín, C., Dixit, P., Momayez, F., and Jönsson, L. J. (2022). Hydrothermal pretreatment of lignocellulosic feedstocks to facilitate biochemical conversion. *Front. Bioeng. Biotechnol.* 10, 846592. doi:10.3389/fbioe.2022.846592

Martín, C., Wu, G., Wang, Z., Stagge, S., and Jönsson, L. J. (2018). formation of microbial inhibitors in steam-explosion pretreatment of softwood impregnated with sulfuric acid and sulfur dioxide. *Bioresour. Technol.* 262, 242–250. doi:10.1016/j.biortech.2018.04.074

Müller, G., Várnai, A., Johansen, K. S., Eijsink, V. G. H., and Horn, S. J. (2015). Harnessing the potential of LPMO-containing cellulase cocktails poses new demands on processing conditions. *Biotechnol. Biofuels* 8, 187. doi:10.1186/s13068-015-0376-y

Østby, H., Hansen, L. D., Horn, S. J., Eijsink, V. G. H., and Várnai, A. (2020). Enzymatic processing of lignocellulosic biomass: Principles, recent advances and perspectives. *J. Ind. Microbiol. Biotechnol.* 47, 623–657. doi:10.1007/s10295-020-02301-8

Pandey, K. K. (1999). A study of chemical structure of soft and hardwood and wood polymers by FTIR spectroscopy. *J. Appl. Polym. Sci.* 71, 1969–1975. doi:10.1002/(sici)1097-4628(19990321)71:12<1969::aid-app6>3.0.co;2-d

Pandey, K. K., and Nagveni, H. C. (2007). Rapid characterisation of brown and white rot degraded chir pine and rubberwood by FTIR spectroscopy. *Holz Roh. Werkst.* 65, 477–481. doi:10.1007/s00107-007-0181-9

Phillips, C. M., Beeson, W. T., Cate, J. H., and Marletta, M. A. (2011). Cellobiose dehydrogenase and a copper-dependent polysaccharide monooxygenase potentiate cellulose degradation by *Neurospora crassa*. *ACS Chem. Biol.* 6, 1399–1406. doi:10.1021/cb200351y

Quinlan, R. J., Sweeney, M. D., Leggio, L. L., Otten, H., Poulsen, J. C. N., Johansen, K. S., et al. (2011). Insights into the oxidative degradation of cellulose by a copper metalloenzyme that exploits biomass components. *Proc. Natl. Acad. Sci. U. S. A.* 108, 15079–15084. doi:10.1073/pnas.1105776108

Ralph, J., Lundquist, K., Brunow, G., Lu, F., Kim, H., Schatz, F. P., et al. (2004). Lignins: Natural polymers from oxidative coupling of 4-hydroxyphenylpropanoids. *Phytochem. Rev.* 3, 29–60. doi:10.1023/b:phyt.0000047809.65444.a4

Rodríguez-Zúñiga, U. F., Cannella, D., Giordano, R. D., Giordano, R. D. C., Jørgensen, H., and Felby, C. (2015). Lignocellulose pretreatment technologies affect the level of enzymatic cellulose oxidation by LPMO. *Green Chem.* 17, 2896–2903. doi:10.1039/c4gc02179g

Sannigrahi, P., Kim, D. H., Jung, S., and Ragauskas, A. (2011). Pseudo-lignin and pretreatment chemistry. *Energy Environ. Sci.* 4, 1306–1310. doi:10.1039/C0EE00378F

Sarkanen, K. V., and Ludwig, C. H. (1971). *Lignins: Occurrence, formation, structure and reactions*. New York: John Wiley & Sons.

Selig, M. J., Viamajala, S., Decker, S. R., Tucker, M. P., Himmel, M. E., and Vinzant, T. B. (2007). Deposition of lignin droplets produced during dilute acid pretreatment of maize stems retards enzymatic hydrolysis of cellulose. *Biotechnol. Prog.* 23, 1333–1339. doi:10.1021/bp0702018

Shinde, S. D., Meng, X. Z., Kumar, R., and Ragauskas, A. J. (2018). Recent advances in understanding the pseudo-lignin formation in A lignocellulosic biorefinery. *Green Chem.* 20, 2192–2205. doi:10.1039/c8gc00353j

Singleton, V. L., Orthofer, R., and Lamuela-Raventós, R. M. (1999). Analysis of total phenols and other oxidation substrates and antioxidants by means of folin-ciocalteu reagent. *Method. Enzymol.* 299, 152–178.

Sjöström, E. (1993). *Wood chemistry – fundamentals and applications*. 2nd ed. New York: Academic Press.

Sluiter, A., Hames, B., Ruiz, R., Scarlata, C., Sluiter, J., Templeton, D., et al. (2012). Determination of structural carbohydrates and lignin in biomass. NREL/TP-510-42618.

Vaaje-Kolstad, G., Westereng, B., Horn, S. J., Liu, Z., Zhai, H., Sørlie, M., et al. (2010). An oxidative enzyme boosting the enzymatic conversion of recalcitrant polysaccharides. *Science* 330, 219–222. doi:10.1126/science.1192231

Van Dyk, J. S., and Pletschke, B. I. (2012). A review of lignocellulose bioconversion using enzymatic hydrolysis and synergistic cooperation between enzymes-factors affecting enzymes, conversion and synergy. *Biotechnol. Adv.* 30, 1458–1480. doi:10.1016/j.biotechadv.2012.03.002

Wang, Z., Winestrand, S., Gillgren, T., and Jönsson, L. J. (2018b). Chemical and structural factors influencing enzymatic saccharification of wood from aspen, birch and spruce. *Biomass Bioenergy* 109, 125–134. doi:10.1016/j.biombioe.2017.12.020

Wang, Z., Wu, G., and Jönsson, L. J. (2018a). Effects of impregnation of softwood with sulfuric acid and sulfur dioxide on chemical and physical characteristics, enzymatic digestibility, and fermentability. *Bioresour. Technol.* 247, 200–208. doi:10.1016/j.biortech.2017.09.081

Westereng, B., Cannella, D., Agger, J. W., Jørgensen, H., Andersen, M. L., Eijsink, V. G. H., et al. (2015). Enzymatic cellulose oxidation is linked to lignin by long-range electron transfer. *Sci. Rep.* 5, 18561. doi:10.1038/srep18561

Yao, L., Yang, H. T., Meng, X. Z., and Ragauskas, A. J. (2022). Toward a fundamental understanding of the role of lignin in the biorefinery process. *Front. Energy Res.* 9, 804086. doi:10.3389/fenrg.2021.804086

Yu, Z., Jameel, H., Chang, H. M., Philips, R., and Park, S. (2012). Evaluation of the factors affecting Avicel reactivity using multi-stage enzymatic hydrolysis. *Biotechnol. Bioeng.* 109, 1131–1139. doi:10.1002/bit.24386

Zhai, R., Hu, J. G., and Saddler, J. N. (2016). What are the major components in steam pretreated lignocellulosic biomass that inhibit the efficacy of cellulase enzyme mixtures? *Acs Sustain. Chem. Eng.* 4, 3429–3436. doi:10.1021/acssuschemeng.6b00481

Zhang, Y. P. (2008). Reviving the carbohydrate economy via multi-product lignocellulose biorefineries. *J. Ind. Microbiol. Biotechnol.* 35, 367–375. doi:10.1007/s10295-007-0293-6

frontiers | Frontiers in Bioengineering and Biotechnology

TYPE Original Research
PUBLISHED 16 December 2022
DOI 10.3389/fbioe.2022.1082341

OPEN ACCESS

EDITED BY
Jiaxing Xu,
Huaiyin Normal University, China

REVIEWED BY
Xiaojun Shen,
Dalian Institute of Chemical Physics (CAS), China
Yu-Cai He,
Changzhou University, China

*CORRESPONDENCE
Chao Wang,
chaowang@qlu.edu.cn
Yu Liu,
leoliuyu@163.com
Feng Xu,
xfx315@bjfu.edu.cn

SPECIALTY SECTION
This article was submitted to Bioprocess Engineering, a section of the journal Frontiers in Bioengineering and Biotechnology

RECEIVED 09 November 2022
ACCEPTED 05 December 2022
PUBLISHED 16 December 2022

CITATION
Shao L, Wang C, Liu Y, Wang M, Wang L and Xu F (2022), Efficient depolymerization of lignin through microwave-assisted Ru/C catalyst cooperated with metal chloride in methanol/formic acid media. *Front. Bioeng. Biotechnol.* 10:1082341. doi: 10.3389/fbioe.2022.1082341

Efficient depolymerization of lignin through microwave-assisted Ru/C catalyst cooperated with metal chloride in methanol/formic acid media

Lupeng Shao[1,2], Chao Wang[1]*, Yu Liu[1]*, Meng Wang[1], Luyan Wang[2] and Feng Xu[1,3]*

[1]State Key Laboratory of Biobased Material and Green Papermaking, Key Laboratory of Pulp and Paper Science & Technology (Ministry of Education), Qilu University of Technology (Shandong Academy of Sciences), Jinan, China, [2]Shandong Chenming Paper Holdings Co., Ltd., Weifang, China, [3]Beijing Key Laboratory of Lignocellulosic Chemistry, Beijing Forestry University, Beijing, China

Lignin, an abundant aromatic biopolymer, has the potential to produce various biofuels and chemicals through biorefinery activities and is expected to benefit the future circular economy. Microwave-assisted efficient degradation of lignin in methanol/formic acid over Ru/C catalyst cooperated with metal chloride was investigated, concerning the effect of type and dosage of metal chloride, dosage of Ru/C, reaction temperature, and reaction time on depolymerized product yield and distribution. Results showed that 91.1 wt% yield of bio-oil including 13.4 wt% monomers was obtained under the optimum condition. Yields of guaiacol-type compounds and 2,3-dihydrobenzofuran were promoted in the presence of $ZnCl_2$. Formic acid played two roles: (1) acid-catalyzed cleavage of linkages; (2) acted as an *in situ* hydrogen donor for hydrodeoxygenation in the presence of Ru/C. A possible mechanism for lignin degradation was proposed. This work will provide a beneficial approach for efficient depolymerization of lignin and controllable product distribution.

KEYWORDS

lignin, microwave, degradation, synergetic catalysis, controllable product distribution

1 Introduction

The global population growth and the development of industrialization lead to a rising demand for fuels and chemicals, resulting in many societal problems, such as energy security and environmental concerns (Sun et al., 2018; Wang et al., 2019; Jing et al., 2020; Ma et al., 2021). Developing renewable and environment-friendly energy has become an essential measure for many countries to promote energy transformation. Lignin, which constitutes up to 40% of the energy content of most terrestrial plants, shows great potential to produce liquid fuel or petroleum-based aromatic chemicals owing to its

aromatic building blocks (Regalbuto, 2009; Barta et al., 2010; Cao et al., 2019; Ekielski and Mishra, 2020; Tang et al., 2022; Zhou et al., 2022).

Despite various challenges associated with lignin valorization, several strategies have emerged that could deliver value-added products, such as biological (Chong et al., 2018) and chemical process (Li et al., 2015). In particular, a wide range of thermochemical approaches for converting lignin into aromatic-rich bio-oil, including pyrolysis (Shao et al., 2017; Cao et al., 2021), acid/base catalytic hydrolysis (Deuss et al., 2015; Hernández-Ramos et al., 2020), oxidation (Lancefield et al., 2015; Sun et al., 2020) and reductive depolymerization (Liu et al., 2019), have been extensively investigated. Bio-oil is a higher energy content transportable liquid for subsequent production of biofuels and aromatic chemicals. Previous researches have indicated that solvents and catalysts have significant effects on lignin depolymerization. Various solvents (such as water, alcohol, formic acid, etc.) were investigated during the lignin valorization process. Shu et al. (2016b) investigated the influence of solvent on lignin depolymerization, and concluded that supercritical methanol showed the bested depolymerization performance. Hidajat et al. (2018) used formic acid as hydrogen source to produce oxygen-free aromatics, achieving high-calorific-value oil (> 40 MJ kg−1) with a high content of oxygen-free aromatics (6.8 wt%). Various kinds of catalysts, including homogeneous and heterogeneous catalysts, have been extensively tested (Wang et al., 2019). Kristianto et al. (2017) reported the depolymerization of concentrated acid hydrolysis lignin using a Ru/C catalyst in ethanol/formic acid media, achieving a high bio-oil yield of ~70 wt% and a high heating value of 32.7 MJ kg^{-1}. Luo et al. (2020) used boric acid as a novel homogeneous catalyst coupled with Ru/C to overcome the product separation problem and perform the hydrodeoxygenation (HDO) of phenolic compounds and raw lignin oil. The content of hydrocarbons increases from 7.9% to 93.1% at 260°C. Most of these thermochemical approaches required relatively harsh reaction conditions (high reaction temperature and/or high pressure). Therefore, it is urgent to explore mild reaction conditions and technologies for converting lignin into high-value liquid fuel and/or aromatic chemicals.

Recently, in comparison with those conventional heating processes, microwave-assisted depolymerization of lignin has attracted increasing attention on account of its advantages of fast heating rate and high heating efficiency (Liu et al., 2017; Zhou et al., 2019; Cederholm et al., 2020). Microwave heating occurs *via* dipole rotation and ionic conduction. Therefore, polar solvents which have high microwave absorption abilities are adopted as additional microwave receptors. Moreover, the addition of molecular hydrogen will increase the cost and risk of the process (Jiang et al., 2019). Consequently, the use of polar hydrogen-donating reagents (methanol, ethanol, formic acid, et al.) would be potentially safer and more cost-effective (Zhou et al., 2018). Toledano et al. investigated the influence of various hydrogen-donating solvents on lignin depolymerization under microwave conditions, finding that formic acid showed the best performance (Toledano et al., 2013). Apart from solvents, catalysts also played an essential role in the microwave-assisted depolymerization of lignin. Noble metal-based catalysts (such as Pd, Pt, and Ru, etc.) were proved to be effective for lignin depolymerization (Zhang et al., 2019; Wang et al., 2021). Previous studies indicated that the combination of the noble metal with acid catalyst had better performances for lignin depolymerization (Klein et al., 2016; Bjelić et al., 2020; Jiang et al., 2021). Shu et al. investigated the catalytic performances of various metal chlorides cooperated with Pd/C for lignin depolymerization and observed that the highest yield (28.5 wt%) of phenolic monomers was obtained with $CrCl_3$ under harsh conditions (4 MPa H_2, 260°C, 5 h) (Shu et al., 2015).

In our previous work, microwave-assisted degradation of alkaline lignin in methanol/formic acid (FA) media was investigated, and 72.0 wt% yield of bio-oil including 6.7 wt% monomers was achieved at 160°C and a FA-to-lignin mass ratio of 4 after a reaction time of 30 min (Shao et al., 2018). Herein, highly efficient depolymerization of lignin in methanol/formic acid over Ru/C catalyst cooperated with metal chlorides assisted by microwave heating is reported. The effects of catalyst, reaction temperature, and reaction time on the product yield and distribution are studied in detail. The possible mechanism of lignin depolymerization is proposed.

2 Materials and methods

2.1 Materials

The alkaline lignin was provided by Shandong Longlive Bio-Technology Co., Ltd., China, a by-product of xylooligosaccharides production from corn cob. The lignin was composed of 90.81% Klason lignin, 3.61% acid-soluble lignin, 0.63% sugars, 2.16% ash, and 2.79% others (Shao et al., 2018). 5 wt% Ru/C, formic acid (FA, 99%), ethyl acetate (HPLC grade, 99.9%), and acetophenone (standard for GC, 99.5%) were provided by Aladdin® company. Methanol (99.5%), ethyl acetate (99.5%), and tetrahydrofuran (THF, 99.0%) were analytical grade and provided by Beijing Chemical Works. $AlCl_3$, $CrCl_3$, LiCl, NaCl, $FeCl_3$, $FeCl_2$, $MgCl_2$, $ZnCl_2$, KCl, and $Zn(OAC)_2$ were also analytical grade and purchased from Macklin® company. All reagents were used as received.

2.2 Lignin depolymerization

Microwave-assisted depolymerization of lignin was carried out in microwave digestion instrument (MDS-6G, Sineo Microwave Technology Co., Ltd., China). Methanol and formic acid (FA) were

TABLE 1 The effect of different metal chloride on the products of lignin depolymerization.

Entry	Metal chloride	Y_{BO} (%)	Y_{AM} (%)	Y_R (%)
1	-[a]	72.0	6.7	20
2	-[b]	74.2	5.4	24.6
3	$ZnCl_2$	84.3	10.2	17.3
4	$AlCl_3$	69.3	5.4	29.6
5	$CrCl_3$	78.8	9.0	18.9
6	LiCl	63.6	5.0	35.7
7	$FeCl_3$	74.5	7.5	24.6
8	NaCl	68.6	6.0	29.2
9	KCl	65.8	5.6	33.6
10	$FeCl_2$	70.2	6.8	31.8
11	$MgCl_2$	71.7	7.5	34.8
12	$Zn(OAC)_2$	69.2	6.9	32.1

[a]without both metal chloride and Ru/C.
[b]without metal chloride.
Y_{BO}: Yield of bio-oil, Y_{AM}: Yield of aromatic monomer, Y_R: Yield of residue.
Condition: 1 g lignin, 1 mmol metal chloride, 0.2 g 5 wt% Ru/C, 20 ml methanol, 4 g formic acid, 160°C, 30 min.

chosen as solvent and hydrogen donor during the depolymerization process. Ru/C and metal chloride were used as catalysts. For a typical experiment, 1 g lignin, 1 mmol metal chloride, 0.2 g 5 wt% Ru/C, 20 ml methanol, and 4 g formic acid (FA) were added into the digestion tank. The reaction was conducted at 400 W under settled reaction temperature (140, 160, and 180°C) and reaction time (15, 30, and 45 min). After the reaction, the mixture was cooled down to ambient temperature.

2.3 Products separation and analysis

The products separation was as follows. The reaction mixture was first filtered, and the filter cake was washed three times with methanol. The solid fraction 1 (including catalyst and residue) was obtained. The filtrate was collected and subjected to rotary evaporation, followed by adding ethyl acetate. The resulting mixture was filtered again. The solid fraction 2 was obtained. The filtrate was rotary evaporated, achieving the bio-oil. The solid fractions were washed with THF and filtered, achieving the residue and catalyst. The yields of bio-oil, aromatic monomers, and residue were calculated according to the following equations:

$$Y_{AM}(\%) = \text{Yield of aromatic monomer} = W_{AM}/W_L \times 100\% \quad (1)$$

$$Y_{BO}(\%) = \text{Yield of bio-oil} = W_{Bo}/W_L \times 100\% \quad (2)$$

$$Y_R(\%) = \text{Yield of residue} = W_R/W_L \times 100\% \quad (3)$$

Where W_{AM}, W_{BO}, W_R, and W_L depict the weight of aromatic monomer, bio-oil, residue, and starting lignin, respectively.

Qualitative and quantitative analysis of aromatic monomers in bio-oil were carried out by SHIMADZU GC–MS-QP 2010 SE and SHIMADZU GC-2010 Plus with a FID detector equipped with HP-5 capillary columns (30 m × 0.25 mm × 0.25 μm), respectively. The oven temperature was programmed from 50°C to 300°C with a 10°C /min heating rate. The injector was kept at 250°C with a split ratio of 20, using helium as carrier gas. Acetophenone was used as the internal standard.

3 Results and discussion

3.1 Product distribution of lignin depolymerization

3.1.1 Effect of metal chloride

Various products can be obtained after lignin depolymerization. Table 1 shows the effect of different metal chloride on bio-oil, aromatic monomer, and residue yields. The specific aromatic monomer distribution and yield are shown in Supplementary Table S1. Generally, the distribution of depolymerized lignin products was complex. According to the specific functional groups, products were classified into four categories: 2,3-dihydrobenzofuran (DHBF), phenol-type compounds (H), guaiacol-type compounds (G), and syringol-type compounds (S). It should be noted that no chloride-contained compounds were detected in products, indicating that dissolved chloride did not react with the lignin.

As shown in Table 1, the bio-oil yield increased slightly after adding Ru/C catalyst, but the promotion effect on the aromatic monomer yield was not significant. The yield of bio-oil increased or decreased when metal chloride was added. It is generally known that Cl is a high electronegativity element, and Cl^{-1} was widely used in biomass dissolution and conversion as an excellent nucleophilic regent (Long et al., 2011; Shu et al., 2015). C-O bond in cellulose was easier to be broken in most cellulose conversion reactions using chloride ionic liquids as solvent (Swatloski et al., 2002). Lignin contained a large number of ether bonds, especially the β-O-4′ bonds. Therefore, it is considered that Cl^{-1} in metal chloride can work in lignin depolymerization. Data in Table 1 showed that $ZnCl_2$, $CrCl_3$, and $FeCl_3$ significantly promoted lignin depolymerization. The common feature was the higher valence of metal cation. The result showed that metal cations also affected lignin depolymerization, which may be related to the Lewis acid strength of metal cation. It has been reported that metal cations can produce more acid centers (Miessler et al., 2013), promoting lignin depolymerization. One more interesting phenomenon, metal cations of $AlCl_3$ and $MgCl_2$ also had high valence, but the bio-oil yield was lower than that of other high-valent metal cations. This might be caused by hydrated metal chloride used in the experiment, such as $AlCl_3{\bullet}6H_2O$ and $MgCl_2{\bullet}6H_2O$. Water present in the reagents might affect lignin depolymerization, which was also confirmed by the high residue yield.

Yields of bio-oil and aromatic monomers were the highest in the presence of $ZnCl_2$. The result differed from Shu et al. (2018)'s research, who believed that $CrCl_3$ provided a better catalytic effect. The higher valence of Cr^{3+} in $CrCl_3$ could produce more acidic centers, which promoted lignin depolymerization. Cr^{3+} was first conjunct with O and benzene ring of lignin molecule to form a stable complex. Synchronously, Cl^- with high electronegativity was connected to lignin molecule, resulting in the breakage of C-O bonds (Tang et al., 2021). Furthermore, hydrogenolysis was promoted by capturing hydrogen under the polarization effect of Cl^- and the synergic effect of Pd/C (Parsell et al., 2013). The product distribution was significantly different by comparing the aromatic monomers generated from $ZnCl_2$ and $CrCl_3$ synergistic Ru/C catalytic depolymerization of lignin. For example, when $ZnCl_2$ was used, the yield of 4-ethylphenol (H2, 0.89 wt%) was the highest among the H-type compounds, without the generation of *p*-coumaric acid (H4). When $CrCl_3$ was used, it showed the opposite result that the yield of H4 (1.55 wt%) was the highest among the H-type compounds without H2. The result indicated that the catalytic mechanism of $ZnCl_2$ and $CrCl_3$ was different. Compared with other metal chloride, using $ZnCl_2$ could facilitate the formation of H4 and increase the yield of G-type compounds. Besides, the highest yield (5.58 wt%) of 2,3-dihydrobenzofuran (DHBF) was obtained. Significant decreases of bio-oil and total aromatic monomers were exhibited when $ZnCl_2$ was replaced by $Zn(OAc)_2$. Meanwhile, a dramatic change of product distribution occurred, especially the S-type compounds. It indicated that the synergic effect between Zn^{2+} and Cl^- was contributed to improve the yields of bio-oil and aromatic monomer. Data showed that lignin could be efficiently depolymerized under the catalyst of $ZnCl_2$ cooperated with Ru/C.

3.1.2 Effect of $ZnCl_2$ dosage

The effect of $ZnCl_2$ dosage on lignin depolymerization was investigated. As shown in Table 2, the category and yield of S-type compounds decreased with the increase of $ZnCl_2$ dosage. Only S3 was produced when the dosage of $ZnCl_2$ was 1 and 2 mmol. As the dosage of $ZnCl_2$ was further increased to 3 mmol, no S-type compounds were produced. In view of the lower yield of S-type compounds in depolymerized products, yields of bio-oil, total monomers, DHBF, H-type, and G-type compounds were mainly discussed as follows.

As shown in Figure 1, the yield of bio-oil increased with increasing $ZnCl_2$ dosage. And the highest bio-oil yield of 93.4 wt % was obtained when 3 mmol $ZnCl_2$ was used. The yield of total monomers rose from 5.38 wt% to 13.4 wt% with increasing $ZnCl_2$ dosage from 0 to 2 mmol. However, as $ZnCl_2$ dosage was further increased to 3 mmol, yield of total monomers decreased to 11.6 wt%. This phenomenon suggested that lignin depolymerization was favored at high $ZnCl_2$ dosage; meanwhile, repolymerization of monomers to form oligomers was also promoted. Among the monomers, DHBF was abundantly produced; the yield first increased to 5.6 wt% and then decreased to 2.03 wt% as a function of $ZnCl_2$ dosage. The yield of H-type compounds increased as the amount of $ZnCl_2$ increased, and the highest yield (5.63 wt%) was obtained when 3 mmol $ZnCl_2$ was used. It should be noted that H2 was produced only in the presence of $ZnCl_2$, and phenol was produced only when the $ZnCl_2$ dosage was more than 2 mmol. The yields of H2 and phenol were proportional to $ZnCl_2$ dosage. This phenomenon indicated that increasing the dosage of $ZnCl_2$ was conductive to the formation of H1 and H2. The highest yield (1.91 wt%) of *p*-coumaric acid appeared when the $ZnCl_2$ dosage was 0.5 mmol. Further increasing $ZnCl_2$ dosage, no *p*-coumaric acid was detected in products. This indicated that high $ZnCl_2$ dosage inhibited the production of *p*-coumaric acid. For G-type compounds, the yield first increased to 6.4 wt% and then decreased to 3.92 wt% as a function of $ZnCl_2$ dosage. The decrease in the yield of G-type compounds was mainly caused by a decline of G3, G4, G5, and G6. The yields of G1 and G2 showed similar variation tendency with H1 and H2, respectively, when increasing $ZnCl_2$ dosage. The result indicated great significance for controlling the selectivity of depolymerized products by varying $ZnCl_2$ dosage.

3.1.3 Effect of Ru/C dosage

The effect of Ru/C dosage had also been carefully examined. Table 3 shows the distribution of aromatic monomers. When the amount of $ZnCl_2$ was 2 mmol, there were basically no S-type

TABLE 2 Effect of $ZnCl_2$ dosage on the distribution of lignin-derived aromatic monomers.

Type[a]	Compound	Retention time (min)	Yield (%)				
			$ZnCl_2$ dosage (mmol)				
			0	0.5	1	2	3
DHBF	2,3-Dihydrobenzofuran	13.832	2.57	3.63	5.6	2.48	2.03
H1	Phenol	8.731				1.26	1.46
H2	Phenol, 4-ethyl-	12.753		0.23	0.89	2.47	3.11
H3	2-Propenoic acid, 3-(4-hydroxyphenyl)-, methyl ester	22.837	0.12	0.29	0.44	0.66	1.06
H4	*p*-Coumaric acid	23.356	1.18	1.91			
G1	Phenol, 2-methoxy-	11.109				0.91	1.1
G2	Phenol, 4-ethyl-2-methoxy-	14.999		0.08	0.25	0.5	0.75
G3	Phenol, 2-methoxy-4-vinyl-	15.679		0.57	0.98	0.66	0.29
G4	Vanillin	17.293	0.23	0.29	0.33	0.52	0.49
G5	2-Propenoic acid, 3-(4-hydroxy-3-methoxyphenyl)-, methyl ester	24.544	0.47	0.39	0.85	1.11	
G6	2-Propenoic acid, 3-(4-hydroxy-3-methoxyphenyl)-	24.763	0.37	0.27	0.6	2.7	1.29
S1	Benzaldehyde, 4-hydroxy-3,5-dimethoxy-	21.572	0.08	0.17			
S2	Phenol, 2,6-dimethoxy-4-propenyl-	22.136	0.15	0.07			
S3	Ethanone, 1-(4-hydroxy-3,5-dimethoxyphenyl)-	22.668	0.13	0.15	0.24	0.17	
S4	3,5-Dimethoxy-4-hydroxycinnamaldehyde	26.137	0.08				

[a]DHBF: 2,3-dihydrobenzofuran, H: phenol-type compounds, G: guaiacol-type compounds, S: syringol-type compounds.
Condition: 1 g lignin, 0.2 g 5 wt% Ru/C, 20 ml methanol, 4 g formic acid, 160°C, 30 min.

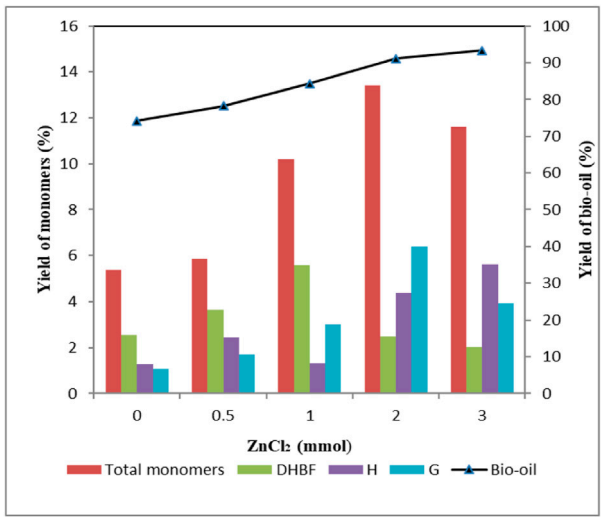

FIGURE 1
Effect of $ZnCl_2$ dosage on the yield of depolymerized products. Condition: 1 g lignin, 0.2 g 5 wt% Ru/C, 20 ml methanol, 4 g formic acid, 160°C, 30 min.

phenolic compounds in the products regardless of the amount of Ru/C. As can be seen from Figure 2, the yield of bio-oil increased after adding Ru/C catalyst. The highest bio-oil yield (91.1 wt%) and total aromatic monomer yield (13.4 wt%) were obtained when 0.2 g Ru/C was used. Further adding Ru/C dosage would decrease the yields of bio-oil and total aromatic monomer. According to Figure 2, the amount of Ru/C had little effect on the yield of DHBF, but mainly affected the yield of H-type and G-type compounds. The yield of H-type compound was proportional to the amount of Ru/C, and the main products were H1 and H2. For G-type compounds, the highest yield (6.4 wt%) was obtained when 0.2 g Ru/C was used. The yield of G1 increased after the addition of Ru/C, but the amount of Ru/C had little effect on the yield, basically keeping at 0.9 wt%. The increase of Ru/C dosage was beneficial to the production of G2, but decreased the yield of G4. According to Table 4, when the amount of Ru/C increased, the yield of the products containing carbonyl group or double bonds in the side chain showed a decreasing trend. In contrast, the yield of products without unsaturated bonds in the side chain tended to increase. The result demonstrated that Ru/C facilitated hydrodeoxygenation in

TABLE 3 Effect of Ru/C dosage on the distribution of lignin-derived aromatic monomers.

Type[a]	Compound	Retention time (min)	Yield (%)			
			Ru/C dosage (g)			
			0	0.1	0.2	0.3
DHBF	2,3-Dihydrobenzofuran	13.832	2.27	2.1	2.48	2.27
H1	Phenol	8.731	0.8	0.86	1.26	1.56
H2	Phenol, 4-ethyl-	12.753	2.07	3.26	2.47	3.7
H3	2-Propenoic acid, 3-(4-hydroxyphenyl)-, methyl ester	22.837			0.66	
G1	Phenol, 2-methoxy-	11.109	0.6	0.9	0.91	0.88
G2	Phenol, 4-ethyl-2-methoxy-	14.999	0.48	0.64	0.5	0.81
G3	Phenol, 2-methoxy-4-vinyl-	15.679	0.6	0.22	0.66	
G4	Vanillin	17.293	0.71	0.45	0.52	0.47
G5	2-Propenoic acid, 3-(4-hydroxy-3-methoxyphenyl)-, methyl ester	24.544	0.57		1.11	
G6	2-Propenoic acid,3-(4-hydroxy-3-methoxyphenyl)-	24.763	1.04	1.27	2.7	1.22
S3	Ethanone, 1-(4-hydroxy-3,5-dimethoxyphenyl)-	22.668			0.17	

[a]:DHBF: 2,3-dihydrobenzofuran, H: phenol-type compounds, G: guaiacol-type compounds, S: syringol-type compounds.
Condition: 1 g lignin, 2 mmol $ZnCl_2$, 20 ml methanol, 4 g formic acid, 160°C, 30 min.

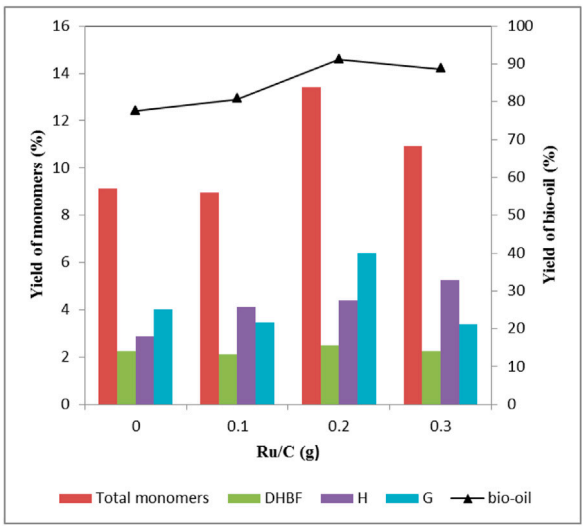

FIGURE 2
Effect of Ru/C dosage on the yield of depolymerized products Condition: 1 g lignin, 2 mmol $ZnCl_2$, 20 ml methanol, 4 g formic acid, 160°C, 30 min.

the side chain of benzene ring (Chen et al., 2015). The reason was that formic acid, as an *in situ* hydrogen source, could generate active hydrogen species using Ru/C catalyst under solvothermal conditions (Kristianto et al., 2017), which could facilitate hydrodeoxygenation. The role of formic acid was different from our previous study (Shao et al., 2018), in which formic acid acted through acid-catalyzed cleavage of linkages in lignin. In the presence of Ru/C, formic acid played two roles: (1) acid-catalyzed cleavage of linkages; (2) acted as an *in situ* hydrogen donor.

3.1.4 Effect of reaction temperature and time

The effect of reaction temperature on lignin depolymerization was investigated (Figure 3). It could be found that lignin depolymerization was highly dependent on temperature. Yields of bio-oil and total aromatic monomers were sharply increased with the elevation of reaction temperature. Remarkably, a noticeable rise was exhibited in the temperature range of 140–160°C. Wherein, yield of bio-oil increased from 77.6 wt% to 91.1 wt%, and yield of total aromatic monomers increased from 8.22 wt% to 13.4 wt%. This indicated that a higher reaction temperature seemed to have a positive influence on lignin depolymerization. However, further increasing the temperature to 180°C, yields of bio-oil and total aromatic monomers decreased to 83.9 wt% and 8.69 wt%, where repolymerization of monomers and oligomers was considered to be responsible for this (Long et al., 2014). As can be seen in Table 4, no other S-type phenolic compounds were produced except for S3 at 160°C. The yield of DHBF first increased to 2.48 wt% and then decreased to 1.45 wt% as a function of temperature. It should be noted that yield of H-type phenolic compounds increased with the elevated reaction temperature, and the highest yield (4.97 wt%) appeared at 180°C. The yield of total G-type phenolic compounds showed a similar tendency with that of bio-oil and total aromatic monomers when reaction

TABLE 4 Effect of reaction temperature on the distribution of lignin-derived aromatic monomers.

Type[a]	Compound	Retention time (min)	Yield (%)		
			Reaction temperature (°C)		
			140	160	180
DHBF	2,3-Dihydrobenzofuran	13.832	1.64	2.48	1.45
H1	Phenol	8.731	1.14	1.26	1.44
H2	Phenol, 4-ethyl-	12.753	2.34	2.47	2.64
H3	2-Propenoic acid, 3-(4-hydroxyphenyl)-, methyl ester methyl ester	22.837		0.66	0.89
G1	Phenol, 2-methoxy-	11.109	0.76	0.91	0.88
G2	Phenol, 4-ethyl-2-methoxy-	14.999	0.42	0.5	0.66
G3	Phenol, 2-methoxy-4-vinyl-	15.679	0.41	0.66	0.2
G4	Vanillin	17.293		0.52	
G5	2-Propenoic acid, 3-(4-hydroxy-3-methoxyphenyl)-, methyl ester	24.544	0.5	1.11	0.73
G6	2-Propenoic acid, 3-(4-hydroxy-3-methoxyphenyl)-	24.763	1.01	2.7	
S3	Ethanone, 1-(4-hydroxy-3,5-dimethoxyphenyl)-	22.668		0.17	

[a]DHBF: 2,3-dihydrobenzofuran, H: phenol-type compounds, G: guaiacol-type compounds, S: syringol-type compounds.
Condition: 1 g lignin, 2 mmol ZnCl2, 0.2 g 5 wt% Ru/C, 20 ml methanol, 4 g formic acid, 30 min.

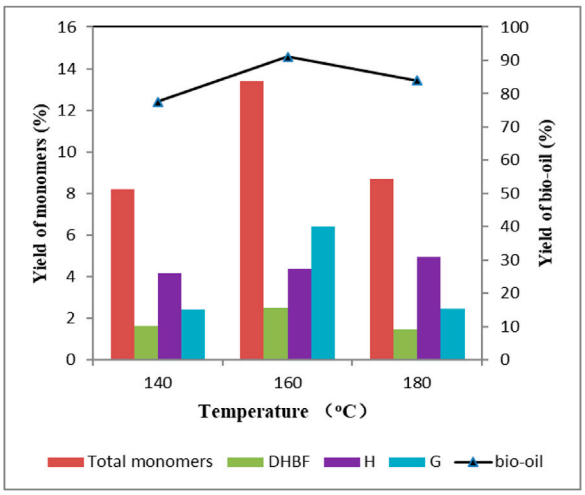

FIGURE 3
Effect of reaction temperature on the yield of depolymerized products Condition: 1 g lignin, 2 mmol $ZnCl_2$, 0.2 g 5 wt% Ru/C, 20 ml methanol, 4 g formic acid, 30 min.

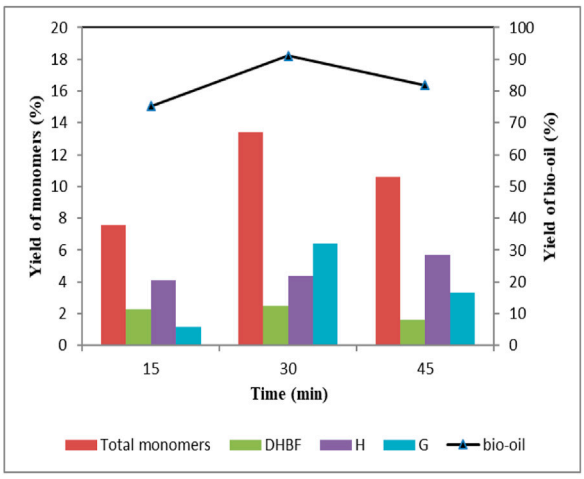

FIGURE 4
Effect of reaction time on the yield of depolymerized products Condition: 1 g lignin, 2 mmol $ZnCl_2$, 0.2 g 5 wt% Ru/C, 20 ml methanol, 4 g formic acid, 160°C.

temperature rose. One more interesting phenomenon, G4 could be detected only reaction temperature was 160°C. Product distribution showed excessive high temperature promoted the production of H-type compounds, but inhibited G-type compounds, aggravating the repolymerization (Lin et al., 2015). An appropriate temperature is adopted to optimize the yield of product.

Figure 4 shows the effect of reaction time on lignin depolymerization, and product distribution is shown in Table 5. As reaction time increased from 15 min to 30 min, bio-oil yield increased from 75.3 wt% to 91.1 wt%, and the total

TABLE 5 Effect of reaction time on the distribution of lignin-derived aromatic monomers.

Type[a]	Compound	Retention Time (min)	Yield (%)		
			Reaction time (min)		
			15	30	45
DHBF	Benzofuran, 2,3-dihydro-	13.832	2.28	2.48	1.61
H1	Phenol	8.731	1.2	1.26	1.64
H2	Phenol, 4-ethyl-	12.753	2.32	2.47	3.53
H3	2-Propenoic acid, 3-(4-hydroxyphenyl)-, methyl ester	22.837	0.35	0.66	0.53
G1	Phenol, 2-methoxy-	11.109	0.69	0.91	1.27
G2	Phenol, 4-ethyl-2-methoxy-	14.999	0.5	0.5	0.78
G3	Phenol, 2-methoxy-4-vinyl-	15.679		0.66	0.16
G4	Vanillin	17.293		0.52	0.45
G5	2-Propenoic acid, 3-(4-hydroxy-3-methoxyphenyl)-, methyl ester	24.544		1.11	0.66
G6	2-Propenoic acid,3-(4-hydroxy-3-methoxyphenyl)-	24.763		2.7	
S3	Ethanone, 1-(4-hydroxy-3,5-dimethoxyphenyl)-	22.668		0.17	

[a]DHBF: 2,3-dihydrobenzofuran, H: phenol-type compounds, G: guaiacol-type compounds, S: syringol-type compounds.
Condition: 1 g lignin, 2 mmol $ZnCl_2$, 0.2 g 5 wt% Ru/C, 20 ml methanol, 4 g formic acid, 160°C.

aromatic monomers yield reached 13.4 wt%. Further prolonging the reaction time to 45 min, significant decrease occurred in bio-oil and total aromatic monomers yield, which were 81.8 wt% and 10.6 wt% respectively. Data in Table 5 showed that there were fewer kinds of aromatic monomers when reaction time was 15 min. DHBF and H-type compounds were the major products, which yields were 2.28 wt% and 3.87 wt% respectively. These indicated that short reaction time led to insufficient bond rupture. For G-type compounds, the total yield first increased and then decreased as reaction time increased from 15 min to 45 min. It should be noted that yields of G1 and G2 had been rising with the increase of time. However, other G-type compounds appeared in the products only when the reaction time reached 30 min, which decreased in the case of prolonging the reaction time. These results illustrated that appropriate reaction time was favorable for lignin depolymerization. Short reaction time would make the reaction incomplete. Repolymerization of lignin-derived intermediates was promoted at long reaction time (Miller et al., 2002; Toledano et al., 2014; Shu et al., 2016a). Therefore, it is necessary to determine the ideal reaction time for the efficient depolymerization of lignin.

3.2 Possible catalytic mechanism

According to the 2D HSQC NMR spectrum of lignin reported in our previous research (Shao et al., 2018), a large number of β-O-4′ and phenylcoumarin structure existed in the lignin structure (Supplementary Figures S1, S2). During lignin depolymerization, the cleavage of C-O and C-C bonds was realized, producing the aromatic monomers and oligomers. DHBF was mainly produced through breaking C_α-C_{ar} bond of phenylcoumaran structure. The possible mechanism of DHBF formation was proposed (Figure 5). It should be noted that the fracture of C_α-C_{ar} bond and ring-opening of phenylfuran ring could not carried out simultaneously according to density functional theory. The result demonstrated yield of lignin-derived bio-oil and aromatic monomers, especially the alkyl phenol and alkyl guaiacol, was effectively improved in the presence of Ru/C and $ZnCl_2$. The possible mechanism of lignin depolymerization under the synergetic catalysis of Ru/C and $ZnCl_2$ was proposed (Figure 6). A stable complex of Zn^{2+} coordinated to the oxygen atoms in lignin molecule was formed (Klein et al., 2016; Wang et al., 2016). Synchronously, the high electronegativity Cl^- was attached to the lignin molecule, selectively weakening the C-O bonds. Afterwards, the cleavage of C-O bonds (including β-O-4 and -OCH_3 bonds) and C-C bonds occurred under the synergic of Ru/C and the polarization effect of Cl^- (Parsell et al., 2013). Finally, various phenols containing alkyl substituents were obtained through a series of typical reactions, such as hydrogenation, dehydration, hydrolysis. Thus, the product distribution can be efficiently controlled by adjusting the type and content of catalyst, reaction temperature, and reaction time.

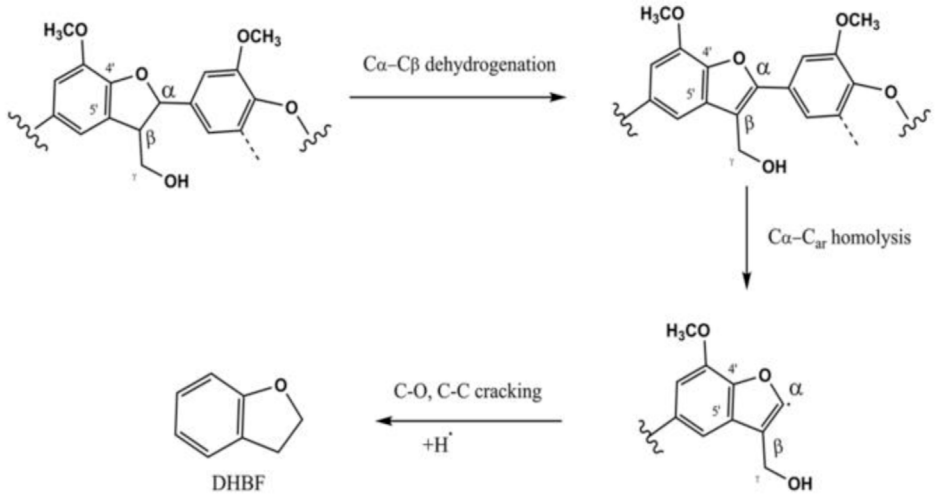

FIGURE 5
Possible mechanisms of DHBF production.

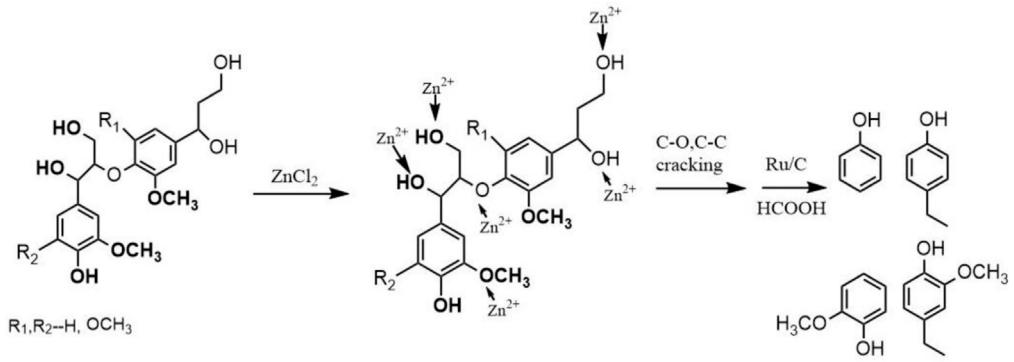

FIGURE 6
Proposed catalytic mechanism for lignin depolymerization over Ru/C and $ZnCl_2$ catalyst.

4 Conclusion

Alkali lignin could be efficiently depolymerized by the synergetic catalysis of Ru/C and $ZnCl_2$ under microwave heating. 91.1 wt% yield of bio-oil including 13.4 wt% monomers was obtained under the optimum condition (FA-to-lignin mass ratio of 4, Ru/C dosage of 0.2 g, $ZnCl_2$ dosage of 2 mmol, 160°C, and 30 min). Formic acid played two roles: (1) acid-catalyzed cleavage of linkages; (2) acted as *in situ* hydrogen donor for hydrodeoxygenation in the presence of Ru/C. This research provided a valuable reference to degrade lignin efficiently and adjust the product distribution under microwave heating.

Data availability statement

The original contributions presented in the study are included in the article/Supplementary Material; further inquiries can be directed to the corresponding authors.

Author contributions

LS: conceptualization, methodology, formal analysis, investigation, writing—original draft preparation, writing—review and editing, funding acquisition. CW: methodology, writing—review and editing, funding

acquisition. YL: formal analysis, writing—review and editing, funding acquisition. MW: methodology, validation, data curation. LW: investigation, software, data curation. FX: conceptualization, writing—review and editing, project administration.

Funding

This research was funded by the National Natural Science Foundation of China (Grant No. 32171718, 32001275), Shandong Provincial Natural Science Foundation (Grant No. ZR2019BC074), the Foundation of Qilu University of Technology (Shandong Academy of Science) (Grant No. 2022JBZ01-05).

Conflict of interest

Authors LS and LW were employed by the company of Shandong Chenming Paper Holdings Co., Ltd.

The remaining authors declare that the research was conducted in the absence of any commercial or financial relationships that could be construed as a potential conflict of interest.

Publisher's note

All claims expressed in this article are solely those of the authors and do not necessarily represent those of their affiliated organizations, or those of the publisher, the editors and the reviewers. Any product that may be evaluated in this article, or claim that may be made by its manufacturer, is not guaranteed or endorsed by the publisher.

Supplementary material

The Supplementary Material for this article can be found online at: https://www.frontiersin.org/articles/10.3389/fbioe.2022.1082341/full#supplementary-material

References

Barta, K., Matson, T. D., Fettig, M. L., Scott, S. L., Iretskii, A. V., and Ford, P. C. (2010). Catalytic disassembly of an organosolv lignin via hydrogen transfer from supercritical methanol. *Green Chem.* 12 (9), 1640–1647. doi:10.1039/C0GC00181C

Bjelić, A., Likozar, B., and Grilc, M. (2020). Scaling of lignin monomer hydrogenation, hydrodeoxygenation and hydrocracking reaction micro-kinetics over solid metal/acid catalysts to aromatic oligomers. *Chem. Eng. J.* 399, 125712. doi:10.1016/j.cej.2020.125712

Cao, X., Shao, L., Huang, W., Wang, C., Mao, J., Xu, F., et al. (2021). Thermal degradation of lignins fractionated by gradient acid precipitation. *J. Anal. Appl. Pyrolysis* 157, 105200. doi:10.1016/j.jaap.2021.105200

Cao, Y., Chen, S. S., Zhang, S., Ok, Y. S., Matsagar, B. M., Wu, K. C. W., et al. (2019). Advances in lignin valorization towards bio-based chemicals and fuels: Lignin biorefinery. *Bioresour. Technol.* 291, 121878. doi:10.1016/j.biortech.2019.121878

Cederholm, L., Xu, Y., Tagami, A., Sevastyanova, O., Odelius, K., and Hakkarainen, M. (2020). Microwave processing of lignin in green solvents: A high-yield process to narrow-dispersity oligomers. *Ind. Crops Prod.* 145, 112152. doi:10.1016/j.indcrop.2020.112152

Chen, M. Y., Huang, Y. B., Pang, H., Liu, X. X., and Fu, Y. (2015). Hydrodeoxygenation of lignin-derived phenols into alkanes over carbon nanotube supported Ru catalysts in biphasic systems. *Green Chem.* 17 (3), 1710–1717. doi:10.1039/C4GC01992J

Chong, G., Huang, X., Di, J., Xu, D., He, Y., Pei, Y., et al. (2018). Biodegradation of alkali lignin by a newly isolated Rhodococcus pyridinivorans CCZU-B16. *Bioprocess Biosyst. Eng.* 41 (4), 501–510. doi:10.1007/s00449-017-1884-x

Deuss, P. J., Scott, M., Tran, F., Westwood, N. J., de Vries, J. G., and Barta, K. (2015). Aromatic monomers by *in situ* conversion of reactive intermediates in the acid-catalyzed depolymerization of lignin. *J. Am. Chem. Soc.* 137 (23), 7456–7467. doi:10.1021/jacs.5b03693

Ekielski, A., and Mishra, P. K. (2020). Lignin for bioeconomy: The present and future role of technical lignin. *Int. J. Mol. Sci.* 22 (1), 63. doi:10.3390/ijms22010063

Hernández-Ramos, F., Fernández-Rodríguez, J., Alriols, M. G., Labidi, J., and Erdocia, X. (2020). Study of a renewable capping agent addition in lignin base catalyzed depolymerization process. *Fuel* 280, 118524. doi:10.1016/j.fuel.2020.118524

Hidajat, M. J., Riaz, A., and Kim, J. (2018). A two-step approach for producing oxygen-free aromatics from lignin using formic acid as a hydrogen source. *Chem. Eng. J.* 348, 799–810. doi:10.1016/j.cej.2018.05.036

Jiang, L., Guo, H., Li, C., Zhou, P., and Zhang, Z. (2019). Selective cleavage of lignin and lignin model compounds without external hydrogen, catalyzed by heterogeneous nickel catalysts. *Chem. Sci.* 10 (16), 4458–4468. doi:10.1039/C9SC00691E

Jiang, W., Cao, J. P., Xie, J. X., Zhao, L., Zhang, C., Zhao, X. Y., et al. (2021). Catalytic hydrodeoxygenation of lignin and its model compounds to hydrocarbon fuels over a metal/acid Ru/HZSM-5 catalyst. *Energy fuels.* 35, 19543–19552. doi:10.1021/acs.energyfuels.1c03169

Jing, Y., Dong, L., Guo, Y., Liu, X., and Wang, Y. (2020). Chemicals from lignin: A review of catalytic conversion involving hydrogen. *ChemSusChem* 13 (17), 4181–4198. doi:10.1002/cssc.201903174

Klein, I., Marcum, C., Kenttämaa, H., and Abu-Omar, M. M. (2016). Mechanistic investigation of the Zn/Pd/C catalyzed cleavage and hydrodeoxygenation of lignin. *Green Chem.* 18 (8), 2399–2405. doi:10.1039/C5GC01325A

Kristianto, I., Limarta, S. O., Lee, H., Ha, J. M., Suh, D. J., and Jae, J. (2017). Effective depolymerization of concentrated acid hydrolysis lignin using a carbon-supported ruthenium catalyst in ethanol/formic acid media. *Bioresour. Technol.* 234, 424–431. doi:10.1016/j.biortech.2017.03.070

Lancefield, C. S., Ojo, O. S., Tran, F., and Westwood, N. J. (2015). Isolation of functionalized phenolic monomers through selective oxidation and C-O bond cleavage of the β-O-4 linkages in lignin. *Angew. Chem.* 127 (1), 260–264. doi:10.1002/ange.201409408

Li, C., Zhao, X., Wang, A., Huber, G. W., and Zhang, T. (2015). Catalytic transformation of lignin for the production of chemicals and fuels. *Chem. Rev.* 115 (21), 11559–11624. doi:10.1021/acs.chemrev.5b00155

Lin, Y. C., Li, C. L., Wan, H. P., Lee, H. T., and Liu, C. F. (2015). Catalytic Hydrodeoxygenation of guaiacol on Rh-based and sulfided CoMo and NiMo catalysts. *Energy fuels.* 25 (3), 890–896. doi:10.1021/ef101521z

Liu, Q., Li, P., Liu, N., and Shen, D. (2017). Lignin depolymerization to aromatic monomers and oligomers in isopropanol assisted by microwave heating. *Polym. Degrad. Stab.* 135, 54–60. doi:10.1016/j.polymdegradstab.2016.11.016

Liu, X., Li, H., Xiao, L. P., Sun, R. C., and Song, G. (2019). Chemodivergent hydrogenolysis of eucalyptus lignin with Ni@ZIF-8 catalyst. *Green Chem.* 21 (6), 1498–1504. doi:10.1039/C8GC03511C

Long, J., Guo, B., Li, X., Jiang, Y., Wang, F., Tsang, S. C., et al. (2011). One step catalytic conversion of cellulose to sustainable chemicals utilizing cooperative ionic liquid pairs. *Green Chem.* 13 (9), 2334. doi:10.1039/c1gc15597k

Long, J., Qi, Z., Wang, T., Zhang, X., Ying, X., and Ma, L. (2014). An efficient and economical process for lignin depolymerization in biomass-derived solvent tetrahydrofuran. *Bioresour. Technol.* 154 (1), 10–17. doi:10.1016/j.biortech.2013.12.020

Luo, B., Li, R., Shu, R., Wang, C., Zhang, J., and Chen, Y. (2020). Boric acid as a novel homogeneous catalyst coupled with Ru/C for hydrodeoxygenation of phenolic compounds and raw lignin oil. *Ind. Eng. Chem. Res.* 59 (39), 17192–17199. doi:10.1021/acs.iecr.0c00888

Ma, C., Kim, T. H., Liu, K., Ma, M. G., Choi, S. E., and Si, C. (2021). Multifunctional lignin-based composite materials for emerging applications. *Front. Bioeng. Biotechnol.* 9, 708976. doi:10.3389/fbioe.2021.708976

Miessler, G., Fischer, P., and Tarr, D. (2013). *Inorganic chemistry: Pearson new international edition*. London: Pearson Higher Education.

Miller, J. E., Evans, L., Mudd, J. E., and Brown, K. A. (2002). Batch microreactor studies of lignin depolymerization by bases. 2. aqueous solvents. *Office Sci. Tech. Inf. Tech. Rep.* 30 (2), 61–78. doi:10.2172/800964

Parsell, T., Owen, B., Klein, I., Jarrell, T., Marcum, C., Haupert, L., et al. (2013). Cleavage and hydrodeoxygenation (HDO) of C-O bonds relevant to lignin conversion using Pd/Zn synergistic catalysis. *Chem. Sci.* 4 (2), 806–813. doi:10.1039/C2SC21657D

Regalbuto, J. R. (2009). Cellulosic biofuels-got gasoline? *Science* 325 (5942), 822–824. doi:10.1126/science.1174581

Shao, L., Zhang, Q., You, T., Zhang, X., and Xu, F. (2018). Microwave-assisted efficient depolymerization of alkaline lignin in methanol/formic acid media. *Bioresour. Technol.* 264, 238–243. doi:10.1016/j.biortech.2018.05.083

Shao, L., Zhang, X., Chen, F., and Xu, F. (2017). Fast pyrolysis of Kraft lignins fractionated by ultrafiltration. *J. Anal. Appl. Pyrolysis* 128, 27–34. doi:10.1016/j.jaap.2017.11.003

Shu, R., Long, J., Xu, Y., Ma, L., Zhang, Q., Wang, T., et al. (2016a). Investigation on the structural effect of lignin during the hydrogenolysis process. *Bioresour. Technol.* 200, 14–22. doi:10.1016/j.biortech.2015.09.112

Shu, R., Long, J., Yuan, Z., Zhang, Q., Wang, T., Wang, C., et al. (2015). Efficient and product-controlled depolymerization of lignin oriented by metal chloride cooperated with Pd/C. *Bioresour. Technol.* 179, 84–90. doi:10.1016/j.biortech.2014.12.021

Shu, R., Xu, Y., Ma, L., Zhang, Q., Wang, C., and Chen, Y. (2018). Controllable production of guaiacols and phenols from lignin depolymerization using Pd/C catalyst cooperated with metal chloride. *Chem. Eng. J.* 338, 457–464. doi:10.1016/j.cej.2018.01.002

Shu, R., Zhang, Q., Ma, L., Xu, Y., Chen, P., Wang, C., et al. (2016b). Insight into the solvent, temperature and time effects on the hydrogenolysis of hydrolyzed lignin. *Bioresour. Technol.* 221, 568–575. doi:10.1016/j.biortech.2016.09.043

Sun, C., Zheng, L., Xu, W., Dushkin, A. V., and Su, W. (2020). Mechanochemical cleavage of lignin models and lignin via oxidation and a subsequent base-catalyzed strategy. *Green Chem.* 22 (11), 3489–3494. doi:10.1039/D0GC00372G

Sun, Z., Fridrich, B., De Santi, A., Elangovan, S., and Barta, K. (2018). Bright side of lignin depolymerization: toward new platform chemicals. *Chem. Rev.* 118 (2), 614–678. doi:10.1021/acs.chemrev.7b00588

Swatloski, R. P., Spear, S. K., Holbrey, J. D., and Rogers, R. D. (2002). Dissolution of cellose with ionic liquids. *J. Am. Chem. Soc.* 124 (18), 4974–4975. doi:10.1021/ja025790m

Tang, W., Huang, C., Ling, Z., Lai, C., and Yong, Q. (2022). Insight into the mechanism of humic acid's dissolution capacity for lignin in the biomass substrates. *ACS Sustain. Chem. Eng.* 10, 14648–14657. doi:10.1021/acssuschemeng.2c05471

Tang, W., Wu, X., Huang, C., Ling, Z., Lai, C., and Yong, Q. (2021). Revealing the influence of metallic chlorides pretreatment on chemical structures of lignin and enzymatic hydrolysis of waste wheat straw. *Bioresour. Technol.* 342, 125983. doi:10.1016/j.biortech.2021.125983

Toledano, A., Serrano, L., and Labidi, J. (2014). Improving base catalyzed lignin depolymerization by avoiding lignin repolymerization. *Fuel* 116, 617–624. doi:10.1016/j.fuel.2013.08.071

Toledano, A., Serrano, L., Labidi, J., Pineda, A., Balu, A. M., and Luque, R. (2013). Heterogeneously catalysed mild hydrogenolytic depolymerisation of lignin under microwave irradiation with hydrogen-donating solvents. *Chemcatchem* 5 (4), 977–985. doi:10.1002/cctc.201200616

Wang, H., Pu, Y., Ragauskas, A., and Yang, B. (2019). From lignin to valuable products–strategies, challenges, and prospects. *Bioresour. Technol.* 271, 449–461. doi:10.1016/j.biortech.2018.09.072

Wang, H., Zhang, L., Deng, T., Hao, R., Hou, X., Cort, J. R., et al. (2016). $ZnCl_2$ induced catalytic conversion of softwood lignin to aromatics and hydrocarbons. *Green Chem.* 18 (9), 2802–2810. doi:10.1039/C5GC02967H

Wang, S., Zhang, K., Li, H., Xiao, L. P., and Song, G. (2021). Selective hydrogenolysis of catechyl lignin into propenylcatechol over an atomically dispersed ruthenium catalyst. *Nat. Commun.* 12 (1), 416–419. doi:10.1038/s41467-020-20684-1

Zhang, K., Li, H., Xiao, L. P., Wang, B., Sun, R. C., and Song, G. (2019). Sequential utilization of bamboo biomass through reductive catalytic fractionation of lignin. *Bioresour. Technol.* 285, 121335. doi:10.1016/j.biortech.2019.121335

Zhou, M., Sharma, B. K., Li, J., Zhao, J., Xu, J., and Jiang, J. (2019). Catalytic valorization of lignin to liquid fuels over solid acid catalyst assisted by microwave heating. *Fuel* 239, 239–244. doi:10.1016/j.fuel.2018.10.144

Zhou, M., Sharma, B. K., Liu, P., Xia, H., Xu, J., and Jiang, J. (2018). Microwave assisted depolymerization of alkaline lignin over hydrotalcite-based CuNiAl mixed oxides. *ACS Sustain. Chem. Eng.* 6 (9), 11519–11528. doi:10.1021/acssuschemeng.8b01697

Zhou, N., Thilakarathna, W. P. D. W., He, Q. S., and Rupasinghe, H. P. V. (2022). A review: Depolymerization of lignin to generate high-value bio-products: Opportunities, challenges, and prospects. *Front. Energy Res.* 9, 758744. doi:10.3389/fenrg.2021.758744

frontiers | Frontiers in Bioengineering and Biotechnology

TYPE Original Research
PUBLISHED 21 December 2022
DOI 10.3389/fbioe.2022.1093755

OPEN ACCESS

EDITED BY
Chen Huang,
Chinese Academy of Forestry, China

REVIEWED BY
Mi Li,
The University of Tennessee, Knoxville, United States
Xiaoting Feng,
Affiliated Hospital of Hunan Institute of Traditional Chinese Medicine, China

*CORRESPONDENCE
Jun Yu,
yujun80324@163.com
Chunlei Yang,
ycl193737@163.com
Xiong Chen,
cx163-qx@163.com

SPECIALTY SECTION
This article was submitted to Bioprocess Engineering, a section of the journal Frontiers in Bioengineering and Biotechnology

RECEIVED 09 November 2022
ACCEPTED 05 December 2022
PUBLISHED 21 December 2022

CITATION
Yao L, Huang C, Ding J, Zhang T, Yu J, Yang C and Chen X (2022), Application of yeast in plant-derived aroma formation from cigar filler leaves. *Front. Bioeng. Biotechnol.* 10:1093755. doi: 10.3389/fbioe.2022.1093755

Application of yeast in plant-derived aroma formation from cigar filler leaves

Lan Yao[1], Chenyi Huang[1], Jingyi Ding[1], Tongtong Zhang[1], Jun Yu[2]*, Chunlei Yang[2]* and Xiong Chen[1]*

[1]Key Laboratory of Fermentation Engineering (Ministry of Education), Cooperative Innovation Center of Industrial Fermentation (Ministry of Education & Hubei Province), HBUT National "111" Center for Cellular Regulation and Molecular Pharmaceutics, College of Bioengineering and Food, Hubei University of Technology, Wuhan, China, [2]Hubei Institute of Tobacco Science, Wuhan, China

Introduction: There are various degrees of defects of cigar filler leaves after air drying.

Methods: In order to improve the quality and plant-derived aroma content of cigar filler leaves, nine aroma-producing yeasts were applied in artificially solid-state fermentation of cigar filler leaves in this study. The differences with various yeasts application were compared by chemical composition and GC-MS analysis.

Results and discussion: The results showed that 120 volatile components were identified and quantified in cigar filler leaves after fermentation, including aldehydes (25 types), alcohols (24 types), ketones (20 types), esters (11 types), hydrocarbons (12 types), acids (4 types) and other substances (23 types). Based on the analysis of odor activity value (OAV), the OVA of fruity and floral aroma components were higher. It was found that floral aroma are the representative aroma types of cigar filler leaves treated with *Clavispora lusitaniae*, *Cyberlindera fabianii*, *Saccharomycosis fibuligera* and *Zygosaccharomyces bailii* R6. After being inoculated with *Hanseniaspora uvarum* J1, *Hanseniaspora uvarum* J4 and *Pichia pastoris* P3, the OAV of fruity aroma in cigar filler leaves was the highest, followed by tobacco aroma and woody aroma. The correlation between volatile components of cigar filler leaves with different yeasts was revealed after PCA analysis. It was concluded that the quality of cigar filler leaves was improved, and cigar filler leaves fermented with different yeasts showed different flavor.

KEYWORDS

plant-derived aroma, cigar filler leaves, aroma-producing yeast, solid-state fermentation, olfactory threshold, aroma characteristics

1 Introduction

Cigar is composed by three parts, cigar wrapper, cigar binder and cigar filler (Li et al., 2015). Cigar wrapper is the clothes of cigars, which can be observed directly, and is a tool to protect and beautify cigars. Cigar Binder is the part covered by the cigar wrapper, which is used to tightly wrap the cigar filler to form the shape of the cigar. Cigar Filler is the most internal structure of a cigar, which accounts for about 75% of the weight of the whole cigar. Cigar Filler determines the style, quality, and the flavor of a cigar during smoking (Chen et al., 2019).

Cigar leaves can't be directly used after being dried. To meet the needs of industrial processing, fermentation process is a necessity. There are many macromolecular substances in cigars leaves, which will produce a lot of unpleasant gases during combustion, affecting the overall quality of cigars. After fermentation, the qualities of tobacco are improved by eliminating harmful odors, degrading harmful substances, reducing offensive odor, and producing tobacco-specific flavors (Yang et al., 2018; Li J et al., 2020).

The mechanism of fermentation mainly includes enzymatic, microbial and chemical reactions (Zhang L et al., 2021). Microbiology plays an important role in the process of fermentation and aging of cigar tobacco leaves. Microbes on the surface of cigar tobacco leaves can synthesize and secrete a variety of extracellular hydrolase, which can accelerate the degradation of starch, pectin, cellulose, protein, lignin and other macromolecular substances into some small molecular compounds to form aroma compounds. (Xu et al., 2021; Zhang et al., 2022).

There are many microorganisms in nature that can produce aroma substances, which provide more ways to develop new natural flavors. Aroma-producing yeasts are a class of yeasts that can produce aroma substances and are now widely used in the food industry (Zhang et al., 2015). In recent years, with the rapid development of microbial technology, more and more scholars pay attention to the screening and application of microorganisms that can enhance the quality of tobacco. It has been proved that fermentation with aroma-producing microorganisms to improve the aroma quality of tobacco is a feasible method.

A strain of *Pichia terricola* MG6 was screened and isolated from the epidermis of grapes (Yan et al., 2021). The fermentation broth was analyzed by GC-MS technique, and results showed that the content of aroma components such as ketones, alcohols and esters was increased by different levels. Furthermore, the tobacco flavors prepared from the fermentation broth of this strain did improve the quality of cigarettes. *Hanseniaspora* strain YG-4 isolated by Guo et al. (2019) proved that it could produce a distinct floral and sweet aroma in the fermentation broth. And the fermentation broth prepared using this strain with tobacco leaf powder showed an increased content of 2-phenylethanol, phenylethyl benzoate, 2-pentenoic acid and 1-phenyl-3-aminopyrazole compared with the control group. A sweet aroma producing strain of bacteria named Lizhi-01 was isolated and purified from fresh litchi and it was found that the aroma components of tobacco leaves after fermentation with this strain were mainly 2-phenylethanol, 2,3-butanediol, furfural and Palmitic acid (Zhou et al., 2010).

The odor activity value (OAV) refers to the ratio of the concentration of an aroma component in the aroma system to its threshold value. It can be used as an indicator of the sensory impact of each volatile compound on the overall aroma (Peinado et al., 2004). Generally, components with OAV >1 are called modified aroma components, components with OAV >10 are considered as key aroma components. And a higher OAV value indicates a greater contribution of the component to the overall aroma (Pino and Queris., 2011).

Raw and lower grade tobacco leaves are often with more impurities, less delicate smoke, less mellow flavor, and even bitterness, pungency, and astringency. Therefore, fermentation is needed to improve the quality of raw tobacco leaves. The fermentation process of cigar tobacco is actually a biochemical reaction process that involves the interaction of substrate with microorganisms and enzymes (Niu et al., 2020). Microorganisms can be added artificially during the processing process to shorten the fermentation time and improve the quality of the cigar leaves including the desired color, aroma and combustion properties. Theoretically, the fermentation of cigar leaves with the addition of microorganisms with known characteristics can result in a more distinctive cigar product. At present, domestic cigar raw materials lack distinguished aroma style, superior aroma quantity and quality. Thus, improving the characteristics of domestic cigar is a crucial step in the development of cigar industry. Many studies have shown that yeast, bacteria as well as fungi can produce aroma. The application of *Bacillus* in tobacco fermentation has been reported frequently, while there are limited reports on the application of aroma producing yeast in cigar filler leaves fermentation so far.

In this paper, nine aroma-producing yeasts were applied in the solid fermentation of cigar filler leaves, among which *Clavispora lusitaniae* can produce alcohols and esters (Wang et al., 2022). *Saccharomyces cerevisiae* has the ability to produce acid and esters (Minebois et al., 2020; Yang et al., 2022). *Cyberlindnera fabianii* could generate complex aromas during the brewing process, whose liquid culture has a better ability to produce ethyl acetate (Van Rijswijck et al., 2019). *ZygoSaccharomyces rouxii* can grow in high salt and high temperature environments, and its main role in the fermentation process is to ferment alcohols and synthesize a variety of ester aroma components, glycerol and polyols, as well as other ketones and phenols (Escott et al., 2018; Dai et al., 2020; Niu et al., 2022). *Saccharomycopsis fibuligera* is applied in various koji. It can produce amylase, glycosylase, and esterase, and has a positive effect on the production of volatile compounds (Lee et al., 2018; Yeong et al., 2018; Ma C et al., 2022). *Hanseniaspora uvarum* can produce volatile acids, organic acids, aldehydes, alcohols and other secondary metabolites (Hu K et al., 2018;

Wei et al., 2020). *Pichia pastoris* is capable of producing esters such as ethyl acetate, isobutyl acetate and isoamyl acetate (Wei et al., 2020; Jia et al., 2021). *Zygosaccharomyces bailii* forms more alcohols, acids, esters and aldehydes (Xu C. P et al., 2018).

After fermentation, the total aroma and OAV value of cigar tobacco leaves inoculated with various strains of aroma-producing yeast were analyzed and compared. Strains that contribute to the unique aroma characteristics of cigar were screened out. This may also provide reference for the further application of bio-fermentation technology to produce cigar with different aromas.

2 Materials and methods

2.1 Materials

The cigar filler leaves were CX-014 after air drying in Enshi, Hubei Province, China. All the chemical reagents used in the study were purchased from Sinopharm group, China.

Saccharomyces cerevisiae, *ZygoSaccharomyces rouxii*, *Clavispora lusitaniae*, *Saccharomycopsis fibuligera*, *Cyberlindnera fabianii*, *Hanseniaspora uvarum* J1, *Hanseniaspora uvarum* J4, *Pichia pastoris* P3 and *Zygosaccharomyces bailii* R6 are all preserved strains in our own laboratory.

Yeast extract peptone dextrose (YEPD) medium, yeast extract powder 10 g/L, glucose 20 g/L, peptone 20 g/L, solid medium with agar 20 g/L.

2.2 Experimental methods

2.2.1 Preparation of yeast seed solution

Yeasts stored in −80°C refrigerator were transferred to liquid YEPD medium and incubated at 30°C and 200 r/min for 24 h.

The obtained seed solution was centrifuged at 4°C and 12000 r/min for 5 min, the supernatant was discarded to collect wet cells, and then resuspended in sterile deionized water. The operation was repeated twice to obtain wet cells without fermentation broth. Then sterile YEPD medium was applied to dilute the yeast cell concentration to 10^8 cfu/ml.

2.2.2 Solid-state fermentation of cigar filler leaves

Referring to the method described earlier (Qin et al., 2020), the obtained yeast cell suspension (10% ml/g, based on the ratio of volume to dry mass of cigar filler leaves) was sprayed on the surface of cigar filler leaves. The control groups were sprayed with sterile water and liquid YEPD medium, respectively. The moisture content of the cigar filler leaves was controlled at 30%. After the moisture was balanced, the cigar filler leaves were put into a sealed bag and placed in a cabinet with constant temperature and humidity (temperature 30°C, humidity 80%) to ferment for 7 days.

2.2.3 Determination of conventional chemical composition of tobacco

Main chemical components in cigar filler leaves, including total sugar, reducing sugar, nicotine, total nitrogen, potassium and chlorine were evaluated by continuous flow analytical system, based on the standard of tobacco industry (YC/T 159-2002, 2002; YC/T 160-2002, 2002; YC/T 161-2002, 2002; YC/T 162-2011, 2011; YC/T 217-2007, 2007). The quantification results were based on dry weight of cigar filler leaves.

2.2.4 Determination of volatile aroma components

The samples were processed using simultaneous distillation extraction (SDE) technique and analyzed for aroma substances by chromatography-mass spectrometry (GC-MS) (Yao et al., 2022). Briefly, after drying and wiley-milled (screen size <2 mm was used), 10 g samples were applied for aroma components extraction. Then, saturated NaCl and dichloromethane were applied as the extraction solvents. After extraction, the extract were collected and concentrated to 2 ml, with 50 μl 1.2028 mg/ml phenylethyl acetate as internal standard.

2.2.5 Data processing

Chromatograms were analyzed using the GCMS solutionver. 4.11 (Agilent Technologies Inc, United States). The mass spectra data were compared with spectra in the NIST reference library (NIST14) of the GC/MS data system for identification of volatile compounds. Origin 9 (Origin Lab, Massachusetts, United States) was applied to draw the histogram. PCA analysis was performed with SIMCA-P 14.1 (Umetrics, Malmo, Sverige), and cluster heat map was drawn with TBtools (Guang zhou, China).

3 Results and analysis

3.1 Chemical composition analysis

The main chemical components of tobacco leaves can affect the smoke characteristics to some extent and can be used as an indicator to identify the quality of tobacco leave (Gao et al., 2011). The contents of nicotine, reducing and total sugars, potassium, and chloride in fermented cigar filler leaves were determined, and the results were shown in Figure 1. It was showed that the nicotine content of cigar filler leaves after fermentation with the addition of *Clavispora lusitaniae*, *Cyberlindnera fabianii*, *ZygoSaccharomyces rouxii* and *Hanseniaspora uvarum* J1 was higher than that of the

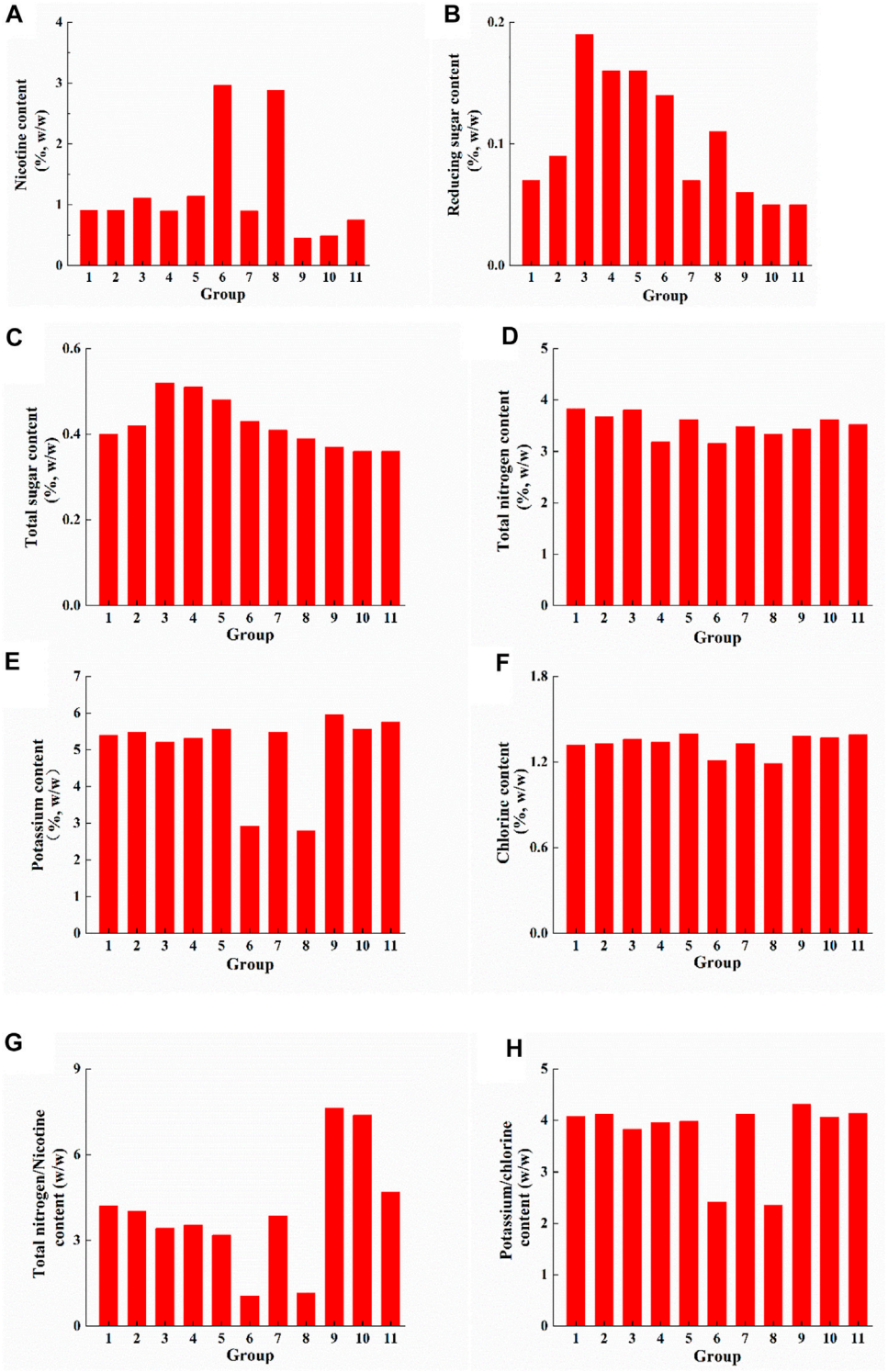

FIGURE 1
Chemical components analysis of cigar filler leaves after fermentation. **(A)** Nicotine content changes; **(B)** Reducing sugar content changes; **(C)** Total sugar content changes; **(D)** Total nitrogen content changes; **(E)** Potassium content changes; **(F)** Chlorine content changes. Note: 1-Water; 2-Medium; 3-Medium + *Clavispora lusitaniae*; 4-Medium + *Saccharomyces cerevisiae*; 5-Medium + *Cyberlindnera fabianii* 6-Medium + *ZygoSaccharomyces rouxii*; 7-Medium + *Saccharomycopsis fibuligera*; 8-Medium + *Hanseniaspora uvarum* J1; 9-Medium + *Hanseniaspora uvarum* J4; 10-medium + *Pichia pastoris* P3; 11-medium + *Zygosaccharomyces bailii* R6.

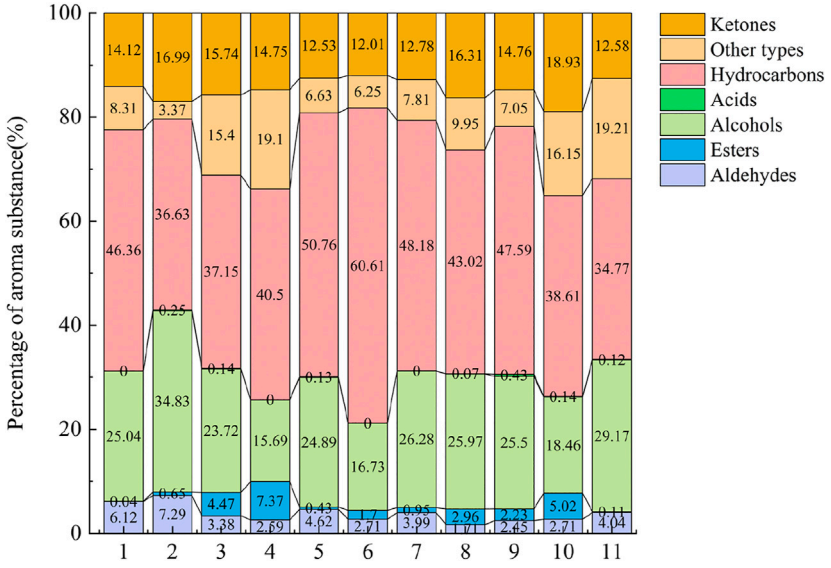

FIGURE 2
Comparison of types of volatile component in cigar filler leaves after fermentation with different yeast. Note: The numbers in the horizontal coordinate represent the same groups as in Figure 1.

control group (Figure 1A). The highest nicotine content was found in the group with the addition of *ZygoSaccharomyces rouxii* (2.99%), followed by the group with the addition of *Hanseniaspora uvarum* J1 (2.88%). The nicotine content of other treatment group decreased to various degrees. The increase in relative nicotine content in some group may be caused by the degradation of other substances, such as starch, protein and cellulose.

Cigar leaves contain very low sugar content (basically below 0.5%), because sugar is almost consumed after drying. Among them, groups treated with *Clavispora lusitaniae*, *Saccharomyces cerevisiae*, and *Cyberlindnera fabianii* showed the highest reducing and total sugar content (Figures 1B,C). Probably because these three yeast strains have the ability to produce α-amylase and glycosylase (Meng and Zhang, 2021), which can degrade the starch in the cigar filler leaves. The reducing and total sugar contents of the other groups were not significantly different compared with the control groups.

The total nitrogen content of high-quality cigar tobacco is generally around 4%–6%, and the ratio of nitrogen to nicotine is between 3 and 4 (Wu et al., 1999). When the total nitrogen content is lower, the taste is insipid. The smoke generated by high total nitrogen content is strong, pungent and irritating (Liu, et al., 2022). Except for nicotine, nitrogenous compounds in cigar leaves include proteins, amino acids, and amide compounds, can often make the smoke bitter and rough (Yang C et at., 2018). The total nitrogen content decreased in all the groups with the addition of yeast (Figure 1D). Among them, the nitrogen-nicotine ratio was less than 3 in the treatment groups with the addition of *ZygoSaccharomyces rouxii* and *Hanseniaspora uvarum* J1, while more than 4 in the treatment groups with the addition of *Hanseniaspora uvarum* J4, *Pichia pastoris* P3, and *Zygosaccharomyces baili* R6 (Figure 1G). Tobacco with a potassium-chloride ratio above 4 show better combustibility, while below 2 is prone to flameout (Yin et al., 2018). The treatment groups with *ZygoSaccharomyces rouxii* and *Hanseniaspora uvarum* J1 had low potassium-chlorine ratios and therefore poor combustibility, while the other groups had better combustibility with potassium-chlorine ratios around 4 (Figure 1H).

3.2 Analysis of the types and contents of volatile substances in cigar filler leaves after addition with different aroma-producing yeasts

Aroma composition is one of the most important indicators to evaluate the quality of cigar. Aroma in tobacco is determined by the composition and ratio of aroma-causing substances. In order to analyze the effects of different aroma-producing yeasts on the types and contents of volatile substances in cigar filler leaves, volatile compounds were identified by GC-MS on the fermented filler leaves, and the results were shown in Figure 2.

Volatile components can be classified into seven categories: aldehydes, alcohols, ketones, esters, hydrocarbons, acids, and others. The quantity and relative content of volatile substances in cigar filler leaves were various after different treatments with yeast. Among them, the amount of aldehydes (25 types) ranked the first, followed by alcohols (24 types), ketones (20 types), esters (11 types), hydrocarbons (12 types), acids (4 types), and others (23 types). The total amount of volatile components after yeast treatment ranged from 311.68 to 637.38 μg/g. And group treated with *Cyberlindnera fabianii* showed the highest total amount of volatile components. More details were shown in SupplementaryTable S1.

Ketones accounted for 12.01%–18.93% of the total aroma, which were mainly cembranoids and carotenoids degradation products. Relatively high content of ketones were solanone, perhydrofarnesyl acetone and farnesyl acetone. Solanone has a fresh carrot aroma and can make the smoke rich, mellow and delicate (Yun, 2016). Its highest content reached 22.69 μg/g and 24.14 μg/g in the *Cyberlindnera fabianii* and *Saccharomycopsis fibuligera* treatment groups, respectively. In terms of aroma composition after different aroma-producing yeast treatments, *Cyberlindnera fabianii* (79.88 μg/g) and *Hanseniaspora uvarum* J1 (78.28 μg/g) treatments showed the highest total amount of ketones in the cigar filler leaves.

Aldehydes that mainly from phenylalanine metabolites were dominantly comprised by A,2,6,6-tetramethyl-1-cyclohexene-1-crotonaldehyde, 3-(2,6,6-trimethyl-1-cyclohexen-1-yl) acrylaldehyde, benzaldehyde and (Z)-7-hexadecenal, which took up for 1.71%–7.29% of the total aroma. A,2,6,6-tetramethyl-1-cyclohexene-1-crotonaldehyde is one of the synthesis products of β-ionone and ethyl chloroacetate (Deng et al., 2021), showing tobacco and nutty aroma. 3-(2,6,6-trimethyl-1-cyclohexen-1-yl) acrylaldehyde is one of the dominant components of the smoke. Benzaldehyde is one of the metabolites of phenylalanine and has a strong almond and cherry flavor, as well as a slight woody aroma (Liu et al., 2019). Compared with other groups, cigar filler leaves innocolated with *Cyberlindnera fabianii* (29.43 μg/g) and *Saccharomycopsis fibuligera* (22.54 μg/g) had higher levels of aldehydes than the other groups.

Alcohols that mainly derived from chlorophyll degradation products, phenylalanine degradation products and maillard reaction products occupy 15.69%–34.83% of the total aroma. Among them, phytol was the predominating alcohols, followed by furfuryl alcohol, 2-phenylethanol and benzyl alcohol. Phytol is converted from the decomposition of neophytadiene, which has a delicate aroma (Wu et al., 2019). Furfuryl alcohol is a kind of Maillard reaction product (Wu et al., 2019) and is one of the main contributing components of the burnt flavor. Benzyl alcohol and 2-phenylethanol are phenylalanine metabolites, which shows rosy aroma (Wu et al., 2019). The alcohol content was relatively high after fermentation with the addition of *ZygoSaccharomyces rouxii* (158.66 μg/g) and *Saccharomycopsis fibuligera* (148.30 μg/g), followed by the treatment groups with *Hanseniaspora uvarum* J4 (130.85 μg/g) and *Hanseniaspora uvarum* J1 (124.63 μg/g), while the control groups only contained 81.66 μg/g and 103.09 μg/g of alcohols, respectively.

Esters that mainly derived from amino acid and fatty acid metabolites accounted for 0.04%–7.37% of the total aroma (Shi et al., 2019). The highest ester content was found in the group treated with *Saccharomyces cerevisiae* (32.00 ug/g) and *Pichia pastoris* P3 (20.08 μg/g), followed by *Hanseniaspora uvarum* J1 (14.22 μg/g), *Clavispora lusitaniae* (13.93 μg/g), and *Hanseniaspora uvarum* J4 (11.42 μg/g). The ester content in the control groups was only 0.12 μg/g (water) and 1.91 μg/g (YEPD medium), respectively, indicating a greater contribution of aroma-producing yeast to the production of esters.

Hydrocarbons that mainly consist of neophytadiene, dipentene dioxide and (+)-Limonene take up for 34.77%–60.61% of the total aroma compounds. Neophytadiene, a kind of chlorophyll degradation products (Wu et al., 2019), is the most abundant component of volatile substances in cigar. It reduces the irritation of the smoke and makes it soft and pleasant, and also could help other volatile aroma substances, aroma-causing substances and added aroma components to enter the smoke (Wang et al., 2015). Among all treatments, the highest levels of neophytadiene were found in the group added with *Cyberlindnera fabianii* (323.54 μg/g) and *Saccharomycopsis fibuligera* (271.92 μg/g), followed by *Hanseniaspora uvarum* J4 (244.16 μg/g) and *ZygoSaccharomyces rouxii* (216.58 μg/g), while the neophytadiene levels in the control group sprayed with sterile water and YEPD medium were 149.7 μg/g and 107.04 μg/g, respectively. Dipentene dioxide showed a menthol aroma and was highest in the group supplemented with *Cyberlindnera fabianii* and *Hanseniaspora uvarum* J4. (+)-Limonene had a pleasant fresh orange aroma and was only present in group supplemented with *Hanseniaspora uvarum* J4 (0.31 μg/g) and *Pichia pastoris* P3 (0.53 μg/g).

The substances in the other classes were mainly products of the Maillard reaction, e.g., pyridines and furans. 3-acetylpyridine showed sweet nut, hawthorn and popcorn aromas and its content was the highest after the addition of *Hanseniaspora uvarum* J4 (8.57 μg/g) and *Pichia pastoris* P3 (8.53 μg/g).

3.3 Analysis of the contribution of aroma components to cigar filler leaves

The OAV value can be used to determine the contribution of aroma components to the aroma system in two dimensions: concentration and threshold. Components with OAV <1 are usually considered as potential aroma substances, while aroma components with OAV >1 are considered to have a certain degree of contribution to the overall aroma. The larger their OAV value, the greater of their contribution (Greger and Schieberi, 2007). The OAV results of each aroma component of the cigar leaves were shown in Table S2. 24 aroma compounds

of OAV >1 were furfuryl alcohol, 4-hydroxy-3-methoxystyrene, 6-methylhept-5-en-2-one, β-cyclocitral, (+)-Limonene, 5,9-dimethyl-deca-4,8-dienal, 2-hexenal, β-damascone, dihydrodamascenone, damascenone, citronellal, 2-phenylethanol, indole, benzyl alcohol, benzaldehyde, (2E,4E)-2,4-Nonadienal, phenylacetaldehyde, geranyl acetone, 4-ketoisophorone, isophorone, 4,7,9-megastigmatrien-3-one, 3-acetylpyridine, hexanal, and L-menthol. However, the contribution of these substances to cigar aroma was various. Although the OAV values of the key aroma compounds in the samples varied, the OAV values of 2-hexenal, β-damascone, dihydrodamascenone, and damascenone were much higher than those of the other aroma compounds in all samples. It is speculated that they play key roles in the aroma of cigars.

β-damascone, dihydrodamascenone, and damascenone contributed more to the floral aroma. The OAV of the three representative substances of baking fragrances were relatively low. Perhaps baking fragrances are not the most prominent characteristic aroma of cigars, but rather serve as auxiliary fragrances to make cigar smoke more harmonious. 5,9-dimethyl-4,8-decadienal and 2-hexenal have much higher OAV values than the other five aroma components, playing a more important role in demonstrating the fruity aroma. Among the 3 components of woody aroma, isophorone and 4-ketoisophorone had low OAV values, and were identified as a modifying aroma substance of cigar. 2-Hexanal had higher OAV values and was the main contributing component of woody aroma. The content of 2 herbal flavor was low, the OAV values of L-menthol were greater than 1, which was more important for the medicinal aroma.

After calculating the odor activity values of the aroma-causing components, they were categorized and summarized according to the flavors provided. And the flavor intensity of cigar leaves after different yeast treatments were compared, as shown in Table S2. The odor activity values were floral > fruity > tobacco > woody > roasted > herbal after addition with *Clavispora lusitaniae*, *Cyberlindnera fabianii and Saccharomycopsis fibuligera*. *Saccharomyces cerevisiae* and *ZygoSaccharomyces rouxii* groups were lower in fruity odor activity values and were dominated by floral odor. *Hanseniaspora uvarum* J1 and *Hanseniaspora uvarum* J4 treatment groups were dominated by fruity odor, followed by woody and tobacco odor. Cigar leaves treated with *Pichia pastoris* P3 was dominated by fruity odor, followed by floral and woody odor. *Zygosaccharomyces bailii* R6 treated cigar leaves showed higher floral and fruity odor activity values. After yeast inoculation, aroma of cigar filler leaves was improved to various degrees. The aroma of the group inoculated with *Hanseniaspora uvarum* J1 and *Pichia pastoris* P3 was the highest, which were increased by 5.75 times and 5.54 times respectively, compared with the control group sprayed with YEPD.

In terms of overall flavor intensity, the 29 aroma-causing components had higher odor activity values for fruity and floral flavors, followed by tobacco and woody flavors. Presumably because of the lower perceptual thresholds for β-damascenone, dihydrodamascenone, damascenone, and 2-hexenal, which possess both fruit and floral of flavors. Due to the large number of aroma-causing components in tobacco, OAV values for only 29 aroma components were found in this study. Furthermore, cross-influences among aroma-causing components were not considered.

3.4 PCA analysis of key aroma components in cigar filler leaves

PCA is a multivariate statistical analysis method, which can be used to analyze databases related to several mutually dependent variables. The aroma components in cigar tobacco leaves are complex and diverse. In order to obtain more accurate and intuitive classification results, 24 volatile components with OAV values greater than 1 in cigar tobacco leaves were used for principal component analysis to observe the difference between cigar tobacco leaves after different treatments. It can be seen from Figure 3 that the variance contribution rates of PC1 and PC2 were 47.41% and 16.86% respectively, which explained 61.9% of the total variance of cigar filler leaves. Most X-variables (OAV of volatile compounds) and Y-variables (different yeast treatments) were around the circle, where *Hanseniaspora uvarum* J1, *Hanseniaspora uvarum* J4, and *Pichia pastoris* P3 were clustered as one category. In addition, *Clavispora lusitaniae*, *Saccharomyces cerevisiae*, and *Cyberlindnera fabianii* were clustered as one category, indicating that there was similarity between the types or concentrations of volatile components in the cigar filler leaves after fermentation. And the treatment group with water only or with medium only was obviously different from other treatment groups.

The correlation between volatile components of cigar filler leaves with different yeasts is indicated by the distance of the principal components on the graph. *Hanseniaspora uvarum* J1, *Hanseniaspora uvarum* J4, and *Pichia pastoris* P3 were mainly closely related to six volatile components, including ketones (geranyl acetone, 4,7,9-methatigmatrien-3-one, 6-methylhept-5-en-2-one, 4-ketoisophone), aldehydes (hexanal), and other types (3-acetylpyridine). *Clavispora lusitaniae*, *Saccharomyces cerevisiae* and *Cyberlindnera fabianii* were mainly related to Damascenone. *ZygoSaccharomyces rouxii* was closely related with β- Damascenone. *Zygosaccharomyces bailii* R6 and *Saccharomycopsis fibuligera* showed great impact on indole, furfuryl alcohol and β- Damascenone formation.

3.5 Cluster analysis of volatile components in cigar filler leaves fermented by different yeasts

During cluster analysis, distance between variables was calculated, which indicates the similarity between variables.

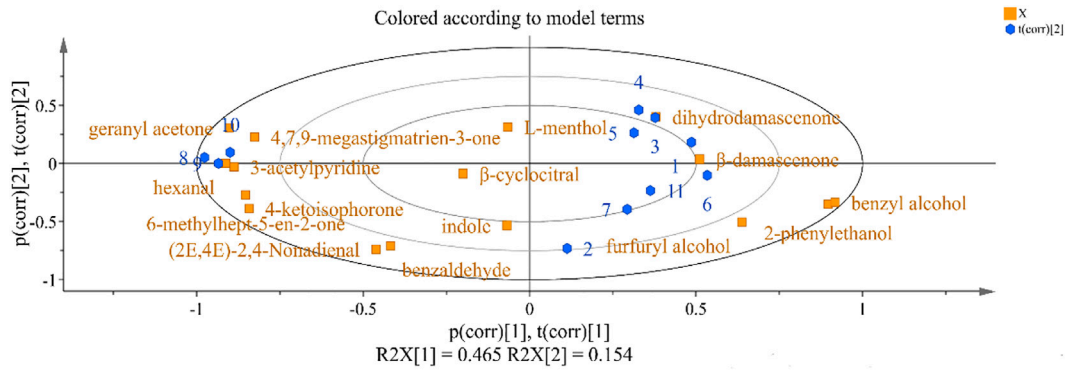

FIGURE 3
Principal component analysis biplot (score and load values) for volatile compounds in different treatment of fermented Cigar filler leaves. Note: The figures in Figure 3 represent the same groups as in Figure 1.

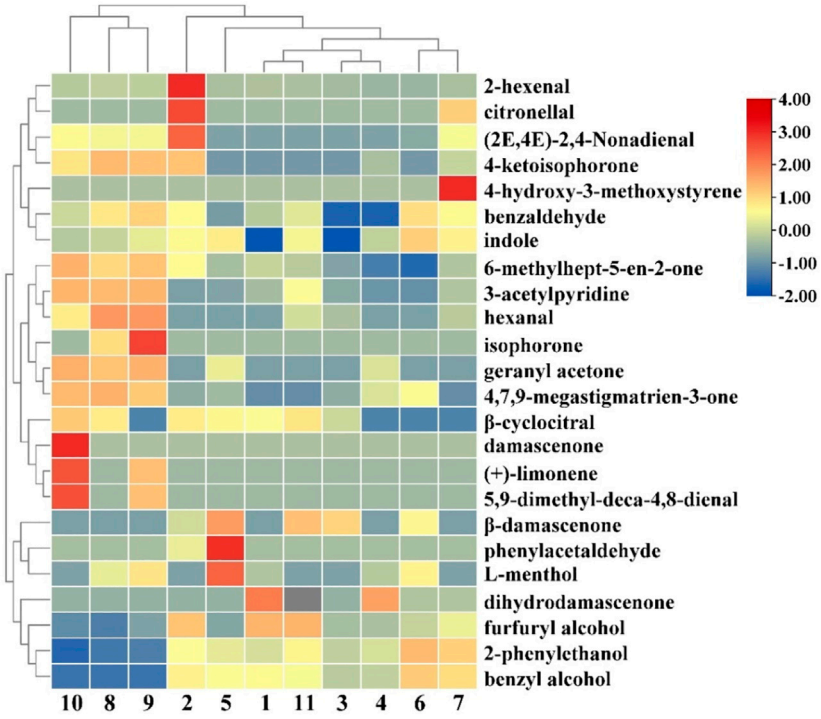

FIGURE 4
Heat map of cluster analysis of flavor compounds in Cigar filler leaves fermented by different yeasts. Note: The numbers in Figure 4 represent the same groups as in Figure 1.

Cluster analysis results of aroma components of cigar filler leaves fermented by different yeasts were shown in Figure 4. The results showed that there were significant differences among different samples, which was consistent with the PCA analysis results. The volatile components were divided into 3 categories. The first category included 7 compounds, which contained many high content characteristic flavor compounds, including 2-hexenal (pleasant green leaf fragrance and fruit aroma), citronellal (clean herbal citrus odor) and 4-ketoisophorone (strong tea aroma). The second category included 10 kinds of

compounds, such as 3-acetylpyridine (sweet, green and earthy smell), geranyl acetone (floral, fruity aroma), and hexanal which not only has the woody aroma, but also has the unique fruit aroma at low concentrations. The third group aggregated seven compounds, such as phenylacetaldehyde (honey, sweet, floral, chocolate and cocoa, with a spice nuance), 2-phenylethanol (floral, sweet, rosy and bready) and furfuryl alcohol (sweet, caramel aroma). Therefore, Category 1 and Category 3 focused on the characteristic aroma compounds of cigar tobacco leaves, ensuring the keynote of cigar tobacco leaves. Category 2 contained the most diverse and dispersed volatile substances, including various styles of aroma substances, reflecting the differences of each sample.

4 Discussion

At present, researches on microbial fermentation of tobacco mainly focus on the isolation and screening of strains that degrade nicotine, nitrosamines, macromolecules, and β-carotene. Limited research has been reported on the fermentation of cigar leaves by adding different aroma-producing yeast (Xu et al., 2021). The results of this study showed that the addition of exogenous aroma-producing yeast during artificial fermentation could significantly increase the aroma content of cigar filler leaves, which is basically consistent with the results of Hu et al. (2018). It is possible that the growth and metabolism of aroma-producing yeast during the fermentation of cigar filler leaves promoted the quality improvement of cigar filler leaves.

In recent years, many scholars have made related studies on aroma producing yeast. In this study, nine strains of yeast with good aroma production ability were selected, among which *Clavispora lusitaniae* has been developed for the production of naturally carbonated beverage with improved taste and aroma (Jairath et al., 2012). *Clavispora lusitaniae* isolated from Daqu shows high ability to produce a large amount of ethyl caproate. Furthermore, a total of 30 flavor compounds were detected after fermentation by *Clavispora lusitaniae*, including isobutanol, isoamyl alcohol, furfuralcohol, 3-methylthiopropanol, phenethyl alcohol, phenylethyl acetate, 2-methyl butyric acid-2-ethyl phenyl ester, 2, 4-dimethylbenzaldehyde, 2, 3-dihydrobenzofuran (Fan et al., 2021). Higher alcohols such as furfuralcohol can impart sweetness and enhance the fragrance of other flavor compounds (Luo et al., 2015). Phenethyl alcohol (honey and rose flavors) is an important compound in many fermented products (Lin et al., 2020). The formation of these compounds contributes to the sweet flavor in fermented cigar filler leaves.

During the fermentation of pear wine, a high yield of ester (hexyl acetate, ethyl caprylate and phenylethyl acetate) and alcohols (isoamyl alcohol, hexanol and 2-phenylethanol) compounds were obtained with the help of *Saccharomyces cerevisiae*, which have an important impact on the taste and aroma of pear wine (Yang et al., 2022). Inoculation of *Saccharomyces cerevisiae* to apple wine fermentation can increase the concentration of acetaldehyde and ethyl acetate (He et al., 2022). After adding *Saccharomyces cerevisiae* to fermentation of Chinese wolfberry wine, high content of isoamyl acetate, isoamyl, alcohol propanol, ethyl cinnamate and β-ionone was detected. β-ionone is a representative fruit aroma substance of wolfberry wine, which has a significant impact on the aroma quality of fruit wine (Zhao et al., 2022). *Saccharomyces cerevisiae* plays an extremely important role in koji fermentation. The production capacity of aromatic compounds, alcohols, esters, and acid volatile flavor substances is strong. It shows a high production capacity for 2-phenylethanol, ethyl palmitate, and guaiacol (Xue, 2016). This is consistent with our results, it was indicated that after fermentation of cigar filler leaves by *Saccharomyces cerevisiae*, the content of β-ionone was increased. Furthermore, the contents of β-ionone, solanone, geranyl acetone, 4,7,9-Megastigmatrien-3-one, perhydrofarnesyl acetone, farnesyl acetone, bis(2-ethylhexyl) benzene-1,3-dicarboxylate were increased. Tobacco leaves were fermented with *Saccharomyces cerevisiae* ULI3 and *Maltophilia oligotrophic* earlier. After fermentation, six important aroma components (4,7,9-Megastigmatrien-3-one, Damascone, Solanone, dihydrodamadone, geranyl acetone and dihydroactinidiolide) was increased by 6.65% compared with that before fermentation (Long et al., 2021). Tobacco leaves treated with organic acids and *Saccharomyces cerevisiae* showed that the total water-soluble sugar content and sugar nicotine ratio was increased. And the content of volatile substances such as alcohols, ketones, esters, aldehydes and neophytadiene also increased (Ma C. L et al., 2022). *Saccharomyces cerevisiae* and *Eurotium cristatum* were inoculated with green tea powder. Then the fermentation broth was sprayed to tobacco leaves to make cigarettes. Tea, wine, honey and special flavors were produced after fermentation. The sensory quality of tobacco was improved (Du et al., 2021). In the present study, after inoculation with *Saccharomyces cerevisiae*, the content of ketones and hydrocarbons in volatile compounds of cigar filler leaves was significantly higher than that of the control group with water, which was helpful to improve the aroma quality of tobacco leaves.

The potential benefit of *C. fabianii* is their relatively high levels of ability to produce esters. Among the ester, the most important compounds are ethyl acetate, 3-methylbutyl acetate, methylpropyl acetate, phenylethyl acetate, ethyl hexanoate and ethyl octanoate (Van Rijswijck et al., 2017). The application of *C. fabianii* in rice wine brewing showed that 21 kinds of main flavor compounds were detected, which have a positive effect on increasing the aroma. Isoamyl alcohol and phenethyl alcohol are common flavor compounds in alcoholic drinks. Isoamyl alcohol can impart sweetness and enhance the fragrance of other flavor compound (Jairath et al., 2012), which could only be detected in cigar filler leaves after fermentation with *C. fabiani*.

Previous studies have shown that *ZygoSaccharomyces rouxii* is a osmophilic yeast, which can grow in a high salt, high sugar,

high temperature and low pH environment, and can endure a very low water activity environment (Escott et al., 2018; Dai et al., 2020). During soybean sauce fermentation, aromatic compounds such as esters (ethylhexanoate, 2-phenylethylacetate) could be produced to make aroma rich (Han et al., 2020). The concentration of volatile organic compounds in the fermentation process of chilli bean sauce can be significantly increased by *ZygoSaccharomyces rouxii*, and various new volatile organic compounds can be formed, such as 2-phenylethanol, 2-methoxy-phenol and pyrazine (Niu et al., 2022). The content of 2-phenylethanol by inoculation with *ZygoSaccharomyces rouxii* to cigar filler leaves was much higher than that of other groups.

Saccharomycopsis fibuligera shows ability to produce aroma and ester. During the fermentation of Chinese rice wine, more 2-phenylethanol, 1-octene-3-ol and 2-octene-1-ol, ethyl acetate, ethyl octanoate, phenylacetaldehyde and ethyl butyrate can be produced. These aromatic substances endow the Chinese rice wine with a comprehensive aroma of flowers, fruits and honey (Lee et al., 2018; Yang et al., 2021). Among the volatile aroma components of solid fermentation products of *Saccharomycopsis fibuligera*, various products also present fruity and floral aromas. The content of ethyl acetate (fruity aroma), isoamyl acetate (banana and pear aroma), 2-phenylethanol (rose aroma), phenethyl acetate (sweet aroma), and ethyl palmitate (fruit and cream aroma) are higher. The sensory evaluation of its solid fermentation products shows a strong fruit flavor, which is the result of these volatile flavor substances (Wang et al., 2017). In this study, the content of ketone compounds (such as solanone, R-(-)-3-Hydroxy-β-ionone, farnesyl acetone) that detected in cigar filler leaves after fermentation by *Saccharomycopsis fibuligera* was the highest.

The contents of methyl caproate, methyl octanoate and methyl caprylate in strawberry fruits fumigated by *Hanseniaspora uvarum* were increased during cold storage (Wang et al., 2019). Farnesol, 2-heptanol, hexan-1-ol, nerol, benzaldehyde, isoamyl acetate, ethyl butanoate, ethyl propionate, phenethyl acetate, linalool, β-damascenone and other aromatic substances produced in the fermentation of grape juice (Ge et al., 2021), make it rich in aroma. In the cigar filler leaves treated by *Hanseniaspora uvarum*, substances such as β-damascenone, 4,7,9-Megastigmatrien-3-one, 4-ketoisophorone, perhydrofarnesyl acetone, farnesyl acetone, 2-hexenal, 4-pyridinecarboxaldehyde, phytol, tributyl phosphate, 3-acetylpyridine were increased.

A large amount of ethyl acetate can be produced by *pichia pastoris* in solid fermentation of millet, showing strong apple flavor (Jia et al., 2021). After inoculation of *pichia pastoris* to distiller's grains for fermentation, the content of ester was the highest. Among the esters, the content and types of ethyl esters were the highest (Huang et al., 2021). In the present study, the highest content of esters was detected in the group inoculated with *Pichia pastoris*, mainly tribehenin and tributyl phosphate. *Hanseniaspora* sp. and *Pichia* sp. were employed to investigate the effects on the volatile aroma components of tobacco leaves (Li M et al., 2020). Results showed that a total of 95 volatile aroma components were detected. Among alcohols, benzyl alcohol, phenylethyl alcohol and other important flavor substances were increased, which are the decomposition products of aromatic amino acids, can increase the floral flavor of tobacco leaves. Cigarettes were fermented with three aroma producing strains, including *Bacillus*, *Saccharomyces cerevisiae*, and *Hanseniaspora*. sp. The aroma components of tobacco leaves after solid fermentation was increased to varying degrees compared with the control group. Ketones are the most important neutral aroma components in tobacco and smoke. The highest content of ketones was from the samples treated with *Hanseniaspora*. sp. (Hu et al., 2020). In this study, the nicotine content of *Hanseniaspora uvarum* J1 treated cigar filler leaves was increased after fermentation, and the ratio of nitrogen to nicotine, the ratio of chlorine to potassium were increased, compared with the control group with water. The volatile aroma substances in tobacco leaves fermented by *Hanseniaspora uvarum* J1 and *Hanseniaspora uvarum* J4 were higher than those of the two control groups, and the contents of ketones, aldehydes and neophytadiene were significantly increased, which was similar to the results of Hu et al. (2018).

Z. Bailii can produce alcohols, acids, esters, aldehydes, ketones and other flavor substances during Baijiu fermentation, which contributes to the flavor and quality of sauce-flavour Baijiu (Xu M. L et al., 2017). *Z. Bailii* is the dominant strain in the brewing process of sauce-flavour Baijiu. It can produce farnesol, 2-nonanol, 2-ethylhexanol, decanoic acid, lauric acid, octanoic acid and ethyl octanoate. The content of alcohols, lipids and ketones in Baijiu is increased by co-fermentation with *Bacillus licheniformis* (Zhuang et al., 2017). In this study, *Z. Bailii* R6 was inoculated to cigar filler leaves, and substances with higher content compared with other yeasts were β-Damascenone, 6-nonenal and 3-methylthiopropanal.

After yeast addition, the total amount of volatile substances in the cigar leaves was increased after fermentation. And cigar leaves fermented by *ZygoSaccharomyces rouxii* shows the highest content of esters. As one of the important flavor substances, easter is a class of volatile compounds with aromatic odors that act as a flavor enhancer and flavoring agent in tobacco (Ruan et al., 2006) and can improve the smoking quality of the tobacco. After fermentation of cigar filler leaves, the increase of some substances can reduce the irritation of tobacco leaves, such as solanone, geranyl acetone, dihydroactinidiolide, megalenone, neophytadiene, etc. The representative substances of aromatic compounds are mainly benzyl alcohol, phenylethanol, benzaldehyde, phenylacetaldehyde, etc., which can improve concentration of the smoke, and play a greater role in the aroma characteristics (Zhang P et al., 2021; Ma X. W et al., 2022).

The fermentation of tobacco bud by aroma producing yeast and Maillard reaction was studied by Xu Y et al. (2018). The results showed that there were 63 kinds of aroma substances, among which palmitic acid, tetradecanoic acid, palmitoleic acid, benzyl alcohol, 2-phenylethanol, fitone were in rich amount. 4,7,9-Megastigmatrin-3-one, dihydroactinidiolide, oleamide and 2-pentylfuran make outstanding contributions to tobacco aroma. Aroma producing

yeast were screened and applied to treat low grade tobacco leaves. Relative contents of aroma components were changed greatly, including phenylethanol, benzyl alcohol, 1-benzofuran, heptadecane, 4,7,9-Megastigmatrien-3-one, palmitic acid, geranyl acetone, geraniol and other alcohols and ketones. Furthermore, the content of aldehydes (pentanal, crotonaldehyde) in low grade tobacco leaves after microbial treatment was significantly reduced, which often caused smoking irritation (Chen, 2013).

PCA has been widely applied in the analysis of main aroma components in food industry (Wang et al., 2016; Xu Y et al., 2017). By PCA, it was concluded that acetic acid, acetoin, 1-octen-3-one, and 3-methylindole are the most important compounds that lead to the difference between mild cheddar cheese and other medium and mature cheddar cheese (Wang et al., 2021). Our analysis results showed that *Hanseniaspora uvarum* J1, *Hanseniaspora uvarum* J4, and *Pichia pastoris* P3 were clustered as one category. *Clavispora lusitaniae*, *Saccharomyces cerevisiae*, and *Cyberlindnera fabianii* were clustered as one category. Because the volatile compounds were formed by biological and chemical transformations, it was concluded that these typical aroma compounds, which made one category different from the other, were largely influenced by the fermentation with different yeasts.

5 Conclusion

Nine strains of aroma-producing yeast with good liquid fermentation were selected for artificial solid-state fermentation, and the aroma-causing components of the fermented cigar leaves were analyzed and compared. A total number of 52 aroma compounds contributed to the flavor of cigar in all treatment groups, among which β-damascenone, dihydrodamascenone, damascenone, and 2-hexenal contributed the most. By comparing the odor activity values, it was found that cigar leaves treated with *Clavispora lusitaniae*, *Cyberlindnera fabianii*, and *Saccharomycopsis fibuligera* had the highest floral odor activity values. The highest fruity odor activity values were found in cigar leaves treated with *Hanseniaspora uvarum* J1, *Hanseniaspora uvarum* J4 and *Pichia pastoris* P3. It was found that yeast addition could make the aroma richer and reduce the original impurities and irritation of the cigar leaves. With the rapid development of biological research, the application of microbiology in tobacco leaves fermentation is of great significance to improve the smoking quality of cigarettes.

Data availability statement

The raw data supporting the conclusions of this article will be made available by the authors, without undue reservation.

Author contributions

LY: Writing, Investigation. CH: Writing, Validation, Methodology. JD: Formal analysis. Tongtong Zhang: review and editing. JY: review and editing. CY: review and editing. XC: review and editing, Funding acquisition.

Funding

The authors are grateful for the support from the National Natural Science Foundation of China (No. 21978074 and 31871789), the China Scholarship Council (No. 2011842330 and 201508420257), key project of Hubei Provincial Department of Education (D20211404), and key Laboratory of Fermentation Engineering (Ministry of Education) (No. 202105FE04).

Conflict of interest

The authors declare that the research was conducted in the absence of any commercial or financial relationships that could be construed as a potential conflict of interest.

Publisher's note

Supplementary material

The Supplementary Material for this article can be found online at: https://www.frontiersin.org/articles/10.3389/fbioe.2022.1093755/full#supplementary-material

References

Chen, D. J. (2013). Effect of aroma-producing yeast on smoking quality of low grade tobacco leaves. *Guizhou Agr. Sci.* 41, 44–47. doi:10.3969/j.issn.1001-3601.2013.04.013

Chen, D., Li, M., Wang, R., Li, L. L., Li, X. N., and Shi, X. D. (2019). Progress of domestic ciger filler tobacco. *J. Yangzhou Univ. Agric. Life Sci. Ed.* 40, 83–90. doi:10.16872/j.cnki.1671-4652.2019.01.015

Dai, J., Li, K., Song, N., Yao, W. T., Xia, H. L., Yang, Q., et al. (2020). *Zygosaccharomyces rouxii*, an aromatic yeast isolated from chili sauce, is able to biosynthesize 2-Phenylethanol via the shikimate or ehrlich pathways. *Frontiers Microbiol.* 11, 597454–597465. doi:10.3389/fmicb.2020.597454

Deng, X. J., Huang, G. H., Tu, Q., Zhou, H. J., Li, Y. L., Shi, H. Y., et al. (2021). Evolution analysis of flavor-active compounds during artificial fermentation of Pu-erh tea. *Food Chem.* 357, 129783–129793. doi:10.1016/j.foodchem.2021.129783

Du, F., Yu, L. Q., Zhou, J. X., Xu, S. H., Huang, X. Z., and Zou, X. (2021). Isolation and identification of two aroma-producing microorganisms and their fermented liquid to increase the aroma of tobacco. *J. Mountain Agr. Biol.* 40, 14–21. doi:10.15958/j.cnki.sdnyswxb.2021.01.003

Escott, C., Del Fresno, J. M., Loira, I., Morata, A., and Suárez-Lepe, J. A. (2018). *Zygosaccharomyces rouxii*: Control strategies and applications in food and winemaking. *Fermentation* 4, 69–80. doi:10.3390/fermentation4030069

Fan, G. S., Liu, P. X., Chang, X., Yin, H., Cheng, L. J., Teng, C., et al. (2021). Isolation and identification of a high-yield ethyl caproate-producing yeast from daqu and optimization of its fermentation. *Front. Microbiol* 12, 663744–633758. doi:10.3389/fmicb.2021.663744

Gao, W. C., Xu, D. Q., Yuan, Y. B., Zhang, J., Wang, Z. M., Pan, W. J., et al. (2011). Relationship between chemicaI composition and smoking quaIity of tobacco in shenmei base. *Guizhou Agric. Sci.* 39, 52–55. doi:10.3969/j.issn.1001-3601.2011.05.015

Ge, Q., Yue, T. L., Yuan, Y. H., Wang, Z. L., Cai, R., Guo, C. F., et al. (2021). *A yeast strain QTX22 and its application in grape juice with high yield of aroma substances*. Chain. CN 112746029A.

Greger, V., and Schieberis, P. (2007). Characterization of the key aroma compounds in apricots (Prunus armeniaca) by application of the molecular sensory science concept. *J. Agric. Food Chem.* 55, 5221–5228. doi:10.1021/jf0705015

Guo, L. Q., Piao, Y. G., Zhu, C. Y., Li, H. L., Ma, D., Wang, J. T., et al. (2019). Screening and identification of aroma-producing yeast YG-4 and analysis of its aroma components. *J. Light Ind.* 34, 27–31. doi:10.3969/j.issn.2096-1553.2019.05.004

Han, R., Zhang, S., Yu, Q. Q., and Hou, L. H. (2020). Effect of addition of *Saccharomyces rouxii* at different time on high-salt dilute soy sauce. *China Condiment* 45, 1. doi:10.3969/j.issn.1000-9973.2020.09.001

He, W. J., Laaksonen, O., Tian, Y., Heinonen, M., Bitz, L., and Yang, B. R. (2022). Phenolic compound profiles in Finnish apple (Malus × domestica Borkh.) juices and ciders fermented with *Saccharomyces cerevisiae* and *Schizosaccharomyces pombe strains*. *Food Chem.* 373, 131437–131448. doi:10.1016/j.foodchem.2021.131437

Hu, T. F., Jiao, K. X., Huang, Q. M., Wu, S. X., Hou, N. N., Li, M., et al. (2020). Screening of solid- state fermentation aroma- producing strains. *Farm Prod. Process.*, 52–54+58. doi:10.16693/j.cnki.1671-9646(X).2020.04.046

Hu, K, K., Jin, G. J., Xu, Y. H., and Tao, Y. S. (2018). Wine aroma response to different participation of selected *Hanseniaspora uvarum* in mixed fermentation with *Saccharomyces cerevisiae*. *Food Res. Int.* 108, 119–127. doi:10.1016/j.foodres.2018.03.037

Hu, Z. Z., Jiang, Y., Long, Z. D., Liu, H., Zou, K. X., Su, Z., et al. (2018). Study on improvement of tobacco quality by fermentation technology with aroma producing yeast. *Food Machinery* 34, 200–204. doi:10.13652/j.issn.1003-5788.2018.11.040

Huang, W., Wang, X. D., Qiu, S. Y., Cao, W. T., Zhou, H. X., Luo, X. Y., et al. (2021). Preliminary analysis of quality and volatile components of sauce-flavor distiller's grains before and after fermentation. *China Brew.* 40, 97–101. doi:10.11882/j.issn.0254-5071.2021.02.019

Jairath, S., Sahota, P., and Pandove, G. (2012). Preparation of non-alcoholic naturally carbonated beverage using yeast isolate from whey beverage. *Czech J. Food Sci.* 30, 135–143. doi:10.17221/248/2010-cjfs

Jia, L. Y., Zhang, L., Li, H. Y., and Zhang, S. Z. (2021). The screening and identification of *Pichia kudriavzevi* FJZ by flavor-oriented technology and it's biological characteristics. *J. Chin. Inst. Food Sci. Technol.* 21, 276–282. doi:10.16429/j.1009-7848.2021.01.033

Lee, S. M., Jung, J. H., Seo, J. A., and Kim, Y. S. (2018). Bioformation of volatile and nonvolatile metabolites by *Saccharomycopsis fibuligera* KJJ81 cultivated under different conditions—Carbon sources and cultivation times. *Molecules* 23, 2762–2777. doi:10.3390/molecules23112762

Li, J. H., Tang, J., Liang, K., Zhu, L. J., and Long, J. (2015). Analysis of main chemical components in cigar leaf from Indonesia and China. *J. Zhejiang Agric. Sci.* 56, 1080–1083. doi:10.16178/j.issn.0528-9017.20150743

Li, J, J., Zhao, Y., Qin, Y., and Shi, H. (2020). Influence of microbiota and metabolites on the quality of tobacco during fermentation. *BMC Microbiol.* 20, 356–370. doi:10.1186/s12866-020-02035-8

Li, M, M., Wang, X, D., Luo, Z. B., Song, J. B., Qu, P., Hou, N. N., et al. (2020). Optimization of mixed microbial Solid-State fermentation and analysis of volatile aroma components in Low-Grade tobacco leaves. *J. Henan Agr. Sci.* 51, 171–180. doi:10.15933/j.cnki.1004-3268.2022.09.018

Lin, X., Hu, X. P., Wang, Q. K., and Li, C. F. (2020). Improved flavor profiles of red pitaya (*Hylocereus lemairei*) wine by controlling the inoculations of *Saccharomyces bayanus* and *Metschnikowia agaves* and the fermentation temperature. *J. Food Sci. Technol.* 57, 4469–4480. doi:10.1007/s13197-020-04484-5

Liu, J. H., Yang, C. Q., Fan, W., Xi, H., Dong, A. J., Wang, D, Z., et al. (2019). Screening of seven note character impact groups in cigarette smoke. *Tobacco. Sci. Technol.* 52, 44–50. doi:10.16135/j.issn1002-0861.2018.0135

Liu, L. L., Guo, W. L., Hu, X., Ding, S. S., Xiang, H., Ye, X. X., et al. (2022). The relationship between the color change of cigar tobacco leaf and the main nitrogen compounds and smoking quality during fermentation. *J. South. Agric.* 53, 497–504. doi:10.3969/j.issn.2095-1191.2022.02.023

Long, D. Z., Su, Z., Li, J. G., Xue, Y., Liu, Q. B., Ning, Z. X., et al. (2021). A mixed microbial fermentation technology for improving the quality of tobacco leaves in Baise, Guangxi. *J. Light Ind.* 36, 59–66. doi:10.12187/2021.05.008

Luo, J., Ao, Z. H., Wang, S. T., Qin, H., Cai, X. B., and Sun, X. (2015). The Correlations of fusel oil in different varieties of base nongxiang Baijiu (Liquor). *Liquor-Making Sci. Technol.* 1, 43–44+47. doi:10.13746/j.njkj.2014093

Ma, C. L, C. L., Wang, J. W., Chen, X., Li, X., Li, P., Li, P., et al. (2022). Investigation on the elimination of yeasty flavour in yeast extract by mixed culture of lactic acid bacteria and yeast. *Int. J. Food Sci. Technol.* 57, 1016–1025. doi:10.1111/ijfs.15463

Ma, C. Y, C. Y., Chen, S. L., Peng, C., Jin, B. F., Tao, H., and Zhao, Q. Z. (2022). Study on adding organic acids combined with fermentation by *Saccharomyces cerevisiae* to improve the quality of upper tobacco leaves. *J. Yunnan Agr. Univ. Nat. Sci.* 37, 630–637. doi:10.12101/j.issn.1004-390X(n).202201044

Ma, X. W, X. W., Shen, D. D., Mi, Q. L., Yin, P. P., Xu, L., Liu, X. R. T., et al. (2022). The influences of Chinese rice wine qu co-fermentation on the quality traits of discarded tobacco leaves K326. *Cereal Food Ind.* 29, 37–43+48.

Meng, Q., and Zhang, T. Z. (2021). An overview of Schwanniomyces occidentalis and its industrial application. *Feed Rev.* 4, 28–32. doi:10.3969/j.issn.1001-0084.2021.04.007

Minebois, R., Pérez-Torrado, R., and Querol, A. (2020). A time course metabolism comparison among *Saccharomyces cerevisiae, S. uvarum and S. kudriavzevii* species in wine fermentation. *Food Microbiol.* 90, 103484–103527. doi:10.1016/j.fm.2020.103484

Niu, C. T., Yang, L. N., Zheng, F. Y., Liu, C. F., Wang, J. J., Xu, X., et al. (2022). Systematic analysis of the aroma profiles produced by *Zygosaccharomyces rouxii* Y-8 in different environmental conditions and its contribution to doubanjiang (broad bean paste) fermentation with different salinity. *LWT - Food Sci. Technol.* 158, 113118–113127. doi:10.1016/j.lwt.2022.113118

Niu, H., Zhou, Z. Y., Bai, J. Y., Zhang, M. G., Sun, Z. W., and Chen, E. L. (2020). Research progress of cigar fermentation. *J. Hunan Univ. Arts Sci. Sci. Technol.* 32, 60–63+68. doi:10.3969/j.issn.1672

Peinado, R. A., Moreno, J., Bueno, J. E., Moreno, J. A., and Mauricio, J. C. (2004). Comparative study of aromatic compounds in two young white wines subjected to pre-fermentative cryomaceration. *Food Chem.* 84, 585–590. doi:10.1016/S0308-8146(03)00282-6

Pino, J. A., and Queris, O. (2011). Characterization of odor-active compounds in guava wine. *J. Agric. Food Chem.* 59, 4885–4890. doi:10.1021/jf2011112

Qin, M. J., Chen, S. L., Zhao, Q. Z., Peng, C., Jin, B. F., and Tao, H. (2020). Application of Lactobacillus plantarum in improving the quality of tabacco leaves from different regions. *Food Mach.* 36, 199–204+226. doi:10.13652/j.issn.1003-5788.2020.05.037

Ruan, X. W., Ren, P., Chen, W. F., and Hu, X. H. (2006). Study on Aroma-producing yeast of tobacco and its application in cigarette flavoring. *Biotechnology*, 57–59. doi:10.16519/j.cnki.1004-311x.2006.01.023

Shi, J., Xie, D. C., Qi, D. D., Peng, Q. H., Chen, Z. M., Schreiner, M., et al. (2019). Methyl jasmonate-induced changes of flavor profiles during the processing of green, Oolong, and Black Tea. *Frontiers Plant Sci.* 10, 781–793. doi:10.3389/fpls.2019.00781

Van Rijswijck, I. M. H., Van Mastrigt, O., Pijffers, G., Wolkers-Rooijackers, J. C. M., Abee, T., Zwietering, M. H., et al. (2019). Dynamic modelling of brewers' yeast and *Cyberlindnera fabianii* co-culture behaviour for steering fermentation performance. *Food Microbiol.* 83, 113–121. doi:10.1016/j.fm.2019.04.010

Van Rijswijck, I. M. H., Wolkers–Rooijackers, J. C. M., Abee, T., and Smid, E. J. (2017). Performance of non-conventional yeasts in co-culture with brewers' yeast for steering ethanol and aroma production. *Microbiol. Biotechnol.* 10, 1591–1602. doi:10.1111/1751-7915.12717

Wang, C., Lv, S. D., Wu, Y. S., Gao, X. M., Li, J. B., Zhang, W. R., et al. (2016). Oolong tea made from tea plants from different locations in Yunnan and Fujian, China showed similar aroma but different taste characteristics. *Springer Plus* 5, 576–590. doi:10.1186/s40064-016-2229-y

Wang, J. W., Yan, C. Y., Ma, C. L., Chang, X., Li, Z. J., Chen, X., et al. (2022). Study on the interaction between two *non-Saccharomyces* yeasts and *Aspergillus oryzae*. *Sci. Technol. Food Ind.*, 1–14. doi:10.13386/j.issn1002-0306.2022050018

Wang, J., Yang, Z. J., Wang, Y. D., Cao, Y. P., Wang, B., and Liu, Y. (2021). The key aroma compounds and sensory characteristics of commercial Cheddar cheeses. *J. Dairy Sci.* 104, 7555–7571. doi:10.3168/jds.2020-19992

Wang, L. Y., Dou, G. X., Guo, H. N., Zhang, Q. Q., Qin, X. J., Yu, W., et al. (2019). Volatile organic compounds of *Hanseniaspora uvarum* increase strawberry fruit flavor and defense during cold storage. *Food Sci. Nutr.* 7, 2625–2635. doi:10.1002/fsn3.1116

Wang, P. Z., Lai, M., Tao, T., Fu, P. P., Ren, W., Du, Y. G., et al. (2015). Relationships between main aroma constituents and aroma notes index of flue-cured tobacco leaves of different flavor styles. *J. Agric. Sci. Technol.* 17, 126–135. doi:10.13304/j.nykjdb.2015.011

Wang, X. D., Chen, M. Z., Ban, S. D., and Qiu, S. Y. (2017). Separation, identification and functional characterization of yeast strains from Moutai-flavor Daqu, a traditional Chinese liquor fermentation starter. *Food Sci.* 38, 51–57. doi:10.7506/spkx1002-6630-201704009

Wei, J. P., Zhang, Y. X., Wang, Y. W., Ju, H. M., Niu, C., Song, Z. H., et al. (2020). Assessment of chemical composition and sensorial properties of ciders fermented with different *non-Saccharomyces* yeasts in pure and mixed fermentations. *Int. J. Food. Microbiol.* 318, 108471–108482. doi:10.1016/j.ijfoodmicro.2019.108471

Wu, D. X., Wang, B., Lin, P., and Luo, D. S. (1999). Several technical problems restricting the development of hybrid cigarette products in China. *Tob. Sci. Technol.* 2, 31.

Wu, Y. H., Bai, J. K., Li, J. H., Shi, H. Z., Pu, T. W., and Zhang, S. J. (2019). Research advances on aroma substances and style cause of strong flavor type tobacco in Henan area. *Mod. Agric. Sci. Technol.* 24, 207–211. doi:10.3969/j.issn.1007-5739.2019.24.114

Xu, Q. Q., Li, S. T., Huang, S., and Mao, D. B. (2021). Review on tobacco-derived microorganisms and its application. *J. Light Ind.* 36, 42

Xu, C. P, C. P., Meng, D. D., Ran, P. P., Liu, S. H., Zheng, K., and Bai, J. F. (2018). Optimization of fermentation treatment condition of tobacco bud and preparation of tobacco flavor. *Hubei Agric. Sci.* 57, 100–103+111. doi:10.14088/j.cnki.issn0439-8114.2018.01.026

Xu, M. L, M. L., Yu, Y., Ramaswamy, H. S., and Zhu, S. M. (2017). Characterization of Chinese liquor aroma components during aging process and liquor age discrimination using gas chromatography combined with multivariable statistics. *Sci. Rep.* 7, 39671–39679. doi:10.1038/srep39671

Xu, Y, Y., Wu, Q., and Xu, Y. (2018). Effects of main functional strains on *Zygosaccharomyces bailii* in Chinese Maotai-flavor liquor fermentation. *Microbiol. China* 45, 42–53. doi:10.13344/j.microbiol.china.170190

Xu, Y, Y., Zhi, Y., Wu, Q., Du, R. B., and Xu, Y. (2017). *Zygosaccharomyces bailii* is a potential producer of various flavor compounds in Chinese Maotai-flavor liquor fermentation. *Front. Microbiol.* 8, 2609–2617. doi:10.3389/fmicb.2017.02609

Xue, J. B. (2016). *Microbial community in Chinese rice wine inoculated raw wheat Qu and analysis of enzyme and flavour produced by isolated microbes*. Jiangnan University. Jiang su.

Yan, H. Y., Huang, Q. M., Cai, X. H., Zhang, L. L., Xu, Z. Q., Ma, L., et al. (2021). Isolation and identification of aroma-producing strains and application of fermentation products in cigarette flavoring. *J. Light Ind.* 36, 47–54. doi:10.12187/2021.06.006

Yang, X. S., Zhao, F. Q., Yang, L., Li, J. N., and Zhu, X. (2022). Enhancement of the aroma in low-alcohol apple-blended pear wine mixed fermented with *Saccharomyces cerevisiae* and non-*Saccharomyces* yeasts. *LWT - Food Sci. Technol.* 155, 112994–113003. doi:10.1016/j.lwt.2021.112994

Yang, Y. R., Zhong, H. Y., Yang, T., Lan, C. H., and Zhu, H. (2021). Characterization of the key aroma compounds of a sweet rice alcoholic beverage fermented with *Saccharomycopsis fibuligera*. *J. Food Sci. Technol.* 58, 3752–3764. doi:10.1007/s13197-020-04833-4

Yang, C, C., Ding, G. S., Wan, L. X., Huang, X. M., Yang, S. G., Mu, L., et al. (2018). Relationships of main hemical components in tobacco blend of cigarette with its sensory quality and style. *Tob. Sci. Technol.* 51, 85–91. doi:10.16135/j.issn1002-0861.2017.0331

Yang, Y, Y., Peng, Q. R., Ou, M. Y., Wu, Y. X., and Fang, J. (2018). Research progress in tobacco fermentation. *J. Biosci. Med.* 6, 105–114. doi:10.4236/jbm.2018.66008

Yao, L., Li, D. Y., Huang, C. Y., Mao, Y. H., Wang, Z., Yu, J., et al. (2022). Screening of cellulase-producing bacteria and their effect on the chemical composition and aroma quality improvement of cigar wrapper leaves. *BioResources* 17, 1566–1590. doi:10.15376/biores.17.1.1566-1590

YC/T 159-2002 (2002). *Tobacco and tobacco products-Determination of water soluble sugars-Continuous flow method*. Beijing, China: Standardization Administration of China.

YC/T 160-2002 (2002). *Tobacco and tobacco products-Determination of total alkaloids-Continuous flow method*. Beijing, China: Standardization Administration of China.

YC/T 161-2002 (2002). *Tobacco and tobacco products-Determination of total nitrogen-Continuous flow method*. Beijing, China: Standardization Administration of China.

YC/T 162-2011 (2011). *Tobacco and tobacco products-Determination of chlorine-continuous flow method*. Beijing, China: Standardization Administration of China.

YC/T 217-2007 (2007). *Tobacco and tobacco products-Determination of potassium-continuous flow method*. Beijing, China: Standardization Administration of China.

Yeong, S. E., Lee, S. M., Kim, M., S, J. A., and Kim, Y. S. (2018). Comparison of volatile and non-volatile metabolites in rice wine fermented by Koji inoculated with *Saccharomycopsis fibuligera* and Aspergillus oryzae. *Food Res. Int.* 109, 596–605. doi:10.1016/j.foodres.2018.05.008

Yin, Q. Y., Xu, X. X., Zhang, Y. L., Li, M. J., Ren, Y. P., Lu, S., et al. (2018). Analysis in main chemical composition of tobacco leaves among different positions. *J. Hunan Univ. Arts Sci. Sci. Technol.* 30, 21.

Yun, L. (2016). Rich collect and application of solanone in tobacco. *Mod. Chem. Res.* 32–33. doi:10.3969/j.issn.1672-8114.2016.09.015

Zhang, A. D., Bei, Z. L., Zhang, X., and Zhang, H. (2015). Application of aroma-producing yeast in food industry. *J. Green Sci. Technol.*, 260–264. doi:10.16663/j.cnki.lskj.2015.11.115

Zhang, Q. Y., Luo, C., Li, D. L., and Cai, W. (2022). Research progress in curing and fermentation technology for cigar tobacco leaf production. *Acta Tabacaria Sin.* 26, 1–6. doi:10.16472/j.chinatobacco.2019.339

Zhang, L, L., Luo, Z. H., Yang, M. C., Li, S. G., Xin, Y. H., Cai, B., et al. (2021). Diversity of fermentation microbes and changes of hydrolytic enzyme activities of cigar leaf raw materials. *J. Agric. Sci. Technol.* 23, 171–180. doi:10.13304/j.nykjdb.2020.0534

Zhang, P, P., Li, W., Shi, C., Gao, J. M., Ren, J., Shen, G. M., et al. (2021). Screening and identification of a fungus with a sweet fruit aroma and its application in flavoured tobacco. *Chin. Tob. Sci.* 42, 95–101. doi:10.13496/j.issn.1007-5119.2021.05.015

Zhao, M. M., Zhao, Z. H., Dong, J. F., Ma, Y., Lu, J., and Wu, D. H. (2022). Selection and breeding of *Saccharomyces cerevisiae* for wolfberry wine and analysis of its flavor-producing properties. *Food Ferment. Ind.* 48, 155–161. doi:10.13995/j.cnki.11-1802/ts.030665

Zhou, L. J., Zheng, L., Liu, Y. Y., Wang, S. F., Duan, L. X., Chen, C. H., et al. (2010). Analysis and study of volatile components and its cigarette utilization from lichee endophyte. *Fine Chem.* 27, 1013–1015. doi:10.13550/j.jxhg.2010.10.016

Zhuang, X. J., Wu, Q., and Xu, Y. (2017). Physiological characteristics of *Zygosaccharomyces bailii* and its interaction with Bacillus licheniformis in Chinese Maotai-flavor liquor making. *Microbiol. China* 44, 251–262. doi:10.13344/j.microbiol.china.160174

frontiers | Frontiers in Bioengineering and Biotechnology

TYPE Original Research
PUBLISHED 05 January 2023
DOI 10.3389/fbioe.2022.1095323

OPEN ACCESS

EDITED BY
Xiaojun Shen,
Dalian Institute of Chemical Physics (CAS), China

REVIEWED BY
Jun Yuan,
Nanjing Agricultural University, China
Yueshu Gao,
Shanghai Jiao Tong University, China

*CORRESPONDENCE
Yun-Juan Sun,
Sunyunjuan@icifp.cn
Jian-Chun Jiang,
Jiangjianchun@icifp.cn

SPECIALTY SECTION
This article was submitted to Bioprocess Engineering, a section of the journal Frontiers in Bioengineering and Biotechnology

RECEIVED 11 November 2022
ACCEPTED 20 December 2022
PUBLISHED 05 January 2023

CITATION
Zhang N, Jiang Y, Sun Y-J, Jiang J-C and Tong Y-J (2023), Breeding of a thermostable xylanase-producing strain of *Myceliophthora thermophila* by atmospheric room temperature plasma (ARTP) mutagenesis.
Front. Bioeng. Biotechnol. 10:1095323.
doi: 10.3389/fbioe.2022.1095323

Breeding of a thermostable xylanase-producing strain of *Myceliophthora thermophila* by atmospheric room temperature plasma (ARTP) mutagenesis

Ning Zhang[1,2], Yue Jiang[1,2], Yun-Juan Sun[1,2]*, Jian-Chun Jiang[1,2]* and Ya-Juan Tong[1,2]

[1]Key Lab of Biomass Energy and Material, Key Lab of Chemical Engineering of Forest Products, National Engineering Research Center of Low-Carbon Processing and Utilization of Forest Biomass, Jiangsu Co-Innovation Center of Efficient Processing and Utilization of Forest Resource, National Forestry and Grassland Administration, Institute of Chemical Industry of Forest Products, Chinese Academy of Forestry (CAF), Nanjing, Jiangsu, China, [2]Co-Innovation Center of Efficient Processing and Utilization of Forest Resources, Nanjing Forestry University, Nanjing, China

Introduction: Hemicellulose is an important component in lignocellulose materials, which is second only to cellulose, accounting for 15%–35% of the dry weight of plants. In the current situation of energy shortage, making full use of lignocellulose materials to produce fuel ethanol has become an important way to solve the energy problem. Xylanase plays a crucial role in the utilization of hemicellulose. It is a necessary means to reduce the cost of hemicellulose utilization by improving the activity of xylanase. Moreover, most naturally xylanases are mesophilic enzymes, which limits their industrial application.

Methods: In this study, *Myceliophthora thermophila* was used to produce xylanases and a thermostable mutant *M* 2103 was obtained by atmospheric room temperature plasma (ARTP) mutagenesis. The research work started with exploring the effects of ARTP mutagenesis on the antioxidase system [superoxide dismutase (SOD), catalase (CAT), peroxidase (POD), polyphenol oxidase (PPO), and antioxidant capacity (AOC)] of *M. thermophile*, and found that superoxide dismutase activity increased by 221.13%, and polyphenol oxidase activity increased by 486.04% as compared with the original strain when the implantation time was 300 s. So as to determine the conditions for subsequent mutagenesis.

Results and Discussion: For the mutant *M* 2103, the reaction temperature for xylanase production remained stable in the range of 70°C–85°C. Its optimum temperature was 75°C, which was 15°C higher than that of the original strain. And its xylanase activity increased by 21.71% as compared with the original strain. *M* 2103 displayed a significantly higher relative xylanase activity than the original strain in the acidic (pH 4.0–7.0) range, and the xylanase activity was relatively stable in the pH range of 6.0–8.5. These results provide an alternative biocatalyst for the production of xylooligosaccharide, and a potential usage of ARTP in the mutagenesis of thermostable mutant.

KEYWORDS

xylanase, *Myceliophthora thermophila*, thermotolerant mutant, antioxidase, ARTP

Introduction

Xylan is one of the major components of the plant cell wall. It is the second richest, renewable resource in nature after cellulose (Biely et al., 2016). The structure of xylan is very complex. Its main chain is formed by the polymerization of D-xylopyranose through a β-1, 4-glycosidic bond, and the side chain carries an acetyl group, galactose, arabinose, glucuronic acid and other substituent groups. The degradation of xylan requires the joint action of an enzyme system composed of variety of enzymes. Among them, xylanase (EC 3.2.1.8) is the key enzyme, which hydrolyzes β-1, 4-glycosidic bonds from the interior of the main chain to produce a mass of xylo-oligosaccharides and a small amount of xylose (Csiszár et al., 2015; Xu et al., 2016). Xylanase has many applications, including baking (Wu et al., 2018), fruit juice processing (Bajaj and Manhas, 2012), brewing (Wang et al., 2016), feed processing, papermaking and biofuels (Wang et al., 2013; Le et al., 2018). In the current situation of energy shortage, xylanase plays an important role in the process of preparing fuel ethanol from lignocellulosic materials. It can promote the degradation of lignocellulosic materials, improve the production of monosaccharides glucose, and then improve the ethanol yield in the next step of fermentation. On the other side, xylanase is used to directly hydrolyze xylan into xylose, and then the xylose is used to produce fuel ethanol by the special bacteria or yeast.

Among the current pretreatment methods for fuel ethanol production, the acidic electrolytiyed water (Shen et al., 2014) (AEW) is pretreated at high temperature (above 140°C) and strong acid (pH 2.0–2.2). Since the pH value of high pressure hot water (above 200°C) is 5.6, liquid hot water (Saksit et al., 2021) (LHW) pretreatment is also a kind of dilute acid pretreatment. In addition, the simultaneous saccharification and fermentation (Suryawati et al., 2009) (SSF) of lignocellulosic materials to produce fuel ethanol is also carried out under the condition of high temperature (40°C–50°C) and weak acid (pH 4.0–5.0). Therefore, it is particularly important to screen and construct the high temperature and acid resistant xylanase.

Thermostable xylanase is a product of numerous thermophilic microorganisms, including *Thermomyces lanuginosus* (Wang et al., 2012), *Thermophilic sporotrichum* (Ghosh et al., 2019), *Paecilomyces thermophila* (Zhang et al., 2010), *Myceliophthera thermophila* (Dahiya and Singh, 2019), *Thermosaccharolyticum* (Jiang et al., 2017) and other thermophilic fungi, as well as thermophilic bacteria (Saleem et al., 2009) and thermophilic archaea (Knapik et al., 2019). It has been reported that bacteria can usually produce low molecular weight alkaline xylanase and high molecular weight acid xylanase, while fungi usually produce only high molecular weight acid xylanase. *M. thermophila* is classified as a thermophilic fungus that produces a variety of thermostable enzymes including cellulase (Fan et al., 2015), pectinase (Hollmann et al., 2016), esterase (Kool et al., 2014), phytase (Seema et al., 2020) and endoxylanase (Gool et al., 2012). Xylanase from *M. thermophila* has been purified and its properties have been studied (Boonrung et al., 2016). It has significant endonuclease β-1,4-xylanase activity without exoxylanase activity (Vafiadi et al., 2010) and it can be used to produce xylooligosaccharides.

At present, there are two primary strategies that can be employed to improve the thermal stability of xylanase. One involves directly screening thermophilic microbial strains from a high temperature environment, and the other involves modifying xylanase *via* genetic engineering technology. Since the end of the 20th century, numerous xylanase gene sequences have been cloned, and their enzymatic properties were determined. However, there are few microorganisms able to produce thermostable xylanase, and the obtained strains usually have low enzymatic activity and harsh culture conditions that make it challenging to meet the demands of industrial production (Zhang et al., 2014a; Ghosh et al., 2019). Therefore, it is imperative to use modern bioengineering technology to genetically improve xylanase-producing strains.

As a new physical mutation method, ARTP technology was developed by Xing Xinhui's team of Tsinghua University based on the radio-frequency atmospheric pressure glow discharge (RF APGD), which was a gentle RF APGD and can be applied in biotechnology research. The operation parameters, including RF power input, helium flow rate, plasma range and processing time, are controlled by programmable controller to make the mutagenesis of microorganisms more efficient and faster. Studies have shown that ARTP can react with biological macromolecules such as DNA (Wang et al., 2020) and protein in biological cells (Zhang et al., 2014b), resulting in lethal or sublethal effects. There are a large number of active oxides, active nitrides and neutral active particles in ARTP, including superoxide anion (O^{2-}), hydroxyl radical (-OH), ozone (O_3), hydroperoxide anion (HO^{2-}), singlet oxygen ($^1O_2$), alkoxy (RO^-), peroxynitroso anion ($ONOO^-$) and so on. Among them, active oxides and active nitrides are the key factors for ARTP to damage DNA double-stranded structure and induce DNA damage repair (DDR) response or SOS response. These active substances will act on the O-H bond, O-P bond and N-C glycosidic bond in the DNA chain structure to damage the molecular structure of DNA, and then make DNA single strand break. When the break sites on different single strands are close, DNA double strand break will occur. Therefore, ARTP can cause a wider range of gene mutations. Moreover, at atmospheric pressure, ARTP temperature can be controlled in the room temperature range, suitable for biological treatment (Zhang et al., 2014a). At present, ARTP has been successfully applied in mutation breeding of more than 40 kinds of microorganisms, including bacteria, fungi and microalgae, which can change the genetic material, protein structure, metabolic level and other factors of microorganisms to improve the production of microbial metabolites. And it has increasingly attracted attention in the field of microbial mutation breeding and biomedicine and has become a considerably active interdisciplinary research field (Li et al., 2015; Cheng et al., 2016; Gu et al., 2017).

The previous studies (Finkel, 2003) have shown that the activities of antioxidant enzymes in microorganisms was sensitive to the ion implantation, and the changes of antioxidant enzymes was also one of various internal factors, which influence their lives activity. So this work started with exploring the effects of ARTP mutagenesis on the antioxidase system of *M. thermophile*, and determined the best mutagenic conditions. For the mutant *M* 2103, its xylanase properties including the optimum pH and optimum reaction temperature were tested.

Materials and methods

Strains

M. thermophila was purchased from the China Center of Industrial Culture Collection (CICC), and numbers for CICC 2441. It was an aerobic microorganism and its culture temperature was 45°C.

Medium

Isolation medium (g/L): glucose 20.00, KH_2PO_4 3.00, $MgSO_4.7H_2O$ 1.50, $(NH_4)_2SO_4$ .75, wheat bran decoction (Cavalcante et al., 2008) (100 g of bran, 900 g of water, boiling for 20 min, filtered through four layers of gauze) 80.00, agar 15.00. Seed medium (g/L): malt extract 30.00, soya peptone 3.00. Xylanase fermentation medium (g/L): glucose 20.00, xylan .1, KH_2PO_4 3.00, $MgSO_4.7H_2O$ 1.50, $(NH_4)_2SO_4$ .75, wheat bran decoction 80.00. All mediums were sterilized at 121°C for 20 min.

Breeding of *M. thermophila via* ARTP

ARTP mutagenesis method

ARTP mutagenesis was performed with the ARTP Mutation Breeding System (Wuxi TMAXTREE Biotechnology Co. Ltd) (Wuxi, Jiangsu, China). *M. thermophila* CICC 2441 was used as the original strain which was purchased from the China Center of Industrial Culture Collection (CICC). Before mutagenesis, *M. thermophila* CICC 2441 was cultured in the isolation medium for 5 days at 45°C. The spores were scraped off with 10 ml of normal saline and transferred to a 150 ml conical flask. For dispersion of the spores, fifty glass beads (4 mm in diameter) were added to the flask, and the flask was shaken on the incubator at 250 revolutions per minute (rpm) for 15 min. The obtained spore suspension was then diluted to make the spore concentration within the range 10^6–10^8 cells/mL. Ten-microliters of spore suspension was painted on the surface of the metal slide for ARTP mutagenesis. The mutagenic treatment distance was 2 mm, the processing power was 120 W, the flow rate of Helium was 10 standard liter per minute (slm), and the implantation time was 0–300 s. Following implantation, the samples were placed in electropolished (EP) tubes containing 1 ml normal saline, and then oscillated for 1 min. Following this, the spore suspension was diluted and painted on the isolation mediums. The strains were incubated at 45°C in an attempt to grow single colonies. Colony number was counted and the survival rate curve was plotted. The survival rate was calculated according to the following Eq. 1:

$$Survival\ rate\ (\%) = \frac{N_C}{N_0} \times 100 \quad (1)$$

N_C —— Colony number of the coated plate after ARTP implantation across different time points.

N_0 —— Colony number of the coated plate without ARTP implantation across different time points.

Screening method for identification of thermostable mutants

Following implantation, dishes were incubated for 48 h at 65°C, and colonies that developed were defined as thermostable mutants. A single colony, characterized as displaying superior xylanase fermentation performance, was selected for the subsequent round of ARTP implantation and domestication at 70°C.

Crude enzyme extraction method

Fermentation broth was centrifuged at 10,000 rpm at 4°C for 15 min. The supernatant was composed of crude enzyme solution, which was stored at 4°C.

Genetic stability analysis

To assess the genetic stability of the thermostable mutant, the xylanase activities in the crude enzyme extraction of each generation were analyzed following five passages.

Xylanase activity determination method

Xylanase activity was determined by the Somogyi Nelson method (Leite et al., 2016). 10% diluted xylanase was added to 1% beech xylan solution, and the ensuing reaction was carried out at a predetermined temperature for 10 min. Following this, dinitrosalicylic acid (DNS) was added and the mixture was incubated in a boiling water bath for 10 min. The absorbance at 540 nm was determined with an enzyme labeling instrument.

Antioxidase activity determination method

Superoxide dismutase (SOD) activity was determined according to the xanthine oxidase method. Catalase (CAT) activity was determined by ammonium molybdate colorimetry. Peroxidase (POD) activity was determined according to the reaction of hydrogen peroxide catalyzed by POD. Polyphenol oxidase (PPO) activity was determined by the chromogenic reaction in which PPO catalyzed phenol to produce quinone. Antioxidant capacity (AOC) activity was determined according to the Fe^{3+} reduction reaction. All of the antioxidant enzyme activity determination kits were provided by the Nanjing Jiancheng Bioengineering Institute (Zhang et al., 2017).

Optimum pH and pH stability

One percent substrate (beech xylan) solutions were prepared with different pH values (200 mmol/L Na_2HPO_4 -100 mmol/L citric acid buffer (for pH 4–8 buffer) and 50 mmol/L glycine-NaOH buffer (for pH 8.5–10 buffer)). Relative enzyme activities were calculated under different pH conditions with a maximum enzyme activity of 100% according to the above enzyme activity determination method. Xylanase was diluted with buffer (pH 4.0–11.0), respectively, and placed at 4°C for 36 h. Relative xylanase activities were measured relative to an untreated xylanase activity of 100%.

Optimum reaction temperature and thermal stability

The substrate (beech xylan) solution was prepared with the optimal pH buffer, and the relative enzyme activities at different temperatures were measured according to the above enzyme

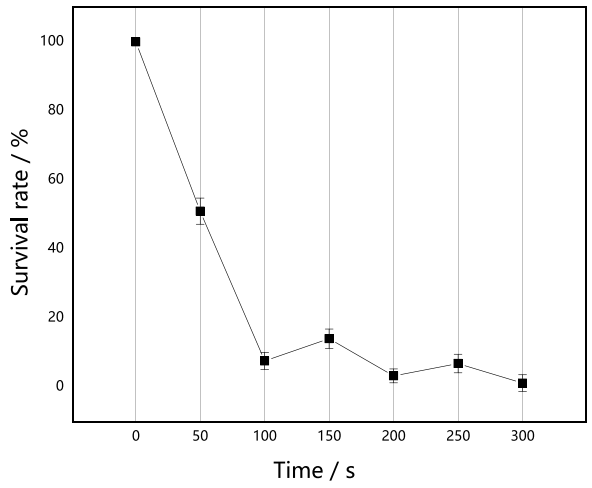

FIGURE 1
Effect of implantation time of ARTP on the survival rate of *M. thermophila*. Survival rate was the percentage of the number of colonies after implanted by ARTP to the none implanted. All experiments were carried out four times (biological duplicates and technical duplicates) and mean values presented with standard deviations.

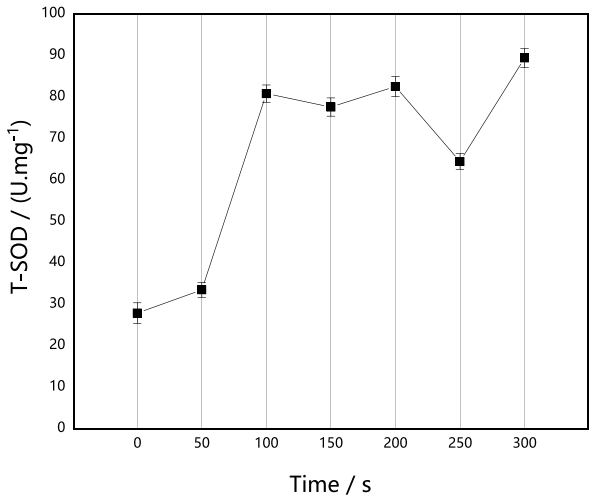

FIGURE 2
Effect of ARTP implantation time on T-SOD activities of *M. thermophila*. T-SOD activity was determined according to the xanthine oxidase method. Reagents preparation and results determination were carried out according to kit requirements. All experiments were carried out four times (biological duplicates and technical duplicates) and mean values presented with standard deviations.

activity determination method. Following this, the xylanases were placed in a 60–80°C water bath for 20 min, and then the enzyme activities were measured with the optimal pH buffer. The relative enzyme activities were calculated relative to an untreated xylanase activity of 100%.

Results and discussion

Mutagenic effect of ARTP on *M. thermophila*

Effect of ARTP mutagenic on the survival rate of *M. thermophila*

As shown in Figure 1, the survival rate curve of *M. thermophila* resembled a "double saddle" shape following ARTP implantation, with two recovery peaks at the implantation times of 150 s and 250 s. Similar results were observed with low-energy ion implantation of *Bacillus. coagulans* (Yu et al., 2012) and *Trichoderma reesei* (Zhang and Jiang, 2011). For these, the "double saddle" survival curve was observed and was characteristics of the interaction between plasma and organisms. It was reminiscent of the classical "saddle" curve (Zhu, 2006), and not attributable to the specific effect produced by ion implantation into a certain microorganism. The appearance of "double saddle type" survival rate curves suggests that the mechanism of interaction between implanted ARTP and the microorganisms is complex, and it suggests that the mechanism of ion implantation mutation is likely different from traditional mutation methods. Previous studies (Zhang and Yu, 2008) have shown that survival rate curves are a reflection of the external performance of biological effects caused by implanted ions, while changes associated with antioxidases activities are reflective of various internal factors. The studies presented here thus focus on investigating the effects of ARTP on antioxidases activities of *M. thermophila*.

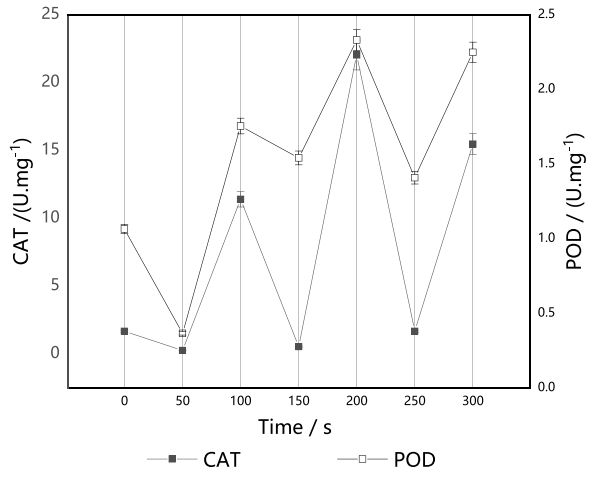

FIGURE 3
Effect of ARTP implantation time on CAT and POD activities of *M. thermophila*. CAT activity was determined by ammonium molybdate colorimetry. Reagents preparation and results determination were carried out according to kit requirements. All experiments were carried out four times (biological duplicates and technical duplicates) and mean values presented with standard deviations.

Effects of ARTP mutagenesis on the activity of antioxidases in *M. thermophila*

Effect of ARTP implantation on SOD activity in *M. thermophila*

SOD is an important member of the antioxidase system in organisms. It can catalyze the disproportionation of superoxide anion free radicals to

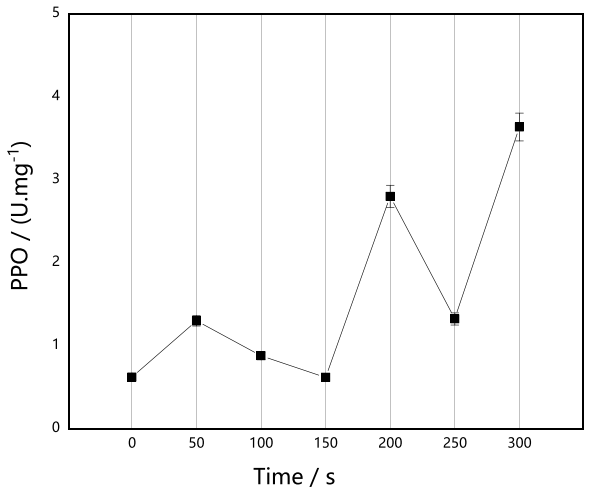

FIGURE 4
Effect of ARTP implantation time on PPO activities of *M. thermophila*. PPO activity was determined by the chromogenic reaction in which PPO catalyzed phenol to produce quinone. Reagents preparation and results determination were carried out according to kit requirements. All experiments were carried out four times (biological duplicates and technical duplicates) and mean values presented with standard deviations.

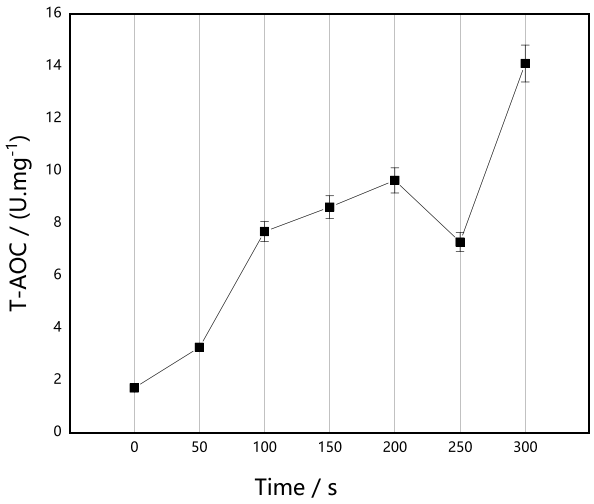

FIGURE 5
Effect of implantation time of ARTP on T-AOC of *M. thermophila*. T-AOC activity was determined according to the Fe^{3+} reduction reaction. Reagents preparation and results determination were carried out according to kit requirements. All experiments were carried out four times (biological duplicates and technical duplicates) and mean values presented with standard deviations.

produce oxygen and hydrogen peroxide, which play an important role in the balance of oxidation and antioxidation. It can resist and block the damage caused by oxygen free radicals to cells, repair damaged cells in time and recover the damage caused by oxygen free radicals. As shown in Figure 2, ARTP implantation induced the increase of SOD activity in *M. thermophila*. When the implantation time was 300 s, SOD activity increased by 221.13% as compared with the control, and it decreased under the conditions of 150 s and 250 s. In general, however, it was higher than that of untreated control strain. This may be attributed to active oxides, including the superoxide anion in ARTP, inducing *M. thermophila* to produce more SOD.

Effect of ARTP implantation on CAT and POD activities in *M. thermophila*

CAT and POD are enzymes that are able to scavenge H_2O_2 in cells. They play a key role in blocking free radical chain reactions. CAT directly catalyzes the decomposition of H_2O_2, while POD consumes H_2O_2 by catalyzing H_2O_2 to decompose other substrates. As shown in Figure 3, the activities of CAT and POD fluctuated with the increase of implantation time, contrary to the change in the trend of the survival curves. These results suggest that the increase of CAT and POD activities induced by ARTP are likely an adaptive response of *M. thermophila*. It is also likely a reason for the fluctuation in survival rate. In a short time (50 s), the implanted ions did not stimulate CAT and POD activities. With prolongation of the implantation time, CAT and POD activities were stimulated, and POD activity was higher than that of the untreated control strain. CAT activity was also much higher than that of the control strain at 100 s, 200 s and 300 s.

Effect of ARTP implantation on PPO activity in *M. thermophila*

PPO is an oxidase that contains copper, which is able to oxidize monophenols and bisphenols to produce quinones. Quinones are able to inhibit and kill pathogenic microorganisms and contribute to resistance to disease. As shown in Figure 4, PPO activities were also activated after ARTP implantation in *M. thermophila*. Following implantation *via* ARTP, PPO activities were higher than those of the untreated control strain. In addition, PPO activity increased by 486.04% when the

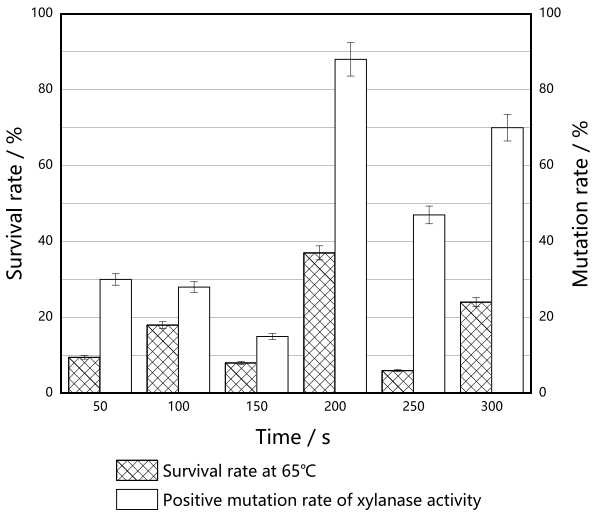

FIGURE 6
Effect of ARTP implantation time on the thermostable *of M. thermophila*. For *M. thermophila*, the optimum temperature was 60°C. On this basis, raised the culture temperature to 65°C. The effects of different ARTP implantation times on the survival rates of *M. thermophila were investigated*, and the xylanase activities of the surviving mutants were determined. The mutation rate was defined as the xylanase activity higher than 5% of the original strain. All experiments were carried out four times (biological duplicates and technical duplicates) and mean values presented with standard deviations.

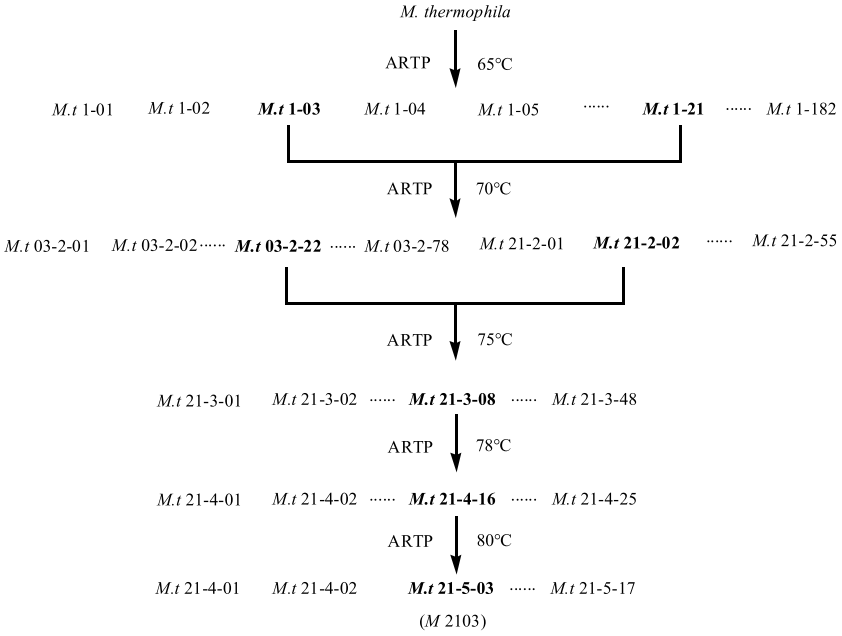

FIGURE 7
Screening spectrogram of the thermotolerant mutant *M* 2103. The first group number for the mutant strains was the serial number of the obtained mutant after the first mutagenesis by ARTP, the second group of number indicate the times of ARTP mutagenesis, and the third group of number was the serial number of the obtained mutant for this time of ARTP mutagenesis, and so on. The mutant strains with high xylanase activities after each mutagenesis were selected for the next mutation. After 5 mutagenesis, the culture temperature was gradually increased from 65°C to 80°C, and the thermostable mutant *M* 2013 with high activity of xylanase was finally obtained.

implantation time was 300 s. Further, the change in trend of PPO activity negatively correlated with the survival rate curve, suggesting that the change of PPO activity was also likely an adaptive response of *M. thermophila* under ARTP implantation.

Effect of ARTP implantation on AOC in *M. thermophila*

AOC is composed of various antioxidant substances and antioxidant enzymes, such as vitamin C, vitamin E and carotene, and it can be used to evaluate the antioxidant capacity of bioactive substances. As shown in Figure 5, with the prolongation of implantation time, AOC activities were higher than those of the untreated control strain, and they generally increased, with the exception of a decrease at 250 s. Based on the effect of ARTP on survival rate and antioxidase activities of *M. thermophila*, we speculated that the enhancement of AOC activity may protect *M. thermophila* from the damage of free radicals and ROS caused by ARTP. In addition, the enhancement of AOC activity of *M. thermophila* could effectively resist oxidative stress after heat stress, which would effectively improve the heat resistance of *M. thermophila*. Therefore, the studies presented herein investigated the effects of ARTP implantation on the thermostability of *M. thermophila*.

Effects of ARTP implantation on the thermostability of *M. thermophila*

Survival rates corresponding to each tested implantation time of ARTP are shown in Figure 6. The survival rate fluctuated with the increase in implantation time, and reached 37% at an implantation time of 200 s. Under this condition, the mutation rate associated with high production of xylase reached 88.0%. Antioxidase activities of *M. thermophila* also increased under this condition, suggesting that antioxidases play an important role in resisting cell death caused by heat stress. Subsequent mutagenesis screening experiments were also carried out at 200 s.

Screening of thermostable xylanase-Producing strains

Screening spectrogram of the thermotolerant mutant

The mutation screening process is shown in Figure 7. In this study, following five ARTP mutagenesis treatments and increasing the culture temperature from 65°C to 80°C, one mutant strain, *M. thermophila* -2103 (*M* 2103), was obtained. Its xylanase activity increased from 1457.30 U/g to 1861.38 U/g and the activity remained stable after five generations. Results are shown in Table1.

Xylanase Properties of *M* 2103 and the original strain *M.thermophila*

Optimum reaction pH and pH stability

The effects of different pH values on xylanase activities are shown in Figure 8A. The mutant *M* 2103 displayed significantly higher relative xylanase activities than the original strain in the acidic (pH 4.0–7.0) range. In the pH range of 6.0–8.5, the xylanase activities were relatively stable, with an optimal pH of 6.5. When the pH was higher than 8.5, xylanase activities began to decrease. When the pH was 10.0, the remaining xylanase activity was 82.63%. The fermentation crude enzyme solution of mutant *M* 2103 was diluted appropriately with buffer solution of pH 4.0–11.0,

TABLE 1 Stability of xylanase activity of *M* 2103 and *M.thermophila*.

Strains	Xylanase activities of every passages/(U·g^{-1})					
	*p*1	*p*2	*p*3	*p*4	*p*5	Averages
M 2103	1862.17	1860.62	1865.57	1860.25	1858.28	1861.38
M.thermophila	1433.87	1458.32	1438.06	1487.88	1468.37	1457.30

The stability experiments were carried out for five consecutive generations. All experiments were carried out four times (biological duplicates and technical duplicates) and mean values presented with standard deviations.

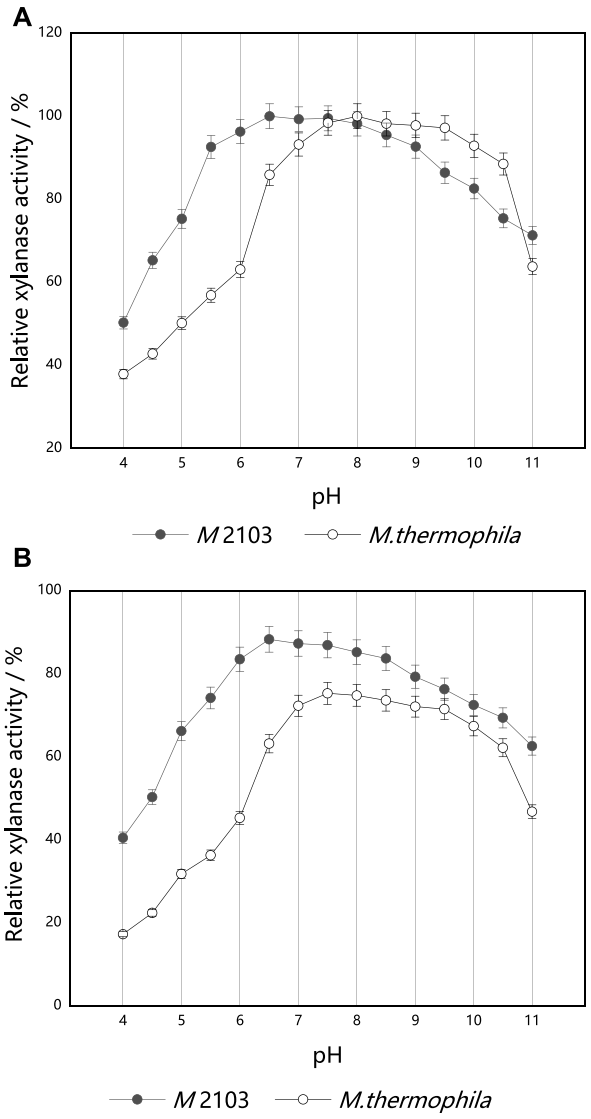

FIGURE 8
Optimum reaction pH and pH stability of xylanase from mutant *M* 2103 and *M. thermophila*; **(A)** The optimum pH of xylanase from mutant *M* 2103 and *M. thermophila*; **(B)** pH stability of xylanase from mutant *M* 2103 and *M. thermophila*. All experiments were carried out four times (biological duplicates and technical duplicates) and mean values presented with standard deviations.

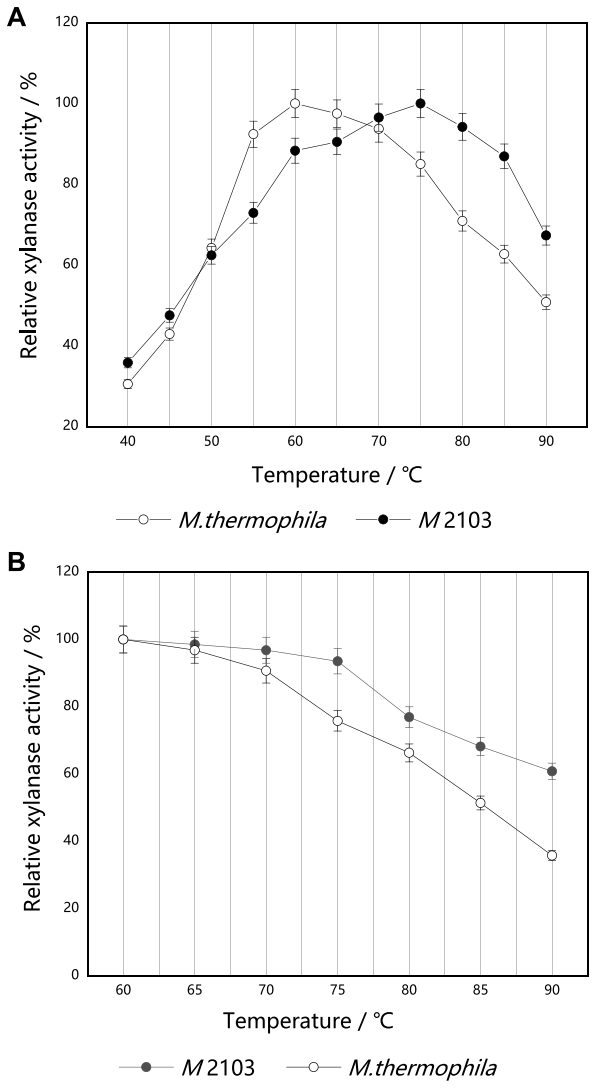

FIGURE 9
Optimum reaction temperature and thermal stability of xylanase from mutant *M* 2103 and *M. thermophila*. **(A)** The optimal reaction temperature of xylanase from mutant *M* 2103 and *M. thermophila* **(B)** Thermal stability of the xylanase from mutant *M* 2103 and *M. thermophila*. All experiments were carried out four times (biological duplicates and technical duplicates) and mean values presented with standard deviations.

respectively. After being placed at 4°C for 36 h, the xylanase activity of *M* 2103 was compared with that of the untreated crude enzyme solution (Figure 8B). At a pH of 11.0, the xylanase activity of *M* 2103 could be maintained above 65%. Compared with the alkaline condition, the xylanase activity of *M* 2103 in the acidic range was higher and relatively stable.

Optimum reaction temperature and temperature stability

The optimum reaction temperature of the original strain *M. thermophila* and mutant *M* 2103 were measured under their corresponding optimum reaction pH (7.5 and 6.5) (Figure 9A). The optimum reaction temperature for *M. thermophila* to produce xylanase was determined to be 60°C, and the optimum reaction temperature for *M* 2103 was 75°C (it remained stable in the range of 70°C–85°C). Its residual xylanase activity was 67% at 90°C. The thermal stability of the original strain *M. thermophila* and mutant *M* 2103 were then determined. As shown in Figure 9B, the residual activity of *M. thermophila* decreased to about 90% after being treated at 70°C for 20 min, while the activity of *M* 2103 was almost unchanged. After being treated at 90°C for 20 min, the residual activity of *M. thermophila* decreased to about 35%, while *M* 2103 had activity of around 60%. These results suggest that the thermal stability of *M* 2103 was superior to that of *M. thermophila*.

Conclusion

A thermostable mutant, *M* 2103, with high xylanase productivity was obtained by ARTP mutagenesis. Compared with the original strain, the xylanase activity increased by 21.71%, the optimum temperature reached 75°C from 60°C, and its reaction temperature for xylanase production remained stable in the range of 70°C–85°C. *M* 2103 displayed a significantly higher relative xylanase activity than the original strain in the acidic (pH 4.0–7.0) range, and the xylanase activity was relatively stable in the pH range of 6.0–8.5. In addition, ARTP mutagenesis can stimulate antioxidase system (SOD, CAT, POD, PPO, and AOC) activities in *M. thermophile*, which SOD activity increased by 221.13%, and PPO activity increased by 486.04%. These studies showed that the increasing of antioxidase system (SOD, CAT, POD, PPO, and AOC) activities in *M. thermophile* reduced the oxidative damage caused by ARTP, and helped to improve its heat resistance.

In this study, ARTP was used to mutate *M. thermophile*, and improved its thermostable and xylanase activity. This method has the advantages of low jet temperature, uniform plasma production, no vacuum device, simple operation, low cost, and obvious interaction with biological macromolecules and cells compared with traditional mutagenesis methods. This study provide an alternative biocatalyst for the production of xylooligosaccharide, and it has potential application in the fuel ethanol industry.

Data availability statement

The raw data supporting the conclusion of this article will be made available by the authors, without undue reservation.

Author contributions

J-CJ and Y-JS conceived and designed the experiments. NZ performed the experiments. YJ, and Y-JT analyzed the data. NZ wrote the manuscript. J-CJ, NZ, and Y-JS revised and approved the final version of the manuscript. All authors contributed to the article and approved the submitted version.

Funding

This work is supported financially by the National Key Research and Development Program of China (2019YFB1503803).

Conflict of interest

The authors declare that the research was conducted in the absence of any commercial or financial relationships that could be construed as a potential conflict of interest.

Publisher's note

All claims expressed in this article are solely those of the authors and do not necessarily represent those of their affiliated organizations, or those of the publisher, the editors and the reviewers. Any product that may be evaluated in this article, or claim that may be made by its manufacturer, is not guaranteed or endorsed by the publisher.

References

Bajaj, B. K., and Manhas, K. (2012). Production and characterization of xylanase from bacillus licheniformis p11(c) with potential for fruit juice and bakery industry. *Biocatal. Agric. Biotechnol.* 1 (4), 330–337. doi:10.1016/j.bcab.2012.07.003

Biely, P., Singh, S., and Puchart, V. (2016). Towards enzymatic breakdown of complex plant xylan structures: State of the art. *Biotechnol. Adances* 34, 1260–1274. doi:10.1016/j.biotechadv.2016.09.001

Boonrung, S., Katekaew, S., Mongkolthanaruk, W., Aimi, T., and Boonlue, S. (2016). Purification and characterization of low molecular weight extreme alkaline xylanase from the thermophilic fungus *Myceliophthora thermophila* BF1-7. *Mycoscience* 57, 408–416. doi:10.1016/j.myc.2016.07.003

Cavalcante, R. S., Lima, H., Pinto, G. A., Gava, C. A., and Rodrigues, S. (2008). Effect of moisture on *Trichoderma* conidia production on corn and wheat bran by solid State fermentation. *Food Bioprocess Technol.* 1, 100–104. doi:10.1007/s11947-007-0034-x

Cheng, G., Xu, J. Z., Xia, X. H., Guo, Y. F., Xu, K., Su, C. S., et al. (2016). Breeding L-arginine-producing strains by a novel mutagenesis method: Atmospheric and room temperature plasma (ARTP). *Prep. Biochem.* 46, 509–516. doi:10.1080/10826068.2015.1084634

Csiszár, E., Urbánszki., K., and Szakács, G. (2015). Biotreatment of desized cotton fabric by commercial cellulase and xylanase enzymes. *J. Mol. Catal. B Enzym.* 11, 1065–1072. doi:10.1016/S1381-1177(00)00149-1

Dahiya, S., and Singh, B. (2019). Enhanced endoxylanase production by *Myceliophthora thermophila* with applicability in saccharification of agricultural substrates. *Biotech.* 9 (6), 214–223. doi:10.1007/s13205-019-1750-4

Fan, Y., Gong, Y., Gang, L., Zhao, S., and Wang, J. (2015). Enhancing cellulase production in thermophilic fungus *Myceliophthora thermophila* ATCC42464 by RNA interference of cre1 gene expression. *J. Microbiol. Biotechnol.* 25 (7), 1101–1107. doi:10.4014/jmb.1501.01049

Finkel, T. (2003). Oxidant signals and oxidative stress. *Curr. Opin. Cell Biol.* 15, 247–254. doi:10.1016/S0955-0674(03)00002-4

Ghosh, A., Sutradhar, S., and Baishya, D. (2019). Delineating thermophilic xylanase from Bacillus licheniformis DM5 towards its potential application in xylooligosaccharides production. *World J. Microbiol. Biotechnol.* 35 (2), 34–51. doi:10.1007/s11274-019-2605-1

Gool, M. P., Muiswinkel, G. C. J., Sandra, W. A. H., Henk, A. S., Arkady, P. S., and Gruppen, H. (2012). Two GH10 endo-xylanases from *Myceliophthora thermophila*

C1 with and without cellulose binding module act differently towards soluble and insoluble xylans. *Bioresour. Technol.* 119 (1), 123–132. doi:10.1016/j.biortech.2012.05.117

Gu, C., Wang, G., Mai, S., Wu, P., Wu, J., Wang, G., et al. (2017). ARTP mutation and genome shuffling of ABE fermentation symbiotic system for improvement of butanol production. *Appl. Microbiol. Biotechnol.* 101 (5), 2189–2199. doi:10.1007/s00253-017-8093-z

Hollmann, F., Gumulya, Y., Tölle, C., Liese, A., and Thum, O. (2016). Evaluation of the laccase from *Myceliophthora thermophila* as industrial biocatalyst for polymerization reactions. *Macromolecules* 41 (22), 8520–8524. doi:10.1021/ma801763t

Jiang, Y. J., Liu, J., Dong, W. L., Zhang, W. M., Fang, Y., Ma, J., et al. (2017). The draft genome sequence of thermophilic *Thermoanaerobacterium thermosaccharolyticum* M5 capable of directly producing butanol from hemicellulose. *Curr. Microbiol. Int. J.* 75 (5), 620–623. doi:10.1007/s00284-017-1425-5

Knapik, K., Becerra, M., and González-Siso, M. I. (2019). Microbial diversity analysis and screening for novel xylanase enzymes from the sediment of the Lobios Hot Spring in Spain. *Sci. Rep.* 9 (1), 11195. doi:10.1038/s41598-019-47637-z

Kool, M. M., Schols, H. A., Wagenknecht, M., Hinz, S., and Gruppen, H. (2014). Characterization of an acetyl esterase from *Myceliophthora thermophila* C1 able to deacetylate xanthan. *Carbohydr. Polym.* 111 (20), 222–229. doi:10.1016/j.carbpol.2014.04.064

Le, C., Du, J. L., Zhan, Y. J., Li, J. A., Zuo, R. R., and Shen, T. (2018). Consolidated bioprocessing for cellulosic ethanol conversion by cellulase–xylanase cell-surfaced yeast consortium. *Prep. Biochem. Biotechnol.* 48, 1–9. doi:10.1080/10826068.2018.1487846

Leite, P., Salgado, J. M., Venancio, A., Domínguez, J. M., and Belo, I. (2016). Ultrasounds pretreatment of olive pomace to improve xylanase and cellulase production by solid-state fermentation. *Bioresour. Technol.* 214, 737–746. doi:10.1016/j.biortech.2016.05.028

Li, X. Y., Liu, R. J., Li, J., Chang, M., Wang, X. G., Jin, Q., et al. (2015). Enhanced arachidonic acid production from mortierella alpina combining atmospheric and room temperature plasma (ARTP) and diethyl sulfate treatments. *Bioresour. Technol.* 177, 134–140. doi:10.1016/j.biortech.2014.11.051

Saksit, I., Torpong, K., Punjarat, K., Navadol, L., Verawat, C., Kowit, S., et al. (2021). Optimization of sugar recovery from pineapple leaves by acid-catalyzed liquid hot water pretreatment for bioethanol production. *Energy Rep.* 7, 6945–6954. doi:10.1016/j.egyr.2021.10.076

Saleem, M., Tabassum, M. R., Yasmin, R., and Imran, M. (2009). Potential of xylanase from thermophilic *Bacillus sp.* XTR-10 in biobleaching of wood kraft pulp. *Int. Biodeterior. Biodegrad.* 63 (8), 1119–1124. doi:10.1016/j.ibiod.2009.09.009

Seema, D., Anil, K., and Bijender, S. (2020). Enhanced endoxylanase production by *Myceliophthora thermophila* using rice straw and its synergism with phytase in improving nutrition. *Bioresour. Technol.* 119 (1), 123–132. doi:10.1016/j.procbio.2020.04.032

Shen, Z., Jin, C., Pei, H., Shi, J., Li, L., and Sun, J. (2014). Pretreatment of corn stover with acidic electrolyzed water and fecl3 leads to enhanced enzymatic hydrolysis. *Cellulose* 21 (5), 3383–3394. doi:10.1007/s10570-014-0353-9

Suryawati, L., Wilkins, M. R., Bellmer, D. D., Huhnke, R. L., Maness, N. O., and Banat, I. M. (2009). Effect of hydrothermolysis process conditions on pretreated switchgrass composition and ethanol yield by ssf with kluyveromyces marxianus imb4. *Process Biochem.* 44 (5), 540–545. doi:10.1016/j.procbio.2009.01.011

Vafiadi, C., Christakopoulos, P., and Topakas, E. (2010). Purification, characterization and mass spectrometric identification of two thermophilic xylanases from sporotrichum thermophile. *Process Biochem.* 45 (3), 419–424. doi:10.1016/j.procbio.2009.10.009

Wang, L., Zhao, H., He, D., Wu, Y., Jin, L., Li, G., et al. (2020). Insights into the molecular-level effects of atmospheric and room-temperature plasma on mononucleotides and single-stranded homo- and hetero-oligonucleotides. *Sci. Rep.* 10, 14298. doi:10.1038/S41598-020-71152-1

Wang, W., Yang, G. H., and Chen, J. C. (2013). Effect of xylanase treatment on papermaking properties of poplar high yield pulp. *Adv. Mater. Res.* 690-693, 1322–1326. doi:10.4028/www.scientific.net/AMR.690-693.1322

Wang, X., Luo, H., Yu, W., Ma, R., You, S., Liu, W., et al. (2016). A thermostable *Gloeophyllum trabeum* xylanase with potential for the brewing industry. *Food Chem.* 199, 516–523. doi:10.1016/j.foodchem.2015.12.028

Wang, Y., Zheng, F., Huang, H., Zhang, H., Yao, B., Xiong, H., et al. (2012). Improved thermal performance of thermomyces lanuginosus GH11 xylanase by engineering of an N-terminal disulfide bridge. *Bioresour. Technol.* 112, 275–279. doi:10.1016/j.biortech.2012.02.092

Wu, J. J., Qiu, C., Ren, Y., Yan, R., Ye, X., and Wang, G. (2018). Novel salt-tolerant xylanase from a mangrove-isolated fungus *Phoma* sp. MF13 and its application in Chinese steamed bread. *Acs Omega* 3 (4), 3708–3716. doi:10.1021/acsomega.8b00345

Xu, Y., Wu, J., Zheng, K., and Wu, D. (2016). A xylanase from streptomyces sp. fa1: Heterologous expression, characterization, and its application in Chinese steamed bread. *J. Industrial Micrology Biotechnol.* 43 (5), 663–670. doi:10.1007/s10295-016-1736-8

Yu, L., Sun, Y., Xie, F., Liu, Y., and An, X. (2012). Compare of N ion implanation effects on *Bacillus coagulans* by use of two kinds of ion sourses. *J. Radiat. Res. Radiat. Process.* 25 (5), 261–265. doi:10.1360/yc-007-1173

Zhang, M., Jiang, Z., Yang, S., Hua, C., and Li, L. (2010). Cloning and expression of a *Paecilomyces thermophila* xylanase gene in *E. coli* and characterization of the recombinant xylanase. *Bioresour. Technol.* 101 (2), 688–695. doi:10.1016/j.biortech.2009.08.055

Zhang, N., and Jiang, J. C. (2011). Mutagenic effects of cellulase-producing strain by N^+ implantation. *J. Basic Sci. Eng.* 19 (6), 900–905. doi:10.3969/j.issn.1005-0930.2011.06.006

Zhang, N., and Yu, L. (2008). Effect of N+ ion implantation on antioxidase activity in Blakeslea trispora. *Radiat. Phys. Chem.* 77, 1046–1049. doi:10.1016/j.radphyschem.2008.04.004

Zhang, S., He, Y., Yu, H., Dong, Z., and Danilo, R. (2014a). Seven n-terminal residues of a thermophilic xylanase are sufficient to confer hyperthermostability on its mesophilic counterpart. *Plos One* 9 (1), e87632. doi:10.1371/journal.pone.0087632

Zhang, T., Gao, Y., Gong, Y., Hui, Z., Xie, P., Guan, S., et al. (2017). Tang-Luo-ning improves mitochondrial antioxidase activity in dorsal root ganglia of diabetic rats: A proteomics study. *BioMed Res. Int.* 2017, 1–7. doi:10.1155/2017/8176089

Zhang, X., Zhang, X. F., Li, H. P., Wang, L. Y., Zhang, C., Xing, X. H., et al. (2014b). Atmospheric and room temperature plasma (ARTP) as a new powerful mutagenesis tool. *Appl. Microbiol. Biotechnol.* 98 (12), 5387–5396. doi:10.1007/s00253-014-5755-y

Zhu, C. (2006). Study on mutagenic effects of avilamycin-producing strain induced by N^+ ion implantation. *Nucl. Tech.* 29 (8), 609–613. doi:10.1007/s11676-006-0017-1

frontiers | Frontiers in Bioengineering and Biotechnology

TYPE Original Research
PUBLISHED 06 January 2023
DOI 10.3389/fbioe.2022.1099118

OPEN ACCESS

EDITED BY
Xiaojun Shen,
Dalian Institute of Chemical Physics (CAS), China

REVIEWED BY
Yingfeng Zuo,
Central South University Forestry and Technology, China
Yanhua Zhang,
Northeast Forestry University, China

*CORRESPONDENCE
Xiahong He,
hexiahong@hotmail.com
Can Liu,
liucan@swfu.edu.cn

SPECIALTY SECTION
This article was submitted to Bioprocess Engineering, a section of the journal Frontiers in Bioengineering and Biotechnology

RECEIVED 15 November 2022
ACCEPTED 20 December 2022
PUBLISHED 06 January 2023

CITATION
Qin S, Sun H, Wan X, Wu Y, Lin X, Kan H, Hou D, Zheng Z, He X and Liu C (2023), Carboxymethylcellulose reinforced starch films and rapid detection of spoiled beverages.
Front. Bioeng. Biotechnol. 10:1099118.
doi: 10.3389/fbioe.2022.1099118

Carboxymethylcellulose reinforced starch films and rapid detection of spoiled beverages

Shijiao Qin[1], Hao Sun[1], Xiaoli Wan[1,2], Yujia Wu[1], Xu Lin[1], Huan Kan[1], Defa Hou[1], Zhifeng Zheng[3], Xiahong He[1]* and Can Liu[1]*

[1]National Joint Engineering Research Center for Highly-Efficient Utilization Technology of Forestry Resources, Southwest Forestry University, Kunming, China, [2]Lincang Academy of Forestry Sciences, Lincang, China, [3]College of Energy, Xiamen University, Xiamen, China

The integrity of the packaging of a liquid foodstuff makes it difficult to detect spoilage. Therefore, it is important to develop a sensitive, fast and real-time material for liquid food detection. CMC, as lignocellulose derivatives and starch are widely used in the food industry. In this study, starch films with pH-responsive properties are successfully prepared from full-component starch and corn amylopectin (CA) by adding CMC. The effects of CMC on the mechanical properties, morphology characteristics, physical and chemical structures, stability and pH responsiveness of the starch films are analyzed. The starch/CMC-1.0 g composite films display good electrical conductivity and reduce the resistance of the composite film by two orders of magnitude. The composite films have pH response ability; in the simulation of orange juice spoilage experiment, the CA/CMC composite film has a more sensitive current response and was more suitable for the application to liquid food quality detection. Additionally, the starch/CMC composite films have potential applications for rapid detection and real-time monitoring of the safety of liquid food.

KEYWORDS

sodium carboxymethyl cellulose, starch films, pH-responsive, rapid detection, food quality

1 Introduction

With the rapid development of society and the economy, the issue of food safety is deeply rooted in people's minds and is closely related to food safety, the social economy and human life (Serge et al., 2022; Jin and Zhong, 2022; He et al., 2017; Seto and Ramankutty, 2016; Liu and Hou, 2022). Food safety problems are mainly caused by the following factors: pesticide residues (Tang et al., 2021), bacterial species and biotoxins (Yesim et al., 2022), heavy metal contamination (Xiang et al., 2021), and illegal use of food additives (Wang et al., 2021). Existing food quality testing techniques mainly adopt spectroscopic methods, such as near-infrared spectroscopy (Wafula et al., 2022) and Raman spectroscopy (Simona et al., 2021). Although these techniques are highly accurate, the detection instruments are expensive, the detection time is long, and experienced personnel is required. However, these techniques cannot achieve the goal of rapid detection and real-time monitoring. The main techniques commonly used for rapid food detection are physicochemical, enzymatic (Martins et al., 2022), and immunoassay analyses (Xu et al., 2018) and bioluminescence (Ibarra et al., 2021). Although the above analytical techniques are applied for rapid detection, they have drawbacks, such as environmental impacts on the detection results and false positives. These techniques cannot simultaneously achieve rapid, simple, real-time and accurate food safety detection. Therefore, it is vital to develop rapid and sensitive food detection methods and functional materials.

10.3389/fbioe.2022.1099118

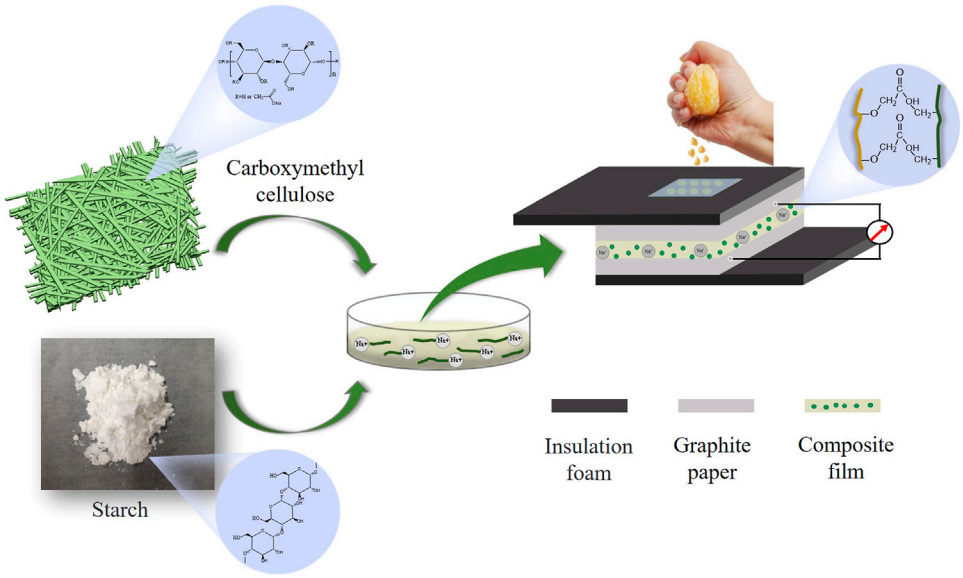

FIGURE 1
Schematic diagram of the structure of the starch/CMC composite film applied to the rapid detection of juice quality.

Since juice is a liquid food, the integrity of the packaging makes it difficult to detect changes in its quality. Hence, it is important to develop a fast, real-time liquid detection material for this characteristic. The mechanical properties and stability of a film as a detection material are of great significance. Accordingly, researchers often develop film materials equipped with the desired functional properties by doping with other substances. Sodium carboxymethyl cellulose (CMC), a derivative of cellulose, has the characteristics of polyelectrolyte properties and good biocompatibility; the films prepared with CMC and starch have functional properties. The thermoplastic starch/CMC composite film prepared by Behera et al. (2022) showed that the mechanical properties and barrier properties of the original starch film were improved with the doping of CMC. Wi et al. (2011) demonstrated that intermolecular interactions between CMC and tapioca starch improve the tensile strength of the composite films, reduce their water solubility, and increase hydrophobicity using Fourier transform infrared (FTIR) spectroscopy. Aytunga et al. (2017) discovered that CMC/starch composite films have better transparency and water vapor barrier properties after adding glycerol. Rungsiri et al. (2019) prepared composite films from self-extracted CMC with rice starch and found that the doping of CMC not only improved the mechanical properties of the films but also enhanced the thermal stability. Lan et al. (2020) added Lactococcus lactis to CMC/starch composite films to give them antibacterial properties, and the optimal mechanical properties were obtained when the mass ratio of CMC to starch was 1:1. Jiang et al. (2020) reported an intelligent responsive packaging material for food quality monitoring. Based on the sensitivity of anthocyanins to pH and volatile ammonia from protein decomposition, the CMC/starch composite film with anthocyanins added can be used to assess the environmental pH and the freshness of fish. The above literature demonstrates that CMC enhances the mechanical properties and stability of starch films and provides a stable carrier for the pH responsiveness of the film.

In foodstuffs, the deterioration of liquid food mostly changes its pH. Therefore, the special pH signal allows the development of intelligent indicator materials suitable for real-time detection. Zhang et al. (2020) developed a label for detecting food spoilage based on the pH sensitivity of the indicator label. The label not only detects the pH of liquid food but also monitors in real time the level of biogenic amines produced by decaying food. In food detection technology, the combination of electrochemical parameters enables the visualization of food spoilage. Deng et al. (2013) proposed a graphene-modified acetylene black paste electrode for the detection of BPA concentration in food with a wide detection range and high sensitivity. Kundan et al. (2019) produced an ultra-sensitive optofluidic-surface enhanced Raman scattering (SERS) sensor for the detection of the food additive rhodamine 6G and the response to trace amounts of chlorobenzene compounds in drinking water. They revealed that smart electrical signal responsive materials have a wide range of applications and show extremely broad use in food quality detection. The growing demand for fruit and vegetable beverages has made the issue of food safety in this field crucial. Thus, the search for a simple, rapid, highly sensitive, real-time method for monitoring fruit and vegetable beverages is imperative.

Considering the above issues, we prepared a composite functional film with starch as the matrix, glycerol as the plasticizer and CMC as the additive; these films provide rapid feedback of electrical signals to the pH of the juice (Figure 1). The mechanical properties, stability performance, and pH response characteristics of the composite film were examined. Based on the above analytical methods, we compared the effect of CMC on starch films with different amylopectin contents and discussed the influence trend of CMC addition on the functions of the composite films. It was found that the composite films responded sensitively to the pH of fruit juice. This study provides a new method for rapid, sensitive and non-destructive monitoring of the quality of liquid

foodstuffs; this has highly promising applications in the field of rapid, non-destructive and real-time online monitoring of food quality.

2 Materials and methods

2.1 Experimental materials

Corn starch (CS), corn amylopectin (CA) and sodium carboxymethyl cellulose (CMC) were purchased from Shanghai Aladdin Biochemical Technology Co., AR grade. Ultrapure water was used throughout this study.

2.2 Preparation process

The starch/CMC composite films were prepared by solution casting. For preparation of 4% starch aqueous solution, 4 g starch and 1.4 g of glycerol (35% of the starch), which was used as a plasticizer, were weighed (mixing time 30 min). This was then transferred to a 90°C water bath and stirred until completely gelatinized (gelatinized for 1 h). Different masses (0, .2, .4, .6, .8, and 1.0 g) of CMC were added to the starch solution and stirred again. The homogeneous film solution (34 g) was poured onto Petri dishes (d = 15 cm) and baked in a constant temperature oven at 45°C for 6 h. The composite film was labeled as starch/CMC-x, where x indicated the amount of CMC added to the starch film. For example, CS/CMC-1.0 means that the amount of CMC doped in the starch film is 1.0 g.

2.3 Characterization and analysis

The component interaction of the sample was analyzed using FTIR (model: is 50 FT-IR). The attenuated total reflectance (ATR) method was used to scan from 4,000 to 600 cm^{-1} with a total of 32 scans per sample. X-ray photoelectron spectroscopy (XPS) was performed using a Thermo Scientific K-Alpha X-ray photoelectron spectrometer. X-ray diffraction (XRD) was performed using a Japanese Neo-D/MAX220 instrument with Cu as the target material; the relative crystallinity was analyzed using Jade six software. The morphology and microstructure of the films were examined by scanning electron microscopy (SEM). An intelligent electronic tensile testing machine (model: XLM (PC)) was used to measure the mechanical properties. Thermogravimetry-differential thermogravimetry (TG-DTG) was performed using a TGA209 F3. The samples (3–5 mg) were weighed, and the heating rate was 20 K/min under a N_2-atmosphere. A contact angle tester (JC 2000D3R) was used to evaluate the surface hydrophilicity of the films; the impedance and chronoamperometry of the film samples were measured using a CHI760E electrochemical workstation. The test frequency was .1 Hz–1 MHz, and the amplitude was .01 V. Layer-by-layer self-assembled devices were produced for electrochemical testing. The device was prepared by coating graphite paper and the innermost film sample with an insulating collodion. The measure liquid was added dropwise to the surface of the film; the steady current and resistance were determined using chronoamperometry and electrochemical impedance spectroscopy (EIS).

3 Results and discussion

3.1 Mechanical properties of different composite films

Figures 2A, B shows the stress–strain curve of the starch/CMC composite film; Figures 2C, D shows the tensile strength and elongation at break of the starch/CMC composite films. As shown in Figure 2, the tensile strength of the CS starch film was higher than that of the CA film, and the elongation at break of the CS films was greater than that of the CA films; this indicated that the mechanical properties of the CS film were better than those of the CA film. Both CMC composite films using 1.0 g of CMC had a large tensile strength of over 40 MPa. The elongation at break of the CS/CMC composite film was 6.55%, which was slightly higher than that of the pure CS film; this indicated that the film was correspondingly soft at this point. As more CMC was added, the tensile strength of both film materials increased. Similarly, the yield strength also showed a direct relationship with the amount of CMC added; as more CMC was added, the yield strength increased. The tensile strength of the CS film increased to 180.7% in comparison to the control group due to the addition of CMC, and the tensile strength of the CA film increased to 281.9%. The addition of CMC significantly increased the yield strength of the film and resulted in a considerable increase in the service life of the composite films. The analysis showed that new hydrogen bonds were formed between the -OH of starch and the -COO- of CMC; this enhanced the interaction between starch and CMC (Ou et al., 2021; Ma et al., 2020), improved the tensile strength of the starch/CMC composite films, and resulted in enhanced rigidity properties. In general, CMC improved the mechanical properties of starch films.

3.2 Morphological characterization

To understand the changes occurring inside the starch film, the cross-section was quenched at low temperature, and the morphology was observed (Figure 3). As shown in Figure 3, the smoothness of both unmodified starch films was good, while the cross-sectional roughness of the starch/CMC composite films increased as the amount of CMC added increased. Compared with the unmodified CS film, the ductile fracture traces of the CS/CMC composite film gradually became evident (Figures 3C,D). The CA/CMC composite films were rougher and more uneven than the pure CA film. With the addition of CMC, the cross-section of the CA/CMC composite film appeared uneven, and the incompatibility of the two phases was observed in Figure 3F; this was more apparent in the CA film with large amounts of CMC added, and caking caused by massive agglomeration appeared (Figure 3H). The analysis showed that CS was compatible with CMC, which enhanced the film. Figure 2 shows that CMC had a better enhancement effect on the CS film, while the enhancement effect on the CA film was not as good as that on the CS film. This was due to the agglomeration of the molecular chains produced by the large amount of CMC, which caused the cross-sectional quenched morphology of the CA/CMC-1.0 composite film to be uneven; lumpy agglomerates were observed The formation of new chemical bonds between CMC and amylopectin increased the crystalline zone; the distribution of the crystalline zone was heterogeneous, and the amylopectin and CMC were not

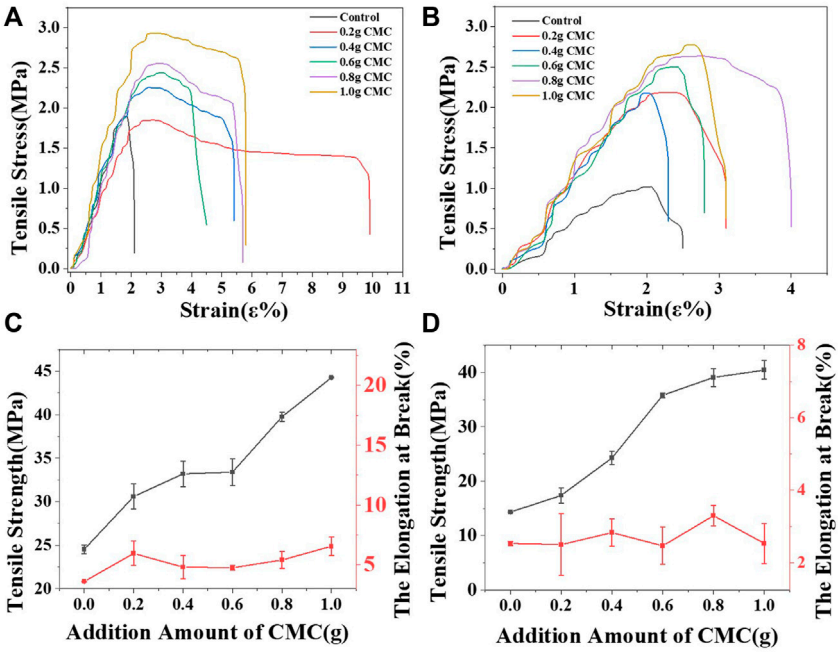

FIGURE 2
Stress-strain curve and the tensile strength with the elongation at break of the starch/CMC composite films. **(A, C)**: CS/CMC composite films; **(B, D)**: CA/CMC composite films.

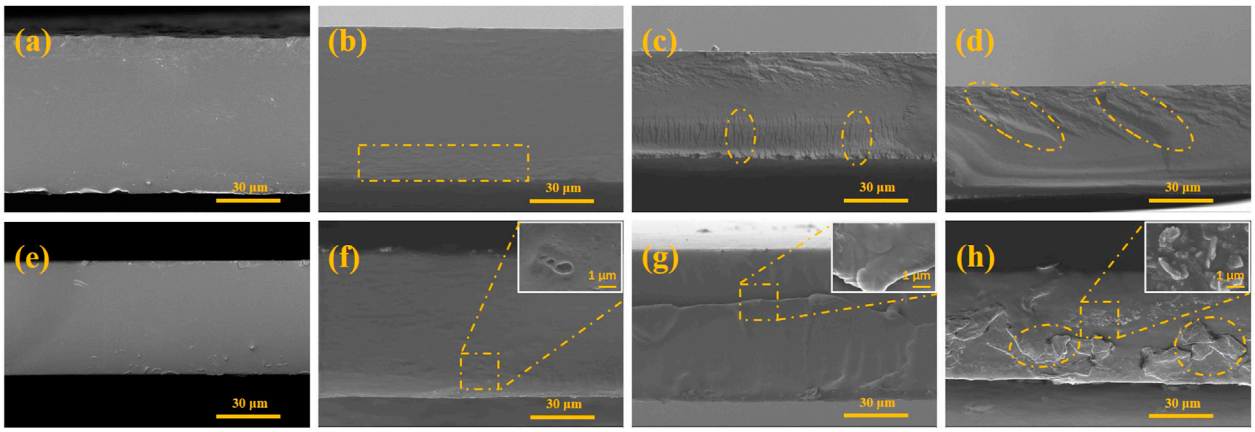

FIGURE 3
SEM of the starch/CMC composite films. **(A)**: pure CS film; **(B)**: CS/CMC-0.2 composite film; **(C)**: CS/CMC-0.6 composite film; **(D)**: CS/CMC-1.0 composite film; **(E)**: pure CA film; **(F)**: CA/CMC-0.2 composite film; **(G)**: CA/CMC-0.6 composite film; **(H)**: CA/CMC-1.0 composite film.

homogeneous in both phases, thus explaining its weaker mechanical properties than the CS/CMC composite film.

3.3 XRD structure analysis

To understand the crystallinity of the starch film material, XRD analysis was performed (Figure 4). As shown in Figure 4, the starch film material showed crystalline peaks at 18°and 20°, and the CA film material showed crystalline peaks at 18.6°, 20.0° and 21.8°. Figure 4 shows that the addition of CMC changed the degree of crystallinity and layer spacing of the starch film. Based on the fitted crystallinity, the crystallinity was less than 10%, and the trend was that as CMC was added, the crystallinity of the starch film material increased; this indicated that the starch film material mainly exhibited amorphous characteristics and that the starch and CMC were largely converted to the amorphous state (Dolas et al., 2020). CMC reduced the layer spacing of the starch composite films.

The analysis showed that after the pasting and cooling process, the starch chains were recrystallized, and the molecular chains of starch were transformed from ordered to disordered to ordered structures. During cooling, the movement of the starch molecular chain was

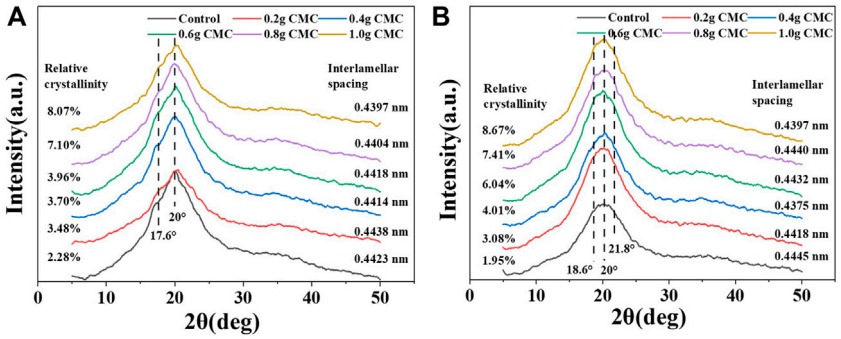

FIGURE 4
XRD curves of the starch/CMC composite films. **(A)**: CS/CMC composite films; **(B)**: CA/CMC composite films.

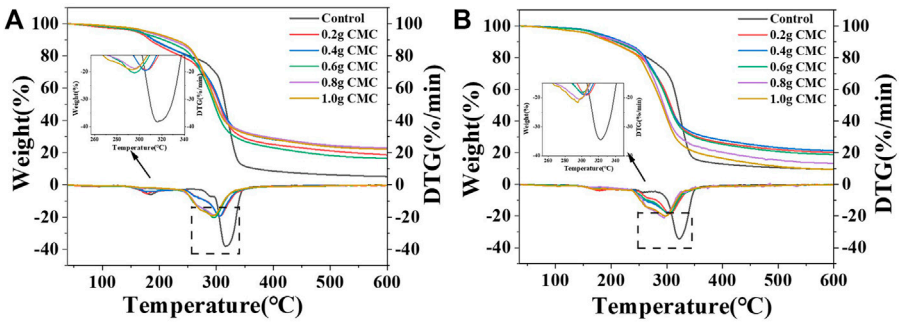

FIGURE 5
TG and DTG curves of the starch/CMC composite film. **(A)**: CS/CMC composite films; **(B)**: CA/CMC composite films.

inhibited, and the system was in a thermodynamic non-equilibrium state. The restricted molecular chains rearranged due to hydrogen bonds, and then the starch recrystallized. The amylose in CS formed double helical enrichment regions, which eventually formed intermolecular hydrogen bonds. In contrast, recrystallization of amylopectin occurred between the branches, with more crystalline regions forming within the molecule. CMC is a chain structure and possesses sites for hydrogen bond formation with starch. At low dosages, the reaction sites between CMC and starch were limited and resulted in little difference in the crystalline regions; the CS and CA films were essentially the same. At a high dosage of CMC, the amylopectin, due to its branching structure, had more hydrogen bond formation sites that tightly attached to the CMC and caused its crystallinity to be greater than that of the CS film. The crystallinity of the two film materials were related the elevated mechanical properties of the starch films in Figure 2; these elevated properties were caused by the increased crystallinity.

3.4 Stability analysis

The influence of CMC on the thermal stability of the two types of films were studied using TG analysis. The TG and DTG curves of the CS/CMC and CA/CMC composite films are shown in Figure 5. As shown in Figure 5; Table 1, with the addition of CMC, the temperature of the maximum weight loss rate of the two composite films decreased. The residual carbon rates of starch/CMC composite films were higher than those of the pure starch films. The analysis showed that the doping of CMC caused the composite films to degrade at a lower temperature because CMC introduced carboxyl groups on the starch surface and reduced the maximum weight loss rate temperature of the CS film (Meng et al., 2016). From the analysis of residual carbon rate data, the addition of CMC improved the thermal stability of the film; the addition of CMC increased the intermolecular bonding force of films and increased the number of hydrogen bonds formed between

TABLE 1 Temperature of maximum weight loss rate (Tp) and residual carbon rate (RC) of the starch composite films.

Sample	Tp (°C)	RC (%)	Sample	Tp (°C)	RC (%)
CS	315.5	5.2	CA	322.9	9.5
CS/CMC-0.2 g	307.1	18.5	CA/CMC-0.2 g	306.2	20.1
CS/CMC-0.4 g	305.0	22.5	CA/CMC-0.4 g	304.1	21.3
CS/CMC-0.6 g	296.1	16.3	CA/CMC-0.6 g	301.1	18.8
CS/CMC-0.8 g	295.2	22.9	CA/CMC-0.8 g	298.2	13.3
CS/CMC-1.0 g	293.2	22.1	CA/CMC-1.0 g	295.2	9.5

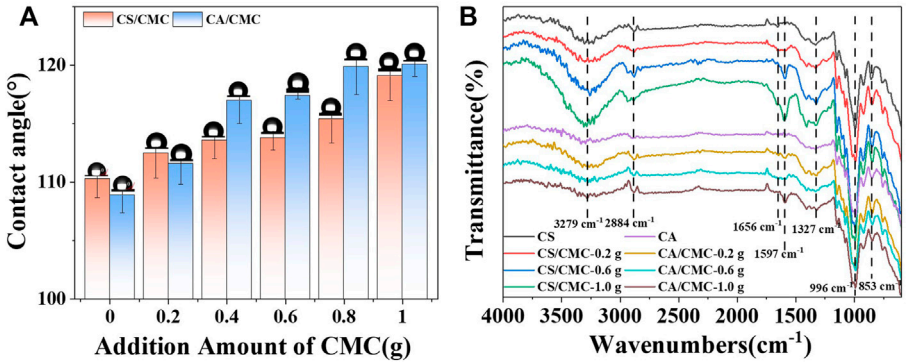

FIGURE 6
The contact angle and FTIR spectra of the starch/CMC composite films. **(A)**: the contact angle; **(B)**: FTIR spectra.

the two macromolecular chains of starch and CMC, which hindered the movement of the macromolecular chains and inhibited the pyrolysis of the films (Siqueira et al., 2010). This result was also verified by the increase in crystallinity. All residual carbon rates of the CS films increased due to the addition of CMC. The CA films started to decrease above the addition of .6 g probably because the crystallinity of the film material did not show a linear increase with the addition of CMC. Compared with a small amount of CMC, the excessive CMC did not significantly improve the crystallinity of the films. It was predicted that there was more CMC free in the amorphous zone of the film material, which caused the decrease in the residual carbon rate.

To investigate the effect of CMC on the hydrophobicity of the CS and CA composite film surfaces, water contact angle tests were conducted. As shown in Figure 6A, the water contact angle was 110.3° for the pure CS film material and 108.1° for the pure CA film. With the addition of CMC, the water contact angle of both starch films increased. When the addition amount reached 1.0 g, the water contact angle of the CS/CMC composite film was 119.1°; this was an 8% increase compared to the pure CS film and a 10.3% increase for the CA/CMC composite film. When the amount of CMC added was more than .4 g, the water contact angle of the CS/CMC composite film was greater than that of the CA/CMC composite film. The analysis showed that when CMC was added in small amounts, the hydrophilicity of their composite films was better because of the higher content of amylopectin in the films (Zhang et al., 2019). When more CMC was added, new hydrogen bonds were formed between CMC and CA, resulting in a tighter structure of the composite film and the destruction of the original structure; this exposed the hydrophobic groups to the surface of the film and caused the surface to be less hydrophilic (Jose et al., 2012). The reaction of starch molecules with CMC introduced carboxylic acid derivative ester groups, which increased hydrophobicity to some extent. This was consistent with the data on the crystallinity of starch.

3.5 Chemical structure analysis

To understand the effect of CMC on the starch film groups, FTIR analysis was performed (Figure 6B). The FTIR spectrum of the starch/CMC composite film showed a stretching vibration peak of -OH at 3,279 cm^{-1}, a stretching vibration peak of -CH_2 at 2,884 cm^{-1}, and an absorption peak of C=O at 1,656 cm^{-1}. The absorption peaks at 1,597 cm^{-1} and 1,327 cm^{-1} corresponded to carboxylate asymmetric stretching (Mansur et al., 2017), the absorption peak at 996 cm^{-1} corresponded to the stretching vibration absorption peak of C-O in C-O-C, and the absorption peak near 853 cm^{-1} corresponded to the C-C skeleton vibration (Zhang et al., 2013). In pure CS films, the peaks at 1,660–1725 cm^{-1} were attributed to the -OH bending vibration of water in the starch molecule (Ren et al., 2017; Shim et al., 2020). Analysis of Figure 6B shows that the two composite film materials exhibited new peaks at 1,656 cm^{-1} and 1,597 cm^{-1}, indicating the formation of hydrogen bonds between CMC and starch and the introduction of carboxylic acid group derivatives (ester groups).

X-ray photoelectron spectroscopy (XPS) analysis was conducted to obtain more in-depth information on the chemical bond composition and surface elements (Figure 7; Table 2). As shown in Figure 7, the total XPS spectra of the starch film samples all showed two distinct characteristic peaks: 286.6 eV (C1s) and 532.8 eV (O1s). The high-resolution XPS spectra of the C1s of the four film samples were further divided into three peaks. The first peak at 284.2 eV was attributed to C-C (sp^3 carbon), while the other two peaks were located at binding energies of 286.0 eV and 287.6 eV and belonged to C-O and C=O in the starch and CMC chains, respectively (Yu and Kwak, 2012). Table 2 shows that the starch/CMC composite films showed an overall enhancement in the percentage of C elements compared to the pure starch films. When CMC was added, the proportion of C-C bonds in the composite films increased, while the proportion of C-O and C=O bonds decreased. In particular, the C=O bond in the CS/CMC-1.0 composite films accounted for only 11.66% of the C1s.

3.6 Electrochemical performance analysis

To assess the electrical conductivity of the films, the starch/CMC composite films were tested using electrochemical impedance spectroscopy (EIS). As shown in Figure 8, the EIS curve consists of a semicircle and a sloping straight line. The semicircular arc region in the plot is the charge transfer impedance due to gain and loss of electrons, while the straight line region is related to the solid-state diffusion process (Xu J. et al., 2018; Xu T. et al., 2018). The diameter of the semicircular arc region represents the magnitude of the resistance of the material. The circuit-fitted EIS profiles showed that the

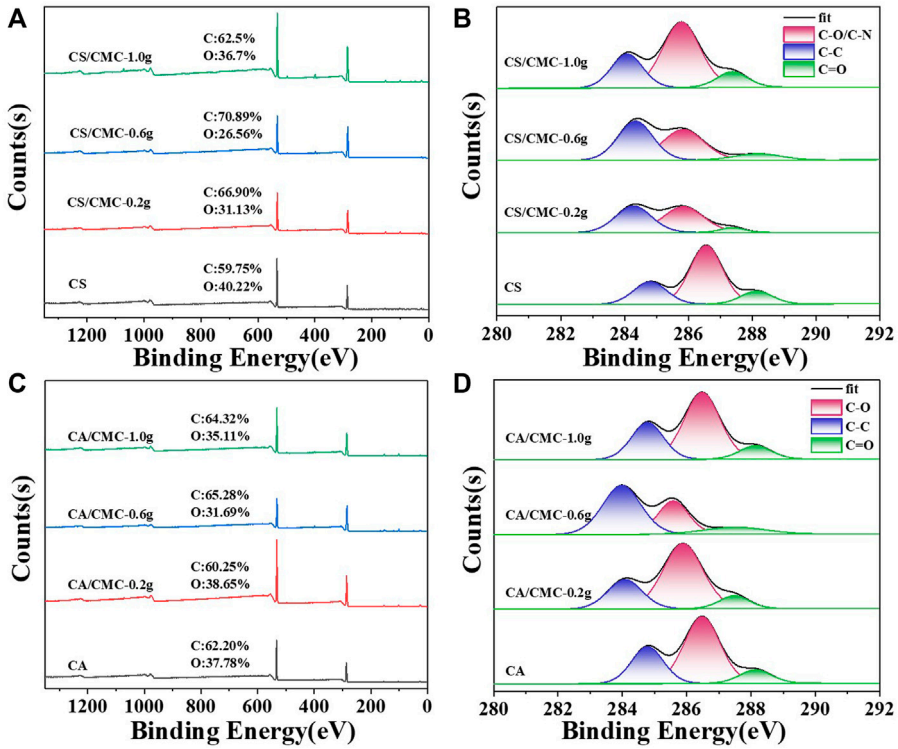

FIGURE 7
XPS survey spectra and high-resolution C1s spectra of the starch/CMC composite films. **(A, C)**: CS/CMC composite films; **(B, D)**: CA/CMC composite films.

TABLE 2 Element proportion and chemical bond for the starch/CMC composite films.

Sample	C1s (%)	O1s (%)	C-C (%)	C-O (%)	C=C (%)
CS	59.75	40.22	24.84	62.11	13.04
CS/CMC-0.2	66.90	31.13	49.50	45.05	5.45
CS/CMC-0.6	70.89	26.56	43.19	46.95	9.86
CS/CMC-1.0	62.50	36.79	26.99	61.35	11.66
CA	62.20	37.78	34.08	55.87	10.06
CA/CMC-0.2	60.25	38.65	25.81	64.52	9.68
CA/CMC-0.6	65.28	31.69	56.81	30.68	12.50
CA/CMC-1.0	64.32	35.11	40.39	49.26	10.34

resistance values of the starch films all decreased as the CMC doping increased, and the resistances of the CA/CMC composite films varied more. The resistance of the pure CS film was 5.41E+7 Ω, while the resistance of the CS/CMC-1.0 composite film was only 1.36E+6 Ω. The resistance of the composite film decreased by one order of magnitude. When the doping amount of CMC was 1.0 g in the CA film, the resistance of the composite film decreased by two orders of magnitude compared to that of the pure CA film. This was due to the presence of Na^+ in the CMC structure, which bound electrostatically to the oxygen-containing functional groups in the starch structure; this built a conductive pathway, provided a charge transfer pathway, and resulted in a better conductivity of the CMC-doped composite films (Cyriac et al., 2022).

To more clearly show the conductivity gap of the films, the current strength of the films in different pH solutions were tested. A sensitive pH response of the composite films was found in the variation of the currents. Different pH solutions caused a change in the current of the film, thus characterizing the acidity of the solution by the current.

As shown in Figure 9, the stable currents for pure CS films ranged from 2.88E-6 A to 9.76E-6 A at different pH values and 4.99E-6 A to 1.32E-5 A for CS/CMC-1.0 composite films; the stable currents for pure CA films ranged from 2.15E-6 A to 9.25E-6 A at different pH values and CA/CMC-1.0 composite films ranged from 5.27E-6 A to 1.29E-5 A. The four films showed the same trend of currents in different pH environments.

The analysis shown in Figure 9 revealed that the doping of CMC improved the electrical conductivity of the starch films; the current of the starch/CMC composite films was higher than that of the pure starch films in different environments due to the Na^+ in the CMC structure. Under acidic or alkaline conditions, the number of ions that could be freed in the film was positively correlated with the current, and thus, the conductivity was better (Tao et al., 2021). According to the CA test results, the doping of CMC effectively reduced the resistance of the starch films and thus enhanced their electrical conductivity; this was consistent with the EIS result described above. The EIS and current of the starch films were comprehensively analyzed, and the current values of the CA films were greater than those of the CS films;

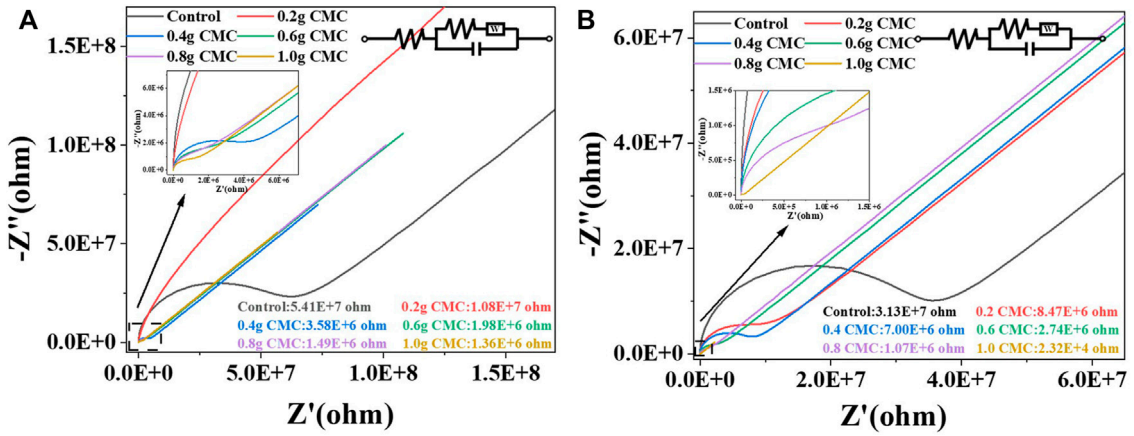

FIGURE 8
EIS of the starch/CMC composite films. **(A)**: CS/CMC composite films; **(B)**: CA/CMC composite films.

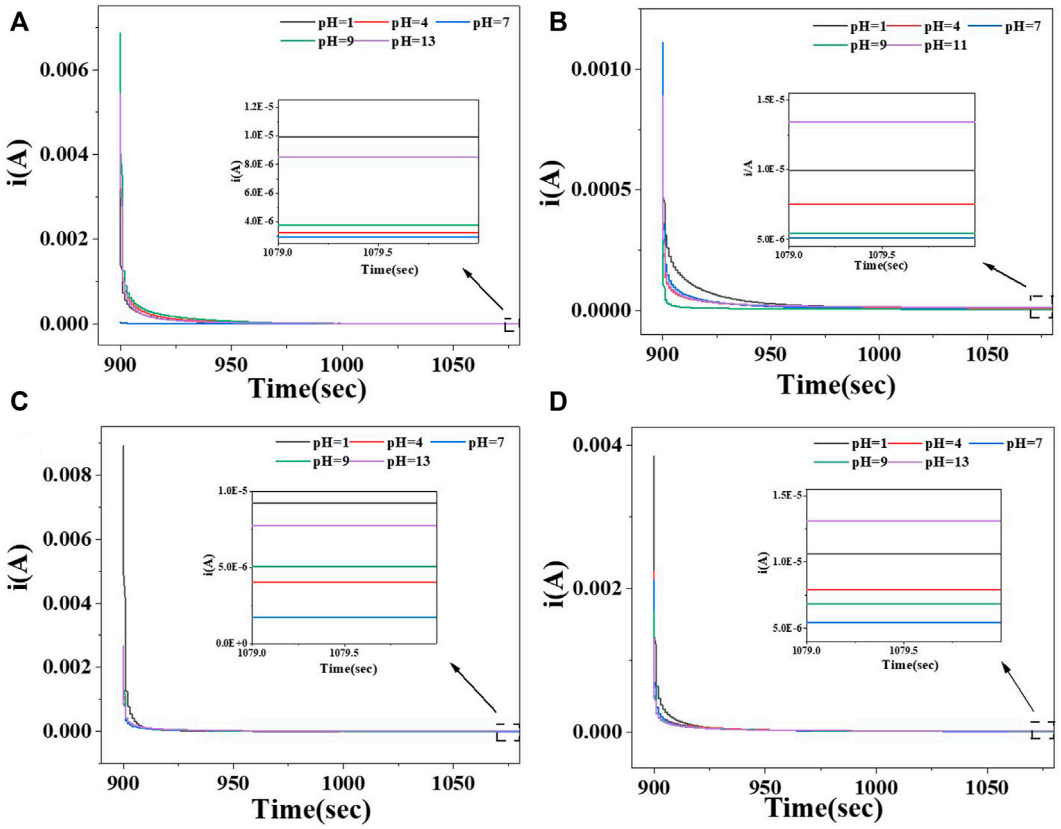

FIGURE 9
Steady current at different pH value of the starch/CMC-1.0 composite film. **(A)**: pure CS film; **(B)**: CS/CMC-1.0 composite film; **(C)**: pure CA film; **(D)**: CA/CMC-1.0 composite film.

this indicated that the CA films were more sensitive to variations in pH.

To verify the pH response of the starch/CMC composite films, we used orange juice after 14 days of storage as the test fluid. Orange juice was added dropwise to self-assembled devices prepared from starch/CMC composite films to test their stable current.

The initial pH of the fresh orange juice was 3.38, and the pH of the spoiled orange juice was 2.68. As microorganisms broke down the large molecules of acid in the orange juice into smaller ones, this increased the H^+ in the orange juice, which in turn decreased the pH of the orange juice (Zhang et al., 2016). As shown in Figure 10, the stable currents measured by the CS/CMC-1.0 composite film

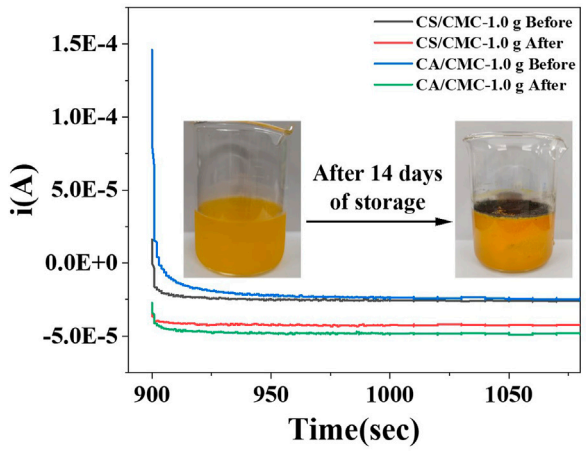

FIGURE 10
Steady current of the starch/CMC-1.0 composite films.

before and after juice deterioration were −2.6E-5 A and −4.28E-5 A, respectively; the stable currents measured by the CA/CMC-1.0 composite film before and after juice deterioration were −2.55E-5 A and −4.83E-5 A, respectively. Comparing the test results of the two composite films, the starch/CMC composite films showed the same trend in current, and the difference in current before and after juice deterioration was similar. Using the current of the starch/CMC composite film device, it was found that the information on the pH change of orange juice before and after spoilage could be captured; the information on the spoilage of orange juice was obtained by combining the relationship between the pH value and the current (Figure 10). Through objective juice experiments, it was determined that the composite film had a current response of −2.88E-5 A order of magnitude, a sensitive pH response ability and application to the rapid detection of juice quality.

4 Conclusion

In conclusion, starch/CMC composite films with different CMC doping levels were prepared by solution casting methods, and their properties and pH responsiveness were evaluated. The tensile strength of the CS/CMC and CA/CMC composite films reached 44.27 MPa and 40.43 MPa, respectively. CMC doping increased the crystallinity of the starch films; the highest crystallinity was only 8.67%. Due to the high crystallinity of the recrystallized CA film, the stability of the CA films was better, and the temperature of the maximum weight loss rate was higher than that of the CS film. The doped CMC caused the starch films to be more hydrophobic, which laid a foundation for the reuse of liquid food testing materials. The starch/CMC-1.0 composite films had good electrical conductivity and sensitively responded to different pH solutions. The results showed that the current difference of the CA/CMC composite film was more evident, which was more conducive to the quality monitoring of juice. In general, the composite material prepared in this study is biodegradable since both starch and CMC are degradable. The acid-base responsive composite films in this work shows some promise for field applications of rapid food detection and biodegradable films and provides a new strategy for the quality detection of liquid food.

Data availability statement

The original contributions presented in the study are included in the article/Supplementary Material, further inquiries can be directed to the corresponding authors.

Author contributions

SQ, CL, ZZ, and XH conceived the project and contributed to the concept of the manuscript. SQ, HS, XW, and YW synthesized and characterized the composite films, and performed experimental works. XL, HK, and DH supervised the preparation and analysis.

Funding

This work was partially supported by the National Key Research and Development Program of China (No. 2021YFD1000202), and the National Natural Science Foundation (No. 31860338, 32260720), Supported by the earmarked fund for CARS(CARS-21), and the Programs of Yun-nan Province (202002AA10007, 202101AT070041, 202004AC100001-B08, and 202102AE090042).

Conflict of interest

The authors declare that the research was conducted in the absence of any commercial or financial relationships that could be construed as a potential conflict of interest.

Publisher's note

All claims expressed in this article are solely those of the authors and do not necessarily represent those of their affiliated organizations, or those of the publisher, the editors and the reviewers. Any product that may be evaluated in this article, or claim that may be made by its manufacturer, is not guaranteed or endorsed by the publisher.

References

Aytunga, E., Kibar, A., and Ferhunde, U. (2017). Starch-cellulose ether films: Microstructure and water resistance. *J. Food Process Eng.* 40, 123822–e13364. doi:10.1111/jfpe.12382

Behera, A. K., Manna, S., and Nigamananda, D. (2022). Effect of soy waste/cellulose on mechanical, water sorption, and biodegradation properties of thermoplastic starch composites. *Starch/Staerke.* 74, 2100123–2100132. doi:10.1002/star.202100123

Cyriac, V., IsmayilNoor, I., M., Mishra, K., Chavan, C., Bhajantri, Ra. F. B., Masti, S. P., et al. (2022). Ionic conductivity enhancement of PVA: Carboxymethyl cellulose poly-blend electrolyte films through the doping of NaI salt. *Cellulose* 29, 3271–3291. doi:10.1007/s10570-022-04483-z

Deng, P. H., Xu, Z. F., and Kuang, Y. F. (2013). Electrochemically reduced graphene oxide modified acetylene black paste electrode for the sensitive determination of bisphenol A. *J. Electroanal. Chem.* 707, 7–14. doi:10.1016/j.jelechem.2013.08.020

Dolas, K. A., Ranveer, R. C., Tapre, A. R., Nandane, A. S., and Sahoo, A. K. (2020). Effect of starch modification on physico-chemical, functional and structural characterization of cassava starch (Manihot esculenta crantz). *Food Res.* 4, 1265–1271. doi:10.26656/FR.2017.4(4).075

He, C. Y., Liu, Z. F., Xu, M., Ma, Q., and Dou, Y. Y. (2017). Urban expansion brought stress to food security in China: Evidence from decreased cropland net primary productivity. *Sci. Total Environ.* 576, 660–670. doi:10.1016/j.scitotenv.2016.10.107

Ibarra, B. L. M. E., Hernandez, S. R., and Kergaravat, S. V. (2021). Glyphosate detection from commercial formulations: Comparison of screening analytic methods based on enzymatic inhibition. *Int. J. Environ. Anal. Chem.* 101, 1821–1835. doi:10.1080/03067319.2019.1691176

Jiang, G., Hou, X., Zeng, X., Zhang, C., Wu, H. J., Shen, G. H., et al. (2020). Preparation and characterization of indicator films from carboxymethyl-cellulose/starch and purple sweet potato (ipomoea batatas (L) lam) anthocyanins for monitoring fish freshness. *Int. J. Biol. Macromol.* 143, 359–372. doi:10.1016/j.ijbiomac.2019.12.024

Jin, T., and Zhong, T. Y. (2022). Changing rice cropping patterns and their impact on food security in southern China. *Food secur.* 14, 907–917. doi:10.1007/s12571-022-01254-3

Jose, F. M., Talens, P., Gavara, R., and Chiralt, A. (2012). Barrier properties of sodium caseinate films as affected by lipid composition and moisture content. *J. Food Eng.* 109, 372–379. doi:10.1016/j.jfoodeng.2011.11.019

Kundan, S., Kenneth, S., Joseph, A. K., Ailing, T., Yong, Z., Gregory, L. R., et al. (2019). Biological photonic crystal-enhanced plasmonic mesocapsules: Approaching single-molecule optofluidic-SERS sensing. *Adv. Opt. Mat.* 7, 1900415. doi:10.1002/adom.201900415

Lan, W., Zhang, R., Ji, T. T., Sameen, D. E., Ahmed, S., Qin, W., et al. (2020). Improving nisin production by encapsulated lactococcus lactis with starch/carboxymethyl cellulose edible films. *Carbohydr. Polym.* 251, 117062. doi:10.1016/j.carbpol.2020.117062

Liu, S., and Hou, M. Y. (2022). Spatiotemporal differences, dynamic evolution and trend of the coupled coordination relationship between urbanization and food security in China. *Foods* 11, 2526. doi:10.3390/foods11162526

Ma, M. T., Liu, Y., Chen, X. J., Brennan, C., Xu, X. M., Su, Z., et al. (2020). Thermal and pasting properties and digestibility of blends of potato and rice starches differing in amylose content. *Int. J. Biol. Macromol.* 165, 321–332. doi:10.1016/j.ijbiomac.2020.09.189

Mansur, A. A. P., de Carvalho, F. G., Mansur, R. L., Carvalho, S. M., de Oliveira, L. C., and Mansur, H. S. (2017). Carboxymethylcellulose/ZnCdS fluorescent quantum dot nanoconjugates for cancer cell bioimaging. *Int. J. Biol. Macromol.* 96, 675–686. doi:10.1016/j.ijbiomac.2016.12.078

Martins, G. C., Coutinho, T. E., Silva, T. L., Andreani, T., and Silva, A. M. (2022). Neurotoxicity assessment of four different pesticides using *in vitro* enzymatic inhibition assays. *Toxics* 10, 448. doi:10.3390/toxics10080448

Meng, X. X., Zhang, X. J., Bing, Y. M., Xu, N., Shi, W., and Cheng, P. (2016). *In situ* generation of NiO nanoparticles in a magnetic metal–organic framework exhibiting three-dimensional magnetic ordering. *Inorg. Chem.* 55, 12938–12943. doi:10.1021/acs.inorgchem.6b02376

Ou, Z. Q., Zhou, Q., Rao, X., Yang, H. F., Hou, C. Q., and Du, X. (2021). Cellulose isolated from waste rubber wood and its application in PLA based composite films. *Front. Bioeng. Biotechnol.* 9, 666399. doi:10.3389/fbioe.2021.666399

Ren, L. L., Yan, X. X., Zhou, J., Tong, J., and Su, X. G. (2017). Influence of chitosan concentration on mechanical and barrier properties of corn starch/chitosan films. *Int. J. Biol. Macromol.* 105, 1636–1643. doi:10.1016/j.ijbiomac.2017.02.008

Rungsiri, S., Rafael, A. A., and Pornchai, R. (2019). Utilization of Carboxymethyl Cellulose from durian rind agricultural waste to improve physical properties and stability of rice starch-based film. *J. Polym. Environ.* 27, 286–298. doi:10.1007/s10924-018-1343-z

Serge, S., Stephen, W., Sonia, A., Conny, J., Jody, H., Lise, K., et al. (2022). Revisiting food security in 2021: An overview of the past year. *Food secur.* 14, 1–7. doi:10.1007/s12571-022-01266-z

Seto, K. C., and Ramankutty, N. (2016). Hidden linkages between urbanization and food systems. *Science* 352, 943–945. doi:10.1126/science.aaf7439

Shim, E., Nore, J., Cavaco, P. A., Kim, H. R., and Silva, C. (2020). Carboxymethyl cellulose (CMC) as a template for laccase-assisted oxidation of aniline. *Front. Bioeng. Biotechnol.* 8, 00438. doi:10.3389/fbioe.2020.00438

Simona, D., Volha, S., Valeria, T., Achim, K., Dana, B., Martin, S., et al. (2021). Assessment of biotechnologically important filamentous fungal biomass by Fourier transform Raman spectroscopy. *Int. J. Mol. Sci.* 22, 6710. doi:10.3390/ijms22136710

Siqueira, G., Bras, J., and Dufresne, A. (2010). Cellulosic bionanocomposites: A review of preparation, properties and applications. *Polym* 2, 728–765. doi:10.3390/polym2040728

Tang, J., Zhang, Q., Zhou, J., Fang, H. C., Yang, H. F., and Wang, F. (2021). Investigation of pesticide residue removal effect of gelatinized starch using surface-enhanced Raman scattering mapping. *Food Chem.* 365, 130448. doi:10.1016/j.foodchem.2021.130448

Tao, E., Ma, Z. Y., Cai, D. Y., Yang, S. Y., and Li, Y. (2021). Enhancement of interfacial charge transfer of TiO_2/graphene with doped Ca^{2+} for improving electrical conductivity. *ACS Appl. Mat. Interfaces.* 13, 41875–41885. doi:10.1021/acsami.1c07401

Wafula, E. N., Onduso, M., Wainaina, I. N., Buve, C., Kinyanjui, P. K., Githiri, S. M., et al. (2022). Antinutrient to mineral molar ratios of raw common beans and their rapid prediction using near-infrared spectroscopy. *Food Chem.* 368, 130773. doi:10.1016/j.foodchem.2021.130773

Wang, L., Huang, X. Y., Wang, C. Q., Tian, X. Y., Chang, X. H., Ren, Y., et al. (2021). Applications of surface functionalized Fe_3O_4 NPs-based detection methods in food safety. *Food Chem.* 342, 128343. doi:10.1016/j.foodchem.2020.128343

Wi, R. T., Lise, J., Sasitorn, W., Pensiri, S., and Pornchai, R. (2011). Effect of carboxymethyl cellulose concentration on physical properties of biodegradable cassava starch-based films. *Chem. Cent. J.* 5 (1), 6–14. doi:10.1186/1752-153X-5-6

Xiang, M. T., Li, Y., Yang, J. Y., Lei, K. G., Li, Y., Li, F., et al. (2021). Heavy metal contamination risk assessment and correlation analysis of heavy metal contents in soil and crops. *Environ. Pollut.* 278, 116911. doi:10.1016/j.envpol.2021.116911

Xu, J., Cao, Z., Zhang, Y. L., Yuan, Z. L., Lou, Z. M., Xu, X. H., et al. (2018). A review of functionalized carbon nanotubes and graphene for heavy metal adsorption from water: Preparation, application, and mechanism. *Chemosphere* 195, 351–364. doi:10.1016/j.chemosphere.2017.12.061

Xu, J., Sun, Y. D., Lu, M. J., Wang, L., Zhang, J., Tao, E., et al. (2018). Fabrication of the porous $MnCo_2O_4$ nanorod arrays on Ni foam as an advanced electrode for asymmetric supercapacitors. *Acta Mater* 152, 162–174. doi:10.1016/j.actamat.2018.04.025

Xu, T., Ding, X. T., Shao, C. X., Song, L., Lin, T. Y., Gao, X., et al. (2018). Electric power generation through the direct interaction of pristine graphene-oxide with water molecules. *Small* 14, e1704473. doi:10.1002/smll.201704473

Yesim, O., Nariman, E. A., and Fatih, O. (2022). Antimicrobial effect of laurel essential oil nano-emulsion on food-borne pathogens and fish spoilage bacteria. *Food Chem.* 368, 130831. doi:10.1016/j.foodchem.2021.130831

Yu, B. Y., and Kwak, S. Y. (2012). Carbon quantum dots embedded with mesoporous hematite nanospheres as efficient visible light-active photocatalysts. *J. Mat. Chem. A* 22, 8345–8353. doi:10.1039/c2jm16931b

Zhang, Liang., Wang, Y. F., Liu, H. S., Yu, L., Liu, X. X., Chen, L., et al. (2013). Developing hydroxypropyl methylcellulose/hydroxypropyl starch blends for use as capsule materials. *Carbohydr. Polym.* 98, 73–79. doi:10.1016/j.carbpol.2013.05.070

Zhang, S. Y., Zhu, J., Liu, Y., Zou, S. Y., and Li, L. (2019). Hierarchical structure and thermal property of starch-based nanocomposites with different amylose/amylopectin ratio. *Polym* 11, 342. doi:10.3390/polym11020342

Zhang, X. Q., Chen, C. Y., Peng, D. P., Zhou, Y. Z., Zhuang, J. L., Zhang, X. J., et al. (2020). pH-responsive carbon dots with red emission for real-time and visual detection of amines. *J. Mat. Chem. C* 8, 11563–11571. doi:10.1039/d0tc02597f

Zhang, Y. K., Zhang, Q. F., Wang, X. Y., and Yue, S. L. (2016). Effect of controlled atmosphere storage on the metamorphism of *Saccharomyces cerevisiae* inoculated fresh orange juice. *Sci. Technol. Food Ind.* 10, 46–53. doi:10.13386/j.issn1002-0306.2016.10.060

frontiers | Frontiers in Bioengineering and Biotechnology

TYPE Original Research
PUBLISHED 09 January 2023
DOI 10.3389/fbioe.2022.1115469

OPEN ACCESS

EDITED BY
Chen Huang,
Chinese Academy of Forestry, China

REVIEWED BY
Chenhuan Lai,
Nanjing Forestry University, China
Yanzhu Guo,
Dalian Polytechnic University, China

*CORRESPONDENCE
Haitao Yang,
pphtyang1979@aliyun.com
Lan Yao,
yaolislan1982@aliyun.com

†These authors have contributed equally to this work

SPECIALTY SECTION
This article was submitted to Bioprocess Engineering, a section of the journal Frontiers in Bioengineering and Biotechnology

RECEIVED 04 December 2022
ACCEPTED 19 December 2022
PUBLISHED 09 January 2023

CITATION
Cui P, Ye Z, Chai M, Yuan J, Xiong Y, Yang H and Yao L (2023), Effective fractionation of lignocellulose components and lignin valorization by combination of deep eutectic solvent with ethanol. *Front. Bioeng. Biotechnol.* 10:1115469. doi: 10.3389/fbioe.2022.1115469

Effective fractionation of lignocellulose components and lignin valorization by combination of deep eutectic solvent with ethanol

Pingping Cui[1†], Zhishang Ye[1†], Mengzhen Chai[1], Jie Yuan[1], Yan Xiong[1], Haitao Yang[1,2*] and Lan Yao[1,3*]

[1]Hubei Provincial Key Laboratory of Green Materials for Light Industry, Hubei University of Technology, Wuhan, China, [2]State Key Laboratory of Biobased Material and Green Papermaking, Shandong Academy of Sciences, Qilu University of Technology, Jinan, Shandong, China, [3]Key Laboratory of Fermentation Engineering (Ministry of Education), Cooperative Innovation Center of Industrial Fermentation (Ministry of Education and Hubei Province), College of Bioengineering, Hubei University of Technology, Wuhan, China

Introduction: A combination of deep eutectic solvent with ethanol was developed for pretreatment of *Broussonetia papyrifera* to effectively extract lignin and promote the subsequent enzymatic hydrolysis.

Methods: In order to further explore the optimal conditions for enzymatic hydrolysis, a central composite design method was applied.

Results and Discussion: The correlation between each factor and glucose yield was obtained, and the optimal conditions was 160°C, 60 min, the ratio of DES to E was 1/1 (mol/mol). The results showed that compared with control, the glucose yield increased by 130.67% under the optimal pretreatment conditions. Furthermore, the specific surface area of biomass was increased by 66.95%, and the content of xylan and lignin was decreased by 86.71% and 85.83%. The correlation between xylan/lignin removal and enzymatic hydrolysis showed that the removal of lignin facilitated the glucose yield more significantly than that of xylan. To further explore the lignin valorization, the structural and antioxidant analysis of recovered lignin revealed that high temperature was favorable for lignin with good antioxidant performance. This pretreatment is a promising method for separating lignin with high antioxidant activity and improving cellulose digestibility.

KEYWORDS

DES, pretreatment, enzymatic saccharification, lignin, antioxidant

1 Introduction

In recent years, the sharp increase in the consumption of fossil fuels results in the rise of crude oil prices and serious environmental problems. As a kind of green energy, renewable energy can replace fossil fuel, which is widely concerned worldwide (Thi and Lee, 2019; Peng et al., 2021). One of them is bioethanol derived from lignocellulose. The composition of lignocellulose biomass is complex, which includes carbohydrate (cellulose, hemicellulose) and aromatic polymer (lignin) (Wang Y. et al., 2022). In the plant cell wall, hemicellulose and lignin are connected by covalent bonds and hydrogen bonds to form heterogenous structure, which is coated on cellulose to form is a strong "natural anti degradation barrier". This barrier greatly limits the efficiency of biomass refinery (Penín et al., 2020). Pretreatment is an essential process

to overcome the recalcitrance of biomass and achieve efficient fractionation of biomass components.

Deep eutectic solvents (DESs) are composed of hydrogen bond receptors (HBAs) and hydrogen bond donors (HBDs), which contain large and asymmetric ions, resulting in low lattice energy and therefore low melting point (Gontrani et al., 2019; Xu et al., 2020; Yu et al., 2021). Because DES could form rich hydrogen bonds, it has good solvability for polar and non-polar compounds (Pandey et al., 2017). DES pretreatment has achieved remarkable results in biomass fractionation and digestibility improvement (Hou et al., 2022). The cellulose conversion of DES pretreated corn stover and corncob exceeds 90% (Xu et al., 2016; Zhang et al., 2016; Hou et al., 2017). Furthermore, DES shows advantages of simple preparation, low toxicity, recyclability and biodegradability, thus wide application potential in the utilization of lignocellulose (Bu et al., 2021; Wang W. et al., 2022).

DES based on choline chloride (ChCL) can effectively break linkages within lignin carbohydrate complex (LCC) (Shen et al., 2019; 2021; Zhou et al., 2021). It was found that the addition of the third HBD component to the ChCL based DES can change fluidity and thermal stability of DES, thus improving the pretreatment performance of biomass (Xia et al., 2018). The most widely applied DES is composed of ChCL/LA (lactic acid). Earlier research showed that lignin re condensed during pretreatment (Bjelic et al., 2022). In our previous research, it was found that DES with ethanol was more efficient in digestibility improvement than ChCL/LA (Yao et al., 2022). However, the previous research on the optimization of pretreatment conditions is still incomplete.

Lignin is an important component that needs to be valorized to obtain total biomass utilization for biorefinery (Wang et al., 2022). Lignin itself has different kinds of active functional groups, which has advantages in scavenging free radicals. Therefore, it is of great interest to explore the value-added utilization of lignin. Organosolv lignins are the most studied one as antioxidant. Our previous research showed that physicochemical properties had great impact on the capability of scavenging free radicals (Yao et al., 2020). To be specific, the contents of phenolic hydroxyl groups had positive effects on the antioxidant activity of lignin. To further explore the impact of DES-E pretreatment on recovered lignin and its valorization, more research needs to be done. In this study, DES with ethanol was synthesized with choline chloride lactic acid and ethanol. The central composite design method was employed to obtain the best pretreatment conditions (mol ratio of DES to ethanol, temperature and time) to promote the enzymatic hydrolysis and saccharification of pretreated biomass. Furthermore, the structural properties and antioxidant activity of recovered lignin after pretreatment were analyzed. The relationship between the structural properties of lignin and its antioxidant activity was studied.

2 Material and methods

2.1 Materials

Broussonetia papyrifera was given by a local farmer in Wuhan, Hubei Province. After size reduction to 60–80 meshes, it was extracted with benzene-alcohol for 6 h. The component analysis results showed that the content of glucan, xylan, lignin and ash was 36.31%, 27.89%, 19.99%, and 1.01% respectively. Cellulase is provided by Baiyin Sainuo Technology Co., Ltd. (Gansu Province, China), with 160U/g filter paper activity. All other chemical reagents were purchased from Sigma without further purification.

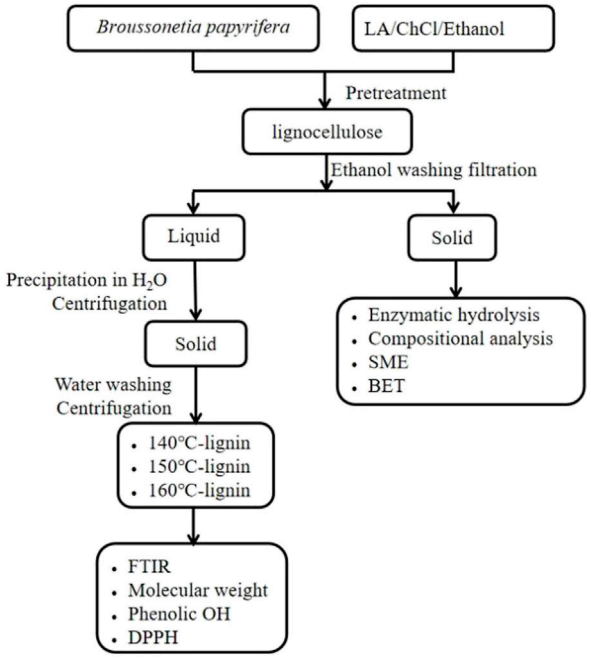

FIGURE 1
Flow chart of the pretreatment process.

2.2 Preparation of DES

After vacuum oven dried at 50°C for 24 h, lactic acid and choline chloride was mixed in a round bottom flask (2:1 M ratio) in an oil bath at 90°C for 2 h to form a uniform, stable and transparent liquid. After cooling to room temperature, it was vacuum oven dried for 1 week before use.

2.3 Pretreatment and lignin isolation

50 g dried wood powder and 500 g DES-E were mixed into a 1-L rotary electrothermal pressure digester (Parr Instrument Company). After keeping at a certain temperature for a period of time, the pretreated liquid and biomass was separated by filtration. The solid residues were first washed with excess ethanol to remove DES, and then washed with deionized water until the pH was neutral. The pretreated solid residues were stored at 4°C for further cellulase saccharification. In order to obtain the optimal pretreatment conditions, pretreatment temperature, time, and the ratio of DES to ethanol were optimized by central composite design (CCD). The statistical analysis software "Statistica 10.0" and "Minitab" (Minitab Inc.) were used for the experimental design and data analysis (p-value analysis), respectively. Pretreatment yield, component analysis and removal rate was calculated as follows:

$$\textbf{Pretreatment yield} = \frac{\textbf{oven dried biomass weight after pretreatment}}{\textbf{oven dried biomass weight before pretreatment}} \times 100\% \quad (1)$$

$$\textbf{Cellulose removal} = 1 - \frac{\textbf{Pretreatment yield} \times \textbf{Cellulose amount in residue after pretreatment}}{\textbf{cellulose amount before pretreatment}} \times 100\% \quad (2)$$

TABLE 1 Experimental design and results of central composite design.

	Ratio of DES to E (mol·mol^{-1})	Temperature (°C)	Time (h)	Pretreatment	Cellulose	Glucose
				Yield (%)	Digestibility (%)	Yield (%)
Untreated	—	—	—	—	20.05 ± 1.18	20.05 ± 1.18
1	0.5	150	0.5	71.33 ± 0.43	27.01 ± 3.44	19.26 ± 0.68
2	2	150	0.5	63.36 ± 0.69	50.78 ± 0.55	32.17 ± 1.26
3	0.5	150	1.5	51.94 ± 1.06	69.85 ± 2.31	36.28 ± 1.17
4	2	150	1.5	47.02 ± 0.20	80.42 ± 2.96	37.81 ± 0.07
5	0.5	170	0.5	48.97 ± 0.20	73.73 ± 5.90	36.11 ± 0.20
6	2	170	0.5	42.89 ± 0.20	74.49 ± 1.89	31.95 ± 0.20
7	0.5	170	1.5	42.05 ± 0.20	75.71 ± 0.57	31.83 ± 0.20
8	2	170	1.5	39.85 ± 0.02	96.43 ± 3.05	38.43 ± 0.15
9	0.5	160	1	52.56 ± 1.09	83.31 ± 1.95	43.78 ± 0.91
10	2	160	1	46.06 ± 1.53	91.11 ± 1.10	41.98 ± 1.63
11	1	150	1	63.11 ± 5.63	66.27 ± 2.13	41.75 ± 1.70
12	1	170	1	45.15 ± 1.75	97.57 ± 0.67	44.03 ± 0.99
13	1	160	0.5	56.91 ± 0.43	64.61 ± 1.59	36.77 ± 0.68
14	1	160	1.5	46.25 ± 1.06	94.27 ± 4.28	43.57 ± 1.17
15	1	160	1	49.45 ± 0.69	93.52 ± 2.18	46.25 ± 1.26

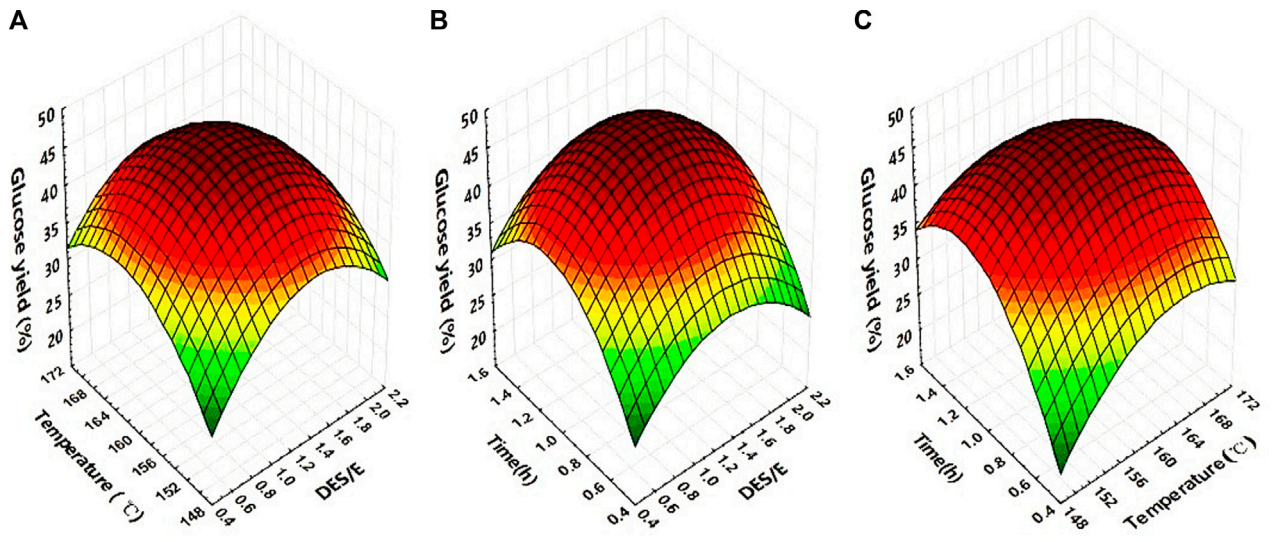

FIGURE 2
Response surface curve representing the interactive effect of DES to E ratio, temperature and time on digestibility of *Broussonetia papyrifera*: effect of temperature and DES to E ratio **(A)**. Effect of DES to E ratio and time **(B)**. Effect of temperature and time **(C)**.

$$Xylan\ removal = 1 - \frac{Pretreatment\ yield \times Xylan\ amount\ in\ residue\ after\ pretreatment}{Xylan\ amount\ before\ pretreatment} \times 100\% \quad (3)$$

$$Lignin\ removal = 1 - \frac{Pretreatment\ yield \times Lignin\ amount\ in\ residue\ after\ pretreatment}{Lignin\ amount\ before\ pretreatment} \times 100\% \quad (4)$$

TABLE 2 Analysis of variance of glucose yield.

	Sum of squares	Df	Mean square	F value	*p*-value prob > F
Model	935.86	10	93.59	52.18	<0.0001
A-Ratio of DES to E	22.74	1	22.74	12.68	0.0061
B-Temperature	19.83	1	19.83	11.06	0.0089
C-Time	99.30	1	99.30	55.36	<0.0001
AB	16.90	1	16.90	9.42	0.0134
AC	0.074	1	0.074	0.041	0.8439
BC	52.33	1	52.33	29.17	0.0004
A^2	43.55	1	43.55	24.28	0.0008
B^2	34.21	1	34.21	19.08	0.0018
C^2	107.33	1	107.33	59.84	<0.0001
ABC	61.27	1	61.27	34.16	0.0002
Residual	16.14	9	1.79	—	—
Lack of Fit	16.14	4	4.04	—	—
Cor Total	952.01	19	—	—	—

After pretreatment, lignin rich liquid fractions were concentrated by rotary evaporation. The recovered lignin was then obtained by precipitating in excess amount of cold DI water. The precipitated lignins (140°C—lignin, 150°C—lignin, and 160°C—lignin) were obtained by centrifugation, washed with DI water and 90% ethanol, and finally freeze-dried, as shown in Figure 1.

2.4 Enzymatic hydrolysis

Pretreated *Broussonetia papyrifera* were enzymatically hydrolyzed with cellulase. The enzyme loading was 25 FPU/g, and the solid concentration was 2%. The enzyme hydrolysis was conducted at 50°C for 72 h. The glucose content was analyzed by HPLC (Shimadzu, Kyoto, Japan) with a refractive index detector (Shimadzu) on an Aminex HPX-87P column (Bio-Rad, Hercules, CA, United States), with water as eluent. The cellulose digestibility and glucose yield were calculated as follows:

$$\textit{Cellulose Digestibility} = \frac{\textit{Cellulose amount in enzymatic hydrolysis solution}}{\textit{Cellulose amount in residue}} \times 100\% \quad (5)$$

$$\textit{Glucose Yield} = \textit{Pretreatment yield} \times \frac{\textit{glucose amount in enzymatic hydrolysis solution} \times 0.9}{\textit{Cellulose amount in residue}} \times 100\% \quad (6)$$

2.5 SEM and BET determination of pretreated biomass

Scanning electron microscope (SU8010; HITACHI Ltd., Tokyo, Japan) was applied to observe the fiber morphology under 5 kV accelerating voltage.

The surface of pretreated biomass was determined by nitrogen adsorption method. The adsorption/desorption isotherms of nitrogen at 77 K were measured applying a BELSORP mini-II surface area and pore size analyzer (MicrotracBEL, Japan).

2.6 Determination of physical and chemical properties of recovered lignin

FT-IR 710 infrared spectrophotometer was employed for FTIR analysis. The Gel permeation chromatography was applied to determine the molecular weight of lignin (LC-10AD, Shimadzu Co., Ltd., Japan) after being acetylated (Kumar et al., 2013). Phenolic hydroxyl group content was determined by ultraviolet spectrophotometer (UV-2550, Shimadzu Co., Ltd., Japan) (Tan et al., 2019).

2.7 Determination of antioxidant activity by DPPH method

The antioxidant activity of lignin was determined by 1,1-diphenyl-2-trinitrophenylhydrazine (DPPH) method. Briefly, lignin was dissolved in 90% dioxane water (v/v) solution with different concentrations. Then lignin was mixed with DPPH solution in dark for 1 h, after which the ultraviolet absorption value of each solution was determined at 517 nm. The free radical scavenging activity and antioxidant activity indexes were calculated according to previous study (Sadeghifar et al., 2017).

3 Results and discussion

3.1 Optimization of pretreatment condition by response surface method

Different DESs (various mol ratios) were synthesized, and their performance in improving glucose yield of *Broussonetia papyrifera* at

TABLE 3 Component analysis of *Broussonetia papyrifera* after different pretreatment conditions.

	Component (%)			Component removal (%)		
	Cellulose	Xylan	Lignin	Cellulose	Xylan	Lignin
Untreated	36.31	23.89	19.99	—	—	—
1	47.01 ± 1.20	13.65 ± 0.25	15.96 ± 0.12	9.16 ± 0.08	59.24 ± 0.09	43.05 ± 0.24
2	52.55 ± 1.31	11.53 ± 0.42	12.77 ± 0.13	9.94 ± 1.17	69.42 ± 0.34	59.52 ± 0.17
3	61.69 ± 0.01	8.25 ± 0.31	5.73 ± 2.74	14.08 ± 0.43	82.06 ± 0.10	85.11 ± 1.46
4	65.46 ± 3.79	4.68 ± 0.35	4.76 ± 1.07	18.25 ± 1.24	90.79 ± 0.13	88.8 ± 0.54
5	63.80 ± 0.70	6.19 ± 0.83	6.74 ± 0.39	16.72 ± 0.63	87.31 ± 0.31	83.49 ± 0.29
6	69.91 ± 0.25	3.30 ± 0.72	5.80 ± 1.40	20.87 ± 0.47	94.08 ± 0.29	87.56 ± 0.63
7	73.42 ± 0.55	3.02 ± 1.48	4.28 ± 0.41	17.94 ± 0.97	94.68 ± 0.65	91.00 ± 0.22
8	74.10 ± 0.01	0.44 ± 0.35	2.88 ± 0.11	22.37 ± 0.12	99.27 ± 0.14	94.26 ± 0.04
9	63.33 ± 2.94	6.50 ± 1.58	9.07 ± 0.72	9.98 ± 1.21	85.7 ± 0.80	76.15 ± 0.45
10	67.81 ± 0.77	5.31 ± 0.61	4.91 ± 0.55	16.75 ± 0.70	89.76 ± 0.21	88.69 ± 0.19
11	50.52 ± 1.32	14.30 ± 0.11	14.86 ± 0.72	14.61 ± 1.49	62.22 ± 0.59	53.09 ± 1.14
12	68.50 ± 1.23	5.39 ± 2.60	3.43 ± 0.18	17.76 ± 0.93	89.81 ± 1.3	92.25 ± 0.16
13	55.77 ± 1.00	9.60 ± 0.19	11.48 ± 0.48	15.08 ± 0.76	77.13 ± 0.13	67.32 ± 0.24
14	66.48 ± 1.70	4.69 ± 0.54	4.14 ± 0.39	18.35 ± 0.21	90.92 ± 0.31	90.42 ± 0.22
15	63.73 ± 1.98	6.42 ± 2.95	5.73 ± 0.31	15.82 ± 0.62	86.71 ± 1.43	85.83 ± 0.18

different temperature and time was evaluated. Based on the preliminary results, three factors (mol ratio of DES to E, temperature, time) were optimized by central composite design. The pretreatment conditions, cellulose digestibility and glucose yield were shown in Table 1.

Trials No. 9, 15, and 10 were conducted with the same pretreatment temperature and time, and the molar ratio of DES to ethanol was 1/2, 1/1 and 2/1, respectively. The results showed that pretreatment yield was decreased with the enhanced DES content (52.56%, 49.45%, and 46.06%), indicating that more DES could dissolve more biomass during pretreatment. The cellulose digestibility (83.31%, 93.52%, and 91.11%) and the glucose yield (43.78%, 46.25%, and 41.98%) was increased first and then decreased with more of DES content. The results showed that more DES loading did not favor enzymatic hydrolysis of pretreated *Broussonetia papyrifera*. This may be due to that the excessive removal of lignin and xylan, which led to the collapse of cellulose structure and the reduction of the available surface area of cellulose for cellulase adsorption (Shen et al., 2019).

Broussonetia papyrifera were pretreated at the same DES to E ratio and time at 150°C, 160°C, and 170°C in scheme No 11, 15, and 12, respectively. It was obvious to see that solid residue yield was decreased at higher pretreatment temperature (63.11%, 49.45%, and 45.15%). The cellulose digestibility was 66.27%, 93.52%, and 97.57%, respectively, indicating that the increase of pretreatment temperature was in favor of cellulose conversion. Earlier literature showed that the cellulose conversion of pretreated poplars with DES was significantly increased with the increase of pretreatment temperature (Yang et al., 2021). Due to the decreased pretreatment yield with increased pretreatment temperature, the glucose yield was increased first and then decreased (41.75%, 46.25%, and 44.03%).

Scheme No 13, 15, and 14 were pretreated with the same DES to E ratio and temperature, but with various time (0.5, 1, and 1.5 h). Results showed that the pretreatment yield was decreased with extension of time (56.91%, 49.45%, and 46.25%). After pretreatment with DES-E, the ether linkage in lignin carbohydrate complex (LCC) was broken (Li et al., 2022). With the extension of pretreatment time, more surfaces and pores were exposed for cellulase, thus increasing the cellulose digestibility (64.61%, 93.52%, and 94.27%). Taking pretreatment yield into consideration, glucose yield was first increased and then decreased with extended time (36.77%, 46.25%, and 43.57%).

The highest glucose yield (46.25%) was in trials No 15, which was 130.67% higher than that of control. Figure 2 was the response surface curves based on the interaction between mol ratio of DES to E, temperature and time, taking glucose yield as the response value.

Table 2 was the variance analysis of the glucose yield of the three studied factors. From the results, it was obvious to see that the regression of this model was extremely significant ($p < 0.0001$). The determination coefficient R^2 was 0.9830, indicating that the linear relationship between the dependent variable and the independent variable was significant. Comparing the value of F, the order of factors affecting the glucose yield was: time > DES to E ratio > temperature. The results also showed that the DES to E ratio, temperature and time, as well as the interaction of the three factors, had a very significant effect on the glucose yield ($p < 0.01$).

3.2 Component analysis of *Broussonetia papyrifera* after pretreatment

The glucose yield is closely related to the composition of biomass. The influence of different pretreatment conditions on chemical

composition of *Broussonetia papyrifera* was shown in Table 3. The content of cellulose, xylan and lignin in untreated raw materials was 36.31%, 23.89%, and 19.99%, respectively. After pretreatment, the cellulose content was increased and that of xylan and lignin was decreased at various extent. This may be because during the pretreatment of DES-E, the chemical linkages between hemicellulose and lignin was cleaved, resulting in removal of hemicellulose and lignin, retaining most of the cellulose, which is consistent with the previous researches (Chen et al., 2019; Li et al., 2022).

Trials No. 9, 15, and 10 were conducted with the same pretreatment temperature and time, the molar ratio of DES to E was 1/2, 1/1 and 2/1, respectively. The removal of cellulose (9.98%, 15.82%, and 16.75%), xylan (85.7%, 86.71%, and 89.76%) and lignin (76.15%, 85.83%, and 88.69%) was increased with the increase of DES to E ratio. DES promotes the cleavage of C-O bond, which favors the dissolution of lignin. However, during pretreatment lignin might re-polymerize with polysaccharide degradation products (such as furfural) to produce pseudo lignin (Li and Zheng, 2017). DES (ChCl/OA/EG) was synthesized to pretreat birch, in which the degree of lignin condensation increased with the increased OA amount (Liu et al., 2021). Therefore, when the DES content increased, the lactic acid content increased accordingly, resulting in enhanced repolymerization of lignin, which made the removal rate of lignin decreased.

Broussonetia papyrifera were pretreated at 150°C, 160°C, and 170°C with the same DES to E ratio and time in schemes 11, 15, and 12. The removal of cellulose (14.61%, 14.61%, and 17.76%), xylan (62.22%, 86.71%, and 89.81%) and lignin (53.09%, 85.83%, and 92.25%) were increased with higher pretreatment temperature. The results indicated that high temperature was in favor for breaking the chemical linkage between cellulose, hemicellulose and lignin, thus the removal of hemicellulose and lignin. However, earlier research showed that pseudo lignin could form under high temperature, which leads to rising in lignin content and a decrease in lignin removal rate (Li et al., 2022).

Schemes 13, 15, and 14 were conducted with the same DES to E ratio and temperature for 0.5, 1, and 1.5 h. The removal of cellulose (15.08%, 15.82%, and 18.35%), xylan (77.13%, 86.71%, and 90.92%) and lignin (67.32%, 85.83%, and 90.42%) were all increased with the extension of time. Earlier study also showed that solubility of pretreated beech by multiple groups of DES was increased with the extension of pretreatment time (Mamilla et al., 2019).

In conclusion, when the DES to E ratio, temperature and time increased independently, the removal of cellulose, hemicellulose and lignin increased. The removal of cellulose was much less than that of hemicellulose and lignin. When the DES to E ratio, temperature and time were increased simultaneously, the changes of chemical composition were the most significant. Pretreatment condition of Scheme 8 was conducted at DES to E of 2:1, 170°C for 1.5 h. The cellulose content in the solid residue was 74.10% and 0.44% xylan and 2 .88% lignin. The cellulose removal of this scheme was relatively high (22.37%), which was not in favor of higher glucose yield.

3.3 Factors affecting cellulose conversion of Broussonetia papyrifera

From the component analysis, it can be observed that DES-E has a strong ability in biomass fractionation. In order to determine whether the improvement of cellulose digestibility is due to the removal of xylan and lignin during pretreatment, the correlation between their removal and cellulose digestibility were evaluated, as shown in Figure 3. It was observed that xylan removal (R^2 = 0.66, Figure 3A) and lignin removal (R^2 = 0.74, Figure 3B) showed great impact on enzyme digestibility of pretreated *Broussonetia papyrifera*. In addition, linear correlation between lignin removal and xylan removal was also found (R^2 = 0.94, Figure 3C). The results indicated that the removal of xylan and lignin had a positive effect on cellulose conversion to glucose. The removal of lignin exhibited a more obvious effect than that of xylan. Earlier studies showed that removal of xylan can improve the accessibility of enzyme to cellulose surface, thus promoting cellulase hydrolysis (Martínez et al., 2015). In addition, our previous research results showed that there was a non-productive binding between lignin and cellulase. Removal of lignin could make more free cellulase for cellulose degradation (Yao et al., 2022). Bamboo residues were pretreated with DES by different molar ratios of choline chloride/lactic acid by Lin and his coworkers (Lin et al., 2020). The results showed that the xylan and lignin removal were positively correlated with the cellulose degradation, which was consistent with our research results.

3.4 Physical property changes after pretreatment

The SEM images of the samples before and after pretreatment by DES-E at were shown in Figure 4. SEM images of untreated *Broussonetia papyrifera* showed a compact and dense cell wall with complete surface (Figure 4A). However, it can be observed that the structure was loose and rough after DES-E pretreatment. In addition, cracks were observed on the pretreated samples obviously (Figure 4B). The chemical linkages between cellulose, hemicellulose and lignin was destroyed during DES-E pretreatment, removing a large amount of xylan and lignin, leaving residue rich in cellulose (Li et al., 2022). Therefore, due to its rough fiber surface after pretreatment with DES-E, the accessibility of cellulose was improved, thus promoting cellulose digestibility. SEM image analysis after DES pretreatment of beech and corn strover showed that the surface is rougher and looser (Zhao et al., 2018; Mamilla et al., 2019), which was also found in the present study.

The average pore size and specific surface area are the two most commonly applied parameters to evaluate the pore structure of porous materials (Maloney and Paulapuro, 1999). SEM analysis showed that DES-E pretreatment had a certain impact on the fiber structure. To further explore the impact, average pore size and specific surface area changes after pretreatment was determined, as shown in Figure 5 and Table 4.

It was showed in Figure 5A that both *Broussonetia papyrifera* was non-porous structured polymer before and after pretreatment (Altwala and Mokaya, 2020). When the relative pressure is less than 0.3, the nitrogen adsorption capacity of *Broussonetia papyrifera* after pretreatment was higher than that of the untreated one, indicating that the surface area was increased after pretreatment. Porous materials were classified into three categories according to the pore size: micropores (radius < 2 nm), mesopore (radius <50 nm); macropore (radius >50 nm). It can be seen from Figure 5B that the wood fibers before and after pretreatment showed obvious double pore distribution characteristics. After pretreatment, more microporous structures were formed, which is beneficial to the cellulase hydrolysis. Results in Table 4 indicated that the pore volume after pretreatment was relatively reduced, but the BET surface area and surface area density were increased. BET surface area was increased from 1.5987 to 2.6691 m^2/g after pretreatment. In

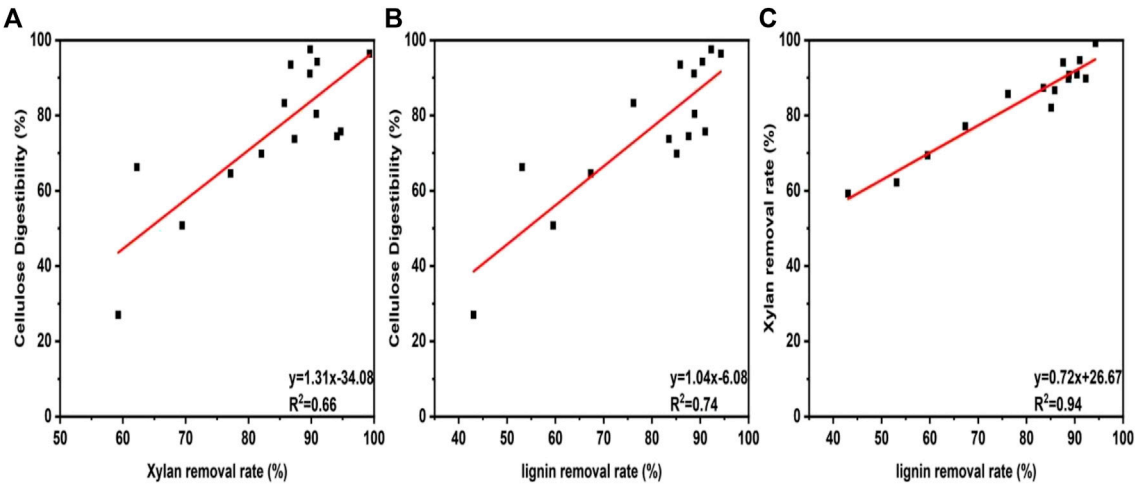

FIGURE 3
Relationship between xylan removal rate and cellulose digestibility **(A)**. Relationship lignin removal rate and cellulose digestibility **(B)**. Relationship between lignin removal rate and xylan removal rate **(C)**.

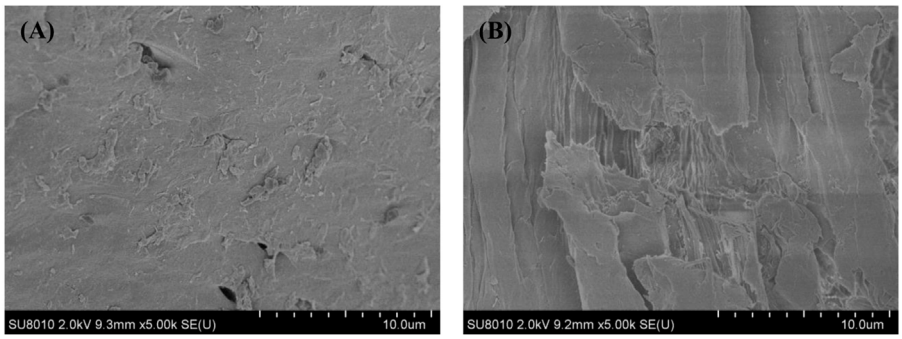

FIGURE 4
SEM images of *Broussonetia papyrifera* before pretreatment **(A)**. After pretreatment at the best conditions **(B)**.

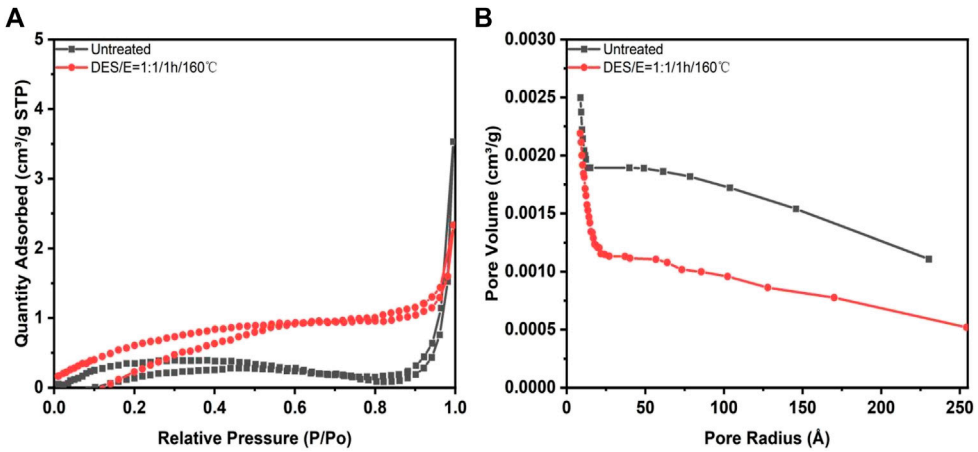

FIGURE 5
Nitrogen adsorption desorption isotherm curve **(A)**. And BJH pore size distribution diagram **(B)**. Of *Broussonetia papyrifera* before and after pretreatment.

TABLE 4 Parameters of *Broussonetia papyrifera* before and after pretreatment.

Sample	S_{BET} (m^2 g^{-1})	Pore volume (cm^3 g^{-1})	*Surface area
			Density (m^2 cm^{-3})
Untreated	1.5987	0.005456	293
After pretreatment	2.6691	0.003538	754

Note: *Surface area density, S_{BET}/Pore volume.

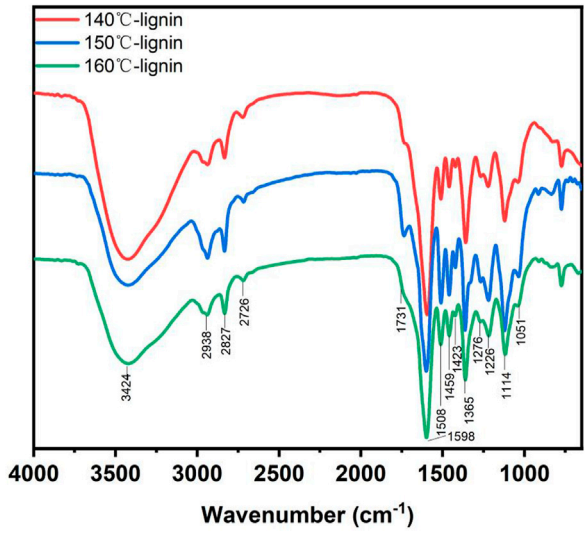

FIGURE 6
FTIR of recovered lignin after DES-E pretreatment.

an early study, bamboo was pretreated with DES composed by choline chloride, oxalic acid and ethylene glycol. After pretreatment, the surface area was increased significantly (Li et al., 2022). The increase of specific surface area can improve the accessibility of cellulose, so as to achieve high cellulose digestibility and promote the increase of glucose yield.

3.5 Physiochemical characteristic analysis of recovered lignin

FTIR is a widely employed method to analysis different functional groups of lignin. A comparison between recovered lignin at different temperatures showed that the common property and signals in the fingerprint region of the three lignin samples were quite similar. The assignment of important signals in FTIR was referred to previous studies (Yang et al., 2016; 2020). As shown in Figure 6, signals at 3424 cm^{-1} were attributed to the stretching vibration of hydroxyl group (O-H) in lignin. The absorption bands at 2938 cm^{-1} was assigned to the C-H stretching. Signals centered at 1731 cm^{-1} was from the carbonyl stretching not conjugated with the aromatic ring. Strong signals at 1598, 1509, and 1423 cm^{-1} corresponding to aromatic rings were clearly observed in all lignin samples. Furthermore, crosspeak at 1365cm^{-1} was corresponded to syringyl and condensed guaiacyl units. Signals at 1226cm^{-1} was assigned to the C-O absorption of guaiacyl based units. Therefore, the recovered lignin from *Broussonetia papyrifera* pretreated by DES-E was composed by guaiacyl and syringyl.

The ratio of relative signal intensity of different functional groups to that at 1509 cm^{-1} was shown in Table 5 (Yao et al., 2018b). By comparing the relative signal intensity of the three recovered lignin, it can be seen that signal from carbonyl not conjugated with the aromatic ring centered at 1731 cm^{-1} was not found in recovered lignin at 160°C, indicating that C=O in the lignin structure was destroyed at higher pretreatment temperature. The intensity of signals at 1051 cm^{-1} was the strongest in recovered lignin at 150°C. The signal peaks at 1126 and 1114 cm^{-1} were corresponded to guaiacyl-type and syringyl-type lignin, respectively. Comparing the three lignin samples, the S/G of 140°C- lignin was significantly higher than that of the other two lignin samples.

The molecular weight analysis could elucidate the variations in depolymerization/repolymerization reactions of lignin during pretreatment. GPC method was employed to determine and compare the weight average molecular weight (M_w), number average molecular weight (M_n) and polydispersity index (PDI) of each lignin sample. As shown in Table 6, M_n of lignin sample recovered in pretreatment liquid decreased with the increase of temperature, which was consistent with the previous research results (Yao et al., 2020a). M_w was increased with the increase of temperature, indicating of enhanced lignin repolymerization occurring with increased temperature during acid-catalyzed pretreatment process (Yao et al., 2018). Earlier studies showed that the extensive repolymerization reactions took over with increasing temperature, forming larger and heterogeneous lignin macromolecules (Wang et al., 2012), which could explain the increased M_w and PDI with the increased pretreatment temperature in the present study.

The results in Table 6 showed that the phenolic hydroxyl content in the recovered lignin increased with the increase of temperature. This may be due to the broken of α, β-ether linkage during pretreatment, resulting in an increase in phenolic hydroxyl group (Wang et al., 2020). When the pretreatment temperature was at 160°C, the content of phenolic hydroxyl group content was 0.40 mmol/g, as twice as that at 140°C. The result of -OH group content determined by FT-IR and UV was contradictory. The possible reason was that UV method was employed to determine the phenolic hydroxyl group, while in the FTIR, the signal around 3400 cm^{-1} was assigned to total hydroxyl group. The least signal intensity of lignin recovered at pretreatment temperature of 160°C might be caused by less content of aliphatic -OH group (Yao et al., 2020). Earlier studies showed that with the increase of temperature, the content of phenolic hydroxyl group of lignin obtained by hydrothermal pretreatment increased by 53.79% (Chen et al., 2016), which was consistent with our research results. More phenolic OH groups is a desired feature for potentially application of lignin as antioxidant, as reported by other researches previously (Sadeghifar et al., 2017; Yao et al., 2018a).

TABLE 5 Signal assignment and relative intensities of recovered lignin at different temperatures.

Assignment	Wavenumber (cm^{-1})	140°C-lignin	150°C-lignin	160°C-lignin
Hydroxyl group	3424	1.84	0.90	1.13
C-H stretching	2938	0.63	0.78	0.81
C=O in unconjugated ketone	1731	0.42	0.71	-
Aromatic ring	1598	3.24	1.50	1.82
Aromatic ring	1509	1.00	1.00	1.00
C-H deformation	1459	0.86	0.96	0.93
Aromatic ring	1423	0.67	0.85	0.83
Syringyl and condensed guaiacyl	1365	1.66	1.21	1.31
C-O stretching	1226	0.83	1.00	0.93
Aromatic C-H deformation in syringyl	1114	1.26	1.18	1.06
C-O-C stretching	1051	0.78	0.89	0.77

Note: the relative intensity was calculated as the ratio of the intensity of the signal to the intensity of the band at 1,509 cm.

TABLE 6 Molecular weight and phenolic OH distribution of recovered lignin samples.

	Mn	Mw	Mw/Mn	Phenolic OH (mmol/g)
140°C-lignin	1352	2731	2.02	0.21 ± 0.01
150°C-lignin	948	3311	3.49	0.22 ± 0.01
160°C-lignin	749	3835	5.12	0.40 ± 0.06

TABLE 7 Parameters of antioxidant activity of recovered lignin by DPPH method.

	Linear equation	R^2	IC_{50} (mg/L)	AAI
Vitamin E	y = 1.55x + 0.34	0.99	32.14	0.77
140°C-lignin	y = 1.36x + 10.28	0.96	29.17	0.84
150°C-lignin	y = 1.29x + 15.82	0.97	26.40	0.93
160°C-lignin	y = 1.58x + 18.34	0.95	20.04	1.23

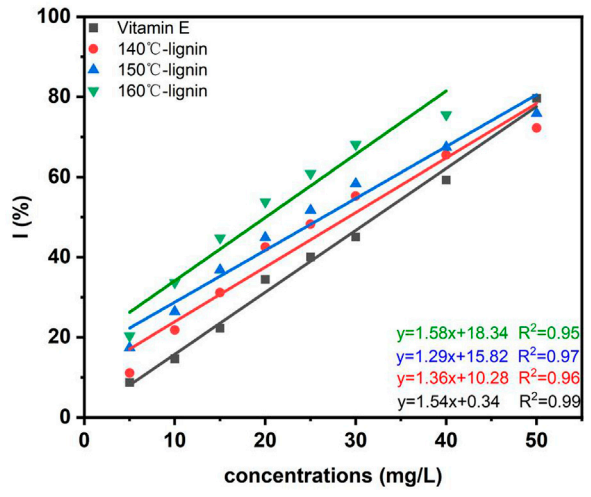

FIGURE 7
Isotherm of DPPH radical scavenging rate of recovered lignin.

3.6 Antioxidant activity determination of recovered lignin

Lignin is a natural aromatic polymer composed of three phenylpropane structural units (*p*-hydroxyphenyl (H), guaiacyl (G) and syringal (S)) connected by various ether bonds and C-C bonds (Sadeghifar and Argyropoulos, 2015). As a compound rich in active functional groups, lignin can capture and neutralize free radicals and shows good antioxidant activity (Lu et al., 2022). In the present study, the *in vitro* antioxidant activity of lignin recovered from the DES-E pretreatment liquid was determined by DPPH method as described earlier (Sadeghifar et al., 2017). The DPPH radical scavenging rates of lignin extracted at different temperatures and water-soluble vitamin E were shown in Figure 7. In the range of 0–50 mg/L, with the increase of lignin concentration, the free radical scavenging capacity of recovered lignin and water-soluble vitamin E was enhanced, and the concentration of lignin is linearly correlated with the free radical scavenging rate ($R^2 \geq 0.95$). The IC_{50} and antioxidant activity index (AAI) were shown in Table 7. IC_{50} represents the concentration of antioxidant required to inhibit 50% free radicals under study. The lower IC_{50} indicates the stronger antioxidant activity. The results showed that compared with vitamin E, the antioxidant activity of recovered lignin pretreated by DES-E was higher. More importantly, the IC50 of these lignin samples was lower than most of published studies (An et al., 2017; Yao et al., 2018b; Dong et al., 2020), indicating advantage of DES-E pretreatment in producing lignin with higher antioxidant activity.

With the increase of pretreatment temperature, the broken of ether linkage and C-C bond was increased (Li et al., 2022), and the content of phenolic hydroxyl group was increased, which favored the capture of free radicals by lignin. The antioxidant properties of

industrial lignin from different sources was studied earlier, and it was found that the phenolic hydroxyl group content in lignin structure was positively correlated with AAI (y = 0.797x + 0.99, R^2 = 0.978), and the phenolic hydroxyl in lignin played a crucial role in the antioxidant properties (Sadeghifar et al., 2017). The antioxidant activity of lignin sample is mainly from their ability to donate H and quench the free radical intermediate, which is primarily from free phenolic hydroxyl groups. That could explain the importance of the phenolic hydroxyl groups in the antioxidant capability of lignin sample. In another research, it was indicated that the carbonyl group in the side chain inhibited the free radical scavenging activity (Dizhbite et al., 2004). Combined with the FTIR analysis results, there was no obvious signal from C=O in recovered lignin at 160°C, which led to the improvement of its antioxidant capacity. Furthermore, the S/G of the three lignin samples were 1.52, 1.18 and 1.27, respectively, based on the FTIR analysis. It was indicated before that AL with a higher S/G ratio had stronger antioxidant activities (Gong et al., 2016), which was not observed in the present study. However, it was found that lignin with higher Mw and PDI showed higher antioxidant ability, which was contradictory with previous study (Yao et al., 2018b). It might due to limited data in this study. The impact of molecular weight and distribution of lignin on its antioxidant capacity needs further investigation.

4 Conclusion

Broussonetia papyrifera was pretreated with DES-E to improve the glucose yield and obtain the recovered lignin for further application. When the ratio of DES to ethanol was 1:1, the pretreatment temperature was 160°C, and time was 1h, the highest glucose yield was 46.25%. The physical and chemical properties of the pretreated solid residue and dissolved lignin were analyzed. It was found that compared with the untreated one, the content of lignin and hemicellulose decreased significantly. The specific surface area was also increased after pretreatment. With the increase of temperature, the content of phenolic hydroxyl of recovered lignin was increased, which was beneficial to the antioxidant capacity.

Data availability statement

The original contributions presented in the study are included in the article/Supplementary Material, further inquiries can be directed to the corresponding authors.

Author contributions

PC: writing, validation. ZY: formal analysis. MC: review and editing. JY: review and editing. YX: review and editing. HY: review and editing, funding acquisition. LY: review and editing, investigation.

Funding

The authors are grateful for the support from the National Natural Science Foundation of China (No. 21978074 and 31871789), the China Scholarship Council (No. 2011842330 and 201508420257), key project of Hubei Provincial Department of Education (D20211404), and key Laboratory of Fermentation Engineering (Ministry of Education) (No. 202105FE04).

Conflict of interest

The authors declare that the research was conducted in the absence of any commercial or financial relationships that could be construed as a potential conflict of interest.

Publisher's note

All claims expressed in this article are solely those of the authors and do not necessarily represent those of their affiliated organizations, or those of the publisher, the editors and the reviewers. Any product that may be evaluated in this article, or claim that may be made by its manufacturer, is not guaranteed or endorsed by the publisher.

References

Altwala, A., and Mokaya, R. (2020). Predictable and targeted activation of biomass to carbons with high surface area density and enhanced methane storage capacity. *Energy Environ. Sci* 13, 2967–2978. doi:10.1039/d0ee01340d

An, L., Wang, G., Jia, H., Liu, C., Sui, W., and Si, C. (2017). Fractionation of enzymatic hydrolysis lignin by sequential extraction for enhancing antioxidant performance. *Int. J. Biol Macromol* 99, 674–681. doi:10.1016/j.ijbiomac.2017.03.015

Bjelic, A., Hočevar, B., Grilc, M., Novak, U., and Likozar, B. (2022). A review of sustainable lignocellulose biorefining applying (natural) deep eutectic solvents (DESs) for separations, catalysis and enzymatic biotransformation processes. *Rev. Chem. Eng* 38, 243–272. doi:10.1515/revce-2019-0077

Bu, C. Y., Yan, Y. X., Zou, L. H., Ouyang, S. P., Zheng, Z. J., and Ouyang, J. (2021). Comprehensive utilization of corncob for furfuryl alcohol production by chemo-enzymatic sequential catalysis in a biphasic system. *Bioresour. Technol* 319, 124156. doi:10.1016/j.biortech.2020.124156

Chen, X., Li, H., Sun, S., Cao, X., and Sun, R. (2016). Effect of hydrothermal pretreatment on the structural changes of alkaline ethanol lignin from wheat straw. *Sci. Rep* 6, 39354–39359. doi:10.1038/srep39354

Chen, Z., Jacoby, W. A., and Wan, C. (2019). Ternary deep eutectic solvents for effective biomass deconstruction at high solids and low enzyme loadings. *Bioresour. Technol* 279, 281–286. doi:10.1016/j.biortech.2019.01.126

Dizhbite, T., Telysheva, G., Jurkjane, V., and Viesturs, U. (2004). Characterization of the radical scavenging activity of lignins - natural antioxidants. *Bioresour. Technol* 95, 309–317. doi:10.1016/j.biortech.2004.02.024

Dong, H., Zheng, L., Yu, P., Jiang, Q., Wu, Y., and Huang, C., (2020). Characterization and application of lignin-carbohydrate complexes from lignocellulosic materials as antioxidants for scavenging *in vitro* and *in vivo* reactive oxygen species. *ACS Sustain. Chem. Eng* 8, 256–266. doi:10.1021/acssuschemeng.9b05290

Gong, W., Xiang, Z., Ye, F., and Zhao, G. (2016). Composition and structure of an antioxidant acetic acid lignin isolated from shoot shell of bamboo (Dendrocalamus Latiforus). *Ind. Crops Prod.* 91, 340–349. doi:10.1016/j.indcrop.2016.07.023

Gontrani, L., Plechkova, N. V., and Bonomo, M. (2019). In-depth physico-chemical and structural investigation of a dicarboxylic acid/choline chloride natural deep eutectic solvent (nades): A spotlight on the importance of a rigorous preparation procedure. *ACS Sustain. Chem. Eng* 7, 9b02402–12543. doi:10.1021/acssuschemeng.9b02402

Hou, S., Shen, B., Zhang, D., Li, R., Xu, X., Wang, K., et al. (2022). Understanding of promoting enzymatic hydrolysis of combined hydrothermal and deep eutectic solvent pretreated poplars by Tween 80. *Bioresour. Technol.* 362, 127825. doi:10.1016/j.biortech.2022.127825

Hou, X. D., Feng, G. J., Ye, M., Huang, C. M., and Zhang, Y. (2017). Significantly enhanced enzymatic hydrolysis of rice straw via a high-performance two-stage deep eutectic solvents synergistic pretreatment. *Bioresour. Technol* 238, 139–146. doi:10.1016/j.biortech.2017.04.027

Kumar, R., Hu, F., Hubbell, C. A., Ragauskas, A. J., and Wyman, C. E. (2013). Comparison of laboratory delignification methods, their selectivity, and impacts on physiochemical characteristics of cellulosic biomass. *Bioresour. Technol* 130, 372–381. doi:10.1016/j.biortech.2012.12.028

Li, N., Meng, F., Yang, H., Shi, Z., Zhao, P., and Yang, J. (2022). Enhancing enzymatic digestibility of bamboo residues using a three-constituent deep eutectic solvent pretreatment. *Bioresour. Technol* 346, 126639. doi:10.1016/j.biortech.2021.126639

Li, X., and Zheng, Y. (2017). Lignin-enzyme interaction: Mechanism, mitigation approach, modeling, and research prospects. *Biotechnol. Adv* 35, 466–489. doi:10.1016/j.biotechadv.2017.03.010

Lin, W., Xing, S., Jin, Y., Lu, X., Huang, C., and Yong, Q. (2020). Insight into understanding the performance of deep eutectic solvent pretreatment on improving enzymatic digestibility of bamboo residues. *Bioresour. Technol* 306, 123163. doi:10.1016/j.biortech.2020.123163

Liu, Y., Deak, N., Wang, Z., Yu, H., Hameleers, L., and Jurak, E., (2021). Tunable and functional deep eutectic solvents for lignocellulose valorization. *Nat. Commun* 12, 5424. doi:10.1038/s41467-021-25117-1

Lu, X., Gu, X., and Shi, Y. (2022). A review on lignin antioxidants: Their sources, isolations, antioxidant activities and various applications. *Int. J. Biol. Macromol* 210, 716–741. doi:10.1016/j.ijbiomac.2022.04.228

Maloney, T. C., and Paulapuro, H. (1999). The formation of pores in the cell wall. *J. Pulp Pap. Sci* 25, 430–436.

Mamilla, J. L. K., Novak, U., Grilc, M., and Likozar, B. (2019). Natural deep eutectic solvents (DES) for fractionation of waste lignocellulosic biomass and its cascade conversion to value-added bio-based chemicals. *Biomass Bioenerg.* 120, 417–425. doi:10.1016/j.biombioe.2018.12.002

Martínez, P. M., Bakker, R., Harmsen, P., Gruppen, H., and Kabel, M. (2015). Importance of acid or alkali concentration on the removal of xylan and lignin for enzymatic cellulose hydrolysis. *Ind. Crops Prod* 64, 88–96. doi:10.1016/j.indcrop.2014.10.031

Pandey, A., BhawnaDhingra, D., and Pandey, S. (2017). Hydrogen bond donor/acceptor cosolvent-modified choline chloride-based deep eutectic solvents. *J. Phys. Chem. B* 16, 4202–4212. doi:10.1021/acs.jpcb.7b01724

Peng, J., Xu, H., Wang, W., Kong, Y., Su, Z., and Li, B. (2021). Techno-economic analysis of bioethanol preparation process via deep eutectic solvent pretreatment. *Ind. Crops Prod* 172, 114036. doi:10.1016/j.indcrop.2021.114036

Penín, L., López, M., Santos, V., Alonso, J. L., and Parajó, J. C. (2020). Technologies for Eucalyptus wood processing in the scope of biorefineries: A comprehensive review. *Bioresour. Technol* 311, 123528. doi:10.1016/j.biortech.2020.123528

Sadeghifar, H., and Argyropoulos, D. S. (2015). Correlations of the antioxidant properties of softwood kraft lignin fractions with the thermal stability of its blends with polyethylene. *ACS Sustain. Chem. Eng* 3, 349–356. doi:10.1021/sc500756n

Sadeghifar, H., Wells, T., Le, R. K., Sadeghifar, F., Yuan, J. S., and Ragauskas, A. J. (2017). Fractionation of organosolv lignin using acetone:water and properties of the obtained fractions. *ACS Sustain. Chem. Eng* 5, 580–587. doi:10.1021/acssuschemeng.6b01955

Shen, B., Hou, S., Jia, Y., Yang, C., Su, Y., and Ling, Z., (2021). Synergistic effects of hydrothermal and deep eutectic solvent pretreatment on co-production of xylo-oligosaccharides and enzymatic hydrolysis of poplar. *Bioresour. Technol* 341, 125787. doi:10.1016/j.biortech.2021.125787

Shen, X. J., Wen, J. L., Mei, Q. Q., Chen, X., Sun, D., and Yuan, T. Q., (2019). Facile fractionation of lignocelluloses by biomass-derived deep eutectic solvent (DES) pretreatment for cellulose enzymatic hydrolysis and lignin valorization. *Green Chem* 21, 275–283. doi:10.1039/c8gc03064b

Tan, Y. T., Ngoh, G. C., and Chua, A. S. M. (2019). Effect of functional groups in acid constituent of deep eutectic solvent for extraction of reactive lignin. *Bioresour. Technol* 281, 359–366. doi:10.1016/j.biortech.2019.02.010

Thi, S., and Lee, K. M. (2019). Comparison of deep eutectic solvents (DES) on pretreatment of oil palm empty fruit bunch (OPEFB): Cellulose digestibility, structural and morphology changes. *Bioresour. Technol* 282, 525–529. doi:10.1016/j.biortech.2019.03.065

Wang, K., Gao, S., Lai, C., Xie, Y., Sun, Y., Wang, J., et al. (2022). Upgrading wood biorefinery: An integration strategy for sugar production and reactive lignin preparation. *Ind. Crops Prod.* 187, 115366. doi:10.1016/j.indcrop.2022.115366

Wang, K., Yang, H., Yao, X., Xu, F., and Sun, R. C. (2012). Structural transformation of hemicelluloses and lignin from triploid poplar during acid-pretreatment based biorefinery process. *Bioresour. Technol* 116, 99–106. doi:10.1016/j.biortech.2012.04.028

Wang, S., Li, H., Xiao, L. P., and Song, G. (2020). Unraveling the structural transformation of wood lignin during deep eutectic solvent treatment. *Front. Energy Res* 8. doi:10.3389/fenrg.2020.00048

Wang, W., Zhu, B., Xu, Y., Li, B., and Xu, H. (2022). Mechanism study of ternary deep eutectic solvents with protonic acid for lignin fractionation. *Bioresour. Technol* 363, 127887. doi:10.1016/j.biortech.2022.127887

Wang, Y., Zhang, W. J., Yang, J. Y., Li, M. F., Peng, F., and Bian, J. (2022). Efficient fractionation of woody biomass hemicelluloses using cholinium amino acids-based deep eutectic solvents and their aqueous mixtures. *Bioresour. Technol* 354, 127139. doi:10.1016/j.biortech.2022.127139

Xia, Q., Liu, Y., Meng, J., Cheng, W., Chen, W., Liu, S., et al. (2018). Multiple hydrogen bond coordination in three-constituent deep eutectic solvents enhances lignin fractionation from biomass. *Green Chem* 20, 2711–2721. doi:10.1039/c8gc00900g

Xu, G. C., Ding, J. C., Han, R. Z., Dong, J. J., and Ni, Y. (2016). Enhancing cellulose accessibility of corn stover by deep eutectic solvent pretreatment for butanol fermentation. *Bioresour. Technol* 203, 364–369. doi:10.1016/j.biortech.2015.11.002

Xu, H., Peng, J., Kong, Y., Liu, Y., Su, Z., Li, B., et al. (2020). Key process parameters for deep eutectic solvents pretreatment of lignocellulosic biomass materials: A review. *Bioresour. Technol.* 310, 123416. doi:10.1016/j.biortech.2020.123416

Yang, H., Xie, Y., Zheng, X., Pu, Y., Huang, F., Meng, X., et al. (2016). Comparative study of lignin characteristics from wheat straw obtained by soda-AQ and kraft pretreatment and effect on the following enzymatic hydrolysis process. *Bioresour. Technol* 207, 361–369. doi:10.1016/j.biortech.2016.01.123

Yang, H., Yoo, C. G., Meng, X., Pu, Y., Muchero, W., Tuskan, G. A., et al. (2020). Structural changes of lignins in natural Populus variants during different pretreatments. *Bioresour. Technol* 295, 122240. doi:10.1016/j.biortech.2019.122240

Yang, J., Wang, Y., Zhang, W., Li, M., Peng, F., and Bian, J. (2021). Alkaline deep eutectic solvents as novel and effective pretreatment media for hemicellulose dissociation and enzymatic hydrolysis enhancement. *Int. J. Biol. Macromol* 193, 1610–1616. doi:10.1016/j.ijbiomac.2021.10.223

Yao, L., Chen, C., Yoo, C. G., Meng, X., Li, M., Pu, Y., et al. (2018a). Insights of ethanol organosolv pretreatment on lignin properties of Broussonetia papyrifera. *ACS Sustain. Chem. Eng* 6, 14767–14773. doi:10.1021/acssuschemeng.8b03290

Yao, L., Cui, P., Chen, X., Yoo, C. G., Liu, Q., Meng, X., et al. (2022). A combination of deep eutectic solvent and ethanol pretreatment for synergistic delignification and enhanced enzymatic hydrolysis for biorefinary process. *Bioresour. Technol* 350, 126885. doi:10.1016/j.biortech.2022.126885

Yao, L., Xiong, L., Yoo, C. G., Dong, C., Meng, X., Dai, J., et al. (2020). Correlations of the physicochemical properties of organosolv lignins from Broussonetia papyrifera their antioxidant activities. *Sustain. Energ. Fuels.* 4, 5114–5119. doi:10.1039/d0se00940g

Yao, L., Yoo, C. G., Meng, X., Li, M., Pu, Y., Ragauskas, A. J., et al. (2018b). A structured understanding of cellobiohydrolase I binding to poplar lignin fractions after dilute acid pretreatment. *Biotechnol. Biofuels.* 11, 96. doi:10.1186/s13068-018-1087-y

Yu, D., Xue, Z., and Mu, T. (2021). Eutectics: Formation, properties, and applications. *Chem. Soc. Rev* 50, 8596–8638. doi:10.1039/d1cs00404b

Zhang, C. W., Xia, S. Q., and Ma, P. S. (2016). Facile pretreatment of lignocellulosic biomass using deep eutectic solvents. *Bioresour. Technol* 219, 1–5. doi:10.1016/j.biortech.2016.07.026

Zhao, Z., Chen, X., Ali, M. F., Abdeltawab, A. A., Yakout, S. M., and Yu, G. (2018). Pretreatment of wheat straw using basic ethanolamine-based deep eutectic solvents for improving enzymatic hydrolysis. *Bioresour. Technol* 263, 325–333. doi:10.1016/j.biortech.2018.05.016

Zhou, X., Huang, T., Liu, J., Gao, H., Bian, H., Wang, R., et al. (2021). Recyclable deep eutectic solvent coupling sodium hydroxide post-treatment for boosting woody/herbaceous biomass conversion at mild condition. *Bioresour. Technol* 320, 124327. doi:10.1016/j.biortech.2020.124327

frontiers | Frontiers in Bioengineering and Biotechnology

TYPE Original Research
PUBLISHED 10 February 2023
DOI 10.3389/fbioe.2023.1146250

OPEN ACCESS

EDITED BY
Xiaojun Shen,
Dalian Institute of Chemical Physics (CAS), China

REVIEWED BY
Shuangquan Yao,
Guangxi University, China
Caoxing Huang,
Nanjing Forestry University, China

*CORRESPONDENCE
Li Shuai,
lishuai@fafu.edu.cn
Jing Liu,
jingliu@fafu.edu.cn

†These authors have contributed equally to this work

SPECIALTY SECTION
This article was submitted to Bioprocess Engineering, a section of the journal Frontiers in Bioengineering and Biotechnology

RECEIVED 17 January 2023
ACCEPTED 31 January 2023
PUBLISHED 10 February 2023

CITATION
Huang L, Bian Z, Li D, Cheng X, Luo X, Shuai L and Liu J (2023), Catalytic conversion of diformylxylose to furfural in biphasic solvent systems.
Front. Bioeng. Biotechnol. 11:1146250.
doi: 10.3389/fbioe.2023.1146250

Catalytic conversion of diformylxylose to furfural in biphasic solvent systems

Lizhen Huang[1†], Zelun Bian[1†], Dalin Li[1†], Xin Cheng[1], Xiaolin Luo[1,2,3], Li Shuai[1,2*] and Jing Liu[1,2*]

[1]College of Materials Engineering, Fujian Agriculture and Forestry University, Fuzhou, China, [2]National Forestry and Grassland Administration Key Laboratory of Plant Fiber Functional Materials, Fuzhou, China, [3]Jiangsu Provincial Key Laboratory of Pulp and Paper Science and Technology, Nanjing Forestry University, Nanjing, China

Biobased furfural is a sustainable alternative to petrochemical intermediates for bulk chemicals and fuel production. However, existing methods for the conversion of xylose or lignocelluloses in mono-/bi-phasic systems to furfural involve non-selective sugar isolation or lignin condensation, limiting the valorisation of lignocelluloses. Herein, we used diformylxylose (DFX), a xylose derivative that is formed during the lignocellulosic fractionation process with formaldehyde protection, as a substitute for xylose to produce furfural in biphasic systems. Under kinetically optimized conditions, over 76 mol% of DFX could be converted to furfural in water-methyl isobutyl ketone system at a high reaction temperature with a short reaction time. Finally, isolation of xylan in eucalyptus wood as DFX with formaldehyde protection followed by converting DFX in a biphasic system gave a final furfural yield of 52 mol% (on the basis of xylan in wood), which was more than two times of that without formaldehyde. Combined with the value-added utilization of formaldehyde-protected lignin, this study would enable the full and efficient utilization of lignocellulosic biomass components and further improve the economics of the formaldehyde protection fractionation process.

KEYWORDS

furfural, diformylxylose, xylose, biphasic system, kinetics, fractionation

Introduction

Furfural has been recognized as a versatile intermediate to synthesize chemicals (e.g., furfuryl alcohol and furoic acid), fuels (e.g., methylfuran and long-chain alkanes), and functional materials (e.g., furfuryl alcohol and furfural-acetone resins) (Lee and Wu, 2021). As a result, the annual global production of furfural is now close to one million tons, and its demand continues to increase (Jaswal et al., 2022). Although furfural could be commercially produced from raw materials with high xylose content such as corn cob, the production of furfural from lignocelluloses such as wood and corn stover is inefficient, which would restrict the economics and development of biorefining industries (Luo et al., 2020).

Brønsted acid-catalyzed dehydration of xylose in aqueous media is a practical method for furfural production (Kabbour and Luque, 2020). However, in addition to the dehydration reaction, Brønsted acid can also catalyze other side reactions such as furan ring-opening and furfural condensation, resulting in low furfural yield (20–40 mol%) (Weingarten et al., 2010). For this reason, a biphasic solvent system consisting of water and organic solvent that is not miscible with water, has been developed to alleviate such undesirable side reactions (Román-

Leshkov et al., 2006). In general, the solubility of furfural in the organic phase (e.g., toluene and methyl isobutyl ketone) is much higher than that in the aquous phase while the mineral acid is more soluble in water (Lin et al., 2021). Therefore, the furfural formed in the aqueous phase could be immediately transferred to the organic phase *via in-situ* extraction, which would effectively alleviate the acid-catalyzed side reactions of furfural in the aqueous phase and thus increase the yield of furfural (30–70 mol%) (Román-Leshkov et al., 2006; Shuai and Luterbacher, 2016; Lin et al., 2021).

Although the biphasic solvent system is promising for conversion of xylose to furfural, isolating xylose from lignocelluloses *via* acid-catalyzed hydrolysis of hemicelluloses in aqueous media is not selective, which highly restricts the application of the pathway (Questell-Santiago et al., 2018). Since Brønsted acid can simultaneously catalyze the hydrolysis of hemicelluloses and the dehydration of monosaccharides, some studies attempted to directly convert hemicelluloses in lignocellulosic feedstocks (e.g., eucalyptus, and bagasse) to furfural by a one-pot method in biphasic solvent systems (Matsagar et al., 2017). However, in the one-pot conversion process, lignin presents negative effects on the xylose conversion and furfural formation (Lamminpää et al., 2015). Degradation products derived from cellulose and lignin may also complicate the product mixture, which would be not conducive to subsequent furfural separation (Daorattanachai et al., 2013). Moreover, acid can also trigger severe lignin condensation during the one-pot conversion process, significantly devaluing lignin in other refining processes such as hydrogenolysis (Shuai et al., 2016; Gong et al., 2022; Luo et al., 2022).

To overcome the inherent defects of the one-pot conversion method, a two-step method, i.e. separating xylose or its derivative from lignocellulose and then converting it into furfural, remains a more attractive strategy if the condensation of lignin and the selectivity of hemicellulose hydrolysis to xylose could be effectively controlled (Questell-Santiago et al., 2018; Kabbour and Luque, 2020; Jaswal et al., 2022). Based on the acetalization of hydroxyl groups of carbohydrates with formaldehyde, Shuai et al. (2016) developed an effective method to fractionate the main components from lignocelluloses, which could simultaneously produce uncondensed lignin and stabilized xylose derivatives, i.e., diformylxylose (DFX). The conversion of DFX to value-added products has rarely reported. Therefore, the study aimed to investigate the acid-catalyzed conversion of DFX to furfural in different solvent systems. We also examined the kinetic behavior of DFX to furfural and compared the fractionation methods with or without formaldehyde addition for furfural production. This study validated the feasibility of a two-step method for furfural production, which would improve the overall refining efficiency of lignocelluloses.

Materials and methods

Materials

Xylose (99%), paraformaldehyde (98%), n-hexadecane (99%), methyl isobutyl ketone (99%), dichloromethane (98%), tetrahydrofuran (98%), dimethyl sulfoxide (98%), furfural (98%) were purchased from Aladdin® Chemicals (Shanghai City, China). Toluene (98%) and concentrated hydrochloric acid (37 wt%) were ordered from XiLONG SCIENTIFIC (Guangzhou City, China), while γ-valerolactone (98%) was obtained from Macklin Inc. (Shanghai City, China). The procedures that used to synthesize DFX were detailed in Supplementary Materials. Synthesized DFX was characterized by Gas Chromatography-Mass Spectrometry (GC-MS) (Supplementary Figure S1) and its purity was determined as 98% by GC measurement based on an effective carbon number (ECN) method (Scanlon and Willis, 1985). Eucalyptus powder (40–60 mesh) was provided by Fujian Qingshan Paper Co., Ltd. (Sanming City, China).

Acid-catalyzed conversion of DFX

Brønsted acid-catalyzed conversions of DFX and xylose were performed with monophasic or biphasic solvent systems in a glass-lined stainless steel reactor. For example, for the conversion of DFX with a biphasic solvent system, DFX, an internal standard (i.e., n-hexadecane) and a magnetic stirrer were successively added into the reactor that had been pre-loaded with HCl aqueous solution and organic solvent. The reactor was pressurized with 2 MPa N_2 and then heated to the reaction temperature for a fixed reaction time. After that, the reactor was immediately cooled to room temperature with cold water and the sample solution was transferred into a centrifuge tube. The reactor was washed with deionized water three times and the washing solution was also poured into the centrifuge tube. The mixed solution in the centrifuge tube was fully separated into two phases through centrifugation at 10,000 rpm for 15 min, in which the organic phase was directly sampled and analyzed by GC. The aqueous phase was further diluted, fixed to a specific volume in a volumetric flask, and then subjected to high-performance liquid chromatography (HPLC) analysis, respectively.

Lignocellulose fractionation and partition coefficient measurements

The hydrolysis of xylan in eucalyptus to obtain xylose or DFX was conducted in the GVL-water mixture according to a reported fractionation method with or without formaldehyde addition (Shuai et al., 2016). The partition coefficient of DFX or furfural in a biphasic system was measured by dissolving it (250 mg) in the mixture of water (1 mL) and organic solvent (1 mL) at room temperature, and measuring its concentration in two phases *via* GC and HPLC methods mentioned below (Lin et al., 2021).

Measurements of the ECNs of DFX and furfural

The ECNs of DFX and furfural were measured by a reported method that used n-hexadecane as an internal standard (Scanlon and Willis, 1985). First, DFX, furfural and n-hexadecane were dissolved in methyl isobutyl ketone to obtain a mother solution. This solution was further diluted by methyl isobutyl ketone into solutions with different concentration gradients. These solutions

were measured by GC, and the ECNs of DFX and furfural were calculated as follows:

$$N_0 = N_{is}\frac{A_0 \times C_{is}}{A_{is} \times C_0} \quad (1)$$

where C_{is} and C_0 are the concentrations of the internal standard and determinand (DFX or furfural) in prepared solutions; A_{is} and A_0 are the peak area of the internal standard and determinand (DFX or furfural) measured by GC; N_{is} is the reported ECN, i.e., 16, of the internal standard (Scanlon and Willis, 1985).

Based on the Eq. 1, the ECNs of DFX and furfural for the solutions with different concentration gradients, and their averages were calculated and listed in Supplementary Table S1, which would be used to calculate the concentrations of DFX and furfural in reaction samples.

Analytical methods

The concentrations of DFX, xylose, and furfural in the diluted aqueous phase or monophasic co-solvent (i.e., the miscible mixture of water and organic solvent) were quantitatively determined by HPLC (Shimazu LC-20A) based on the external standard method. The HPLC was equipped with a refractive index detector (RID) and a Shodex SUGARSH-1011 column (8 × 300 mm^2) using a sulfuric acid aqueous solution with a pH value of 2.2 as a mobile phase. The flow rate of the mobile phase was 0.8 mL/min, while the detector temperature, column temperature, sample injection volume, and detection time were fixed at 35°C, 30°C, 3 μL, and 60 min. After the fractionation of eucalyptus, the concentration of xylose or DFX in the GVL-water mixture was also analyzed by this HPLC method.

Based on the ECN method (Scanlon and Willis, 1985; Shuai et al., 2016), the molar amounts of DFX and furfural in the organic phase were determined by GC (Techcomp SCION 436C) equipped with a flame ionization detector (FID) and a capillary column (Techcomp SCION-5) using N_2 as carrier gas at 1.5 mL/min. The column temperature program was fixed as follows: held at 50°C for 5 min, heated from 50°C to 300°C at 10°C/min, and held at 300°C for 5 min. The inlet temperature, split ratio and injection volume for GC-FID measurements were fixed as 300°C, 100:1, and 1 μL. The molar amount of DFX or furfural in the organic phase was calculated as:

$$\frac{n_1 N_1}{n_2 N_2} = \frac{A_1}{A_2} \quad (2)$$

where n_1 is the molar amount (mmoL) of the internal standard (i.e., n-hexadecane) added into the reactor; n_2 is the molar amount (mmoL) of the product formed in the organic phase; N_1 and N_2 are the ECNs of the internal standard and product; A_1 and A_2 are the measured peak area of the internal standard and product in the GC-FID chromatogram.

Since no xylose was detected in the organic phase that was not miscible with water, the conversion of DFX and the yield of product (xylose or furfural) in biphasic phases were calculated as:

$$X_{DFX} = \frac{n_{DFX} - \left(n_{DFX-org} + C_{DFX-aqu} \times V\right)}{n_{DFX}} \times 100 \quad (3)$$

$$Y_{xyl} = \frac{C_{xyl-aqu} \times V}{n_{DFX}} \times 100 \quad (4)$$

$$Y_{fur-aqu} = \frac{C_{fur-aqu} \times V}{n_{DFX}} \times 100 \quad (5)$$

$$Y_{fur-org} = \frac{n_{fur-org}}{n_{DFX}} \times 100 \quad (6)$$

$$Y_{fur-tol} = Y_{fur-aqu} + Y_{fur-org} \quad (7)$$

$$S_{fur} = \frac{Y_{fur-tol}}{X_{DFX}} \times 100 \quad (8)$$

where X_{DFX} is the conversion (mol%) of DFX after reaction; n_{DFX} is the initial molar amount (moL) of DFX added into the reactor; $n_{DFX\text{-}org}$ and $n_{fur\text{-}org}$ are the molar amounts (moL) of DFX and furfural measured in organic phase; $C_{DFX\text{-}aqu}$, $C_{xyl\text{-}aqu}$, $C_{fur\text{-}aqu}$, and V are the concentration (mol/L) of DFX, xylose, and furfural measured in the aqueous phase, and the total volume (L) of the aqueous phase after dilution; $Y_{fur\text{-}aqu}$ and $Y_{fur\text{-}org}$ are the yield (mol%) of furfural obtained in the aqueous and organic phases; Y_{xyl} is the yield (mol%) of xylose in the aqueous phase; $Y_{fur\text{-}tol}$ and S_{fur} are the total yield (mol%) and selectivity (%) of furfural in the two phases.

For the monophasic reaction system, the conversion of DFX and the yield of product (xylose or furfural) were calculated based on the analysis results of HPLC in water or miscible co-solvent mixture. In particular, the total concentration of DFX, xylose, or furfural in two phases used for subsequent kinetic analysis was approximately calculated according to its measured or calculated molar amounts (moL), and the mass and density of the biphasic solvents that were initially added to the reactor.

$$C_{tol} = \frac{n_{tol}}{0.001 \times \left(m_{aqu}/\rho_{aqu} + m_{org}/\rho_{org}\right)} \quad (9)$$

where C_{tol} and n_{tol} are the total concentration (moL/L) and molar amounts (moL) of DFX, xylose, or furfural in two phases; m_{aqu} and m_{org} are the mass (g) of HCl aqueous solution and organic solvent initially added into the reactor; ρ_{aqu} and ρ_{org} are densities of the HCl aqueous solution and organic solvent.

The contents of main components in eucalyptus wood were analyzed by a reported two-step hydrolysis method (Sluiter et al., 2008), and the results were listed in Supplementary Table S2.

Results and Discussion

Development of a biphasic solvent system

For Brønsted acid-catalyzed dehydration of monosaccharides (e.g., xylose and glucose) to furanics (e.g., furfural, and 5-hydroxymethylfurfural), previous studies reported that the solvation effect presents an important role in controlling the product yield and selectivity (Mellmer et al., 2014; Shuai and Luterbacher, 2016; Walker et al., 2018). By using HCl as a catalyst, three typical monophasic co-solvent systems, i.e., water-tetrahydrofuran (W-THF), water-γ-valerlactone (W-GVL), and water-dimethyl sulfoxide (W-DMSO), and three biphasic solvent systems, i.e., water-toluene (W-T), water-dichloromethane (W-DCM), and water-methyl isobutyl ketone (W-MIBK), were investigated for the conversion of DFX to furfural (Figure 1A).

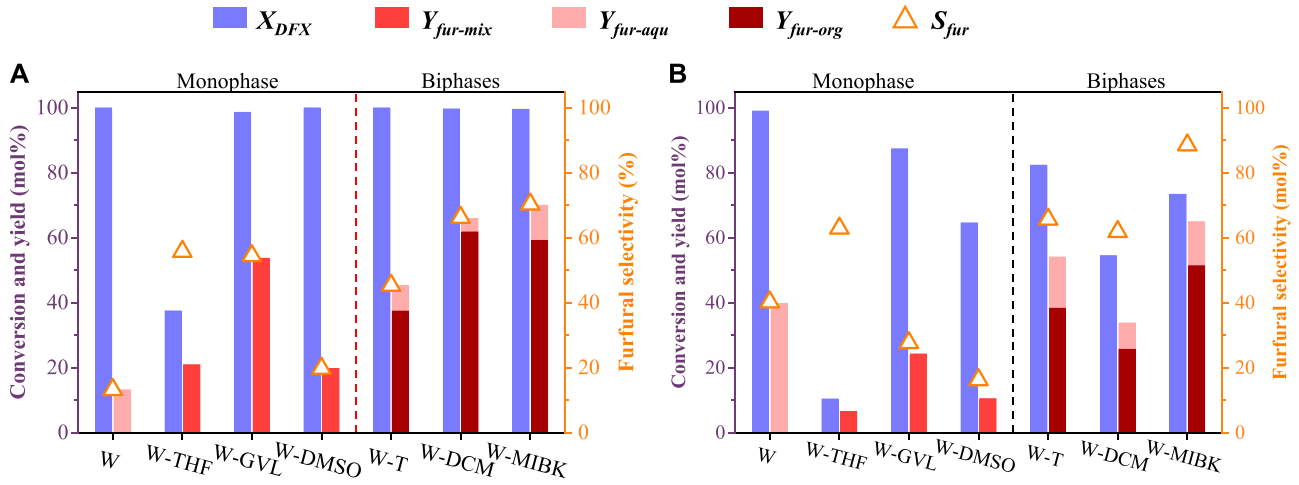

FIGURE 1
Conversion of DFX to furfural in different solvent systems at a HCl concentration and a reaction time of **(A)** 0.4 mol/L and 30 min and **(B)** 0.2 mol/L and 10 min. Other reaction conditions: DFX 0.5 g, 170°C, 2 g HCl aqueous solution and 8 g organic solvent, 400 rpm.

For comparison, an aqueous HCl solution (W) was also investigated as a control.

Under mild reaction conditions (10 min and 0.2 M H^+), the conversion of DFX (99%, Figure 1B) in the W system was higher than that in other mixing solvent systems. This is mainly due to that the apparent concentration of hydrogen ions in water was diluted by organic solvent added into the monophasic or biphasic solvent system (Lin et al., 2021). For the monophasic or biphasic solvent systems, the W-GVL system achieved the highest DFX conversion (87%, Figure 1B). The reported molecular dynamics (MD) simulation results show that the solvation effects, i.e., adding co-solvent (e.g., GVL) to the acidic aqueous solution increases the local density of hydrated hydrogen ions near the reactant, is conducive to improving the hydrolysis efficiency of biomass-derived oxygenates such as cellobiose and ethyl tert-butyl ether (Walker et al., 2018). GVL may possess a similar solvation effect on the conversion of DFX in the monophasic co-solvent system (Mellmer et al., 2014). However, THF may exhibit the opposite solvation effect (Lee and Wu, 2021; Lin et al., 2021) because the conversion of DFX in W-THF system was much lower than those in other solvent systems under the same reaction conditions (Figure 1).

As the reaction conditions (30 min and 0.4 M H^+) intensified, the DFX in all solvent systems except the W-THF system was almost completely converted (Figure 1A). However, the yield and selectivity of furfural in monophasic systems were lower than those in biphasic systems except the W-T system (Figure 1). This would be mainly caused by the severe condensation of furfural catalyzed by acid in the monophasic systems (Shuai and Luterbacher, 2016; Lee and Wu, 2021). For example, with the nearly complete conversion of DFX in the W system, increasing reaction time (10–30 min) and H^+ concentration (0.2–0.4 mol/L) resulted in the decrease of furfural yield and selectivity from 40% to 13% (Figure 1). Based on the MD simulations, the solvation free energies (ΔG_{sol}) of furfural in water-immiscible organic solvents such as toluene, MIBK, and DCM were reported to be much lower than that in water (Lin et al., 2021). As a result, most of the furfural formed in the aqueous phase could be quickly extracted into the organic phase, which would significantly reduce such adverse side reactions. For the biphasic systems, the ΔG_{sol} of furfural in MIBK and DCM were lower than that in toluene, making the extraction rate of the former towards furfural higher than the latter (Lin et al., 2021). In addition to other solvation effects such as solubility, this may be the key reason why the yield and selectivity of furfural in the W-MIBK and W-DCM systems were higher than those of W-T and monophasic systems (Lee and Wu, 2021; Lin et al., 2021).

The transfer process of reactants and products in the two phases is useful to identify the influence of different biphasic systems on the conversion efficiency of DFX to furfural. Based on the chromatographies of the standards, only DFX and furfural were detected by GC in the organic phase (Figure 2A), whereas DFX, xylose, and little furfural were present in the aqueous phase (Figure 2B). Therefore, the conversion of DFX and the interphase transfer of furfural in the biphasic system could be simply described as follows (Figure 2C): 1) DFX was dissolved in the organic and aqueous phases according to its partition coefficient (Figure 2D). 2) Acid catalyzed the hydrolysis of DFX to xylose in the aqueous phase. When the concentration of DFX in the aqueous phase decreased, DFX was transferred from the organic phase to the aqueous phase. 3) In the aqueous phase, the acid further catalyzed the dehydration of xylose to furfural, which was rapidly extracted to the organic phase. However, acid-catalyzed furfural condensation competed with the *in-situ* extraction of furfural by organic solvents, which resulted in some unindentified compounds in the liquid chromatogram (Figure 2B).

In the above DFX conversion and furfural transfer process, it was found that in addition to the ΔG_{sol} effect, the partition coefficient of DFX ($[DFX]_{org}/[DFX]_{aqu}$) in the W-T system was slightly lower than that in W-MIBK system (Figure 2D), which would lead to relatively low solubility of DFX in toluene and the rapid conversion of DFX to xylose in the aqueous phase (Figure 1B). However, the partition coefficient of furfural ($[furfural]_{org}/[furfural]_{aqu}$) in the W-MIBK system was three times more than

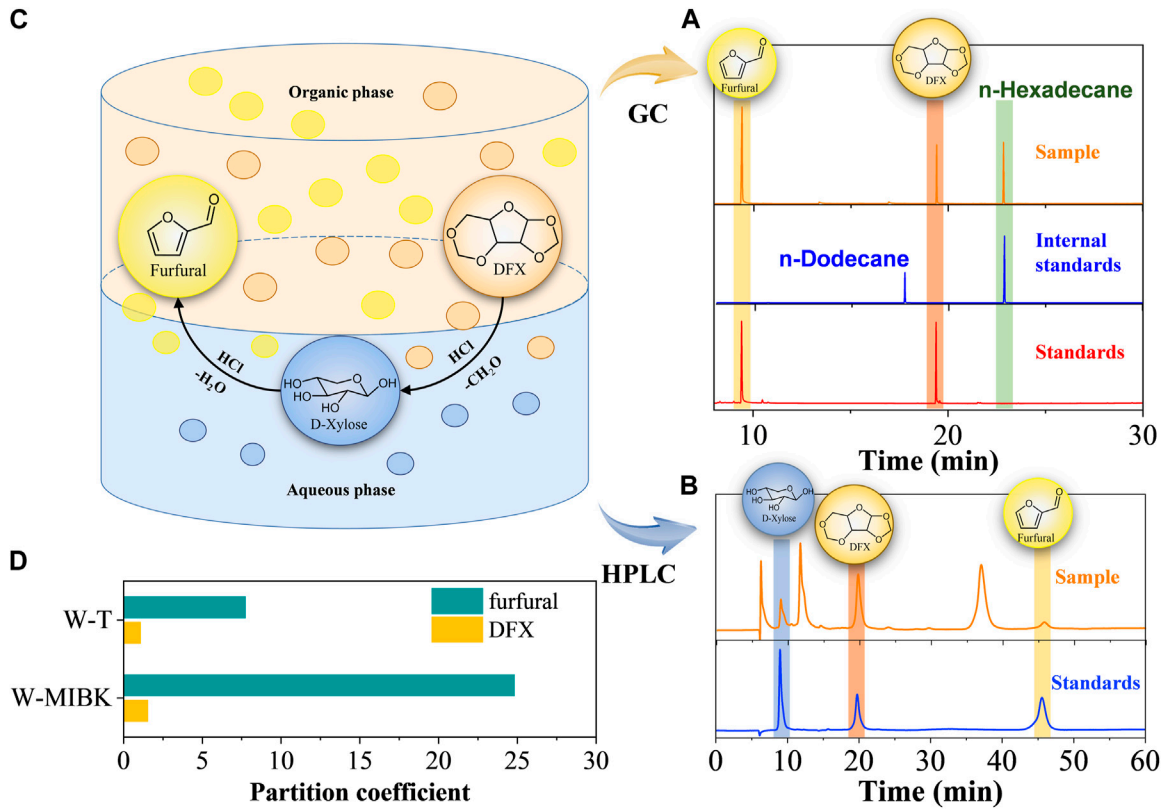

FIGURE 2
(A) GC and **(B)** HPLC analysis of samples and standards; **(C)** proposed transfer process of reactant and products in the biphasic system; **(D)** the partition coefficients of DFX and furfural in the biphasic system.

that of the W-T system (Figure 2D), which would contribute to the extraction of more furfural from the aqueous phase to the MIBK phase, thereby improving the final yield and selectivity of furfural (Figure 1) after complete conversion. Since the DFX conversion rate (Figure 1B) and furfural selectivity (Figure 1A) of W-MIBK system was slightly higher than those of W-DCM system, the biphasic W-MIBK system was investigated for the production of furfural from DFX.

Conversion of DFX to furfural in W-MIBK system

Since the mass transfer efficiencies of reactant and products were reported to be much faster than their reaction rates (Weingarten et al., 2010), stirring speeds showed no obvious effects on the DFX conversion, and furfural yield and selectivity in aqueous solution (Supplementary Figure S2A). However, in addition to solvation effects (e.g., ΔG_{sol} and solubility), stirring is also an important factor affecting the transfer and conversion efficiencies of DFX and furfural in the biphasic system. Under the same reaction conditions (170°C, 30 min, and 0.4 M H^+), stirring at 600 rpm was beneficial to improve the conversion of DFX from 82% to 99% and the yield of furfural from 37% to 72% in the W-MIBK system (Supplementary Figures S2B), compared with the reactions without stirring. Similar phenomena were also observed for W-T and W-DCM systems (Supplementary Figures S2C, D). Possibly due to the accelerated furfural condensation, further increasing the stirring speed led to a slight decrease in the yield and selectivity of furfural (Supplementary Figures S2). Besides, the concentration of HCl in the aqueous phase also affected the conversion and selectivity of DFX to furfural. When the concentration of HCl in the aqueous phase increased from 0.1 M to 0.2 M, the furfural yield increased from 57% to 73% (Figure 3A), indicating that high-concentration acid could improve the dehydration efficiency of DFX-derived xylose to furfural. However, the furfural yield and selectivity decreased from 73% to 59% after increasing the acid concentration to 0.8 M (Figure 3A).

Without changing the total mass of the two solvents, increasing the mass ratio of MIBK to HCl aqueous solution in the W-MIBK system would be beneficial to improve the extraction efficiency of furfural from aqueous phase to organic phase, which may favor increasing the final furfural yield and selectivity. As expected, with the increase of the mass ratio of MIBK to HCl aqueous solution from 1:1 to 4:1, the yield and selectivity of furfural increased gradually (Figures 3B, C). However, when the mass ratio of MIBK to HCl aqueous solution further increased to 16:1, the DFX conversion dramatically decreased from about 90% to less than 20%. For the production of furfural in the biphasic system using xylose as a substrate, xylose was only dissolved in the aqueous phase (Lin et al., 2021). Unlike xylose, DFX was soluble in both the aqueous and organic phases. Since the partition coefficient of DFX ($[DFX]_{org}$/

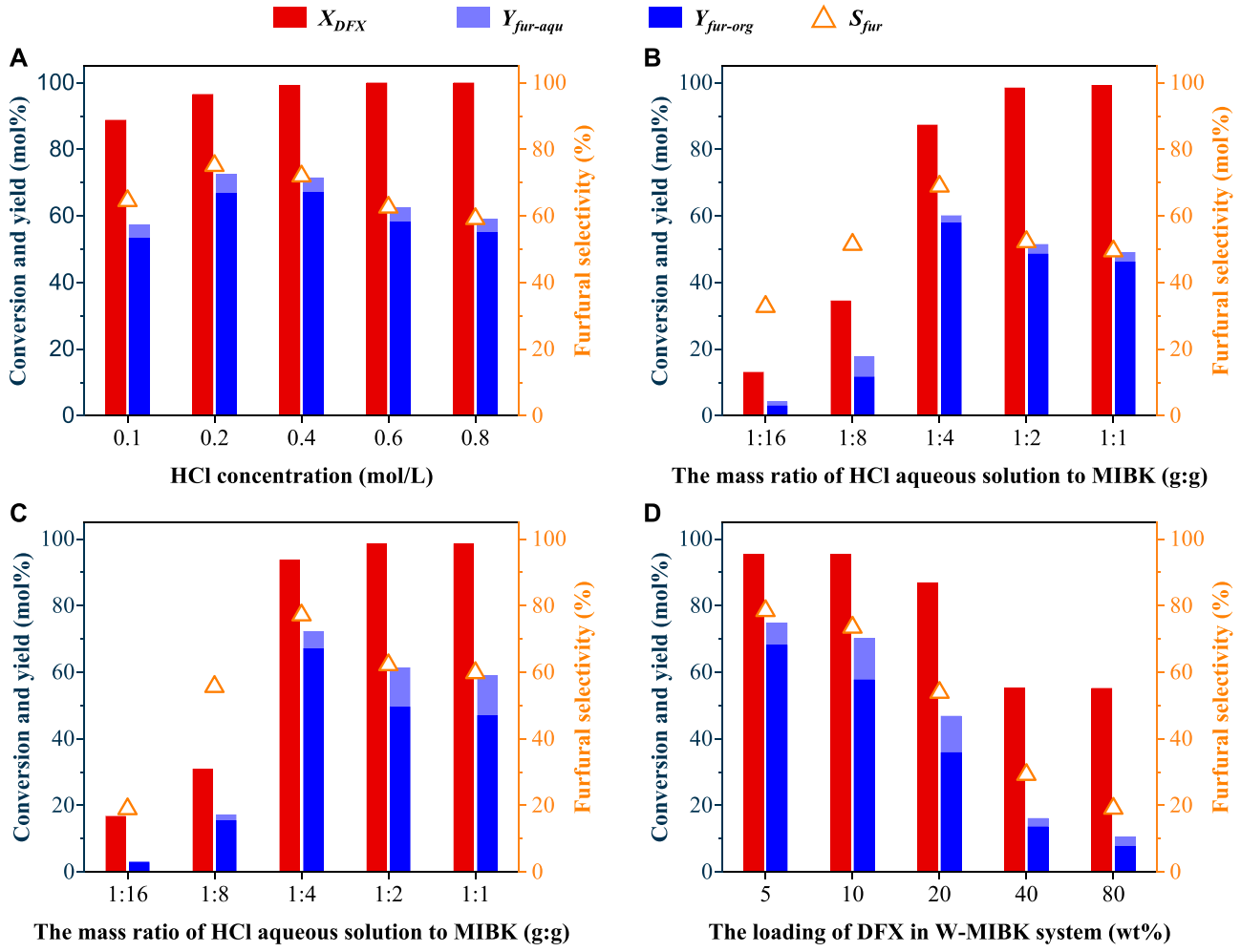

FIGURE 3
Effects of **(A)** acid concentration in aqueous phase, **(B)** and **(C)** solvent composition, and **(D)** DFX loading on the conversion efficiency of DFX to furfural in theW-MIBK system. The stirring speed and total mass of solvents for all reactions were 600 rpm and 10 g, the acid concentration used in Figures B~D was 0.2 mol/L, and the DFX loading for Figure **(A–C)** was 5 wt%. A 1:4 (wt:wt) mass ratio of HCl aqueous solution to organic solvent was used for Figure **(A, D)**. Other reaction conditions of **(A)** and **(B)**: 170°C, 30 min; **(C, D)**: 185°C, 10 min.

$[DFX]_{aqu}$) in the W-MIBK system is greater than one (Figure 1D), increasing the MIBK proportion will be not conducive to the transfer of DFX from the organic phase to the aqueous phase, the hydrolysis of DFX to xylose as well as the dehydration reaction of xylose to furfural.

For W-MIBK system with a 4:1 mass ratio of MIBK to HCl aqueous solution, DFX loading did not show obvious effects on the DFX conversion as well as furfural selectivity when the loading of DFX in the biphasic system was within 10 wt% (Figure 3D). Unexpectedly, DFX conversion and furfural selectivity significantly decreased with the further increase in DFX loading, possibly due to the solubility limitation and intensified side reactions. Further explorations such as regulating the partition coefficients of reactants and products in a biphasic system would be necessary to clarify the reasons behind this adverse effect and to obtain high DFX-to-furfural efficiency at high DFX loading.

Kinetic modeling of DFX conversion to furfural in the W-MIBK system

With a 4:1 (g:g) mass ratio for the W-MIBK system and a 5 wt% DFX loading, the kinetic modeling of DFX conversion to furfural was conducted at varied temperatures and HCl concentrations (Figure 4). Based on the products measured in two phases, the reaction pathway of DFX in the biphasic system was proposed in Scheme 1. It consists of the hydrolysis of DFX to xylose (reaction 1), the dehydration of xylose to furfural (reaction 2), and furfural degradation (reaction 3).

The reactions of 2 and 3 in biphasic systems are reported to be pseudo-first-order reactions (Weingarten et al., 2010). The disappearing trends of DFX as depicted in Figure 4 also coincides with the pseudo-first-order reaction. Thus, the overall rate equations for these three reactions can be written as:

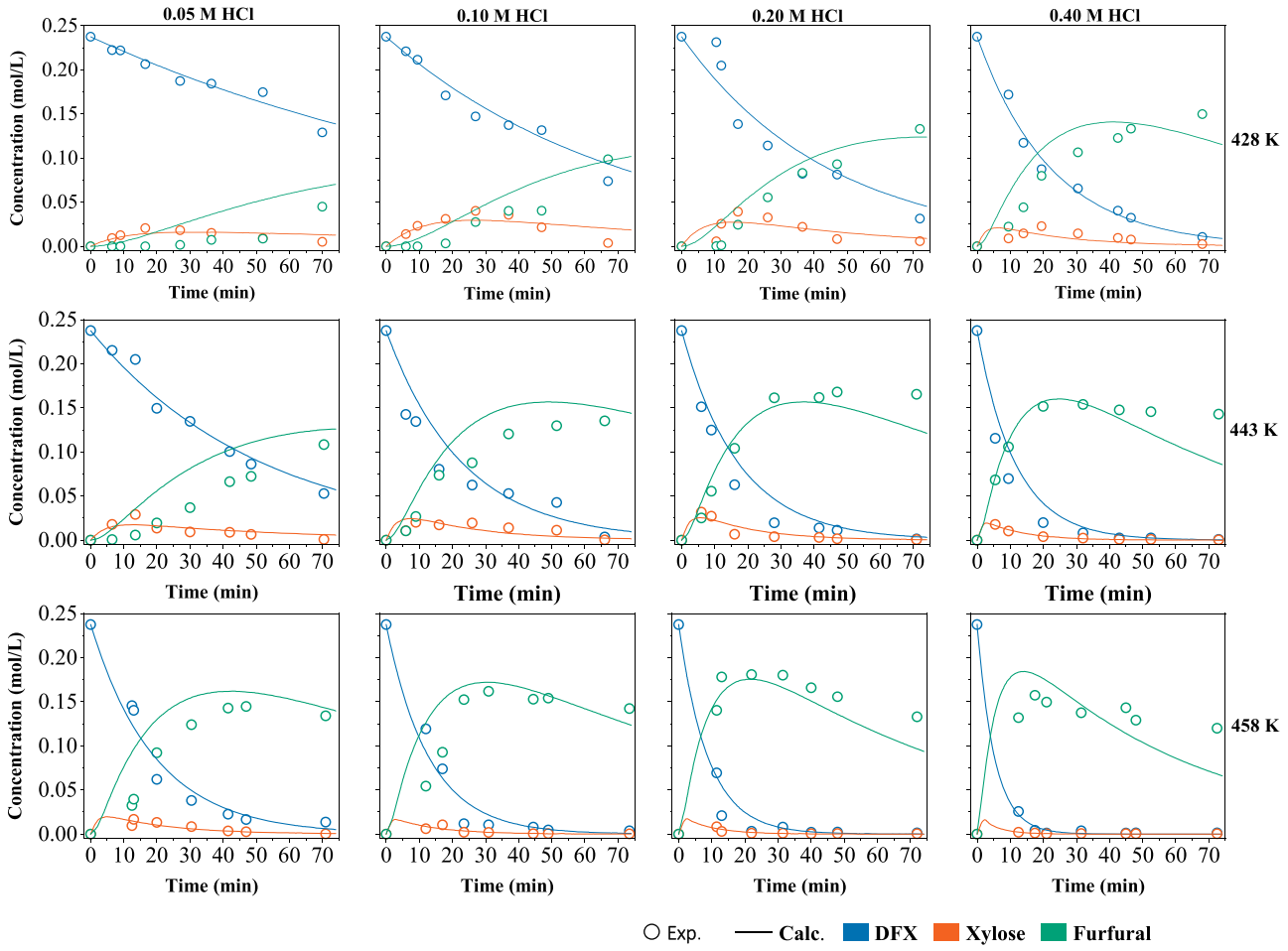

FIGURE 4
Measured concentrations of DFX, xylose and furfural in W-MIBK system and their kinetically predicted plots. Reaction conditions: DFX 0.5 g, 155–185°C, 0–74 min, 2 g HCl aqueous solution and 8 g MIBK, HCl 0.05–0.4 M, 600 rpm.

$$\frac{dC_{DFX}}{dt} = -k_1 C_{DFX} \tag{10}$$

$$\frac{dC_{xyl}}{dt} = k_1 C_{DFX} - k_2 C_{xyl} \tag{11}$$

$$\frac{dC_{fur}}{dt} = k_2 C_{xyl} - k_3 C_{fur} \tag{12}$$

where C_{DFX}, C_{xyl}, and C_{fur} are the total concentrations (mol/L) of DFX, xylose, and furfural in two phases; k_1, k_2, and k_3 present the apparent rate constants of the reactions 1–3 in Scheme 1 (min^{-1}); t is the reaction time (min) that considering the heating process ($t = t_{reaction} + t_{heating}/2$) (Luo et al., 2013).

Based on the initial conditions ($t = 0$ min, $C_{DFX} = C^0_{DFX}$; $C_{xyl} = 0$ mol/L, and $C_{fur} = 0$ mol/L), the time-dependent expressions of C_{DFX}, C_{xyl}, and C_{fur} were integrated as:

$$C_{DFX} = C^0_{DFX} e^{-k_1 t} \tag{13}$$

$$C_{xyl} = \frac{k_1 C^0_{DFX}}{k_2 - k_1}\left(e^{-k_1 t} - e^{-k_2 t}\right) \tag{14}$$

$$C_{fur} = \frac{k_1 k_2 C^0_{DFX}}{k_2 - k_1}\left(\frac{e^{-k_1 t} - e^{-k_3 t}}{k_3 - k_1} - \frac{e^{-k_2 t} - e^{-k_3 t}}{k_3 - k_2}\right) \tag{15}$$

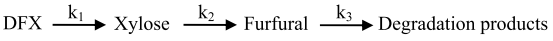

SCHEME 1
The reaction pathway of DFX in the biphasic system.

Based on the least squares method, the apparent rate constants of these kinetic equations were fitted in Table 1. As the fitted rate constants are a function of the acid concentration (Supplementary Figure S3), the Arrhenius equation can be modified as:

$$k = k_0 [C_{acid}]^{\alpha} e^{-\frac{Ea}{RT}} \tag{16}$$

where k_0 and Ea are the pre-exponential factor (min^{-1}) and apparent activation energy (J/mol) of these kinetic models; C_{acid} is the concentration of acid in the aqueous phase (mol/L); α is the reaction order of acid; R and T are the ideal gas constant (J/mol/K) and the reaction temperature (K).

For reactions 1 and 2 in Scheme 1, the rate constants of k_1 and k_2 were exponentially correlated with the concentration of acid in the

TABLE 1 The rate constants of the reactions 1–3 in Scheme 1 at different reaction temperatures and acid concentrations.

HCl concentration (mol/L)	Rate constants (min^{-1})								
	428 *K*			443 *K*			458 K		
	k_1	k_2	k_3	k_1	k_2	k_3	k_1	k_2	k_3
0.05	0.007	0.086	0.006	0.019	0.207	0.008	0.052	0.485	0.010
0.10	0.014	0.077	0.008	0.043	0.307	0.009	0.078	0.925	0.011
0.20	0.022	0.137	0.010	0.058	0.392	0.012	0.113	1.306	0.015
0.40	0.045	0.383	0.014	0.087	0.852	0.017	0.190	2.116	0.019

TABLE 2 Pre-exponential factor, apparent activation energy, and the reaction order of acid for the developed kinetic models.

	k_0 (min^{-1})	*Ea* (kJ/moL)	α
k_1	1.17×10^{10}	91.7	0.72
k_2	1.87×10^{13}	111.1	0.69
k_3	2.44×10^{5}	55.3	1.00

aqueous phase (Supplementary Figures S3A, B). After logarithmic transformation, Eq. 16 was modified as

$$lnk = ln\,k_0 + \alpha lnC_{acid} - \frac{Ea}{R} \times \frac{1}{T} \tag{17}$$

However, the relationship between k_3 and acid concentration was linear (Supplementary Figure S3C). As a result, the reaction order of acid for k_3 was fixed as 1.0, and Eq. 16 was rearranged as

$$ln\left(\frac{k}{C_{acid}}\right) = ln\,k_0 - \frac{Ea}{R} \times \frac{1}{T} \tag{18}$$

Based on the multivariate linear regression, the kinetic parameters (k_0, *Ea*, and α) of Eqs.16–18 were further fitted in Table 2. Based on these parameters, experimental results were well plotted against the predicted data (Supplementary Figure S4, $R^2 > 0.92$), showing good fits for these kinetic models towards the conversion of DFX to furfural and furfural degradation in the biphasic system.

As shown in Table 2, the activation energies and reaction orders of acid for the reactions 1 and 2 in Scheme 1 are comparable, indicating that the sensitivities of these two reactions to the temperature and acid concentration would be similar. Non-etheless, for the reactions conducted at the same temperature and acid concentration, the rate constant of the reaction 1 is lower than that of the reaction 2 by nearly an order of magnitude (Table 1). Unlike the production of furfural using xylose as a substrate, the reaction 1 thus becomes the rate-determining step for the DFX-to-furfural conversion process in the biphasic system. This is mainly caused by the low partition coefficient of DFX ($[DFX]_{org}/[DFX]_{aqu}$) in the biphasic system (Figure 1D), which limits the overall hydrolysis rate of DFX to xylose. Because the solubility of mineral acid catalysts such as HCl in the MIBK phase is almost negligible. DFX can be catalyzed to xylose by the acid in the aqueous phase only when DFX in the organic phase is gradually transferred to the aqueous phase.

Since the activation energies and pre-exponential factors for the first two reactions are higher than those of the reaction 3 (Table 2), high reaction temperatures and short reaction times would be preferred for maximizing the furfural yield. Although increasing acid concentration favors improving the reaction rates (k_1 and k_2) of the reactions 1 and 2, furfural degradation (the reaction 3 with a α of 1.0) is more acid-dependent than the first two reactions ($\alpha < 1.0$). As a result, a high acid concentration would decrease furfural selectivity (Figure 3A). According to the measured data and fitting plots (Figure 4), a maximum furfural yield of 76 mol% (Supplementary Figure S5) was eventually optimized at 185°C for 22 min with a moderate acid concentration of 0.2 M. This yield was two times that obtained in the monophasic aqueous solution (Figure 1), validating the distinct advantage of the biphasic system such as W-MIBK for converting DFX to furfural.

Effect of fractionation process on the furfural production

According to the previously-reported fractionation method (Shuai et al., 2016), the hydrolysis of xylan in eucalyptus to xylose or DFX was conducted in GVL-water (9:1, v/v) mixture without or with formaldehyde addition. For the fractionation with formaldehyde, 136.3 g of DFX was obtained from 1,000 g of eucalyptus wood that containing 171.3 g xylose (Figure 5). However, under the same fractionation conditions, the formaldehyde-free fractionation method only yielded 55.5 g of xylose. Assuming that the conversion efficiency of xylose in a biphasic system such as W-MIBK is the same as that of DFX (76 mol% furfural yield, Figure 4), the final furfural yield (on xylan in eucalyptus) for the formaldehyde-containing method was found to be twice that of the fractionation without formaldehyde (Figure 5). This discrepancy mainly lies in the acetalization of xylose with formaldehyde that can effectively inhibit the acid-catalyzed degradation of xylose during fractionation process (Shuai et al., 2016; Questell-Santiago et al., 2018).

Although the one-pot method can simplify the furfural production process (Matsagar et al., 2017), it inevitably causes the condensation of lignin under acidic conditions, devaluing the utilization efficiency of renewable aromatic carbon resources. With formaldehyde protection, Shuai's study reported that lignin condensation could be effectively avoided in the formaldehyde-involved fractionation process (Shuai et al., 2016). Compared to one-pot furfural production methods (Matsagar et al., 2017; Kabbour and Luque, 2020; Jaswal et al., 2022), the two-step method consisting of formaldehyde-protected fractionation and

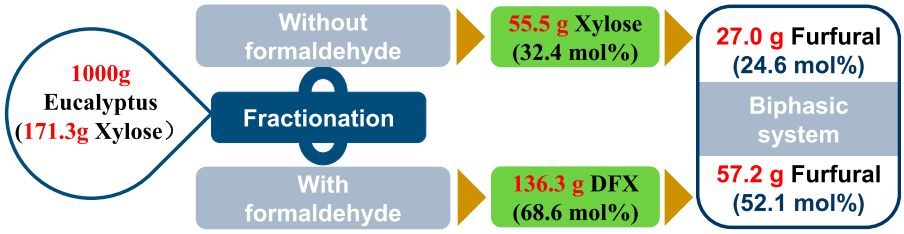

FIGURE 5
Comparsion of fractionation without or with formaldehyde addition for furfural production.

biphasic conversion could not only obtain comparable furfural yield (52 mol%) but also provide an alternative strategy for the valorization of lignocelluloses.

Conclusion

We have shown that the use of DFX as an alternative to xylose for furfural production could improve the utilization efficiency of xylan in lignocelluloses. Compared with aqueous solution and monophasic co-solvent systems, biphasic systems such as W-MIBK mixture enabled the efficient conversion of DFX to furfural, in which the conversion process mainly included the hydrolysis of DFX to xylose, the dehydration of xylose to furfural, and the transfer of furfural from the aqueous phase to the organic phase. In the biphasic W-MIBK system, we were able to obtain a decent furfural yield under kinetically optimized conditions. These results pushed forward the combination of the DFX conversion in the biphasic system and lignocellulosic fractionation that used formaldehyde to stabilize xylose *via* acetalization. As a result, such a combined two-step method achieved an overall furfural yield of 52 mol% based on the content of xylan in eucalyptus wood, which was almost two times the yield of the control process without formaldehdye addition. Because formaldehyde-stabilized fractionation also has the advantage of isolating highly active lignin, this combination approach could not only lead to the high conversion efficiency of xylan to furfural but also facilitate the integrated utilization of the three major biopolymers in lignocelluloses.

Data availability statement

The original contributions presented in the study are included in the article/Supplementary Material, further inquiries can be directed to the corresponding authors.

Author contributions

LS, XL, and JL proposed the concept, designed the experiments, analyzed the data, and wrote the manuscript; LH, ZB, DL, and XC carried out the experiments and analyzed the data; LS, XL, and JL supervised the experiments, reviewed and revised the manuscript. All authors read and approved the final manuscript.

Funding

This work was supported by National Natural Science Foundation of China (31870559, 31901262, and 32071716), Outstanding Youth Funding of National Forestry and Grassland Administration (20201326005), Outstanding Youth Funding of Fujian Provincial Department of Science and Technology (2021J06017) and Fujian Agriculture and Forestry University (xjq201923). We also acknowledge the financial support from the Jiangsu Provincial Key Laboratory of Pulp and Paper Science and Technology (KL201911).

Acknowledgments

The authors gratefully acknowledge Fujian Qingshan Paper Co., Ltd. for providing eucalyptus wood.

Conflict of interest

The authors declare that the research was conducted in the absence of any commercial or financial relationships that could be construed as a potential conflict of interest.

Publisher's note

Supplementary material

The Supplementary Material for this article can be found online at: https://www.frontiersin.org/articles/10.3389/fbioe.2023.1146250/full#supplementary-material

References

Daorattanachai, P., Viriya-empikul, N., Laosiripojana, N., and Faungnawakij, K. (2013). Effects of Kraft lignin on hydrolysis/dehydration of sugars, cellulosic and lignocellulosic biomass under hot compressed water. *Bioresour. Technol.* 144, 504–512. doi:10.1016/j.biortech.2013.06.124

Gong, Z., Yang, G., Huang, L., Chen, L., Luo, X., and Shuai, L. (2022). Phenol-assisted depolymerisation of condensed lignins to mono-/poly-phenols and bisphenols. *Chem. Eng. J.* 29, 140628. doi:10.1016/j.cej.2022.140628

Jaswal, A., Singh, P. P., and Mondal, T. (2022). Furfural – A versatile, biomass-derived platform chemical for the production of renewable chemicals. *Green Chem.* 24 (2), 510–551. doi:10.1039/D1GC03278J

Kabbour, M., and Luque, R. (2020). "Chapter 10 - furfural as a platform chemical: From production to applications," in *Biomass, biofuels, biochemicals*. Editors S. Saravanamurugan, A. Pandey, H. Li, and A. Riisager (Amsterdam: Elsevier), 283–297.

Lamminpää, K., Ahola, J., and Tanskanen, J. (2015). Acid-catalysed xylose dehydration into furfural in the presence of kraft lignin. *Bioresour. Technol.* 177, 94–101. doi:10.1016/j.biortech.2014.11.074

Lee, C. B. T. L., and Wu, T. Y. (2021). A review on solvent systems for furfural production from lignocellulosic biomass. *Renew. Sustain. Energy Rev.* 137, 110172. doi:10.1016/j.rser.2020.110172

Lin, Q., Zhan, Q., Li, R., Liao, S., Ren, J., Peng, F., et al. (2021). Solvent effect on xylose-to-furfural reaction in biphasic systems: Combined experiments with theoretical calculations. *Green Chem.* 23 (21), 8510–8518. doi:10.1039/D1GC02812J

Luo, X., Gong, Z., Yang, G., Huang, L., Chen, L., and Shuai, L. (2022). *In-situ* oxidation/reduction facilitates one-pot conversion of lignocellulosic biomass to bulk chemicals in alkaline solution. *Chem. Eng. J.* 429, 132365. doi:10.1016/j.cej.2021.132365

Luo, X., Li, Y., Gupta, N. K., Sels, B., Ralph, J., and Shuai, L. (2020). Protection strategies enable selective conversion of biomass. *Angew. Chem. Int. Ed.* 59 (29), 11704–11716. doi:10.1002/anie.201914703

Luo, X., Ma, X., Hu, H., Li, C., Cao, S., Huang, L., et al. (2013). Kinetic study of pentosan solubility during heating and reacting processes of steam treatment of green bamboo. *Bioresour. Technol.* 130, 769–776. doi:10.1016/j.biortech.2012.12.088

Matsagar, B. M., Hossain, S. A., Islam, T., Alamri, H. R., Alothman, Z. A., Yamauchi, Y., et al. (2017). Direct production of furfural in one-pot fashion from raw biomass using brønsted acidic ionic liquids. *Sci. Rep.* 7 (1), 13508. doi:10.1038/s41598-017-13946-4

Mellmer, M. A., Sener, C., Gallo, J. M. R., Luterbacher, J. S., Alonso, D. M., and Dumesic, J. A. (2014). Solvent effects in acid-catalyzed biomass conversion reactions. *Angew. Chem. Int. Ed.* 53 (44), 11872–11875. doi:10.1002/anie.201408359

Questell-Santiago, Y. M., Zambrano-Varela, R., Talebi Amiri, M., and Luterbacher, J. S. (2018). Carbohydrate stabilization extends the kinetic limits of chemical polysaccharide depolymerization. *Nat. Chem.* 10 (12), 1222–1228. doi:10.1038/s41557-018-0134-4

Román-Leshkov, Y., Chheda, J. N., and Dumesic, J. A. (2006). Phase modifiers promote efficient production of hydroxymethylfurfural from fructose. *Science* 312 (5782), 1933–1937. doi:10.1126/science.1126337

Scanlon, J. T., and Willis, D. E. (1985). Calculation of flame ionization detector relative response factors using the effective carbon number concept. *J. Chromatogr. Sci.* 23 (8), 333–340. doi:10.1093/chromsci/23.8.333

Shuai, L., Amiri, M. T., Questell-Santiago, Y. M., Héroguel, F., Li, Y., Kim, H., et al. (2016). Formaldehyde stabilization facilitates lignin monomer production during biomass depolymerization. *Science* 354 (6310), 329–333. doi:10.1126/science.aaf7810

Shuai, L., and Luterbacher, J. (2016). Organic solvent effects in biomass conversion reactions. *ChemSusChem* 9 (2), 133–155. doi:10.1002/cssc.201501148

Sluiter, A., Hames, B., Ruiz, R., Scarlata, C., Sluiter, J., Templeton, D., et al. (2008). "Determination of structural carbohydrates and lignin in biomass," in *Laboratory analytical procedure* (Golden, United States: National Renewable Energy Laboratory).

Walker, T. W., Chew, A. K., Li, H., Demir, B., Zhang, Z. C., Huber, G. W., et al. (2018). Universal kinetic solvent effects in acid-catalyzed reactions of biomass-derived oxygenates. *Energy & Environ. Sci.* 11 (3), 617–628. doi:10.1039/C7EE03432F

Weingarten, R., Cho, J., Conner, J. W. C., and Huber, G. W. (2010). Kinetics of furfural production by dehydration of xylose in a biphasic reactor with microwave heating. *Green Chem.* 12 (8), 1423–1429. doi:10.1039/C003459B

frontiers | Frontiers in Bioengineering and Biotechnology

TYPE Original Research
PUBLISHED 16 March 2023
DOI 10.3389/fbioe.2023.1144787

OPEN ACCESS

EDITED BY
Chen Huang,
Chinese Academy of Forestry, China

REVIEWED BY
Liangzhi Li,
Suzhou University of Science and Technology, China
Zhi-Jun Zhang,
East China University of Science and Technology, China

*CORRESPONDENCE
Yu-Cai He,
heyucai2001@163.com
Jianren Ye,
jrye@njfu.edu.cn

SPECIALTY SECTION
This article was submitted to Bioprocess Engineering, a section of the journal Frontiers in Bioengineering and Biotechnology

RECEIVED 15 January 2023
ACCEPTED 17 February 2023
PUBLISHED 16 March 2023

CITATION
He W, He Y-C and Ye J (2023), Efficient synthesis of furfurylamine from biomass *via* a hybrid strategy in an EaCl: Gly–water medium.
Front. Bioeng. Biotechnol. 11:1144787.
doi: 10.3389/fbioe.2023.1144787

Efficient synthesis of furfurylamine from biomass *via* a hybrid strategy in an EaCl: Gly–water medium

Wei He[1], Yu-Cai He[2]* and Jianren Ye[3]*

[1]College of Biology and the Environment, Nanjing Forestry University, Nanjing, China, [2]School of Pharmacy, Changzhou University, Changzhou, China, [3]College of Forestry, Nanjing Forestry University, Nanjing, China

The objective of this work was to develop an efficient approach for chemoenzymatically transforming biomass to furfurylamine by bridging chemocatalysis and biocatalysis in a deep eutectic solvent of EaCl:Gly–water. Using hydroxyapatite (HAP) as support, heterogeneous catalyst SO_4^{2-}/SnO_2–HAP was synthesized for transforming lignocellulosic biomass into furfural using organic acid as a co-catalyst. The turnover frequency (TOF) was correlated with the pKa value of the used organic acid. Corncob was transformed by oxalic acid (pKa = 1.25) (0.4 wt%) plus SO_4^{2-}/SnO_2–HAP (2.0 wt%) to produce furfural with a yield of 48.2% and a TOF of 6.33 h^{-1} in water. In deep eutectic solvent EaCl:Gly–water (1:2, v/v), co-catalysis with SO_4^{2-}/SnO_2–HAP and oxalic acid was utilized to transform corncob, rice straw, reed leaf, and sugarcane bagasse for the production of furfural with the yield of 42.4%–59.3% (based on the xylan content) at 180°C after 10 min. The formed furfural could be efficiently aminated to furfurylamine with *E. coli* CCZU-XLS160 cells in the presence of NH_4Cl (as an amine donor). As a result of the biological amination of furfural derived from corncob, rice straw, reed leaf, and sugarcane bagasse for 24 h, the yields of furfurylamine reached >99%, with a productivity of 0.31–0.43 g furfurylamine per g xylan. In EaCl:Gly–water, an efficient chemoenzymatic catalysis strategy was employed to valorize lignocellulosic biomass into valuable furan chemicals.

KEYWORDS

lignocellulose, furfural, furfurylamine, SO_4^{2-}/SnO_2–HAP, deep eutectic solvent

1 Introduction

Biorefinery concept is highly promising for the sustainable utilization of biomass to manufacture energy molecules, platform chemicals, and functional materials (Himmel et al., 2007; Delidovich et al., 2016; He et al., 2017a; Riva et al., 2021). The cost-efficient transformation of lignocellulosic biomass has attracted much attention for achieving a sustainable society (Cai et al., 2014; Guenic et al., 2015). Lignocellulose is mainly composed of three primary components including lignin, hemicellulose, and cellulose (Gong et al., 2019; Riva et al., 2021), which is regarded as a sustainable bioresource because of its availability, abundance, low cost, and renewable characteristics (Hu et al., 2014; Kaiprommarat et al., 2016). Hemicellulose, an amorphous heteropolysaccharide, is mainly composed of different C5 and C6 sugar monomers (Peleteiro et al., 2014; Lee and Wu, 2021). Xylan, which consists of *D*-xylose units, represents the main component of

hemicellulose (Morais et al., 2020). As an important xylan-based product, furfural (FF) is a key building block (Zang and Chen, 2015; He et al., 2017b; Sweygers et al., 2018), which was listed in the "Top10 + 4" chemicals by the US Department of Energy (DOE) in 2004 (Bozell and Petersen, 2010). FF is a good solvent. It has been utilized as a renewable material for biofuels, detergents, lubricants, polymers, resins, food additives, pharmaceuticals (antiseptics and disinfectors), and agrochemicals (herbicides, insecticides, and pesticides) (Agirrezabal-Telleria et al., 2014; Douthwaite et al., 2017; Peng et al., 2019; Gong et al., 2022). It is an important precursor for widely synthesizing furan bio-based chemicals such as 2-methylfuran, furoic acid, cyclopentanone, furfuryl alcohol, succinic acid, furfurylamine (FAM), tetrahydrofuran, γ-valerolactone, and maleic acid (Lange et al., 2012; Möller and Schröder, 2013; Feng et al., 2016; Qiu et al., 2020; Zheng et al., 2020).

FAM, as a valuable furan-based chemical, has a vital role in manufacturing chemical intermediates, bioactive molecules, medicines, *etc.* (Dong et al., 2020). Industrially, FAM can be prepared *via* the chemical amination of FF under high temperature/pressure conditions, and this kind of amination requires a harsh performance and expensive catalysts, accompanied with potential environmental pollution (Zhang et al., 2019). Distinct from the chemical amination of FAM, biological amination of FF has gained great interest due to its mild performance condition, simple reaction, high catalytic activity, low toxicity, and environmental friendliness. ω-Transaminase is a pyridoxamine 5′-phosphate (PLP)-dependent enzyme, which has good selectivity for reversibly transforming the exchange of ketone groups (C=O) and an amino group (-NH_2). The biomass-derived FF (90 mM) was aminated into FAM (74%) by *Escherichia coli* CV-PRSFDuet expressing ω-transaminase at 35°C (Zhang et al., 2019). To chemoenzymatically valorize biomass into FAM in a tandem reaction with a chemocatalyst and biocatalyst, it is necessary to employ an efficient strategy for the conversion of biomass into FF with biocompatible catalysts in an eco-friendly reaction system.

In recent years, homogeneous and heterogeneous catalysts have been utilized for FF production. Various acids (H_2SO_4, HCl, H_3PO_4, oxalic acid, formic acid, acetic acid, *etc.*) and salts ($AlCl_3$, $CoCl_2$, $CrCl_3$, $MaCl_2$, $MnCl_2$, NaCl, $NiCl_2$, $SnCl_4$, *etc.*) are used as homogeneous catalysts (Rong et al., 2012; Enslow and Bell, 2015), which can be uniformly distributed in solvents. These homogeneous catalysts have high catalytic activity. However, their high loading will cause serious environmental pollution, and their recycle is a challenge. Heterogeneous catalysts that can be prepared by using a series of supports (e.g., graphene, zeolite, niobium oxide, niobium phosphate, sepiolite, kaoline, fly ash, carbon nanotube, resin, and carbon) have gained much attention because of their large surface areas, strong acidity, low corrosion, easy separation, and good thermal stability (Garcia-Sancho et al., 2013; Pholjaroen et al., 2013; Ma et al., 2019; Zhu et al., 2020; Di et al., 2021; Li et al., 2021). Although heterogeneous catalysts are easy to be recovered and have low corrosion (Li et al., 2019), the catalytic efficiency is still not satisfactory. The co-catalysis of homogeneous and heterogeneous catalysts might be used for the efficient transformation of biomass into FF, which deserves in-depth exploration.

In the production of FF from lignocellulosic biomass, used solvents have a crucial role in the enhancement of FF productivity (Lee and Wu, 2021). It is known that some organic solvents can confine the undesired side reactions (e.g., FF condensation and FF resinification) in water (Lam et al., 2012). Various solvents (e.g., dimethyl sulfoxide, ethanol, hexane, ionic liquids, toluene, γ-valerolactone, and dioctyl phthalate) have been employed to transform biomass or *D*-xylose, which resulted in the increased FF productivity (Tau et al., 2016; Xu et al., 2017; Widsten et al., 2018; Ma et al., 2020). Recently, it is of great interest to select more eco-friendly and thermostable solvents for enhancing FF production. Deep eutectic solvents (DESs), which are composed of mixing HBAs (hydrogen-bond acceptors) with HBDs (hydrogen-bond donors) (Li et al., 2018), have recently gained tremendous attention for FF production because of their low vapor pressure, good reusability, low toxicity, high thermostability, and ease of preparation (Xu et al., 2020; Pan et al., 2022). In acetone–ChCl:EG–water at 180°C, *D*-xylose was transformed to FF in 0.5 h at 75% yield by $AlCl_3$ (Chen and Wan, 2019). Thus, DESs can be utilized as promising solvents for improving FF production because of their unique properties, which would restrict the undesired side reactions and promote FF formation.

To enhance FAM yield from renewable biomass, a chemoenzymatic conversion was developed in a tandem reaction by bridging chemocatalysis and biocatalysis in an eco-friendly DES–water system (Scheme 1). Hydroxyapatites (HAPs, $Ca_{10}(PO_4)_6(OH)_2$), which are naturally occurring phosphate minerals, were used as a carrier to prepare sulfonated tine-based heterogeneous catalyst SO_4^{2-}/SnO_2–HAP. First, biomass was converted into FF *via* co-catalysis with a homogeneous catalyst and a heterogeneous catalyst in an EaCl:Gly–water system. An optimized system for the production of FF from lignocellulose was established by combined homogeneous organic acids with heterogeneous SO_4^{2-}/SnO_2–HAP. The turnover frequency (TOF) was correlated with the pKa value of organic acids. The catalytic reaction parameters (e.g., type of organic acid, organic acid loading, SO_4^{2-}/SnO_2–HAP loading, DES EaCl:Gly dosage, performance temperature, and catalytic time) were examined to improve FF production. Furthermore, biomass-valorized FF was biologically aminated into FAM in EaCl:Gly–water. An efficient chemoenzymatic strategy was employed to valorize biomass into valuable furan-based chemicals, realizing the high-value utilization of biomass.

2 Materials and methods

2.1 Reagents and materials

Corncob (CC), rice straw (RS), reed leaf (RL), and sugarcane bagasse (SB) were collected in a village market in Tieling city (Liaoning province, P.R. China). Hydroxyapatite (HAP), oxalic acid, $SnCl_4{\cdot}5H_2O$, NaCl, and other chemicals were bought from Aladdin Industrial Inc. (Shanghai, China) and other commercial sources.

2.2 SO_4^{2-}/SnO_2–HAP and DES EaCl:Gly preparation

Sulfonated heterogeneous catalyst SO_4^{2-}/SnO_2–HAP was prepared with $SnCl_4{\cdot}5H_2O$ and HAP in a mass ratio of 1:3 in

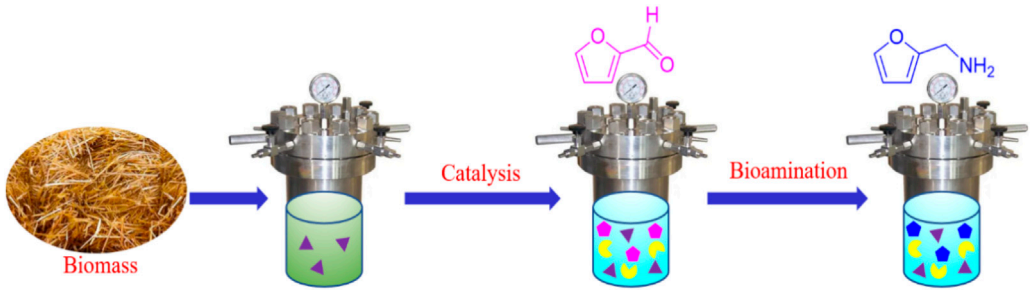

SCHEME 1
Chemoenzymatic conversion of biomass into furfurylamine (FAM).

1 L of ethanol by stirring. The preparation procedure of SO_4^{2-}/SnO_2–HAP was carried out according to the method proposed by Zhang et al. (2019). DES EaCl:Gly was prepared according to the procedure proposed by Xu et al. (2020).

2.3 Co-catalysis of CC organic acids and SO_4^{2-}/SnO_2–HAP in EaCl:Gly–water

To test the co-catalysis of biomass into FF with organic acids and SO_4^{2-}/SnO_2–HAP on the effects of FF formation, water (40 mL), CC (7.5 wt%), and SO_4^{2-}/SnO_2–HAP (2.0 wt%) were mixed with different pKa values of the organic acid (0.4 wt%) at 180°C for 10 min. For testing the oxalic acid dosage on the effect of FF generation, different loads of oxalic acid (0–0.6 wt%) were mixed with water (40 mL), CC (7.5 wt%), and SO_4^{2-}/SnO_2–HAP (2.0 wt%) in a reactor (180°C) for 10 min. To establish an appropriate DES–water system for improving FF production, several volumetric ratios of EaCl:Gly–water (0:1, 1:3, 1:2, 1:1, 2:1, and 3:1, v/v) were examined in the transformation of CC (7.5 wt %) *via* co-catalysis with EaCl:Gly–water (40 mL), SO_4^{2-}/SnO_2–HAP (2.0 wt%), and oxalic acid (0.4 wt%) in a reactor (180°C) for 10 min. To examine the performance temperature and reaction time of FF generation, co-catalysis with SO_4^{2-}/SnO_2–HAP (2.0 wt%), EaCl: Gly–water (40 mL; EaCl:Gly–water volumetric ratio 1:2), and oxalic acid (0.4 wt%) in a reactor (160–180°C) for 5–40 min was carried out. After the given residence time at the certain performance temperature, this reactor was placed in an ice-water bath to cool down quickly. The product FF was determined using high-performance liquid chromatography (HPLC). FF yield is defined as follows:

$$\text{Yield of FF} = \frac{\text{FF produced (g)} \times 0.88}{\text{Xylan in biomass (g)}} \times \frac{150}{96} \times 100\%.$$

Molecular weights of *D*-xylose and FF are 150 and 96, respectively. The coefficient for catalyzing xylan in biomass into *D*-xylose is 0.88.

2.4 Bioamination of FF into FAM

The enzyme gene of ω-transaminase from *C. violaceum* ATCC 12472 (CV) was amplified. The linearized pET28aDuet-1 and purified CV were transformed into one *E. coli* DH5α and ligated by T5 exonuclease through an exonuclease-mediated seamless assembly. The obtained fragment was inserted into MCS-1 of pET28aDuet-1 after His-tag to obtain CV-pET28aDuet-1. *L*-Alanine dehydrogenase (AlaDH, GenBank ID 936557) from *B. subtilis* 168 was amplified. The fragments of CV and Ala were linked together *via* an overlap extension PCR. Ribosome binding sites were inserted between CV and AlaDH fragments. The ligated plasmid pET28a–CV–AlaDH was transformed into one *E. coli* BL21 (DE3). The constructed *E. coli* CCZU-XLS160 cells expressing CV ω-transaminase and AlaDH were cultured in a terrific broth by a supplement of ampicillin (100 mg/L) in a shaker (37°C; 180 rpm). When OD_{600} of CCZU-XLS160 cells reached 0.60, isopropyl β-*D*-1-thiogalactopyranosyl (IPTG) was added to the culture system at 20°C. After incubation for 20 h, CCZU-XLS160 cells were harvested for the biological amination of FF into FAM:

$$\text{Yield of FAM} = \frac{\text{FAM produced (mM)}}{\text{FF (mM)}} \times 100\%.$$

Biomass-derived FF, CCZU-XLS160 cells (0.05 g/mL), and NH_4Cl (2 mol NH_4Cl/mol FAL) were mixed in EaCl:Gly–water (1:2, v/v; pH 7.5) at 35°C. During the biological transamination, the samples were withdrawn. FF and FAM were quantified using HPLC.

2.5 Analytical methods

Components of CC were measured according to the procedure proposed by Selig et al. (2008). SO_4^{2-}/SnO_2–HAP was captured using FT-IR, XRD, BET, and SEM procedures proposed by Peng et al. (2019). FF and FAM were quantified using Waters-2414 HPLC by using an Aminex HPX-87H column (Bio-Rad Laboratories, Hercules, CA) (Zhang et al., 2019). The mixture was composed of 80 vol% water, 20 vol% CH_3OH, and 0.1 wt% trifluoroacetic acid, which was used as an eluent at a flow rate of 0.8 mL/min. FAM was determined at 210 nm, and FF was assayed at 254 nm.

3 Results and discussion

3.1 Characteristics of SO_4^{2-}/SnO_2–HAP

Using hydroxyapatite (HAP) as support, a sulfonated HAP-based heterogeneous catalyst was prepared for transforming CC into

TABLE 1 BET results of the SO_4^{2-}/SnO_2–HAP catalyst and the HAP carrier.

Sample	BET surface area, m^2/g	Pore volume, cm^3/g	Pore size, nm
SO_4^{2-}/SnO_2–HAP	51.9	0.14	10.7
HAP	17.2	0.06	12.9

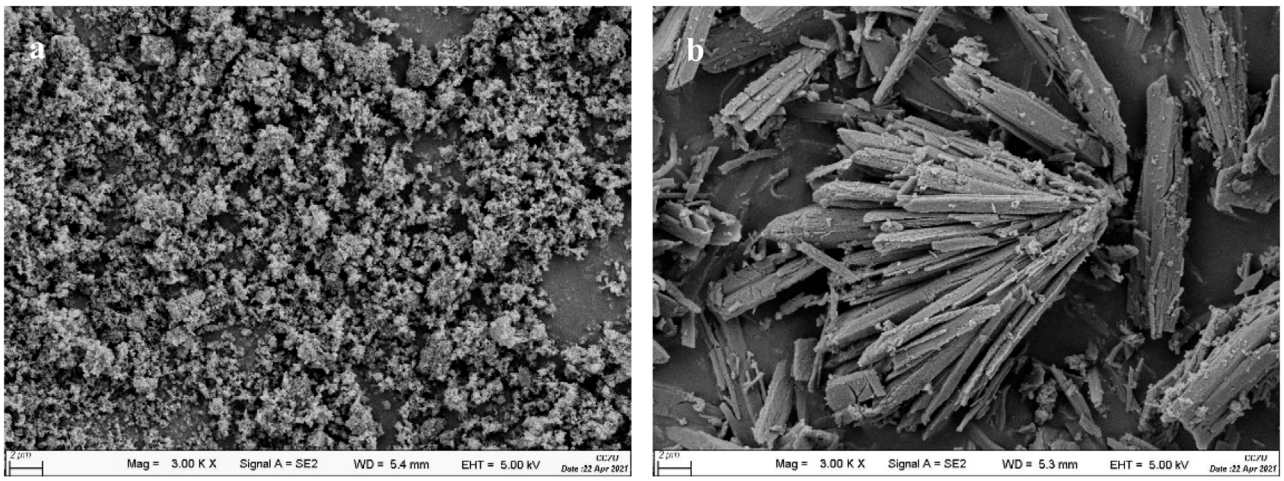

FIGURE 1
SEM of HAP **(A)** and SO_4^{2-}/SnO_2–HAP **(B)**.

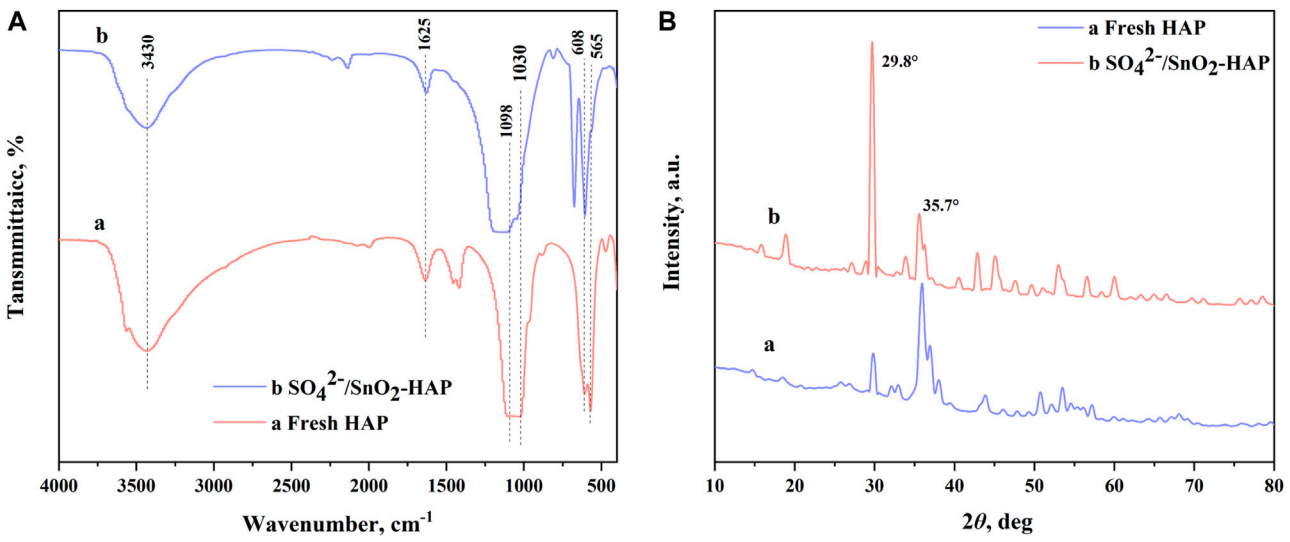

FIGURE 2
FT-IR **(A)** and XRD **(B)** of HAP and SO_4^{2-}/SnO_2–HAP.

FF. Relative to carrier support HAP, SO_4^{2-}/SnO_2–HAP had an enlarged surface area (51.9 m^2/g) and decreased pore diameter (10.7 nm) (Table 1). Pore volumes of SO_4^{2-}/SnO_2–HAP were increased to 0.14 cm^3/g. SEM illustrated that SO_4^{2-}/SnO_2–HAP had more voids (Figure 1), which caused the increased surface area and pore volume. FT-IR illustrated that the SO_4^{2-}/SnO_2–HAP surface was distinct with a carrier HAP surface (Figure 2A). The bond of ~ 3,430 cm^{-1} was related to Si–OH stretching. The bond of ~ 1,098 cm^{-1}, which was related to asymmetric stretching vibrations of Si–O–Si (Gong et al., 2019), increased after the synthesis of SO_4^{2-}/SnO_2–HAP. The bond of ~ 1,030 cm^{-1} was related to S=O (Peng et al., 2019), verifying the

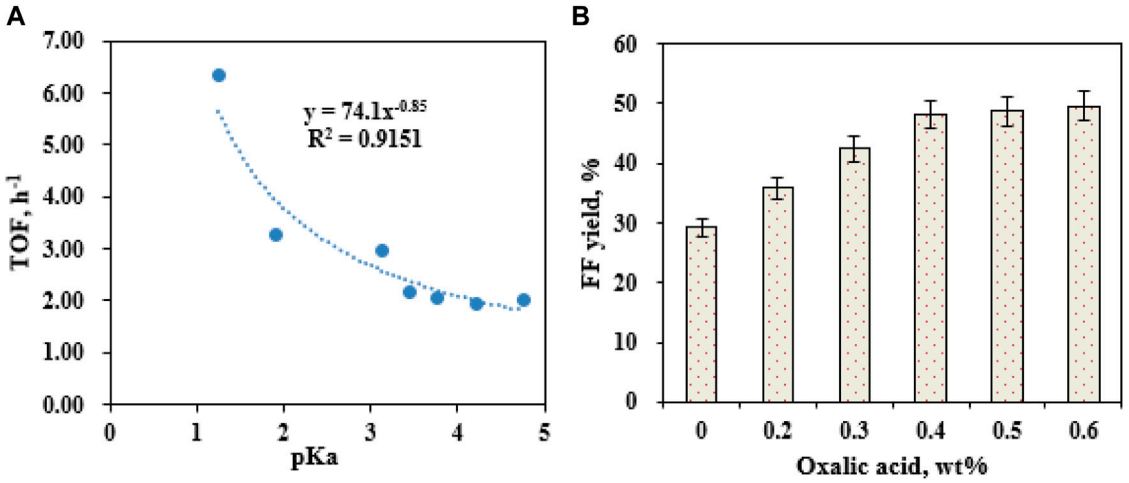

FIGURE 3
Effects of organic acids with different pKa values on the SO_4^{2-}/SnO_2–HAP-catalyzed conversion of CC to FF after 10 min at 180°C **(A)**; effects of the oxalic acid dose (0.1–0.8 wt%) on FF generation after 10 min at 180°C **(B)**.

occurrence of SO_4^{2-} on a catalyst. The bond of ~ 790 cm^{-1} was related to Si–O–Si bending. XRD indicated that Sn ions modified the carrier HAP structure to some extent (Figure 2B). At 2θ = 20–30°, the SO_4^{2-}/SnO_2–HAP intensity dropped compared to that of carrier HAP.

3.2 Co-catalysis of CC with organic acids and SO_4^{2-}/SnO_2–HAP in water

The catalytic system's acidity might greatly affect FF generation (Marcotullio and de Jong, 2010). Maleic acid (pKa = 1.92), glyoxalate (pKa = 3.18), fumaric acid (pKa = 3.02), malic acid (pKa = 3.46), citric acid (pKa = 3.13), formic acid (pKa = 3.77), oxalic acid (pKa = 1.25), succinic acid (pKa = 4.21), acetic acid (pKa = 4.76), and propionic acid (pKa = 4.87) (0.5 wt%) were used to assist SO_4^{2-}/SnO_2–HAP in the co-catalysis of CC into FF. The turnover frequency (TOF) of the catalytic reaction and pKa value of organic acids were well fitted into a curve equation (TOF = 74.1 × $(pKa)^{-0.85}$; R^2 = 0.9151) (Figure 3A). In the acidic condition, a lower pKa value of organic acids favored FF formation with a higher TOF (Figure 3A). H^+ in the lower pKa value of carboxylic acids was easier to dissociate into water. An increased acidity of the catalytic system would enhance the hydrolysis of hemicelluloses in lignocellulose into pentoses (e.g., *D*-xylose) and accelerate their dehydration to form FF (Lee and Wu, 2021). The highest TOF reached 6.33 h^{-1} *via* the co-catalysis of CC using oxalic acid (pKa = 1.25) and SO_4^{2-}/SnO_2–HAP. Different dosages of oxalic acid (0.1–0.8 wt%) were separately supplemented to the catalytic system for assisting SO_4^{2-}/SnO_2–HAP catalysis of CC within 10 min at 180°C (Figure 3B). Upon raising the oxalic acid dose from 0.1 to 0.4 wt%, FF yields increased from 24.6% to 48.2%. Over 0.4 wt %, FF yields had no significant change. Hence, 0.4 wt% of oxalic acid was utilized as a suitable additive to assist the SO_4^{2-}/SnO_2–HAP catalysis of CC into FF.

3.3 Optimization of transforming CC into FF in DES EaCl:Gly–water

In the aqueous catalytic system, the low FF solubility might restrict FF generation, resulting in a decreased FF production (Li et al., 2021). DESs might be used as promising solvents for enhancing FF yields due to their unique properties, which would facilitate the generation of FF and confine undesired FF degradation or cross-polymerization (Pan et al., 2022). Using CC as a feedstock for producing FF, four factors including DES dosage, catalyst dose, performance temperature, and reaction time were examined for the effect of FF formation in DES EaCl:Gly–water.

When the ratio of DES–water is changed, the formed DES–water media might influence the production of FF (Pan et al., 2022). To examine EaCl:Gly dosage on FF generation, four volumetric ratios of EaCl:Gly–water (0:1, 1:3, 1:2, 1:1, 2:1, and 3:1; v/v) were individually utilized as catalytic reaction media (180°C) (Figure 4A). By raising the volumetric ratio of EaCl:Gly–water from 0:1 (EaCl:Gly, 0 vol%) to 1:2 (EaCl:Gly, 33.3 vol%), FF yields increased from 48.2% to 59.3%. Upon increasing the EaCl:Gly–water volumetric ratio from 1:2 to 1:1, FF yields increased slightly. Compared to the aqueous phase system, the merit of the DES–water system is that FF might be extracted into EaCl:Gly *in situ* quickly. Thus, not only the generation of by-products is confined but also the tedious performance steps for the extraction of FF are also saved. Over 1:1 (v/v), FF yields decreased from 59.3% to 50.1% in EaCl:Gly–water. In view of FF yields and EaCl:Gly dosage, the appropriate EaCl:Gly–water volumetric ratio was chosen as 1:2 (EaCl:Gly, 33.3 vol%). As the EaCl:Gly dose increased in EaCl:Gly–water, excessive solvent loading would reduce the contact opportunity of lignocellulose to catalysts and cause the reduction of FF yields (Li et al., 2021).

During the conversion of biomass into FF with solid acids, catalyst loading had a profound influence on FF production (Peng et al., 2019). It was observed that the loading of SO_4^{2-}/SnO_2–HAP (1–4 wt%) had a crucial effect on FF formation in EaCl:Gly–water (1:2, v/v) by supplementary oxalic acid (0.4 wt%)

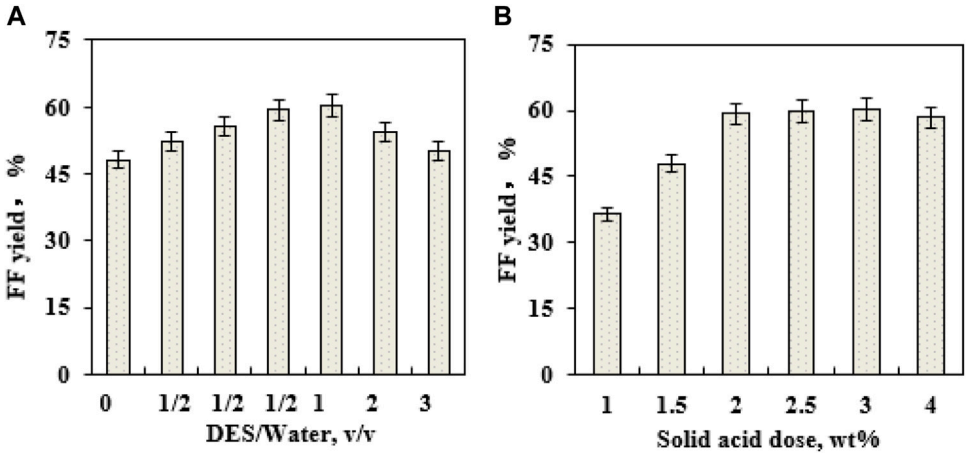

FIGURE 4
Effects of DES EaCl:Gly loading on FF generation (180°C; 10 min) **(A)**; effects of the SO_4^{2-}/SnO_2–HAP dose on FF generation (180°C; 10 min) **(B)**.

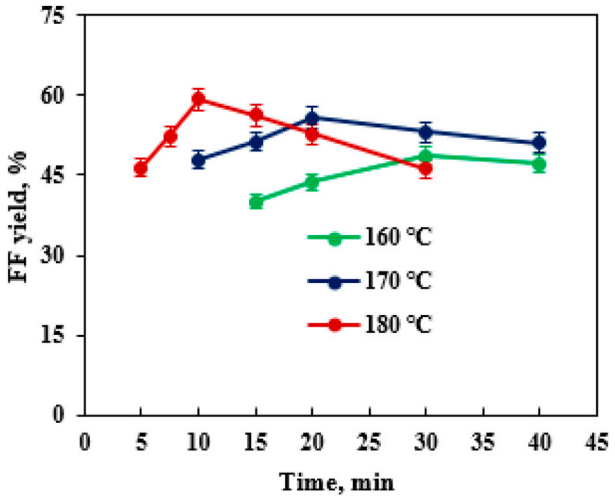

FIGURE 5
Effects of the performance temperature and time on FF generation.

(Figure 4B). As the SO_4^{2-}/SnO_2–HAP dosage increased from 1 to 2 wt%, FF yields improved from 36.4% to 59.3%, and when SO_4^{2-}/SnO_2–HAP loading exceeded 2.0 wt%, FF yields showed no significant change. Thus, the optimal SO_4^{2-}/SnO_2–HAP dosage was 2.0 wt%. The performance temperature and reaction time were pronounced as vital parameters that affected the production of FF (Zhang et al., 2019). After the transformation of CC was conducted for 5–40 min in a reactor (160–180°C) containing 40 mL EaCl:Gly–water (1:2, v/v), it was found that the highest FF yield (59.3%) was obtained at 180°C after 10 min *via* co-catalysis with SO_4^{2-}/SnO_2–HAP (2.0 wt%) and oxalic acid (0.4 wt%) (Figure 5). By increasing the reaction time from 5 to 10 min, the FAL yield was increased significantly. Over 10 min, the FAL yield dropped gradually. Sn–sepiolite (3.0 wt%) catalyzed rice straw to FF (42% yield) in water after 20 min at 170°C (Peng et al., 2019). Sn–vermiculite (4.0 wt%) converted reed to FF (55.0 mM; 38.4% yield) in water at 170°C after 20 min (Zhu et al., 2020). Evidently, SO_4^{2-}/SnO_2–HAP could be utilized to catalyze CC into FF with a high yield (59.3%) in EaCl:Gly–water (1:2, v/v) containing oxalic acid (0.4 wt%).

In the EaCl:Gly–water system, lignocellulosic biomass was catalyzed to FF and its derivatives by synergetic catalysis with SO_4^{2-}/SnO_2–HAP and oxalic acid. Water molecules could break the complicated matrix of cellulose–lignin–hemicellulose, which would facilitate the promotion of the dissolution of hemicellulose (Lam et al., 2012). Carboxylic acids as Brönsted catalysts, which are also used as components of DESs, had a good biomass pretreatment ability (Yin et al., 2021). DES EaCl:Gly, which has good biomass pretreatment, could reduce the degradation of hemicellulose that enhanced the selective conversion of hemicellulose (Zhang et al., 2014). The xylan-derived *D*-xylose was dehydrated and opened in the presence of Cl^- and finally closed to FF (Marcotullio and de Jong, 2010). FF could also be obtained *via* the transformation of xylulose derived from isomerized *D*-xylose (Choudhary et al., 2011; Li et al., 2014). Glucan-derived glucose was isomerized to fructose, which would be further dehydrated to form 5-HMF and then hydrolyzed to produce HCOOH and levulinic acid (Wang et al., 2017).

3.4 Reuse of SO_4^{2-}/SnO_2–HAP

Reusability is a key indicator in assessing the performance of a heterogeneous catalyst (Gong et al., 2019). In this work, the catalyst SO_4^{2-}/SnO_2–HAP was reused for eight cycles. After each catalytic cycle in EaCl:Gly–water (1:2, v/v), the mixture of biomass residue and SO_4^{2-}/SnO_2–HAP was isolated by filtration and further washed with distilled water three times. Then, this solid mixture was burned in an oven to remove biomass residue. The remaining solid was further sulfonated before starting the next batch. The activity of SO_4^{2-}/SnO_2–HAP was maintained during four consecutive tests (41.7%–59.3%) (Figure 6). FF yields decreased gradually after each batch. From the first to the fourth run, FF yields dropped from 59.3% to 51.6%. From the fifth to the sixth run, a significant

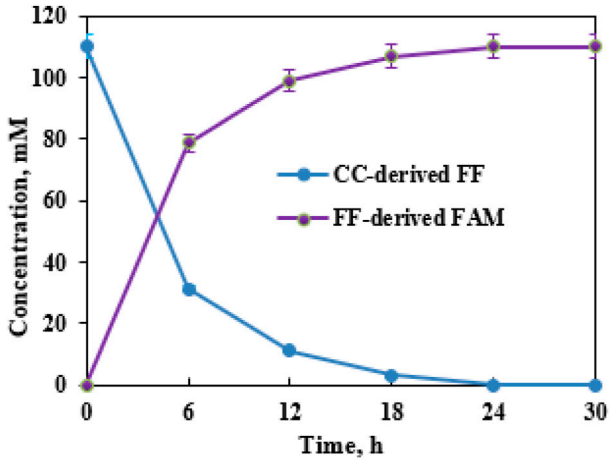

FIGURE 6
Bioamination of the CC-derived FF into FAM in EaCl:Gly–water (1:2, v/v; pH 7.5) at 35°C.

decrease in FF yields (41.7%–47.8%) was obtained. After Sn–sepiolite was recovered and reused for six runs, the FF yield decreased from 42% to 35% (Peng et al., 2019). Evidently, SO_4^{2-}/SnO_2–HAP had good stability and reusability. An efficient recovery and reuse process could reduce the operation cost of FF production.

3.5 Valorization of biomass-derived FF to FAM in EaCl:Gly–water

DESs can be utilized as eco-friendly reaction solvents for chemocatalysis and biocatalysis (Ni et al., 2021). In 40 mL EaCl:Gly–water (1:2, v/v), a tandem conversion of biomass into FAM was attempted *via* a sequential acidified SO_4^{2-}/SnO_2–HAP chemocatalyst and a CCZU-XLS160 cell biocatalyst. Through co-catalysis with SO_4^{2-}/SnO_2–HAP (2.0 wt%) and oxalic acid (0.4 wt%), corncob (CC), sugarcane bagasse (SB), rice straw (RS), and reed leaf (RL) (3.0 g, 75 g/L) could be catalyzed into 114.9, 79.6, 74.5, and 50.8 mM FF at 180°C after 10 min (Table 2), respectively. FF yields were obtained as follows: $Yield_{(CC)}$ = 59.3% > $Yield_{(SB)}$ = 47.3% > $Yield_{(RS)}$ = 45.2% > $Yield_{(RL)}$ = 42.4%. Various types of agro- and forest-wastes could be used to produce FF (Guenic et al., 2015; Gong et al., 2019; Lee and Wu, 2021). In this work, different types of biomass samples with different contents of xylan were used as feedstock for the production of FF. Overall, CC was a good feedstock for FF production due to the high xylan content (34.1 wt%) and FF yield (59.3%).

The formed FF liquor, which was adjusted to pH 7.5, could be aminated into FAM by supplementary CCZU-XLS160 cells (0.050 g/mL) and NH_4Cl (2 mol NH_4Cl/mol FF) in EaCl:Gly–water (1:2, v/v). Time courses for the biotransformation of dilute CC-derived FF (110.0 mM) were monitored. By increasing the bioreaction time from 0 to 12 h, FF concentrations decreased quickly (Figure 7). After biological amination for 6 and 12 h, FAM concentrations reached 78.7 and 99.0 mM, respectively. When biological amination was carried out for 24 h, FF was fully transformed into FAM, achieving the productivity of 0.43 g FAM per g xylan. After biological transformations of SB-, RS-, and RL-derived FF for 24 h, the yields of FAM reached >99%, with the productivity of 0.31–0.34 g FAM per g xylan (Table 2). FF could be prepared from xylan in biomass *via* hydrolysis, dehydration, and cyclization reaction (Lee and Wu, 2021; Gong et al., 2022). Hence, the titer of FF derived from lignocellulosic biomass was mainly based on the xylan content in biomass. The biomass-derived FF could be wholly aminated to FAM by CCZU-XLS160 cells. It was observed that the generated FAM titer was largely determined by the xylan content of biomass in the tandem reaction with acidified SO_4^{2-}/SnO_2–HAP and CCZU-XLS160 cells. Hence, CC could produce high productivity of FAM *via* a chemoenzymatic approach in EaCl:Gly–water (1:2, v/v).

Lignocellulosic biomass is an available, inexpensive, and renewable source, which has been widely used for the production of value-added chemicals (Mika et al., 2018; Lee and Wu, 2021). FF is a key bio-based chemical. One of its common preparation methods is conducted *via* catalysis by using metal salts, mineral acids, and organic acids as homogeneous catalysts. Recently, heterogeneous catalysts are regarded as environmentally friendly catalysts, which can be easily recovered and reused as compared to some homogeneous ones (Gong et al., 2019). It is known that the establishment of an efficient valorization process would achieve high concentrations of FF (Weingarten et al., 2010; Metkar et al., 2015). DESs have gained considerable interest as reaction solvents for FF production due to their low toxicity, good reusability, high thermostability, and ease of preparation (Xu et al., 2020). In this work, biomass samples (7.5 wt%) were utilized as feedstocks for preparing FF after 10 min in EaCl:Gly–water (1:2, v/v; 180°C) by co-catalysis with SO_4^{2-}/SnO_2–HAP (2.0 wt%) and oxalic acid (0.4 wt%). Furthermore, biological amination of the prepared FF with whole-cell of CCZU-XLS160 could be used for the efficient production of FAM under an ambient performance condition. Tandem catalysis by bridging chemocatalysis and biocatalysis was constructed for the efficient

TABLE 2 Examination of the chemoenzymatic conversion potency toward different biomasses in EaCl:Gly–water (1:2, v/v).

Biomass	Xylan content in biomass, wt%	FF, mM (yield, %)[a]	FAM productivity, g FAM/g xylan[b]
Corncob (CC)	34.1	114.9 (59.3)	0.43
Sugarcane bagasse (SB)	29.6	79.6 (47.3)	0.34
Rice straw (RS)	29.0	74.5 (45.2)	0.33
Reed leaf (RL)	21.1	50.8 (42.4)	0.31

[a]Various biomass samples (7.5 wt%) were used as feedstocks for the production of FF, after 10 min at 180°C in EaCl:Gly–water (1:2, v/v) by co-catalysis with SO_4^{2-}/SnO_2–HAP (2.0 wt%) and oxalic acid (0.4 wt%).
[b]The formed FF was aminated to FAM by supplementary CCZU-XLS160 cells (0.050 g/mL) and NH_4Cl (2 mol NH_4Cl/mol FF) in EaCl:Gly–water (1:2, v/v; pH 7.5) at 35°C for 24 h.

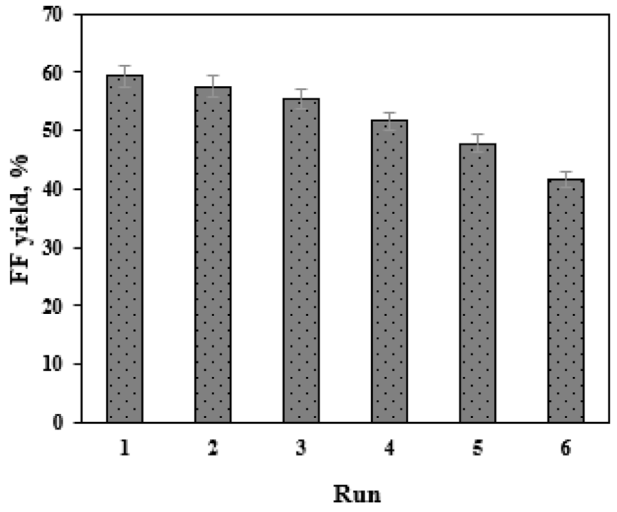

FIGURE 7
Reuse of SO_4^{2-}/SnO_2–HAP in EaCl:Gly–water (1:2, v/v) at 180°C for 10 min.

and sustainable valorization of biomass into FAM. In the future, it is of great interest to establish a cost-effective catalytic process to obtain high FF concentration and thus further improve FAM productivity with high ω-transaminase activity.

4 Conclusion

To summarize, the establishment of an efficient chemoenzymatic approach for converting abundant, cheap, and renewable lignocellulosic biomass into value-added furans can be used as a sustainable strategy in the biorefinery process. In an eco-friendly reaction system, various types of lignocellulosic biomasses can be converted to FAM *via* sequential catalyses with solid acid catalysts and transaminase biocatalysts.

Using hydroxyapatite (HAP) as a carrier, solid acid catalyst SO_4^{2-}/SnO_2–HAP was prepared for catalyzing xylan-rich biomass in this work. Organic acids were used to assist newly synthesized SO_4^{2-}/SnO_2–HAP for FF production. It was found that oxalic acid (pKa = 1.25; 0.4 wt%) plus SO_4^{2-}/SnO_2–HAP (2.0 wt%) gave the highest FF yield in EaCl:Gly–water (1:2, v/v) at 180°C after 10 min. SO_4^{2-}/SnO_2–HAP had a good reusability performance, which could be reused for six runs.

FF liquors, which were obtained from different biomasses by co-catalyses with oxalic acid and SO_4^{2-}/SnO_2–HAP in EaCl:Gly–water, could be fully aminated into FAM with the yield >99% with CCZU-XLS160 cells within 24 h. This established chemoenzymatic conversion strategy could be utilized in the valorization of renewable lignocellulosic biomass to valuable furan-based compounds in the eco-friendly EaCl:Gly–water system.

Data availability statement

The original contributions presented in the study are included in the article/Supplementary Material; further inquiries can be directed to the corresponding authors.

Author contributions

WH: conceptualization, methodology, and writing original draft; Y-CH and JY: data curation, software, supervision, review, and revision of the manuscript. All authors have read and agreed to the published version of the manuscript.

Conflict of interest

The authors declare that the research was conducted in the absence of any commercial or financial relationships that could be construed as a potential conflict of interest.

Publisher's note

All claims expressed in this article are solely those of the authors and do not necessarily represent those of their affiliated organizations, or those of the publisher, the editors, and the reviewers. Any product that may be evaluated in this article, or claim that may be made by its manufacturer, is not guaranteed or endorsed by the publisher.

References

Agirrezabal-Telleria, I., Gandarias, I., and Arias, P.-L. (2014). Heterogeneous acid-catalysts for the production of furan-derived compounds (furfural and hydroxymethylfurfural) from renewable carbohydrates: A review. *Catal. Today* 234, 42–58. doi:10.1016/j.cattod.2013.11.027

Bozell, J.-J., and Petersen, G.-R. (2010). Technology development for the production of biobased products from biorefinery carbohydrates-the US Department of Energy's "Top 10" revisited. *Green Chem.* 12, 539–554. doi:10.1039/b922014c

Cai, C.-M., Zhang, T.-Y., Kumar, R., and Wyman, C.-E. (2014). Integrated furfural production as a renewable fuel and chemical platform from lignocellulosic biomass. *J. Chem. Technol. Biotechnol.* 89, 2–10. doi:10.1002/jctb.4168

Chen, Z., and Wan, C.-X. (2019). A novel deep eutectic solvent/acetone biphasic system for high-yield furfural production. *Bioresour. Technol. Rep.* 8, 100318. doi:10.1016/j.biteb.2019.100318

Choudhary, V., Pinar, A.-B., Sandler, S.-I., Vlachos, D.-G., and Lobo, R.-F. (2011). Xylose isomerization to xylulose and its dehydration to furfural in aqueous media. *ACS Catal.* 1, 1724–1728. doi:10.1021/cs200461t

Delidovich, I., Hausoul, P.-J.-C., Deng, L., Pfutzenreuter, R., Rose, M., and Palkovits, R. (2016). Alternative monomers based on lignocellulose and their use for polymer production. *Chem. Rev.* 116, 1540–1599. doi:10.1021/acs.chemrev.5b00354

Di, J.-H., Gong, L., Yang, D., He, Y.-C., Tang, Z.-Y., and Ma, C.-L. (2021). Enhanced conversion of biomass to furfurylamine with high productivity by tandem catalysis with sulfonated perlite and ω-transaminase whole-cell biocatalyst. *J. Biotechnol.* 334, 26–34. doi:10.1016/j.jbiotec.2021.05.003

Dong, C.-L., Wang, H.-T., Du, H.-C., Peng, J.-B., Cai, Y., Guo, S., et al. (2020). Ru/HZSM-5 as an efficient and recyclable catalyst for reductive amination of furfural to furfurylamine. *Mol. Catal.* 482, 110755. doi:10.1016/j.mcat.2019.110755

Douthwaite, M., Huang, X.-Y., Iqbal, S., Miedziak, P.-J., Brett, G.-L., Kondrat, S.-A., et al. (2017). The controlled catalytic oxidation of furfural to furoic acid using AuPd/Mg(OH)(2). *Catal. Sci. Technol.* 7, 5284–5293. doi:10.1039/C7CY01025G

Enslow, K.-R., and Bell, A.-T. (2015). The role of metal halides in enhancing the dehydration of xylose to furfural. *ChemCatChem* 7, 479–489. doi:10.1002/cctc.201402842

Feng, L., Bo, C., Rui, M., Liang, J., Hua, S., and Song, H. (2016). Performance of Cu/TiO_2-SiO_2 catalysts in hydrogenation of furfural to furfuryl alcohol. *Can. J. Chem. Eng.* 94, 1368–1374. doi:10.1002/cjce.22503

Garcia-Sancho, C., Sadaba, I., Moreno-Tost, R., Merida-Robles, J., Santamaria-Gonzalez, J., Lopez-Granados, M., et al. (2013). Dehydration of xylose to furfural over MCM-41-supported niobium-oxide catalysts. *ChemSusChem* 6, 635–642. doi:10.1002/cssc.201200881

Gong, L., Xu, Z.-Y., Dong, J.-J., Li, H., Han, R.-Z., Xu, G.-C., et al. (2019). Composite coal fly ash solid acid catalyst in synergy with chloride for biphasic preparation of furfural from corn stover hydrolysate. *Bioresour. Technol.* 293, 122065. doi:10.1016/j.biortech.2019.122065

Gong, L., Zha, J., Pan, L., Ma, C., and He, Y.-C. (2022). Highly efficient conversion of sunflower stalk-hydrolysate to furfural by sunflower stalk residue-derived carbonaceous solid acid in deep eutectic solvent/organic solvent system. *Bioresour. Technol.* 351, 126945. doi:10.1016/j.biortech.2022.126945

Guenic, S.-L., Delbecq, F., Ceballos, C., and Len, C. (2015). Microwave-assisted dehydration of *D*-xylose into furfural by diluted inexpensive inorganic salts solution in a biphasic system. *J. Mol. Catal. A Chem.* 410, 1–7. doi:10.1016/j.molcata.2015.08.019

He, Y.-C., Ding, Y., Ma, C.-L., Di, J.-H., Jiang, C.-L., and Li, A.-T. (2017a). One-pot conversion of biomass-derived xylose to furfuralcohol by a chemo-enzymatic sequential acid-catalyzed dehydration and bioreduction. *Green Chem.* 19, 3844–3850. doi:10.1039/c7gc01256j

He, Y.-C., Jiang, C.-X., Chong, G.-G., Di, J.-H., Wu, Y.-F., Wang, B.-Q., et al. (2017b). Chemical-enzymatic conversion of corncob-derived xylose to furfuralcohol by the tandem catalysis with SO_4^{2-}/SnO_2-kaoline and *E coli* CCZU-T15 cells in toluene–water media. *Bioresour. Technol.* 245, 841–849. doi:10.1016/j.biortech.2017.08.219

Himmel, M.-E., Ding, S.-Y., Johnson, D.-K., Adney, W.-S., Nimlo, M.-R., Brady, J.-W., et al. (2007). Biomass recalcitrance: Engineering plants and enzymes for biofuels production. *Science* 315, 804–807. doi:10.1126/science.1137016

Hu, D.-X., Ju, X., Li, L.-Z., Hu, C.-Y., Yan, L.-S., Wu, T.-Y., et al. (2014). Improved *in situ* saccharification of cellulose pretreated by dimethyl sulfoxide/ionic liquid using cellulase from a newly isolated *Paenibacillus sp. LLZ1*. *Bioresour. Technol.* 201, 8–14. doi:10.1016/j.biortech.2015.11.039

Kaiprommarat, S., Kongparakul, S., Reubroycharoen, P., Guan, G.-Q., and Samar, C. (2016). Highly efficient sulfonic MCM-41 catalyst for furfural production: Furan-based biofuel agent. *Fuel* 174, 189–196. doi:10.1016/j.fuel.2016.02.011

Lam, E., Chong, J.-H., Majid, E., Liu, Y., Hrapovic, S., Leung, A.-C.-W., et al. (2012). Carbocatalytic dehydration of xylose to furfural in water. *Carbon* 50, 1033–1043. doi:10.1016/j.carbon.2011.10.007

Lange, J., Heide, E.-V.-D., Buijtenen, J.-V., and Price, R. (2012). Furfural–a promising platform for lignocellulosic biofuels. *ChemSusChem* 4, 150–166. doi:10.1002/cssc.201100648

Lee, C.-B.-T.-L., and Wu, T.-Y. (2021). A review on solvent systems for furfural production from lignocellulosic biomass. *Renew. Sust. Energ Rev.* 137, 110172. doi:10.1016/j.rser.2020.110172

Li, A.-L., Hou, X.-D., Lin, K.-P., Zhang, X., and Fu, M.-H. (2018). Rice straw pretreatment using deep eutectic solvents with different constituents molar ratios: Biomass fractionation, polysaccharides enzymatic digestion and solvent reuse. *J. Biosci. Bioeng.* 126, 346–354. doi:10.1016/j.jbiosc.2018.03.011

Li, H.-L., Deng, A.-J., Ren, J.-L., Liu, C.-Y., Lu, Q., Zhong, L.-J., et al. (2014). Catalytic hydrothermal pretreatment of corncob into xylose and furfural via solid acid catalyst. *Bioresour. Technol.* 158, 313–320. doi:10.1016/j.biortech.2014.02.059

Li, Q., Hu, Y., Tao, Y.-Y., Zhang, P.-Q., Ma, C.-L., Zhou, Y.-J., et al. (2021). Improving biocatalytic synthesis of furfuryl alcohol by effective conversion of *D*-xylose into furfural with tin-loaded sulfonated carbon nanotube in cyclopentylmethyl ether-water media. *Catal. Lett.* 148, 3189–3196. doi:10.1007/s10562-021-03570-3

Li, X.-Y., Yang, J.-X., Xu, R., Lu, L.-F., Kong, F.-K., Liang, M., et al. (2019). Kinetic study of furfural production from Eucalyptus sawdust using H-SAPO-34 as solid Brønsted acid and Lewis acid catalysts in biomass-derived solvents. *Ind. Crop Prod.* 135, 196–205. doi:10.1016/j.indcrop.2019.04.047

Ma, J., Li, W., Guan, S., Liu, Q., Li, Q., Zhu, C., et al. (2019). Efficient catalytic conversion of corn stalk and xylose into furfural over sulfonated graphene in γ-valerolactone. *RSC Adv.* 9, 10569–10577. doi:10.1039/c9ra01411j

Ma, Z., Liao, Z., Ma, C., He, Y., Gong, C.-J., and Yu, X. (2020). Chemoenzymatic conversion of sorghum durra stalk into furoic acid by a sequential microwave-assisted solid acid conversion and immobilized whole-cells biocatalysis. *Bioresour. Technol.* 311, 123474. doi:10.1016/j.biortech.2020.123474

Marcotullio, G., and de Jong, W. (2010). Chloride ions enhance furfural formation from *D*-xylose in dilute aqueous acidic solutions. *Green Chem.* 12, 1739–1746. doi:10.1039/b927424c

Metkar, P.-S., Till, E.-J., Corbin, D.-R., Pereira, C.-J., Hutchenson, K.-W., and Sengupta, S.-K. (2015). Reactive distillation process for the production of furfural using solid acid catalysts. *Green Chem.* 17, 1453–1466. doi:10.1039/c4gc01912a

Mika, L.-T., Csefalvay, E., and Nemeth, A. (2018). Catalytic conversion of carbohydrates to initial platform chemicals: Chemistry and sustainability. *Chem. Rev.* 118, 505–613. doi:10.1021/acs.chemrev.7b00395

Möller, M., and Schröder, U. (2013). Hydrothermal production of furfural from xylose and xylan as model compounds for hemicelluloses. *RSC Adv.* 3, 22253–22260. doi:10.1039/c3ra43108h

Morais, E.-S., Freire, M.-G., Freire, C., Coutinho, J., and Silvestre, A. (2020). Enhanced conversion of xylan into furfural using acidic deep eutectic solvents with dual solvent and catalyst behavior. *ChemSusChem* 13, 784–790. doi:10.1002/cssc.201902848

Ni, J., Li, Q., Gong, L., Liao, X.-L., Zhang, Z.-J., Ma, C., et al. (2021). Highly efficient chemoenzymatic cascade catalysis of biomass into furfurylamine by a heterogeneous shrimp shell-based chemocatalyst and an ω-transaminase biocatalyst in deep eutectic solvent–water. *ACS Sustain Chem. Eng.* 9, 13084–13095. doi:10.1021/acssuschemeng.1c05109

Pan, L., Li, Q., Tao, Y., Ma, C., Chai, H., Ai, Y., et al. (2022). An efficient chemoenzymatic strategy for valorisation of corncob to furfuryl alcohol in CA: Betaine-water. *Ind. Crop. Prod.* 186, 115203. doi:10.1016/j.indcrop.2022.115203

Peleteiro, S., Garrote, G., Santos, V., and Parajó, J.-C. (2014). Furan manufacture from softwood hemicelluloses by aqueous fractionation and further reaction in a catalyzed ionic liquid: A biorefinery approach. *J. Clean. Prod.* 76, 200–203. doi:10.1016/j.jclepro.2014.04.034

Peng, B., Ma, C.-L., Zhang, P.-Q., Wu, C.-Q., Wang, Z.-W., Li, A.-T., et al. (2019). An effective hybrid strategy for converting rice straw to furoic acid by tandem catalysis via Sn-sepiolite combined with recombinant *E coli* whole cells harboring horse liver alcohol dehydrogenase. *Green Chem.* 21, 5914–5923. doi:10.1039/C9GC02499A

Pholjaroen, B., Li, N., Wang, Z., Wang, A., and Zhang, T. (2013). Dehydration of xylose to furfural over niobium phosphate catalyst in biphasic solvent system. *J. Energy Chem.* 22, 826–832. doi:10.1016/S2095-4956(14)60260-6

Qiu, M., Guo, T., Li, D., and Qi, X. (2020). Highly efficient catalytic transfer hydrogenation of biomass-derived furfural to furfuryl alcohol using UiO-66 without metal catalysts. *Appl. Catal. A Gen.* 602, 117719. doi:10.1016/j.apcata.2020.117719

Riva, L., Fiorati, A., and Punta, C. (2021). Synthesis and application of cellulose-polyethyleneimine composites and nanocomposites: A concise review. *Materials* 14, 473. doi:10.3390/ma14030473

Rong, C.-G., Ding, X.-F., Zhu, Y.-C., Li, Y., Wang, L.-L., Qu, Y.-N., et al. (2012). Production of furfural from xylose at atmospheric pressure by dilute sulfuric acid and inorganic salts. *Carbohyd Res.* 350, 77–80. doi:10.1016/j.carres.2011.11.023

Selig, M., Weiss, N., and Ji, Y. (2008). *Enzymatic saccharification of lignocellulosic biomass*. Golden, Golden, Colorado: National Renewable Energy Laboratory.

Sweygers, N., Harrer, J., Dewil, R., and Appels, L. (2018). A microwave-assisted process for the *in-situ* production of 5-hydroxymethylfurfural and furfural from lignocellulosic polysaccharides in a biphasic reaction system. *J. Clean. Prod.* 187, 1014–1024. doi:10.1016/j.jclepro.2018.03.204

Tau, L.-Y., Nurabiyiah, M., and Nor, M.-M.-Y. (2016). Furfural production from oil Palm biomass using a biomass-derived supercritical ethanol solvent and formic acid catalyst. *Procedia Eng.* 148, 392–400. doi:10.1016/j.proeng.2016.06.495

Wang, C., Zhang, L., Zhou, T., Chen, J., and Xu, F. (2017). Synergy of Lewis and Brønsted acids on catalytic hydrothermal decomposition of carbohydrates and corncob acid hydrolysis residues to 5-hydroxymethylfurfural. *Sci. Rep.* 7, 40908–40909. doi:10.1038/srep40908

Weingarten, R., Cho, J., Conner, J.-W.-C., and Huber, W.-G. (2010). Kinetics of furfural production by dehydration of xylose in a biphasic reactor with microwave heating. *Green Chem.* 12, 1423–1429. doi:10.1039/c003459b

Widsten, P., Murton, K., and West, M. (2018). Production of 5-hydroxymethylfurfural and furfural from a mixed saccharide feedstock in biphasic solvent systems. *Ind. Crop Prod.* 119, 237–242. doi:10.1016/j.indcrop.2018.04.032

Xu, G., Li, H., Xing, W., Gong, L., Dong, J., and Ni, Y. (2020). Facilely reducing recalcitrance of lignocellulosic biomass by a newly developed ethylamine-based deep eutectic solvent for biobutanol fermentation. *Biotechnol. Biofuels* 13, 166. doi:10.1186/s13068-020-01806-9

Xu, J., Hou, H., Liu, B., and Hu, J. (2017). The integration of different pretreatments and ionic liquid processing of eucalyptus: Hemicellulosic

products and regenerated cellulose fibers. *Ind. Crop Prod.* 101, 11–20. doi:10.1016/j.indcrop.2017.02.038

Yin, X., Wei, L., Pan, X., Liu, C., and Wang, K. (2021). The pretreatment of lignocelluloses with green solvent as biorefinery preprocess: A minor review. *Front. Plant Sci.* 12, 670061–670076. doi:10.3389/fpls.2021.670061

Zang, H., and Chen, E. Y. X. (2015). Organocatalytic upgrading of furfural and 5-hydroxymethyl furfural to C10 and C12 furoins with quantitative yield and atom-efficiency. *Int. J. Mol. Sci.* 16, 7143–7158. doi:10.3390/ijms16047143

Zhang, L.-X., Yu, H., Yu, H. B., Chen, Z., and Yang, L. (2014). Conversion of xylose and xylan into furfural in biorenewable choline chloride–oxalic acid deep eutectic solvent with the addition of metal chloride. *Chin. Chem. Lett.* 25, 1132–1136. doi:10.1016/j.cclet.2014.03.029

Zhang, P., Liao, X., Ma, C., Li, Q., and He, Y. (2019). Chemoenzymatic conversion of corncob to furfurylamine via tandem catalysis with tin-based solid acid and transaminase biocatalyst. *ACS Sustain Chem. Eng.* 7 (21), 17636–17642. doi:10.1021/acssuschemeng.9b03510

Zheng, Z.-J., Xu, Q., Tan, H., Zhou, F., and Ouyang, J. (2020). Selective biosynthesis of furoic acid from furfural by Pseudomonas Putida and identification of molybdate transporter involvement in furfural oxidation. *Front. Chem.* 8, 587456. doi:10.3389/fchem.2020.587456

Zhu, X., Ma, C.-L., Xu, J.-X., Xu, J.-X., and He, Y.-C. (2020). Sulfonated vermiculite-mediated catalysis of reed (phragmites communis) into furfural for enhancing the biosynthesis of 2-furoic acid with a dehydrogenase biocatalyst in a one-pot manner. *Energ Fuel* 34, 14573–14580. doi:10.1021/acs.energyfuels.0c02707

frontiers | Frontiers in Bioengineering and Biotechnology

TYPE Original Research
PUBLISHED 30 June 2023
DOI 10.3389/fbioe.2023.1211410

OPEN ACCESS

EDITED BY
Krist V. Gernaey,
Technical University of Denmark,
Denmark

REVIEWED BY
Ralf Pörtner,
Hamburg University of Technology,
Germany
Johannes Felix Buyel,
University of Natural Resources and Life Sciences, Austria

*CORRESPONDENCE
Lucas Nik Reger,
lucas.reger@sartorius.com

RECEIVED 24 April 2023
ACCEPTED 22 June 2023
PUBLISHED 30 June 2023

CITATION
Reger LN, Saballus M, Kappes A, Kampmann M, Wijffels RH, Martens DE and Niemann J (2023), A novel hybrid bioprocess strategy addressing key challenges of advanced biomanufacturing.
Front. Bioeng. Biotechnol. 11:1211410.
doi: 10.3389/fbioe.2023.1211410

A novel hybrid bioprocess strategy addressing key challenges of advanced biomanufacturing

Lucas Nik Reger[1,2]*, Martin Saballus[1], Annika Kappes[1], Markus Kampmann[1], Rene H. Wijffels[2], Dirk E. Martens[2] and Julia Niemann[1]

[1]Corporate Research, Sartorius, Göttingen, Germany, [2]Bioprocess Engineering, Wageningen University, Wageningen, Netherlands

Monoclonal antibodies (mAb) are commonly manufactured by either discontinuous operations like fed-batch (FB) or continuous processes such as steady-state perfusion. Both process types comprise opposing advantages and disadvantages in areas such as plant utilization, feasible cell densities, media consumption and process monitoring effort. In this study, we show feasibility of a promising novel hybrid process strategy that combines beneficial attributes of both process formats. In detail, our strategy comprises a short duration FB, followed by a fast media exchange and cell density readjustment, marking the start of the next FB cycle. Utilizing a small-scale screening tool, we were able to identify beneficial process parameters, including FB interval duration and reinoculation cell density, that allow for multiple cycles of the outlined process in a reproducible manner. In addition, we could demonstrate scalability of the process to a 5L benchtop system, using a fluidized-bed centrifuge as scalable media exchange system. The novel process showed increased productivity (+217%) as well as longer cultivation duration, in comparison to a standard FB with a significantly lower media consumption per produced product (–50%) and a decreased need for process monitoring, in comparison to a perfusion cultivation. Further, the process revealed constant glycosylation pattern in comparison to the perfusion cultivation and has strong potential for further scale-up, due to the use of fully scalable cultivation and media exchange platforms. In summary, we have developed a novel hybrid process strategy that tackles the key challenges of current biomanufacturing of either low productivity or high media consumption, representing a new and innovative approach for future process intensification efforts.

KEYWORDS

CHO cell culture, process intensification, fluidized bed centrifuge, monoclonal antibodies, intermediate harvest, continuous biomanufacturing

1 Introduction

The development and manufacturing of biopharmaceuticals including monoclonal antibodies (mAb) have gained major importance due to their growing demand in treatments of cancerous, immunological and infectious diseases (Johnson, 2018). MAbs offer higher target specificities and elongated half-lives compared to pharmaceuticals of low molecular weight, such as small molecule drugs, resulting in a high interest in these molecules as demonstrated by increasing numbers of antibodies entering clinical trials,

and getting regulatory approval (Hansel et al., 2010). Additionally, their mode of action can be modified and optimized in various ways by molecular engineering (Presta, 2008). However, to achieve the desired bioactivity and avoid immunogenicity, host-specific posttranslational modifications (PTM) of the expressed mAb, like glycosylation, are essential (Jayapal et al., 2007). Therefore, mAbs are commonly expressed in mammalian cells capable of PTM, especially in Chinese Hamster Ovary (CHO) cells due to their status as secure production host and their proven high volumetric productivity (Kim et al., 2012). Thereby, different process modes are utilized within the upstream manufacturing of mAb based therapeutics comprising distinct sets of advantages and disadvantages.

A commonly used upstream process operation in mAb production is the fed-batch (FB) mode, comprising feed additions throughout a batch cultivation to supply fresh nutrients to the cells. This process comprises an exponential growth phase in which cell numbers increase and cell viability is high, followed by a stationary- and death phase with stable or decreasing viable cell counts and decreasing viability. Commonly, the accumulation of metabolic byproducts or nutrient limitation triggers the transition from the growth phase to the stationary phase and hence, limits the achievable cell density, cultivation time and volumetric productivity (Abu-Absi et al., 2014). The advantages of the FB operation are efficient utilization of growth media in comparison continuous processes, resulting in lower operational costs which increases the economic potential (Pollock et al., 2013).

To overcome the FB specific limitations, like decreased cell densities and cultivation durations, continuous processes like perfusion are applied (Hiller et al., 2017). Thereby, a continuous media exchange is applied, while cells are kept in the reactor using cell retention devices, which usually are filter-based-systems in either tangential flow or alternative tangential flow. Alternative cell retention can be achieved, for example, by using hydrocyclones, acoustic separation or gravitational settlers (Castilho and Medronho, 2002; Voisard et al., 2003; Bettinardi et al., 2020). Thereby, spent media containing the product, residual nutrients as well as metabolic byproducts passes the cell retention device and consecutive enters the downstream operations, meanwhile new media is added to the process to supply fresh nutrients. With the application of cell bleed, i.e., removing spent medium with cells, a pseudo-steady state can be introduced, allowing for stable high cell densities. This process modification allows for an up to 5-fold increase in volumetric productivity and can strongly enhance plant utilization compared to a fed-batch process (Dowd et al., 2003; Xu et al., 2017). However, high media expenses due to media exchange rates up to 3 bioreactor volumes per day, limited filter capacities and operational complexity are the downsides of perfusion processes (Hiller et al., 2017; MacDonald et al., 2022).

Besides the two main process operations, novel process intensification strategies have emerged during recent years, aiming to combine on FB and perfusion cell culture techniques to reach high volumetric productivities as in perfusion with a reduced use of medium as in fed-batch. One example comprises enhanced cell counts in the seed train, facilitated by perfusion operation, followed by a FB operation in the production bioreactor. This intensification strategy not only allows for significantly reduced seed culture volumes and steps as well as increased n-stage inoculation cell densities that consecutively eliminate the less productive initial growth phase in the production reactor (Schulze et al., 2021). This so called high inoculation FB decreases the total process time, while keeping final mAb titers constant, resulting in an overall increase in process productivity (Yang et al., 2014; Yongky et al., 2019; Schulze et al., 2022). Another approach by (Hiller et al., 2017) involves a perfusion process in the beginning of the cultivation to increase the overall cell density, subsequently the process is changed to a FB operation to minimize media consumption. Thereby, the overall output of the process could be enhanced with a relatively low increase of media consumption. A third hybrid approach recently demonstrated by our group is the so-called intermediate harvest (IH) strategy, a single and fast media exchange during a FB operation done by a fluidized-bed-centrifuge (FBC) (Reger et al., 2023). By doing a single media exchange in this way increased peak cell densities as well as volumetric productivities could be achieved similar to the process from (Hiller et al., 2017). All of these intensified processes rely on a beneficial combination of high cell densities of the perfusion culture mode and the low media consumption of the FB process mode, However, all introduced intensification have a limited process duration and thus still result in a discontinuous process mode. Therefore, a process with continuous characteristics alongside to low media consumption and high cell densities is highly desirable.

The aim of this study was to identify a possible process scheme to enable a continuous process operation based on a hybrid process strategy between perfusion and fed-batch. Thereby, this new process should combine increased volumetric productivities, as achieved in common discontinuous FB process, with significant lower media consumption as required in typical continuous perfusion cultivation. In addition, the process should comprise comparably low process control and monitoring needs. To enable this hybrid process strategy the rapid media exchange by Intermediate Harvests (IH) should be utilized, followed by a short duration fed-batch (FB cycle). This process will be further referred to as continuous fed-batch (cFB). In a first step, the feasibility and limitations of this new concept should be investigated in a 15 mL small-scale system utilizing a IH mimic method. Thereby, different re-inoculations densities and FB durations should be evaluated. In a second step the most promising concept should be scaled-up to benchtop-scale to demonstrate feasibility, and further process optimization. Subsequently, a comparison to the standard process, FB and steady-state perfusion, should be conducted.

2 Materials and methods

2.1 Cell line and medium

A DHFR-deficient Chinese hamster ovary (CHO- DG44) monoclonal cell line was used, stably expressing an IgG_1 (pI: 7.3) product. The chemically defined 4Cell SmartCHO (Sartorius Stedim Biotech) media system, comprising the Stock and Adaption media as well as the Production Media with a two feed solution (Feed A and Feed B) was used for all n-stage processes as well as seed train cultivations. All seed trains were conducted with similar passage counts to secure consistency.

2.2 Process characterization: small scale trials

The small-scale screening was conducted in an Ambr15 (Sartorius Stedim Biotech) high throughput system. Thereby, re-inoculation densities were tested from 20 × 10^6 to 30 × 10^6 cells/mL and FB durations between 2 and 3 days. After preparation of the system, temperature setpoint was set to 36.8°C, pH was controlled at 7.1 through CO_2 gassing. DO was controlled at 40% with O_2 gassing and stirrer speed set to 1.300 rpm with a liquid volume at around 11 mL. Bioreactors were inoculated with 0.3 × 10^6 cells/mL. After a 72-h batch phase, daily bolus feeds (Feed A with 4% and Feed B with 0.4%) with decreasing volumetric percentage and glucose (setpoint 4.5 g/L) were started. On day 6, all cultures were processed by using the semi-perfusion method (Janoschek et al., 2019) to mimic the FBC operation and consecutive fresh media enriched basal media according to Janoschek et al. (2019) was supplied to each vessel. Subsequent, a flexible feeding scheme was implemented based on the daily viable cell volume. Thereby, the viable cell volume on peak cell density of the common FB process (34.9 mm^3/mL) was fixed as single multiplication factor. Subsequent, the viable cell volume was determined daily and the multiplication factor was calculated and applied to the feed. Feeding volumes were split into two boluses for feeding 12 h apart. For all cultures the vessels were changed at day 12. On days of IHs, feeding scheme was adjusted to a single half feed to avoid overfeeding of cells cultured. Cell cultures were ended when reaching 70% cell viability or when observing stagnating cell growth between IHs.

2.3 Proof of concept: 5 L benchtop scale

The proof of concept was conducted in a 5 L Univessel (Sartorius Stedim Biotech) system utilizing the 2-day IH interval with re-inoculation at 20 × 10^6 cells/mL for a total of six repetitions. Two different sets of experiments were done mainly differing in the wash media matrix and re-inoculation matrix for the FBC operations further explained in Section 2.4. Bioreactors were inoculated with 0.3 × 10^6 cells/mL from seed-cultures with a working volume of 3 L and similar DO, pH and temperature settings. Similar to small scale, an initial batch phase for 72 h was conducted with subsequent daily bolus feeding of the two complementary feeding solutions. On day 5, the cultures were processed by the FBC operations, with a subsequent cell bleed to reach a starting density of 20 × 10^6 cells/mL. Similar to the small scale a flexible fixed feeding twice a day in a multiplication factor of IVCV was implemented, on harvest days a decreased feeding was utilized to diminish possibility of excessive feeding. After six repetitions the cultivation was ended.

2.4 FBC operation

For cell separation, concentration, and washing, an automated single-use centrifuge Ksep® 400 system with a Ksep® 400 Cell Wash Harvest Consumable Kit (Sartorius) was used. Thereby, the FBC operation consists of the steps loading, washing and discharging in cyclic repetition. The tubing of all receptions to the FBC system was sterile connected by a BioWelder® system (Sartorius) and disconnected by a BioSealer® TC system (Sartorius).

To achieve almost complete cell retention and replacement of the spent medium during each IH step by the FBC, cell broth was loaded and washed according to a protocol established by (Saballus et al., 2021). In brief, the FBC was set to constant 1,000 × g at flow rate of 100 mL/min/chamber for loading and washing, with a maximal loading per chamber of around 90%. High concentration of the washed cells was enabled by an adapted FBC discharging recipe of the processed cells, applying an initial dump volume of 100 mL with a subsequent harvest volume of 300 mL at a harvest flow rate of 300 mL/min per FBC chamber. Both tested wash media, the pH 7.4 phosphate buffered saline (PBS, chemicals supplied by Carl Roth) and the fresh enriched basal medium generated according to Janoschek et al. (2019) were pre-tempered at 37°C, the subsequent FBC process was not temperature controlled.

2.5 Sampling and analytics

Cell characteristics were measured by Cedex HiRes (Roche), metabolic parameters and pH by ABL800 basic (Radiometer) and ammonia analyzed via BioProfile® FLEX2™ (Nova Biomedical). Residual samples were centrifuged at 6600 × g for 5 min (Centrisart A-14, Sartorius) at RT and stored at −20°C until further analysis.

IgG concentrations were determined by size exclusion chromatography (SEC) utilizing the Vanquish™ Flex UHPLC System (Thermo Scientific) and Yarra™ 3 µm SEC-3000 (Phenomenex). For each measurement a standard curve with an IgG specific standard was prepared. The running buffer included 100 mM Na_2SO_4, 50 mM NaH_2PO_4 and 50 mM Na_2HPO_4 with pH 6.6 and was adjusted to a flowrate at 1 mL/min and 5 µL loading volume for each sample.

The relative amount of different IgG glycans was analyzed by capillary gel electrophoresis with the LabChip® GXII Touch™ HT Protein Characterization System (PerkinElmer). First, supernatant samples were purified using PreDictor MabSelect SuRe 96-well plates (Cytiva) and the Ab buffer kit (Cytiva). Buffer from protein A purification was exchanged and desalted using Vivaspin® 500 Centrifugal Concentrators (Sartorius) with a molecular mass cut off at 10 kDa. Purified and desalted samples were further processed with the Glycan Release and Labeling kit (PerkinElmer) for glycan measurement with the LabChip GXII Touch (Perkin Elmer).

Values for cell specific productivity (qP) as well as integral of viable cell concentration (IVCC) determination were calculated equivalent to Janoschek et al. (2019). Integral of viable cell volume (IVCV) and specific growth rate (µ) was calculated according to Schulze et al. (2021). Product recoveries for the IH operation were calculated in correspondence to Saballus et al. (2021). All calculations are specified further in the Supplementary Eqs S1–S5.

GraphPad Prism version 9.3.1 was used for statistical evaluation given in the single graphs. Threshold for significance level was α = 0.05, for normal distributed data sets analysis of variance (ANOVA) with Tukey's multiple comparison test was conducted. If standard deviation differed significantly according to Brown-Forsythe test, Dunnett's T3 multiple comparisons test was performed.

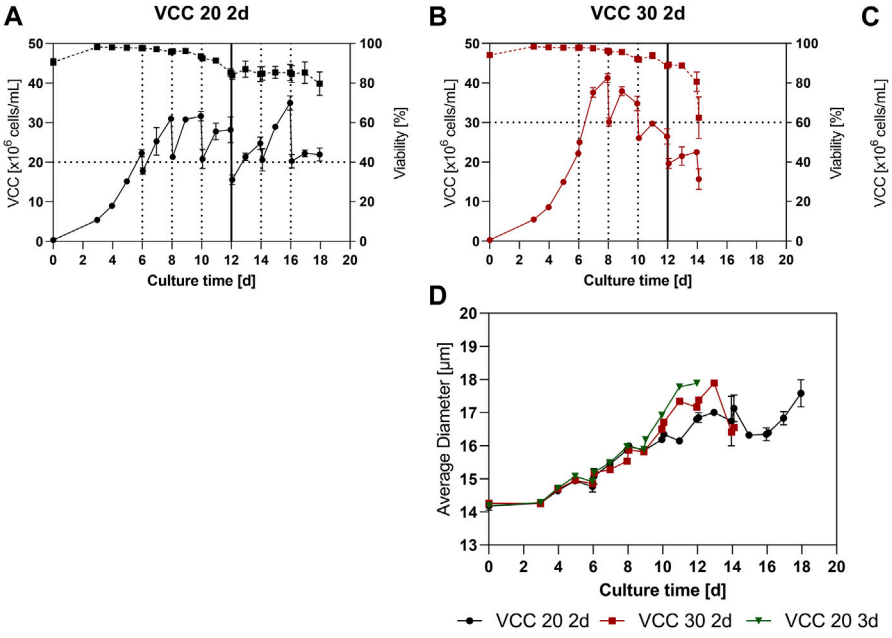

FIGURE 1
Cellular characteristics for the continuous fed-batch (cFB) process conducted in small scale. **(A–C)** Viable cell counts (solid line) and viabilities (dotted line) overtime for the scenarios VCC 20 d2 **(A)**, VCC 30 d2 **(B)** and VCC 20 d3 **(C)**. **(D)** Average diameter for each investigated approach over the course of the cultivation. All cultivations were done in duplicate and error bars represent the distance of the mean to the values obtained in both duplicates.

3 Results

The aim of this study was to combine the advantages of a perfusion process like elongated duration and increased cell densities overtime with the low media and consumable consumption of a discontinuous process format. In detail, this new designed process, called continuous fed-batch (cFB) should comprise a fixed FB duration (FB cycle) with a consecutive rapid and complete media exchange (IH operation) including a cell density adjustment (bleed). To test the applicability of this process a high throughput small-scale screening was conducted, utilizing a commercially relevant CHO cell line, comprising different durations and starting cell counts. Subsequent, the most promising approach was scaled up to a benchtop system (5L) to investigate the influence of the scalable exchange method via the fluidized bed centrifuge (FBC).

3.1 Process characterization at small scale

A small-scale trial was conducted to investigate a suitable cultivation scheme, including optimal FB cycle duration and cell density for reinoculation after the IH. Cells should remain in the logarithmic growth phase between IHs and therefore the cell bleed after each harvest cycle aims on keeping the cells in the proliferative state, defined as positive range of the cell specific growth rate (μ), to enable a continuous process mode. Three different approaches were investigated, re-inoculation at a viable cell count (VCC) of 20 × 10^6 cells/mL and an interval of 2 days (VCC 20 2d), re-inoculation at 30 × 10^6 cells/mL and an interval of 2 days (VCC 30 2d) and re-inoculation at 20 × 10^6 cells/mL and an interval of 3 days (VCC 20 3d), further explanation for the design space is discussed in Section 4.1. The VCC as well as the viability for the different conditions over time is shown in Figures 1A–C. All approaches show a similar growth and viability for the first 6 days as expected and reached VCCs of around 20 × 10^6 cells/mL. Subsequent, the first IH operations were conducted for each approach, indicated by the dotted lines.

The VCC 20 2d approach (Figure 1A) grew reproducible to a peak cell density of ~30 × 10^6 cells/mL over the first two FB cycles. Subsequent, from day 12 to the end of the cultivation a variation in peak cell density was visible (25–35 × 10^6 cells/mL), partially due to variations in reinoculation densities caused by vessel change which will be discussed further in Section 4.3. This trend is supported by the specific growth rate over time visible in Supplementary Figure S1. In total six repetition could be conducted in the small-scale trials showing decreased growth in the last repetitions. The viability values for the VCC 20 d2 approach showed a decrease to 85% at day 12, after which a stabilization of viabilities is visible and a final viability of 79% is reached at day 18. Interestingly, the stabilization of the viability and high variation in peak VCC start occurring from day 12, concomitant with the change of the bioreactor vessel.

The approach with increased cell densities (VCC 30 d2) reached a peak cell density of 41.2 × 10^6 cells/mL during the first FB phase, visible in Figure 1B. Consecutively, after the following IH operation the reinoculation cell density was set to 30 × 10^6 cells/mL (d8) and the next FB phase was initiated. During the subsequent FB intervals, a decline in cell growth was visible, resulting in a decrease of peak cell densities for this approach, even with the bioreactor change at day 12. Similar to the VCC the viability and specific growth rate

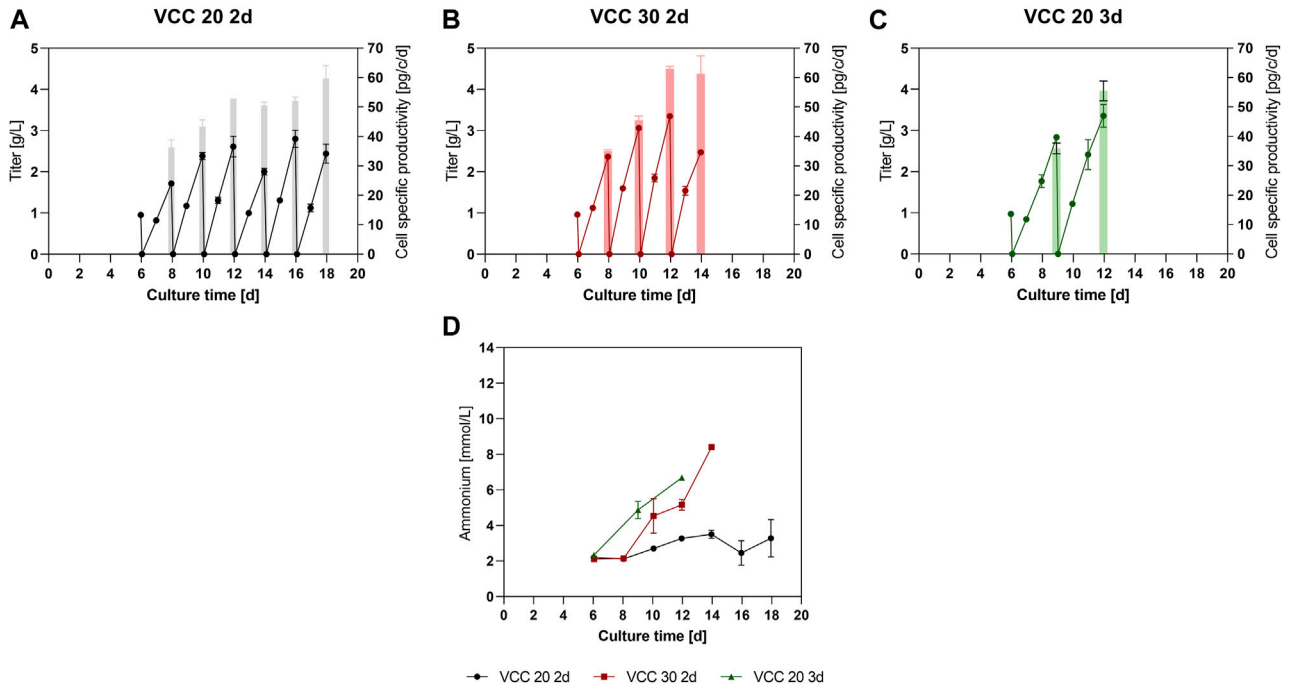

FIGURE 2
Expression levels of product and byproduct in the new designed process. **(A–C)** Titer values in g/L and cell specific productivity (pg/c/d) for the small-scale trials of the approaches VCC20 d2, VCC30 d2 and VCC 20 d3. **(D)** Ammonia level in mmol/L for each approach measured after the complete media exchange. All cultures were done in duplicate and error bars represent the distance of the mean to the values obtained in each duplicate.

decreased over the time course, and especially after the last IH procedure at day 14 leading to the termination of the culture.

Finally, the third investigated scenario (Figure 1C) with an elongated FB duration of 3 days and reinoculation cell densities of 20 × 10^6 cells/mL, VCC 20 3d, showed a stable cell growth after the first IH (d6) up to the end of the first FB cycle on day 9, reaching peak cell densities of 32.5 × 10^6 cells/mL. However, after this no further cell growth, in cell count and specific growth rate, within the second FB cycle could be detected and a decrease in cell viability occurred, leading to an end of the cultivation on day 12. Further data of lactate and glucose levels can be found in the Supplementary Material.

To gain further insight into the process the average cell diameter of each approach is displayed in Figure 1D. Interestingly, all approaches show a similar increase overtime from around 14 µm up to 18 µm. Notably, both cultures that received a vessel exchange (VCC20 2d and VCC30 2d) showed a temporary decrease in cell diameter shortly after the vessel change. Afterwards, the VCC20 2d showed a stabilization of the cellular diameter up to day 17.

To further analyze the approaches within the new designed process, product titers were quantified from day 6 on (Figures 2A–C). Thereby, all three approaches showed similar mAb titers of around 1 g/L up to day 6 before the initial IH operation. Subsequently, due to limited sampling volume at 15 mL scale no residual mAb titer sample was measured after the media exchange. Therefore, to improve visibility within Figures 2A–C, 0 g/L was assumed as starting point. For the approach VCC 20 2d, a mAb titer of 1.7 g/L (Figure 2A) could be detected after the first 2-day FB cycle on day 8. In the subsequent FB cycles, an increase to final titers of 2.0–2.8 g/L mAb, respectively, could be observed. Interestingly, an increase for the cell specific productivity (qP) over time is visible (bars in Figure 2A) from 36 pg/c/d within the first 2-day cultivation interval to 50–60 pg/c/d for the last four cycles. Accordingly, the mAb titer of the VCC 30 2d approach, Figure 2B, inclined from 2.3 g/L in the second IH (day 8) to over 3 g/L in the subsequent harvests. This increase is also reflected in the qP values, starting at around 35 pg/c/d for the second IH and reaching around 61–63 pg/c/d in the latest harvests. The titer values for the approach VCC 20 d3, shown in Figure 2C, indicate a stronger increase in titer in comparison to the VCC 20 2d approach with around 2.8–3.3 g/L in the first vs. the second 3 days of FB operation, respectively. Similar to other investigated approaches the qP values are increased from the second harvest (35 pg/c/d) to the third harvest (55 pg/c/d). Furthermore, the integrated titer over the complete cultivation duration is shown within the Supplementary Material. Interestingly, the incline in qP and titer correlates with the diameter increase shown in Figure 1D, indicating a proportional relation.

As an important byproduct and cell culture state indicator, the ammonia concentration was monitored over time. The VCC 20 d2 approach showed constant and low levels ranging between 2.2- and 3.5-mM ammonia over the entire cultivation time of 18 days. However, the ammonia concentrations for VCC 30 d2 and VCC 20 d3 increased to 6.6 and 8.4 mmol/L over the course of cultivations, indicating a significant ammonia accumulation in these cultures.

The data overall show that for each investigated approach at least 2 IH intervals could be carried out and an increase in qP with

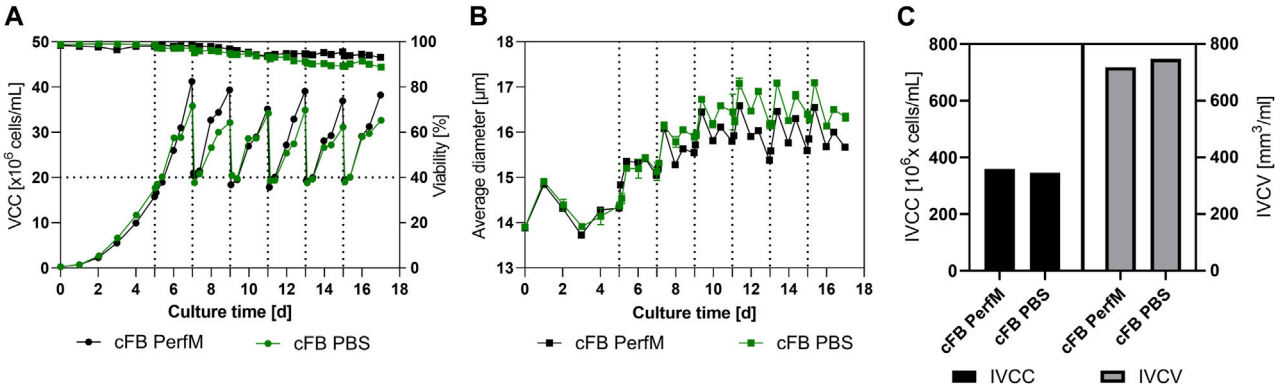

FIGURE 3
Cellular characteristics of the proof-of-Concept experiment at benchtop scale. **(A)** Viable cell counts (circles) and Viability (squares) for both experimental approaches over time, the horizontal bar shows the targeted re-inoculation VCC. **(B)** Cellular diameter for both set of experiments overtime. **(C)** Summarized Integral of viable cell count (IVCC) and Integral of viable cell volume (IVCV) for the conducted experiments. All Media exchange (IH) events were indicated by a dotted vertical line at the specific timepoints.

increasing process duration could be obtained, indicating a beneficial process strategy. Based on our data set the most promising approach, characterized by longest proliferating phase and low and stable amounts of ammonia over multiple IH cycles was the VCC20 d2. Therefore, the conducted small-scale screening indicates a feasible scenario for the proposed cFB process if a reinoculation cell density of 20 × 10^6 cells/mL and an FB duration of 2 days is pursued (VCC20 d2). In accordance, this approach was chosen for a scale-up to a 5 L bioreactor scale, comprising a fluidized-bed centrifuge (FBC) as scalable cell separation method for the IH operations.

3.2 Proof of concept at benchtop scale

Following the process characterization of the different proposed cFB scenarios at screening scale a process scale-up with the identified preferential parameters, re-inoculation cell density 20 × 10^6 cells/mL and a 2-day interval, was conducted. This proof-of-concept run was pursued utilizing a 5 L benchtop reactor and a single-use FBC system for time saving, gentle and complete media exchange. Two parallel cultivations were conducted, comprising one approach with enriched cell culture media, further explained in Section 2.4, as wash buffer for the FBC operation (cFBPerfM) and a second approach utilizing PBS as wash buffer (cFB PBS).

The course of VCC and viability for both benchtop reactors over time is displayed in Figure 3A. The cultivation conducted with enriched media as wash buffer (cFB PerfM; black line) showed overall consistent growth between the FB cycles. Overall peak cell densities after 2 days ranging from 35 × 10^6 to 41 × 10^6 cells/mL were reached throughout all six repetitions. This consistent growth is as well confirmed by the stable specific growth rate of around 0.37 1/d visible in the Supplementary Material. Additionally, the cell culture maintained a high cell viability of over 93% until the last day of the process. The approach utilizing PBS as wash buffer during IH operations (blue line) showed very similar trends. In this approach slightly decreased peak cell densities between 31 × 10^6 and 35 × 10^6 cells/mL were reached verified by a constant but lower specific growth rate of 0.29 1/d (Supplementary Material). This was accompanied by a minor reduction in viability down to 89% on day 17 in comparison to the cFB PerfM approach. Overall, cells showed better and more consisted growth behavior between IH operations as well as increased viability profiles overtime in comparison to the small-scale trials.

To further characterize the new process the average cell diameter was analyzed and is shown in Figure 3B. A similar increase for both reactors is visible during the first few days of cultivation. Subsequent, a stabilization of the diameter at 16–17 µm is visible for both set of experiments. Interestingly, after day 8 first small differences are visible with an overall increased diameter for the cFB PBS experiment of around 0.5 µm over the course of the cultivation. Overall, a specific behavior is noticeable in the diameter oscillation, with a clear increase during the first 12 h after IH operation, and a subsequent decrease over the following 12 h. Interestingly, the cell counts show an inverse behavior meaning that cells either grow in cell count or in cellular diameter within one period. To further analyze the cellular characteristics between both approaches the IVCC (Integral of Viable cell count) and IVCV (Integral of viable cell volume) were calculated. The reactor washed with PBS showed slightly decreased amounts of final IVCC for the overall process compared to the cFB PerfM (345 × 10^6 cells/mL vs. 359 × 10^6 cells/mL, respectively). This decrease can be explained by the small difference in peak cell densities visible in Figure 3A. Vice versa, the values for the IVCV showed a small increase for the cFB PBS experiment, as a result of the increase in diameter visible in Figure 3B.

To further gain insight into the process product specific parameters for both approaches like titer and cell specific productivity (qP) were determined and compared. Figure 3A shows the mAB titer overtime for the cFB PerfM cultivation indicated as solid line and the qP within a FB cycle represented by the individual bars. The titer curve steadily increases to the first IH operation to around 0.5 g/L, consecutively titers within FB cycles showed enhancing values from 1.5 up to 2.2 g/L in the 4th IH cycle

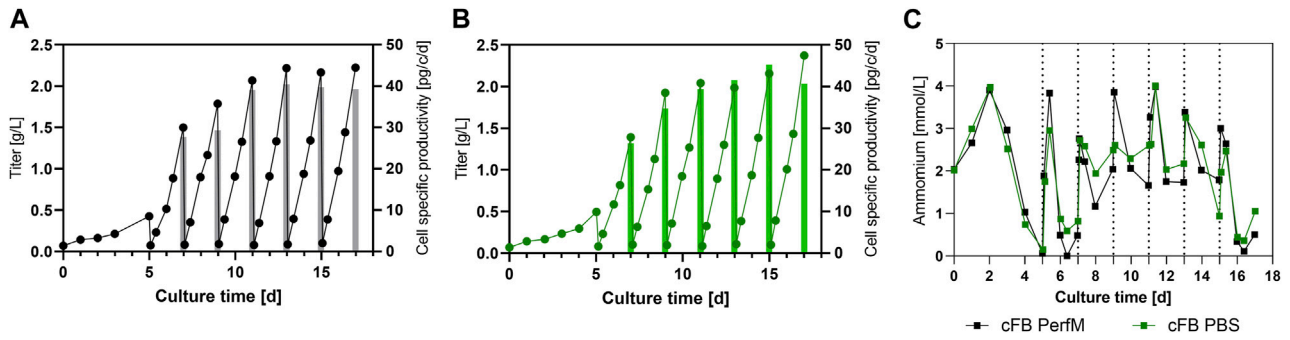

FIGURE 4
Expression characteristics for the benchtop scale reactors for the cFB experiment. **(A, B)** Titer in g/L (line) and cell specific productivity in pg/c/d (bars) for each of the conducted experiments; cFB PerfM **(A)**, cFB PBS **(B)**, respectively. **(C)** Level of Ammonia in mmol/L over the course of the cultivation for both conducted benchtop reactors.

(day 11) and then remained constant around 2.1–2.2 g/L. Similar to the titer values the qP values increased over time from around 27–40 pg/c/d at day 9 after which values remained constant around 40 pg/c/d. Similar to the results from the cFB PerfM reactor the titer in the cFB PBS reactor showed a constant increase in the first days to around 0.5 g/L. Consecutive, an increase of titer up to around 2 g/L on day 9 is visible, after which a constant value could be detected to the end of each cultivation. The qP values show similar values for the PBS reactor as for the PerfM reactor, increasing from 27 up to 40 pg/c/d, with a small outlier on day 15 with 45 pg/c/d. Additionally, during the washing step almost all mAb was removed and thus very high mAb recoveries of approximately 95% were obtained in all FBC operations (data not shown) and titer measurements after IH operation revealed only minor amounts of mAB were left behind in the cell culture resulting in low start concentrations of about 0.1 g/L at the beginning of a cycle (Figures 4A, B). Besides product titers, the ammonia levels were tracked over the term of the cultivations to monitor potential byproduct inhibition (Figure 4C). Overall, ranges between 0 and 4 mmol/L were measured, with values at harvest days ranging from 0 to 2.6 mmol/L for both cultivated reactors. These values matched with the small-scale data shown in Figure 2D for the VVC20 d2 approach. Overall, this data underlines the feasibility of the cFB approach over multiple IH and FB cycles. Furthermore, our data suggest no significant impact due to PBS washing on the process performance.

3.3 Process benchmark

Besides expression levels and metabolic byproducts, the glycan distribution should be investigated and compared to the standard operations. As reference a standard FB operation in duplicate 5L UniVessel, resulting in 3.85 g/L mAb in 12 days and a duplicate perfusion process in 250 mL small-scale system, with perfusion target of 50 × 10^6 cells/mL at 2.5 VVD and 1.54 g/l/d mAb production was utilized. Both processes comprised similar cell line and media systems and are established as processes in our facility. The glycosylation pattern were investigated comparing eight different IgG glycan variants (Figure 5A). While only minor differences could be detected between both cFB variants, we were able to identify distinctions to the other process formats, except for the proportion of G1F. The majority of glycan ratios for the cFB process seemed to be rather comparable to the results of the perfusion process, such as the proportions of Man5, G1, G1F', G0F and G2. However, the other glycan forms G0 and G2F seem to be more comparable to the FB operation. Interestingly, the data reveal a distinct difference between the continuous process types (cFB, perfusion) and the discontinuous process type (FB). However, overall the glycosylation profile of the novel process seems to be rather comparable with the perfusion glycans and exhibit a trend towards higher galactosylated forms.

In addition to the glycan distribution, performance attributes were compared to the standard process types. Therefore, the space time yield (STY) in g/L/d of the processes as well as the media consumption per produced mAb were calculated to assess benchmark characteristics in comparison to the existing process formats (Figure 5B). Of note, the STY for the continuous operations were calculated on daily basis for either the permeate (perfusion) or supernatant (cFB) within the constant phase, the discontinuous STY was calculated with the titer at the last day over the overall process time. As expected, the perfusion process showed the highest STY around 1.54 g/L/d, while the FB process only reached values of 0.32 g/L/d. Both cFB processes reached a STY in between of the standard processes around 1.0 g/L/d due to the elongated process times compared to the FB but decreased cell densities compared to the perfusion process. Furthermore, the ratio between the amount of dry media components, incorporating basal-, feed media and glucose, needed to produce 1 g of mAb was calculated as an indication of the media consumption of each process. Therefore, the total amount of vessel volume exchange per day (VVD) needed to be determined, comprising 1.3 Reactor volume per day (RV) for the cFB PerfM approach and 0.47 RV for the cFB PBS trial. Thereby, to decrease the residual PBS within the cFB PBS trials a high concentration of cells after centrifugation (+100 × 10^6 cells/mL) were executed with the FBC system, possible throughout the functional principle of the system (Saballus et al., 2021). Thereby, this approach shows unbeneficial characteristics for the cFB PerfM trials due to increased wash buffer consumption up to 2.6 reactor volumes per single media exchange (=1.3 RV). However, former studies incorporating a different FBC method showed diminished

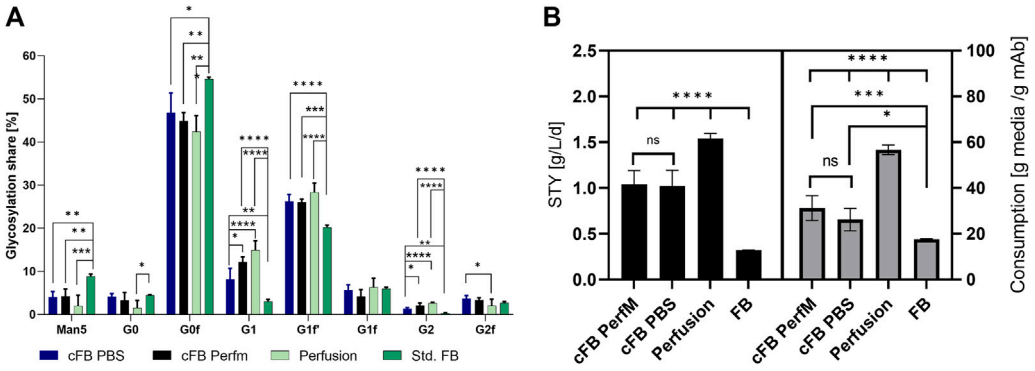

FIGURE 5
Analyzed Critical quality attributes and performance attributes for the proof of concept of the cFB cultivation in comparison to the standard FB and perfusion process. **(A)** Glycan distribution of all four conducted experiments in percentage for the eight investigated glycans. **(B)** Calculations for titer per day and reactor volume (g/L/d) and consumed dry media per mAb (g/g) for the four investigated process types.

values of 1.3 reactor volumes for a single exchange, resulting in 0.7 RV per 2 day FB cycle, which was used for calculation (Reger et al., 2023). The highest media usage per produced Gram mAb was observed for the perfusion process with ~56 g/g, while a very low media consumption could be identified for the FB process with ~17 g/g. Similar to the productivity, the cFB process showed a media consumption ranging in between that of both standard processes from ~31 g/g (cFB PerfM) to ~26 g/g (cFB PBS). As an alternative measure, the cost per mAb produced was calculated utilizing assumptions of Klutz et al., 2016, with basic medium price of 35 €/L, feed media price of 90 €/L and perfusion media price of 15 €/L. Thereby, a similar trend is visible with the lowest cost for the FB with 7.0 €/g mAb, followed by cFB PBS (12.9 €/g mAb); cFB Perf (15.4 €/g mAb) and the highest values for perfusion with 24.45 €/g mAb. This difference within the approaches is caused mainly by the optimized media exchange method in the cFB PBS trials.

Overall, the presented data proofs feasibility of the proposed FB-perfusion hybrid process over a relevant process duration of 17 days to be considered a continuous operation and successful scale-up to benchtop scale. Furthermore, the novel process allows for an efficient combination of the advantages from both standard process types, long duration and increased peak cell densities known from perfusion cultures and low media usage as in a fed batch operation. Therefore, the novel hybrid process format exhibits great potential towards highly productive continuous process.

4 Discussion

The aim of this study was to develop a hybrid process, that combines advantages from discontinuous process operations, such as low media consumption, with the benefits of continuous processes, such as high volumetric productivity. Therefore, a semi-continuous process operation was established, encompassing consecutive FB cycles, each started with a complete media exchange. To identify the most promising process strategy, we firstly varied essential parameters, such as inoculation VCC and FB cycle duration in a small-scale screening approach. The most promising set points could be identified as initial VCCs of 20 × 10^6 cells/mL and a FB duration of 2 days. Subsequent, this approach was successfully transferred to a 5L bench-top reactor combined with a fluidized-bed centrifuge to enable fast, complete, and gentle media renewal. Overall, our data suggest that the established hybrid process represents a feasible and scalable new strategy to successfully combine beneficial characteristics from discontinuous and continuous process operations.

4.1 Small scale process development

For a first assessment of utilizable parameter set in terms of cell concentration at the start of each cycle and the duration of a cycle, the two existing process types, FB and perfusion, were used as a starting point. With the FB data a regular peak VCC of ~25 × 10^6 cells/mL can be reached, indicating that at this cell concentration nutrient limitations or product inhibitions started occurring for this cell line and medium, leading to a transition to the stationary phase. Meanwhile, the perfusion cultivation requires around 2.5 VVD exchange per day to keep a steady cell concentration at 50 × 10^6 cells/mL revealing a possible media supply rate to support proliferating cells at these high densities. With this evidence we hypothesized that a single media renewal in the range of every 2–3 days should allow to sustain cell densities in the following FB cycles of 20–40 × 10^6 cells/mL. Hereby, a reinoculation cell density of 20 × 10^6 cells/mL and a 2-day FB duration could be identified as most promising approach, indicated by elongated cell growth over multiple cycles (six repetitions as shown in Figure 1A) and a small but acceptable decrease in cell viabilities that could partially result from biomass attaching to the vessel and building up in the bioreactors and the utilized semi-perfusion method which is further discussed in Section 4.3. Furthermore, this approach produced around 2 g/L of mAb during each interval with stable ammonia values and increasing cell specific productivities. Increased starting cell counts (30 × 10^6 cells/mL) as well as enhanced FB cycle duration of the cFB process showed undesired process characteristics like diminished proliferation of the cells, enhanced decrease of viabilities over time and build-up of ammonia concentrations. Therefore, these processes were not subjected to

further investigation due to lack in continuous process characteristics. However, this approach did show a strong increase in cell-specific productivities over time. This effect especially with increasing expression levels for the two respective cultures is a known effect from previous studies where a media exchange in the stationary phase overall increased expression, but did not result in additional cell proliferation (Reger et al., 2023). The explanation for lack of continuous process characteristics, i.e., the decreasing viabilities and cell proliferation, within these cultures could be an irreversible transition of the cells into the stationary phase without further proliferation potential. This transition can be triggered by the accumulation of metabolic byproducts, which ultimately limit further proliferation and finally reduce viabilities (Lao and Toth, 1997; Mulukutla et al., 2017; Sha et al., 2021). Another explanation for this irreversible transition of the respective cultures (30 d2; 20 d3) could be a limitation of nutrients (Xie and Wang, 1994; Xie et al., 1997; Lu et al., 2013). The commonly analyzed nutrients, such as glucose and glutamine showed no obvious limitations (data not shown), but further nutrients analysis, e.g., to assess amino acid concentrations or organic acid contents, could be conducted to investigate the nutrient levels in the unstable cultures. Nevertheless, the primary goal of this proof-of-concept study was to find a viable process set up that will allow for a continuous process operation with existing cell line and media platforms.

4.2 Proof of concept

In the next step the preferential process parameter set was scaled-up to two 5L bioreactor utilizing a fully scalable FBC system for cell and media separation. Both reactors were run in parallel, only differing in the media exchange method. Thereby, the reactors differed in media matrix, PBS and enriched basal media ratio. With this modification the media usage of the cell wash could be diminished to 0.47 RV instead of around 1.3 RV for a single FB cycle. Yet, due to this method small amounts (5%–10%) of PBS remained in the cell culture, which might influence process performance. Indeed, small differences between the reactors could be seen for peak cell densities, viability, and cellular diameter over time. An explanation for the decreased peak VCCs alongside the increase in cell diameter for the PBS process could be a minor shift from cell proliferation towards cell size increase. This hypothesis is supported by the IVCC and IVCV data (Figure 3C), which confirm a similar overall cell volume (IVCV) for both reactors, while slight differences in the cell counts (IVCC) can be seen. The shift from cell proliferation to cell size increase could have been triggered by the increased ion concentration that the cells of the cFB PBS reactor have been subjected to by the residual PBS. The main components of the utilized PBS are sodium, chloride and potassium ions, which are commonly utilized to induce hyper osmolality within cell cultures (Pfizenmaier et al., 2015). In accordance, these "hyper osmolality" studies have shown similar effects on cellular behavior, e.g., reduced peak cell densities and increased cell volume (Alhuthali et al., 2021; Romanova et al., 2021). Therefore, the observed shift towards cell size increase is most likely triggered by the residual PBS. However, overall our data suggest only minimal influences based on the washing buffer, since both cultivations were characterized by steady growth, high viability and comparable product titers over all six conducted repetitions (Figures 3A, B). This leads to the conclusion that PBS can be used as wash buffer without notable impact on the process, resulting it a significant reduction of nutrient-rich and costly perfusion media.

Of note, within the conducted experiment we could observe an increasing cell specific productivity for the novel process, consistent among the screening cultivations as well as the processes at bench-top scale (Figures 2A–C, 4A, B). Exemplified for the 5L cultivations, the qP values showed an increase up to 1.5-fold over the course of cultivation stabilizing around day 11 for both reactors. The increase of cell specific productivity is one of the major goals within the upstream bioprocessing to further boost the productivity with similar plant size and process operation. The enhanced cellular expression thereby is most likely connected to the respective cell diameter increase, that correlates very nicely and also reaches a steady state from ~day 11 (Figure 3B). Further, a similar behavior could be reported in earlier studies using an FBC system (Reger et al., 2023) as well as other studies revealing a strong correlation of cellular diameter and cell specific productivity within a common FB design (Lloyd et al., 2000; Pan et al., 2017). Therefore, the new developed process format should be further analyzed to reveal the genetic and metabolic background of this beneficial behavior towards the cellular expression, but this was not the scope of this work.

Besides the expression levels of the mAb the glycosylation pattern of the product needs to be classified and compared for new designed process. Thereby the glycosylation pattern can impact the *in-vivo* half-life, therapeutic potency as well as toxicological profile of the antibody (Liu, 2015; Smith and Bertozzi, 2021). To assess these a glycan analysis was conducted release a percentage share in glycan distribution for alle conducted processes visible in Figure 5A. Thereby, significant differences were visible between the continuous and discontinuous processes for all glycans except G0, G1F and G2F. For the continuous processes shifted glycans towards higher galactosylated forms, like G1, G1F' and G2 were visible, meanwhile Man5 and G0F showed lower shares in comparison to the discontinuous process. An explanation for the shift could be the decreased amount of inhibitory molecules for the continuous process, due to the exchange of spend media (Pereira et al., 2018). Vice versa, discontinuous process types, comprising a stationary phase, show an increased amount of inhibitory molecules. These inhibitory molecules can have an influence on intracellular processes and influence the glycosylation pattern of the product as described in different studies (Gramer and Goochee, 1993; Lipscomb et al., 2005, 2005; Rodriguez et al., 2005). One example for inhibitory molecules is ammonia, for which it has been shown in different studies to influence the galactosylation of the desired product (Borys et al., 1994; Gawlitzek et al., 2000; Yang and Butler, 2002). Interestingly, the ammonia concentration showed high discrepancy between the continuous process (≈4–6 mM) and the discontinuous operations (≈12 mM) (data not shown). Therefore, an influence of the ammonia could be suggested, but other impacts of the diverse inhibitory matrix cannot be suspended. Further studies would be needed to investigate the impact of the inhibitory matrix.

The glycans between the cFB process comprising PBS as wash media showed smaller alterations for the G1, G2 and G2F to the

perfusion process. Furthermore, significant shifts between both the cFB processes for the G1 and G2 glycans were visible. An explanation for these shifts could be the increased concentration of ions, mainly sodium and chloride as main ingredients of PBS, which could impact the intracellular processes. However, this shift mainly occurs for glycan structures with low percentage share, especially for the comparison of the two IH operation, which could indicate none or just small impact of the PBS. Further studies need to be conducted to define if the changed glycans impact the expressed product. Overall, the cFB processes showed comparable glycan distributions to those of the perfusion process, while the distribution deviated from that of the discontinuous FB.

4.3 Process benchmark and challenges

Main goals of all process intensification strategies are to increase volumetric productivity, decrease production time or plant footprint. To show the impact of the novel process scenario a comparison with the respective standard FB as well as perfusion process was conducted. Firstly, we calculated the space time yield (STY) of all processes. We could identify increasing values from the FB process with 0.32 g/L/d over both cFB processes with 1.0 g/L/d to the perfusion process with 1.54 g/L/d (Figure 5B). The increase in STY from discontinuous to continuous processes is well known and can be mainly traced back to the significantly higher cell densities that can be maintained with continuous operations. This is in accordance with the new developed processes analyzed in this study. While the common FB process comprise a VCC from 0.3–25 × 10^6 cells/mL, the cFB process reaches cell counts between 20–40 × 10^6 cells/mL, while the highest cell densities could be reached with the perfusion culture at constant values around 50 × 10^6 cells/L. A further important factor is the process duration. In this context, cultivations comprising an elongated phase with high cell densities that result in high product titers, like cFB and perfusion processes, increases the STY (MacDonald et al., 2022). Vice versa, the FB process, incorporating a substantial process time share of low cell counts during the growth phase, characterized by a lower STY value. Overall, the novel hybrid process is characterized by a significant productivity increase compared to the FB operation, represented by an impressive +217% STY, but still below (~34%) of the values that can be reached via perfusion cultivation. However, a strong drawback of perfusion processes is the comparably high media consumption, usually exceeding the two media exchanges per day within a common perfusion cultivation (Meuwly et al., 2006; Walther et al., 2019). This could be clearly confirmed for the processes evaluated in the present study. Our data show that the respective perfusion process utilizes ~222% more media to produce an equal amount of the mAB compared to the discontinuous FB operation (compare Figure 5B). This pattern can be easily explained, since during the last cultivation phase of the FB no cell proliferation needs to be supported by excessive media exchange, while constant proliferation and therefore nutrient supply is required for continuous processes. Interestingly, despite its continuous character, the novel cFB process shows again values between both process formats that results in a clear increase in media usage compared to FB (~+48%) but still an up to ~50% saving with respect to the standard continuous (perfusion) process. This low media consumption for a (semi)-continuous process can be explained by the process design which is enabled by the FBC as media renewal system. Advantages of the FBC operation are the fast and complete media exchanged at specified times. Common filter-based retention devices utilize a continuous exchange creating a intermixture of fresh and spend media in the reactor (Brantley et al., 2021). This intermixture leads to partial loss of fresh media into the following downstream operation. This loss in non-utilized media can be significantly reduced with the FBC operation due to the complete media exchange. A further advantage is the complete transfer of the produced mAB into the downstream, while during standard perfusion cultivation usually significant amounts are lost in the bleed or retained in the bioreactor due to filter sieving (Bielser et al., 2021). In contrast, due to the utilization of the FBC the complete produced mAB is harvested and fed into the subsequent downstream. Moreover, by using PBS during the wash step of the operation a 1:1 media exchange can be achieved, further decreasing the media consumption of the process.

Besides the discussed decreased media consumption and productivity, the new developed process could combine several advantageous characteristics from both cultivation types. Firstly, the elongated duration could be transferred from the continuous cultivation not only improve the STY but as well possibly diminish the number of necessary seed train runs further decreasing labor costs and good expenditures. Secondly, the cFB process comprises the process monitoring of a FB process, which is far simpler than the complex, continuous control of the peripherical devices within a filter-based perfusion cultivation. This advantage not only decrease the process monitoring but as well increase the flexibility to pursue the media exchange with the fast and gentle FBC operation. Another benefit of the utilized separation method towards filter-based system is comprised by the impossibility of filter fouling, further improve stability of the new developed process. Overall, a new process could be established comprising a continuous character with elongated plant utilization and increased productivity with the diminished media utilization and process monitoring of a discontinuous process. Further, leading to our conclusion that the continuous fed-batch shows a great potential to improve current bioprocess technologies not only in technical but as well in economical perspective.

As usual, new developments, especially within the bioprocess manufacturing, typically arise with a new set of challenges. One clear challenge is the need for suitable small-scale screening platforms (Gagliardi et al., 2019). As can be seen from the results gained in this study, repeatability of the small-scale experiments in comparison to the benchtop-scale is limited and clear difference within growth and viability at the end of the process became apparent for the scale down model, possibly caused by the utilized IH mimic method. This mimic comprised a manually exchange of media after a common dead-end centrifugation. Thereby, not only residuals of media components could be retained within the cell pellet but as well small cell debris and dead cells which subsequent could impact the performance of the cell culture within the next FB cycle of the process. These residuals of media as well as cell debris possibly can be removed by an higher extent with the FBC due to the functional principle. Therefore, a more suitable small-scale system would be desirable to increase the insight into the process on a screening level. One possibility thereby would be to develop a scale-down model for the utilized FBC system and couple it with a suitable high throughput upstream system. However, the utilized method showed adequate comparability of the current process

characteristics and limitations to gain sufficient predictivity for the scale-up of the process. Very similar challenges are known for the scale down models utilized for the development of perfusion cultivation formats, were commonly semi-perfusion methods, either in spin tubes or 15 mL reactor systems, are used based on centrifugation or sedimentation strategies to renew the media. These methods proofed feasible for a first assessments of, for example, media consumption, clone feasibility and impact on CQAs (Kreye et al., 2019). However transferability of the processes into larger scale including filter membrane based cell separation methods remain limited especially in regard to continuous media flow, removal of cell debris and filter utilization (Mayrhofer et al., 2021). Nonetheless, the first processes assessments in high-throughput are important for a fast and streamlined transfer of clones and prove towards the new process strategy. Thereby, the fast and easy transfer of cell lines is one key challenge for to facilitate bioprocess development.

Further, new process strategies result in modified requirements towards the bioreactor set-up, may include new or repurposed equipment, which accordingly will require validation studies and risk assessments to be suitable for clinically relevant biopharmaceutical manufacturing processes. In the presented work, two main alterations to the platform processes and equipment have been introduced. One the one hand, an FBC system was utilized, that has been primarily been developed and used as cell harvest operation unit to separate product and cells at the end of a process. Therefore, further qualification of the FBC system for this continuous application needs to be conducted to show the feasibility especially in an GMP environment. As note, in the current study no further challenges occurred due to the continuous application, therefore we do not see any obvious obstacles from the current point of view in further qualification of this method.

Secondly, in comparison to the fed-batch and also the perfusion process the cell broth leaves the bioreactor and therefore, the controlled cultivation vessel, completely for a short period of time. However, the uncontrolled time is increased for the cFB method, in comparison to the perfusion, mainly due to the complete processing of the reactor. This elongated uncontrolled time can impact the cell culture performance and should be investigated in more depth for further risk assessments. However, for now no further negative impacts due to the uncontrolled environment could be detected in our studies. Furthermore, as mentioned, an additional step for media exchange in the cFB and perfusion is applied, therefore a similar risk or both processes can be assumed. Moreover, the increase in peripheral devices can be seen as negative impact on the process economics. Thereby, a holistic examination of the underlying process economics including all three upstream process operations and the subsequent downstream operation would be necessary to draw any comprehensive conclusion on overall economic implications of the novel process. Similar to the business case, process scale-up into pilot and production scale should be investigated within further studies. Thereby, suitable approaches like a scale-up model of the utilized FBC system are available however, a proof of concept needs to be conducted to show applicability for the mentioned scales. Despite the several challenges for implementation, the developed hybrid process operation indicates a set of significant improvements with the potential to outperform the established process operations.

5 Conclusion and outlook

In this study an innovative process at the interface of FB and perfusion was developed, facilitating high volumetric productivity and low media consumption in a continuous process format. Further, our proof-of concept study confirmed feasibility over extended culture durations, indicating the potential to be utilized in a continuous process approach. Due to the scalable FBC system alongside a standard FB-bioreactor this process is easy scalable and requires no physical filter-based cell retention device with the associated filter-related issues. This makes the novel process highly interesting for further investigations and process development efforts, for example, further screening of cell lines or media systems. Furthermore, transferability of the presented concept should be investigated for further processes, including non-CHO cell lines and a variety of products such as viral vectors or cell therapies. Overall, the novel developed process showed potential to further enhance the product yields by simultaneously decreasing expenditures.

Data availability statement

The raw data supporting the conclusion of this article will be made available by the authors, without undue reservation.

Author contributions

LR: conceptualization, methodology, investigation, visualization, writing—original draft, writing—review and editing. MS: conceptualization, methodology, investigation, writing—review and editing. AK: methodology, investigation, visualization, writing—original draft. MK: Writing—review and editing. RW: writing—review and editing. DM: supervision, methodology, writing—review and editing. JN: supervision, methodology, writing—review and editing. All authors contributed to the article and approved the submitted version.

Funding

The authors declare that this study received funding from Sartorius Stedim Biotech GmbH. The funder was not involved in the study design, collection, analysis, interpretation of data, the writing of this article, or the decision to submit it for publication.

Acknowledgments

The authors thank the BioProcessing team of Sartorius Corporate Research, without whose support this study would not have been feasible.

Conflict of interest

Authors LR, MS, AK, MK, and JN were employed by the company Sartorius.

The remaining authors declare that the research was conducted in the absence of any commercial or financial relationships that could be construed as a potential conflict of interest.

Publisher's note

All claims expressed in this article are solely those of the authors and do not necessarily represent those of their affiliated organizations, or those of the publisher, the editors and the reviewers. Any product that may be evaluated in this article, or claim that may be made by its manufacturer, is not guaranteed or endorsed by the publisher.

Supplementary material

The Supplementary Material for this article can be found online at: https://www.frontiersin.org/articles/10.3389/fbioe.2023.1211410/full#supplementary-material

References

Abu-Absi, S., Xu, S., Graham, H., Dalal, N., Boyer, M., and Dave, K. (2014). "Cell culture process operations for recombinant protein production," in *Mammalian cell cultures for biologics manufacturing*. Editors W. Zhou, and A. Kantardjieff (Berlin, Heidelberg: Springer Berlin Heidelberg), 35–68.

Alhuthali, S., Kotidis, P., and Kontoravdi, C. (2021). Osmolality effects on CHO cell growth, cell volume, antibody productivity and glycosylation. *Int. J. Mol. Sci.* 22, 3290. doi:10.3390/ijms22073290

Bettinardi, I. W., Castan, A., Medronho, R. A., and Castilho, L. R. (2020). Hydrocyclones as cell retention device for CHO perfusion processes in single-use bioreactors. *Biotechnol. Bioeng.* 117, 1915–1928. doi:10.1002/bit.27335

Bielser, J.-M., Aeby, M., Caso, S., Roulet, A., Broly, H., and Souquet, J. (2021). Continuous bleed recycling significantly increases recombinant protein production yield in perfusion cell cultures. *Biochem. Eng. J.* 169, 107966. doi:10.1016/j.bej.2021.107966

Borys, M. C., Linzer, D. I., and Papoutsakis, E. T. (1994). Ammonia affects the glycosylation patterns of recombinant mouse placental lactogen-I by Chinese hamster ovary cells in a pH-dependent manner. *Biotechnol. Bioeng.* 43, 505–514. doi:10.1002/bit.260430611

Brantley, T., Bogue, J., Denny, K., Elouafiq, S., Madren, S., Nakhle, B., et al. (2021). A novel approach to residence time distribution characterization in a mAb continuous process. *Biotechnol. Bioeng.* 118, 3486–3498. doi:10.1002/bit.27775

Castilho, L. R., and Medronho, R. A. (2002). Cell retention devices for suspended-cell perfusion cultures. *Adv. Biochem. Eng. Biotechnol.* 74, 129–169. doi:10.1007/3-540-45736-4_7

Dowd, J. E., Jubb, A., Kwok, K. E., and Piret, J. M. (2003). Optimization and control of perfusion cultures using a viable cell probe and cell specific perfusion rates. *Cytotechnology* 42, 35–45. doi:10.1023/A:1026192228471

Gagliardi, T. M., Chelikani, R., Yang, Y., Tuozzolo, G., and Yuan, H. (2019). Development of a novel, high-throughput screening tool for efficient perfusion-based cell culture process development. *Biotechnol. Prog.* 35, e2811. doi:10.1002/btpr.2811

Gawlitzek, M., Ryll, T., Lofgren, J., and Sliwkowski, M. B. (2000). Ammonium alters N-glycan structures of recombinant TNFR-IgG: Degradative versus biosynthetic mechanisms. *Biotechnol. Bioeng.* 68, 637–646. doi:10.1002/(sici)1097-0290(20000620)68:6<637:aid-bit6>3.0.co;2-c

Gramer, M. J., and Goochee, C. F. (1993). Glycosidase activities in Chinese hamster ovary cell lysate and cell culture supernatant. *Biotechnol. Prog.* 9, 366–373. doi:10.1021/bp00022a003

Hansel, T. T., Kropshofer, H., Singer, T., Mitchell, J. A., and George, A. J. T. (2010). The safety and side effects of monoclonal antibodies. *Nat. Rev. Drug Discov.* 9, 325–338. doi:10.1038/nrd3003

Hiller, G. W., Ovalle, A. M., Gagnon, M. P., Curran, M. L., and Wang, W. (2017). Cell-controlled hybrid perfusion fed-batch CHO cell process provides significant productivity improvement over conventional fed-batch cultures. *Biotechnol. Bioeng.* 114, 1438–1447. doi:10.1002/bit.26259

Janoschek, S., Schulze, M., Zijlstra, G., Greller, G., and Matuszczyk, J. (2019). A protocol to transfer a fed-batch platform process into semi-perfusion mode: The benefit of automated small-scale bioreactors compared to shake flasks as scale-down model. *Biotechnol. Prog.* 35, e2757. doi:10.1002/btpr.2757

Jayapal, K. P., Wlaschin, K. F., Hu, W-S., and MirandaYap, G. S. (2007). Recombinant protein therapeutics from CHO cells - 20 Years and counting. *Chem. Eng. Prog.* 103, 40.

Johnson, D. (2018). Biotherapeutics: Challenges and opportunities for predictive toxicology of monoclonal antibodies. *IJMS* 19, 3685. doi:10.3390/ijms19113685

Kim, J. Y., Kim, Y.-G., and Lee, G. M. (2012). CHO cells in biotechnology for production of recombinant proteins: Current state and further potential. *Appl. Microbiol. Biotechnol.* 93, 917–930. doi:10.1007/s00253-011-3758-5

Klutz, S., Holtmann, L., Lobedann, M., and Schembecker, G. (2016). Cost evaluation of antibody production processes in different operation modes. *Chem. Eng. Sci.* 141, 63–74. doi:10.1016/j.ces.2015.10.029

Kreye, S., Stahn, R., Nawrath, K., Goralczyk, V., Zoro, B., and Goletz, S. (2019). A novel scale-down mimic of perfusion cell culture using sedimentation in an automated microbioreactor (SAM). *Biotechnol. Prog.* 35, e2832. doi:10.1002/btpr.2832

Lao, M. S., and Toth, D. (1997). Effects of ammonium and lactate on growth and metabolism of a recombinant Chinese hamster ovary cell culture. *Biotechnol. Prog.* 13, 688–691. doi:10.1021/bp9602360

Lipscomb, M. L., Palomares, L. A., Hernández, V., Ramírez, O. T., and Kompala, D. S. (2005). Effect of production method and gene amplification on the glycosylation pattern of a secreted reporter protein in CHO cells. *Biotechnol. Prog.* 21, 40–49. doi:10.1021/bp049761m

Liu, L. (2015). Antibody glycosylation and its impact on the pharmacokinetics and pharmacodynamics of monoclonal antibodies and Fc-fusion proteins. *J. Pharm. Sci.* 104, 1866–1884. doi:10.1002/jps.24444

Lloyd, D. R., Holmes, P., Jackson, L. P., Emery, A. N., and Al-Rubeai, M. (2000). Relationship between cell size, cell cycle and specific recombinant protein productivity. *Cytotechnology* 34, 59–70. doi:10.1023/A:1008103730027

Lu, F., Toh, P. C., Burnett, I., Li, F., Hudson, T., Amanullah, A., et al. (2013). Automated dynamic fed-batch process and media optimization for high productivity cell culture process development. *Biotechnol. Bioeng.* 110, 191–205. doi:10.1002/bit.24602

MacDonald, M. A., Nöbel, M., Roche Recinos, D., Martínez, V. S., Schulz, B. L., Howard, C. B., et al. (2022). Perfusion culture of Chinese Hamster Ovary cells for bioprocessing applications. *Crit. Rev. Biotechnol.* 42, 1099–1115. doi:10.1080/07388551.2021.1998821

Mayrhofer, P., Castan, A., and Kunert, R. (2021). Shake tube perfusion cell cultures are suitable tools for the prediction of limiting substrate, CSPR, bleeding strategy, growth and productivity behavior. *J. Chem. Technol. Biotechnol.* 96, 2930–2939. doi:10.1002/jctb.6848

Meuwly, F., Weber, U., Ziegler, T., Gervais, A., Mastrangeli, R., Crisci, C., et al. (2006). Conversion of a CHO cell culture process from perfusion to fed-batch technology without altering product quality. *J. Biotechnol.* 123, 106–116. doi:10.1016/j.jbiotec.2005.10.013

Mulukutla, B. C., Kale, J., Kalomeris, T., Jacobs, M., and Hiller, G. W. (2017). Identification and control of novel growth inhibitors in fed-batch cultures of Chinese hamster ovary cells. *Biotechnol. Bioeng.* 114, 1779–1790. doi:10.1002/bit.26313

Pan, X., Dalm, C., Wijffels, R. H., and Martens, D. E. (2017). Metabolic characterization of a CHO cell size increase phase in fed-batch cultures. *Appl. Microbiol. Biotechnol.* 101, 8101–8113. doi:10.1007/s00253-017-8531-y

Pereira, S., Kildegaard, H. F., and Andersen, M. R. (2018). Impact of CHO metabolism on cell growth and protein production: An overview of toxic and inhibiting metabolites and nutrients. *Biotechnol. J.* 13, e1700499. doi:10.1002/biot.201700499

Pfizenmaier, J., Matuszczyk, J.-C., and Takors, R. (2015). Changes in intracellular ATP-content of CHO cells as response to hyperosmolality. *Biotechnol. Prog.* 31, 1212–1216. doi:10.1002/btpr.2143

Pollock, J., Ho, S. V., and Farid, S. S. (2013). Fed-batch and perfusion culture processes: Economic, environmental, and operational feasibility under uncertainty. *Biotechnol. Bioeng.* 110, 206–219. doi:10.1002/bit.24608

Presta, L. G. (2008). Molecular engineering and design of therapeutic antibodies. *Curr. Opin. Immunol.* 20, 460–470. doi:10.1016/j.coi.2008.06.012

Reger, L. N., Saballus, M., Matuszczyk, J., Kampmann, M., Wijffels, R. H., Martens, D. E., et al. (2023). Boosting productivity for advanced biomanufacturing by Re-using viable cells. *Front. Bioeng. Biotechnol.* 11, 1106292. doi:10.3389/fbioe.2023.1106292

Rodriguez, J., Spearman, M., Huzel, N., and Butler, M. (2005). Enhanced production of monomeric interferon-beta by CHO cells through the control of culture conditions. *Biotechnol. Prog.* 21, 22–30. doi:10.1021/bp049807b

Romanova, N., Niemann, T., Greiner, J. F. W., Kaltschmidt, B., Kaltschmidt, C., and Noll, T. (2021). Hyperosmolality in CHO culture: Effects on cellular behavior and morphology. *Biotechnol. Bioeng.* 118, 2348–2359. doi:10.1002/bit.27747

Saballus, M., Nisser, L., Kampmann, M., and Greller, G. (2021). A novel clarification approach for intensified monoclonal antibody processes with 100 million cells/mL using a single-use fluidized bed centrifuge. *Biochem. Eng. J.* 167, 107887. doi:10.1016/j.bej.2020.107887

Schulze, M., Lemke, J., Pollard, D., Wijffels, R. H., Matuszczyk, J., and Martens, D. E. (2021). Automation of high CHO cell density seed intensification via online control of the cell specific perfusion rate and its impact on the N-stage inoculum quality. *J. Biotechnol.* 335, 65–75. doi:10.1016/j.jbiotec.2021.06.011

Schulze, M., Niemann, J., Wijffels, R. H., Matuszczyk, J., and Martens, D. E. (2022). Rapid intensification of an established CHO cell fed-batch process. *Biotechnol. Prog.* 38, e3213. doi:10.1002/btpr.3213

Sha, S., Kuang, B., and Yoon, S. (2021). Characterization of dynamic regulation in Chinese hamster ovary (CHO) cell cultures in the late exponential phase. *Biochem. Eng. J.* 167, 107897. doi:10.1016/j.bej.2020.107897

Smith, B. A. H., and Bertozzi, C. R. (2021). The clinical impact of glycobiology: Targeting selectins, siglecs and mammalian glycans. *Nat. Rev. Drug Discov.* 20, 217–243. doi:10.1038/s41573-020-00093-1

Voisard, D., Meuwly, F., Ruffieux, P.-A., Baer, G., and Kadouri, A. (2003). Potential of cell retention techniques for large-scale high-density perfusion culture of suspended mammalian cells. *Biotechnol. Bioeng.* 82, 751–765. doi:10.1002/bit.10629

Walther, J., Lu, J., Hollenbach, M., Yu, M., Hwang, C., McLarty, J., et al. (2019). Perfusion cell culture decreases process and product heterogeneity in a head-to-head comparison with fed-batch. *Biotechnol. J.* 14, e1700733. doi:10.1002/biot.201700733

Xie, L., and Wang, D. I. (1994). Fed-batch cultivation of animal cells using different medium design concepts and feeding strategies. *Biotechnol. Bioeng.* 43, 1175–1189. doi:10.1002/bit.260431123

Xie, L., Nyberg, G., Gu, X., Li, H., Möllborn, F., and Wang, D. I. C. (1997). Gamma-interferon production and quality in stoichiometric fed-batch cultures of Chinese hamster ovary (CHO) cells under serum-free conditions. *Biotechnol. Bioeng.* 56, 577–582. doi:10.1002/(SICI)1097-0290(19971205)56:5<577:AID-BIT11>3.0.CO;2-9

Xu, S., Gavin, J., Jiang, R., and Chen, H. (2017). Bioreactor productivity and media cost comparison for different intensified cell culture processes. *Biotechnol. Prog.* 33, 867–878. doi:10.1002/btpr.2415

Yang, M., and Butler, M. (2002). Effects of ammonia and glucosamine on the heterogeneity of erythropoietin glycoforms. *Biotechnol. Prog.* 18, 129–138. doi:10.1021/bp0101334

Yang, W. C., Lu, J., Kwiatkowski, C., Yuan, H., Kshirsagar, R., Ryll, T., et al. (2014). Perfusion seed cultures improve biopharmaceutical fed-batch production capacity and product quality. *Biotechnol. Prog.* 30, 616–625. doi:10.1002/btpr.1884

Yongky, A., Xu, J., Tian, J., Oliveira, C., Zhao, J., McFarland, K., et al. (2019). Process intensification in fed-batch production bioreactors using non-perfusion seed cultures. *mAbs* 11, 1502–1514. doi:10.1080/19420862.2019.1652075

Frontiers in
Bioengineering and Biotechnology

Accelerates the development of therapies, devices, and technologies to improve our lives

A multidisciplinary journal that accelerates the development of biological therapies, devices, processes and technologies to improve our lives by bridging the gap between discoveries and their application.

Discover the latest Research Topics

See more →

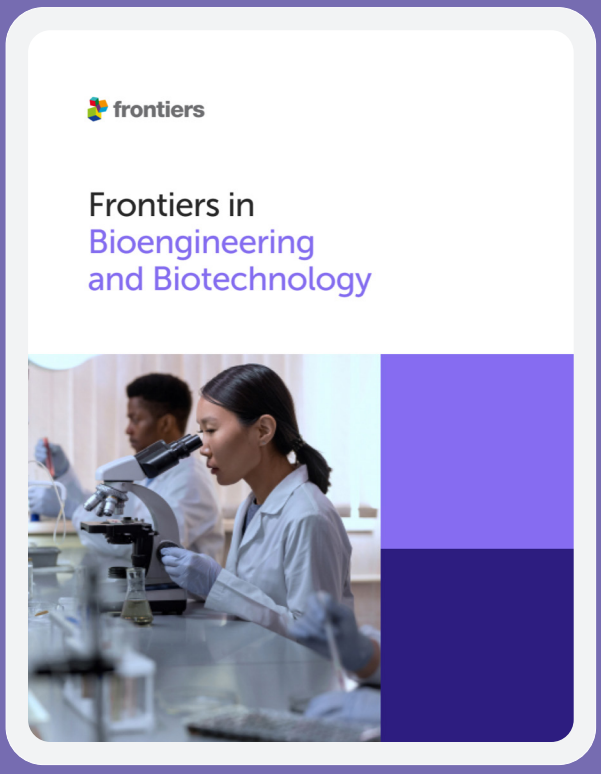

Frontiers

Avenue du Tribunal-Fédéral 34
1005 Lausanne, Switzerland
frontiersin.org

Contact us

+41 (0)21 510 17 00
frontiersin.org/about/contact